ISSN 2398-6611 (Online)

Faculty of Engineering and Technology

Faculty Research Week

2017 Proceedings

22nd – 26th May

2017

Faculty of Engineering and Technology
James Parsons Building, Byrom Street, Liverpool, L3 3AF

MMXVII

Contents

Curtis Maines

A framework for the extension and visualisation of cyber security requirements in modelling languages

Curtis Maines[1], Bo Zhou[2], Stephen Tang[3] and Qi Shi[4]
Department of Computer Science, Byrom Street, L3 3AF
E-mail address: c.l.maines@2011.ljmu.ac.uk[1], b.zhou@ljmu.ac.uk[2], s.o.tang@ljmu.ac.uk[3], q.shi@ljmu.ac.uk[4]

Abstract: Every so often papers are published presenting a new extension for modelling cyber security requirements in *Business Process Model and Notation* (BPMN). The frequent production of new extensions by experts belies the need for a richer and more usable representation of security requirements in BPMN processes. In this paper, we present our work considering an analysis of existing extensions and identify the notational issues present within each of them. We discuss how there is yet no single extension which represents a comprehensive range of cyber security concepts. Consequently, there is no adequate solution for accurately specifying cyber security requirements within BPMN. To address this, we propose a new framework that can be used to extend, visualise and verify cyber security requirements in not only BPMN, but any other existing modelling language. We investigate a new approach to modelling security and propose a solution that overcomes current issues whilst still providing functionality to include all concepts potentially modellable in BPMN related to cyber security.

Keywords: security framework; modelling language; BPMN; business process

1. Introduction

BPMN fulfils the requirement of visually representing business processes and is now the industry standard for their modelling [1, 2]. Nevertheless, even though security directly affects the functionality of business processes, BPMN has no support for specifying cyber security requirements [3, 4]. Current BPMN security extensions have made attempts, but they are being constructed unsystematically, without any empirical evidence to support their choice of concepts [5] or notational design.

The objective of this paper is to propose a new framework for visualising and verifying comprehensive cyber security requirements within not only BPMN, but any modelling language. Unlike current approaches, our framework is built upon existing literature and empirical evidence. From our evaluation of existing extensions, we are able to identify the problem areas and propose a new set of requirements for avoiding them. Along with these and existing theories, we are able to propose a framework that can be used for extending any modelling language with security requirements.

2. Existing BPMN Security Extensions

For existing extensions, the "Physics of Notations" (PoN) principles defined by Moody [6] are used for their evaluation. This is to ensure a scientific approach is kept in their assessment. These principles are frequently used in the evaluation of modelling languages including that of BPMN [7, 8].

These principles are as follows: *semiotic clarity, perceptual discriminability, semantic transparency, complexity management, cognitive integration, visual expressiveness, dual coding, graphic economy,* and *cognitive fit* [6]. Due to lack of space, we are unable to include definitions in this paper. For any uncertainties please refer to the respective paper. We have already evaluated most existing extensions against the PoN in previous papers [9, 10] and therefore will be brief in their assessment for this one. Of the nine principles, we do not consider *cognitive integration* in our assessment. We feel this is a principle that can only be fairly evaluated against a standalone language. It is difficult for an extension to meet this requirement if the parent language does not.

Rodriguez *et al.* [3] extension managed to satisfy just one, *graphic economy*, of the eight principles (disregarding *cognitive integration*). With the passed principle being solely down to the fact that the notation is *symbol deficit*. Saleem *et al.* [4], slightly newer, security extension satisfies four PoN principles (*perceptual discriminability*, *semantic transparency*, *graphic economy* and *cognitive fit*). Salnitri *et al.* SecBPMN2 [2] notation is also able to satisfy four of the eight principles (*perceptual discriminability, semantic transparency, graphic economy* and *cognitive fit*), matching that of Saleem *et al.* Labda *et al.* security notation [12] managed to satisfy two (*perceptual discriminability* and *graphic economy*) of the eight PoN principles. Koh and Zhou's notation [13] also satisfies just two (*dual coding* and *graphic economy*) of the eight principles. An example of existing approaches to BPMN security extensions can be seen in figure 1; poor *complexity management* and nearing *cognitive limits*.

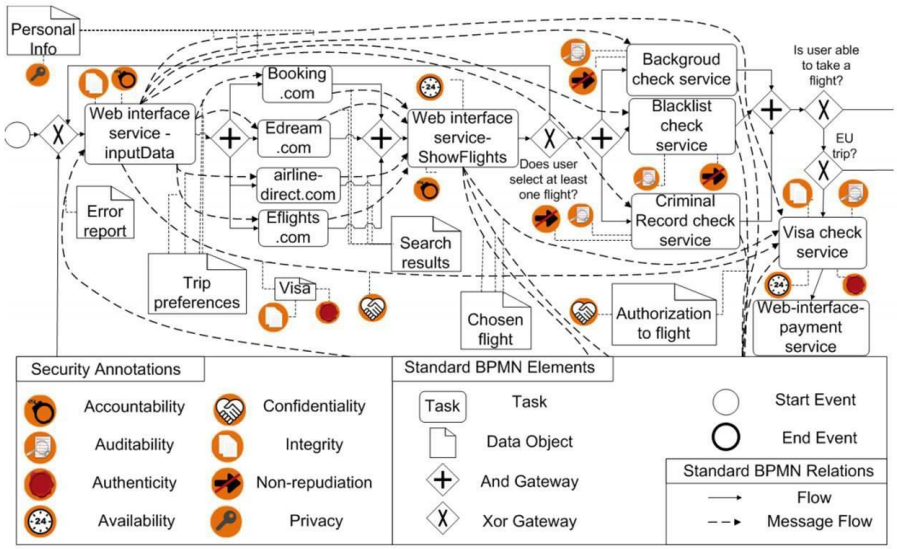

Figure 1 Salnitri et al. SecBPMN2 notation

From this review, of the five extensions evaluated we can see that none manage to satisfy an adequate number of Moody's principles. Moody discussed how there are trade-offs amongst the principles and satisfying one may have a negative effect on another. Nevertheless, certain principles such as *complexity management* should always be achieved, especially in software engineering [11]. There is need for an extension that is not only comprehensive to the domain but can also satisfy the most optimal number of principles.

3. Proposed Framework

This leads onto the core novelty of our work to overcome the aforementioned issues: a framework for the extension and visualisation of cyber security requirements in modelling languages, see figure 2. Our framework consists of three core roles; *language architect, application developer* and *end user*. All of which, are necessary for the successful design, implementation and utilisation of a security extension. The roles are structured vertically in the framework and represent the strict chronological order of development from bottom-to-top, (like that of a brick wall). For the most part, this rule is also

true when reading the framework from left-to-right. Regardless of this however, each component is numbered to reiterate the order that should be followed when creating an extension.

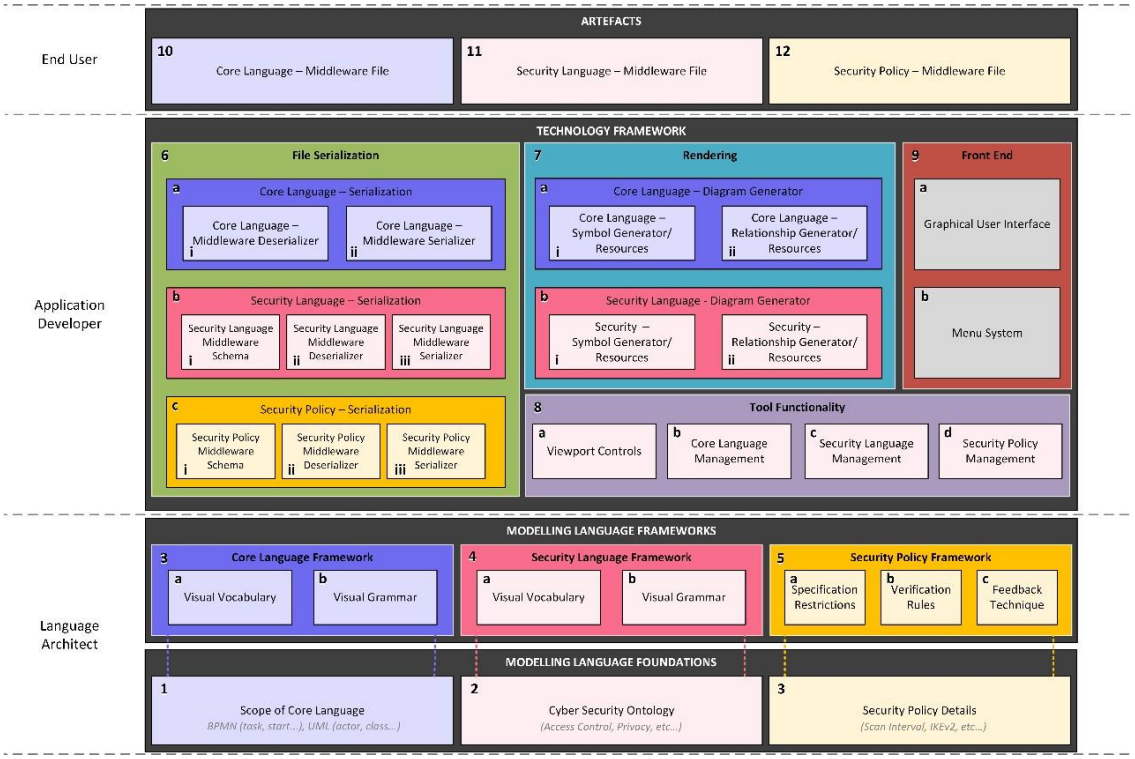

Figure 2 A framework for the extension and visualisation of cyber security requirements in modelling languages.

Using BPMN as a case study, we created our own application based on this framework. Acting not only as the first comprehensive security extension to BPMN but also as a way of validating our framework. A screenshot of the tool we created using our framework can be seen in figure 3.

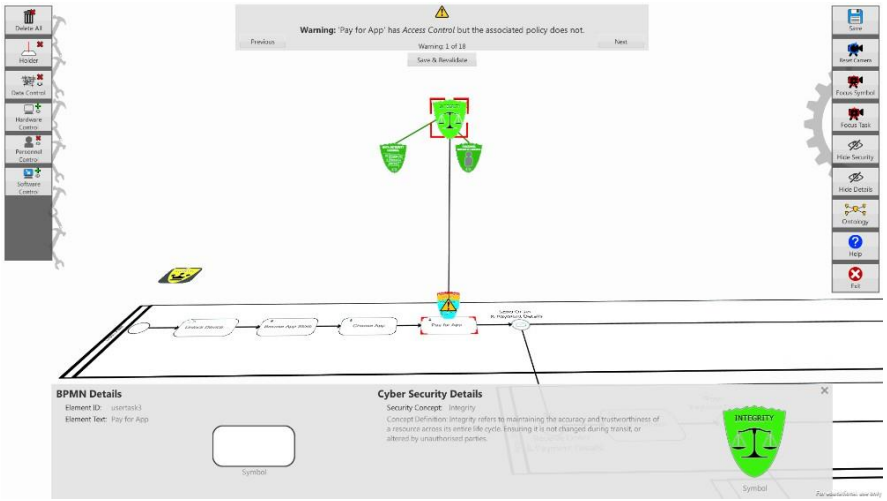

Figure 3 BPMN 3D screenshot.

Utilising the third dimension we managed to represent 76 unique security requirements within BPMN, at a similar abstraction level, whilst still maintaining *complexity management*. Overcoming the issues experienced by current extensions and proving our framework as a usable means of extending a language with security requirements. Our motivation for this work stemmed from the absence of any comprehensive means of specifying security within BPMN. Nevertheless, we have made several contributions to the area beyond this. We have provided a usable and justified framework for creating and verifying security within modelling languages. We have proposed a new

means of visualising said requirements in modelling languages and by consequence, created a new tool capable of representing comprehensive security requirements in BPMN.

4. Conclusion

Throughout this paper we reviewed existing security extensions to BPMN, quantifying the number of PoN principles they could satisfy. From this review, we proposed a novel framework for the extension and visualisation of cyber security requirements in modelling languages.

To justify this framework, we created our own tool which takes a new approach to modelling language extension. Our 3D platform proved capable of specifying 76 security requirements per BPMN element, greatly exceeding that of current approaches. All the while overcoming the issues experienced by current attempts and satisfying seven of the eight PoN principles (disregarding *cognitive integration*).

References

[1] M. Chinosi and A. Trombetta, "BPMN: An introduction to the standard," *Computer Standards & Interfaces*, vol. 34, no. 1, pp. 124-134, January 2012.

[2] M. Salnitri, F. Dalpiaz and P. Giorgini, "Modeling and Verifying Security Policies in Business Processes," *Enterprise, Business-Process and Information and Information Systems Modeling, Springer LCBIP*, vol. 175, pp. 200-214, 2014.

[3] A. Rodríguez, E. Fernández-Medina and M. Piattini, "A BPMN extension for the modeling of security requirements in business processes," *IEICE Transactions on Information and Systems*, Vols. E90-D, no. 4, pp. 745-752, April 2007.

[4] M. Q. Saleem, J. B. Jaafar and M. F. Hassan, "A Domain-Specific Language for Modelling Security Objectives in a Business Process Models of SOA Applications," *Advances in Information Sciences and Service Sciences*, vol. 4, no. January, pp. 353-362, January 2012.

[5] M. Leitner, M. Miller and S. Rinderle-Ma, "An Analysis and Evaluation of Security Aspects in the Business Process Model and Notation," in *International Conference on Availability, Reliability and Security*, Regensburg, 2nd-6th September, 2013.

[6] D. Moody, "The "Physics" of Notations: Toward a Scientific Basis for Constructing Visual Notations in Software Engineering," *IEEE Transactions on Software Engineering*, vol. 35, no. 6, pp. 756-779, 2009.

[7] N. Genon, P. Heymans and D. Amyot, "Analysing the Cognitive Effectiveness of the BPMN 2 . 0 Visual Notation," *Software Language Engineering, Springer LNCS*, pp. 377-396, 2010.

[8] G. Popescu and A. Wegmann, "Using the Physics of Notations Theory to Evaluate the Visual Notation of SEAM," in *16th IEEE Conference on Business Informatics (CBI)*, Geneva, pp. 166-173, 14th-17th July, 2014.

[9] C. L. Maines, D. Llewellyn-Jones, S. Tang and B. Zhou, "A cyber security ontology for BPMN- security extensions," in *The 13th IEEE International Conference on Dependable, Autonomic and Secure Computing (DASC 2015)*, Liverpool, UK, 26th-28th October, 2015.

[10] C. L. Maines, B. Zhou, S. Tang and Q. Shi, "Adding a Third Dimension to BPMN as a means of Representing Cyber Security Requirements," in *2016 International Conference on Developments of E- Systems Engineering (DeSE)*, Liverpool, 31st - 2nd September 2016.

[11] C. P. Pfleeger and S. L. Pfleeger, Security in Computing, Prentive Hall PTR, 4th Edition, 2006.

[12] W. Labda, N. Mehandjiev and P. Sampaio, "Modeling of Privacy-Aware Business Processes in BPMN to Protect Personal Data," in *29th ACM Symposium on Applied Computing*, Gyeongju, pp. 1399-1405, 24th - 28th March, 2014.

[13] K. S. Sang and B. Zhou, "BPMN security extensions for healthcare process," in *The 13th IEEE International Conference on Dependable, Autonomic and Seecure Computing*, Liverpool, UK, 26th- 28th October, 2015.

John Bayly

An exploration of on-line safety issues for children and young people.

John Bayly, Computer Science, Faculty of Engineering and Technology, Liverpool John Moores University, Liverpool, UK

j.f.bayly@2013.ljmu.ac.uk

Abstract:

This research focussed on establishing children's usage of social networking sites, the level of parental oversight, their awareness and exposure to danger, risk and potential for running away. There appears to have been limited research into utilising such analyses to inform the development of software-based approaches to address the concerns identified. Our questionnaire survey of 566, 11 to 16 year-olds demonstrated that almost half of parents (44%) do not monitor their children's use of social media and a high number (22%) of young people admit to hiding their online behaviour from adults. A significant proportion (20%) of the respondents were not aware of online dangers or risks, had met someone in person that they met online (15%), and would be unlikely to report danger or risk (65%). The results show that software analysis tools could provide early warning for parents by identifying risky online behaviour or children at risk of running away.
Keywords*: e-safety, risk, children, running away, vulnerable, young people, Social Networking Sites, danger, parents, guardians*

1. Introduction

Online safety is an area of increasing concern for teenagers, parents, teachers and the police. The motivation of this research was to explore existing e-safety issues for children and young people with a view to providing computing and software-based interventions. Although previous research has examined the area of online safety [1] [2] [3] [4] [5], there appears to have been limited research into utilising such analyses to inform the development of software-based approaches to address the concerns identified. We found that children are developing an online presence at a young age with the largest number declaring they first used social networking sites at 10 years old. Our project hopes to provide parents with tools to help them share their Internet experiences with their children especially at a young age rather than imposing rules and restrictions about how the Internet can be used.

1.1. Goals of the survey

The main aims of the research study are to understand the extent and popularity of social networking sites' use by children and young people while examining the methods, frequency and effectiveness of parental mediation of Internet use.

This research aims to identify which are the most popular electronic devices for social networking site use and the role social networking sites and mobile smartphones play when children run away.

1.2. Requirements

This research serves as a requirements gathering exercise to inform the development of software tools, algorithms and techniques to work on behalf of parents to help them monitor their children and identify when they are indulging in risky behaviour.

2. Background and Literature review:

2.1. Social Networking and the psychological effects

EU kids Online which is a multinational research network that seeks to enhance knowledge of European children's online opportunities, risks and safety, [2] found that 68% of European 11-16 year-olds have a social networking site profile and studies show that this level of use can have profound psychological effects and raise developmental concerns [6].

2.2. What are the most common risks in children's Internet use?

More recently, EU Kids Online [2] produced valuable evidence mapping children's and parents' experience of the Internet. Project director Sonia Livingstone's analysis of results found that the most common risk of children's Internet use in Europe is associated with communicating online with someone the child has not met face-to-face before [7]. The danger exists when the child ventures out to meet those new-found online contacts without informing friends and family

2.3. Risk of running away

The National Survey of Young Runaways [8] estimated that there were somewhere in the region of 100,000 incidents of young people under the age of 18 being reported missing in the UK annually and this figure has stayed the same since 1999. This equates to, around one in nine young people within the UK having run away overnight on at least one occasion before the age of 16.

2.4. Can software solve the problem?

Research initiatives that use software tools to monitor or track adults are limited. To covertly track an adult is illegal in the UK, Europe and the USA. Children, on the other hand, are the responsibility of their parents/carers/guardians and using software to track or monitor their communications and behaviour is a method that may help support parents who are not confident in their ability to monitor their children online.

3.0. Research Methodology

The research was carried out using a paper-based questionnaire survey of 570 children and young people from the northwest region of the UK.

3.1 Rationale and Data Collection

The survey needed a suitable sample of 11-16 year-olds to provide credible, current and useful data that would inform the development of software tools that would provide useful interventions..

3.2 Ethics, Safeguarding and Consent

The questionnaire was given full Ethical approval by Liverpool John Moores University Research Ethics Committee (REC).

3.3 Design

The questions had to be suitable for a wide range of ages, namely 11-16 year-olds and had to be a suitable number to account for the time needed to administer them. As well as the constructs mentioned above the personal details of the respondents were required to apply demographics. The questionnaire was designed with multiple choice questions and a number of closed questions.

3.4 Data Analysis

A statistical software package, namely IBM SPSS Statistics [9] was chosen for the data analysis. Frequency analyses were conducted via histograms, contingency tables, and two-way chi-square analyses. Cross-tabulations were used and in suitable cases, significance tests were carried out.

4.0 Research results

The results are grouped into six sections or domains following section *4.1. Respondents* which is age/gender information.

4.1. Respondents

The subject school is a comprehensive school in the NW of England and the ages ranged from Age 11 to Age 16.. (See Figure 1)

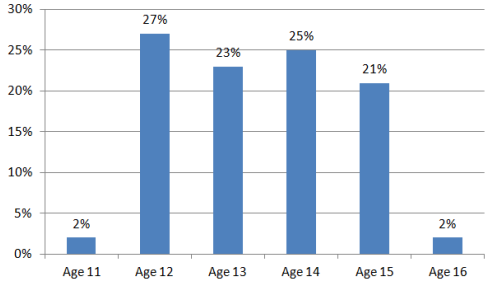

Figure 1: Respondents by age group

4.2. Social Media Applications / Social Networking Sites (SNS)

In this domain, we can see that in the first use of social networking sites, the median is 10 years old and there are significant numbers who declare ages much younger than that.(See Figure 2)

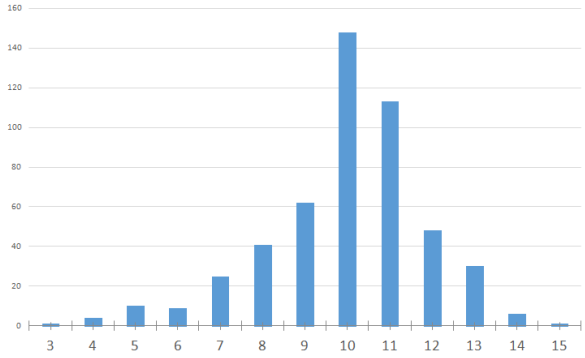

Figure 2: Respondents by age, first use of Social networking sites

4.3. Behaviour at home

This domain focuses on the interaction between students and parents at home and the young people stated that almost half of parents do not monitor them. Less than a third do monitor and the majority are parents of females. (See Figures 3 & 4)

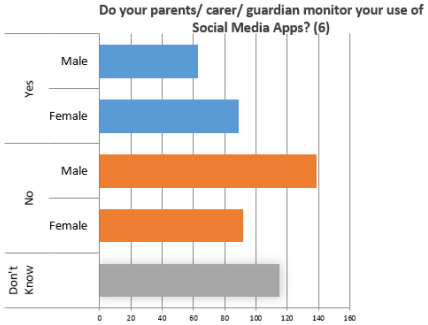

Figure 3: Parental Monitoring – Gender split

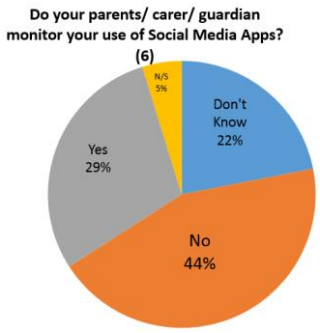

Figure 4: Parental Monitoring – No Gender split

We asked whether the children hide their online behaviour from their parents bearing in mind that more than 40% have already stated that their parents do not check on them anyway. More than a fifth (21.6%) admitted to it.

4. 4. Awareness of danger or risk

Over four-fifths of young people say they set privacy settings to protect themselves. The remaining at risk group of 20% is made up of do not know or missing values and 8.7% that do not use privacy settings at all.

4.5. Exposure to danger or risk

The majority of young people (48.7%) had been contacted by someone they did not know. Extending the question to, "Have you been to meet someone you only know on social media?" produced an alarming number (14.9%) of young people who have done this.

4.6. Reporting danger or risk

We found that females are more likely to report unsolicited contact but the majority (65%) do not think it is serious enough to report it.

4.7. Running Away

We asked our contingent of runaways, "Did you have your mobile phone with you when you ran away?" Three-quarters of young people (74%) had their smartphones with them when they ran away.

5. Conclusions and Discussion

There has been considerable research around e-safety and, generally, the conclusions of the research signpost relevant and improved education programmes. From our results, one can see that education has made a significant impact on children and young people.

At home, children and young people are not always honest about what they do, openly declaring in our study that they hide their online behaviour. Either a lack of monitoring, inadequate monitoring or children using covert methods of concealment means the majority of children are free to indulge in risky behaviour and are vulnerable to threats. This leads the way open to software solutions to overcome attempts to conceal their behaviour by scanning, capturing, analysing and reporting the risky behaviour to parents.

Our results revealed that young people vulnerable to the negative effects of unsolicited contact as they are reluctant to report it when it happens. It is hoped that software tools would report this contact to parents, removing the expectation that children and young people would have to report it.

Research into the types of communications children make leading up to their risky behaviour or before they run away, combined with the gathering of location data to track movements leading up to risky behaviour or during a runaway event, will support the development of software tools that could significantly reduce the time taken to provide an intervention or locate a child could reduce the possibility of exploitation.

6. Further Work

Further work will focus on using computational methods to harvest communications and location data from users. The aim will then be to analyse the communication data using a variety of methodologies such as sentiment analysis and machine learning methodologies to interpret the nature of the communications with a view to developing predictive models of risky and runaway behaviour. A cloud-based traffic light reporting system is an example of the software tools and techniques proposed by the authors to establish a decision-support tool for parents to better support their children online.

References

[1] Karen Wespieser, "Young people and e-safety: The results of the 2015 London Grid for Learning e-safety survey," Slough, 2015.

[2] LSE. (2016) EU Kids Online. [Online]. http://www.lse.ac.uk/media@lse/research/EUKidsOnline/About-the-project.aspx

[3] Birgy Lorenz, Kaido Kikkas, and Mart Laanpere, "Comparing Children's E-safety Strategies with Guidelines Offered by Adults," *The Electronic Journal of e-Learning*, vol. 10, no. 3, pp. pp297-309, 2012. [Online]. http://www.ejel.org/volume10/issue3/p297

[4] Mariska De Lange and Rossouw Von Solms, "The importance of raising e-safety awareness amongst children," in *Annual Conference on WWW Applications*, Johannesburg, ZA, 2011.

[5] Jill Burgess and Catherine McLoughlin, "Investigating cyberbullying -Emerging research and e-safety strategies within families and communities," *Communities, Children and Families Australia*, vol. 6, no. 1, pp. 1-12, 2011.

[6] Kaveri Subrahmanyama, Stephanie M. Reich, Natalia Waechterb, and Guadalupe Espinozab, "Online and offline social networks: Use of social networking sites by emerging adults," *Journal of*

Applied Developmental Psychology, vol. 29, no. 6, pp. 420–433, 2008. [Online]. http://www.sciencedirect.com/science/article/pii/S0193397308000713

[7] Sonia Livingstone, Leslie Haddon, Anke Görzig, and Kjartan Ólafsson, "Risks and safety on the Internet: the perspective of European children: full findings and policy implications from the EU kids Online survey of 9-16 year-olds and their parents in 25 countries," London, 2012.

[8] Gwyther Rees. (2011, Jan) http://www.childrenssociety.org.uk. [Online]. http://www.childrenssociety.org.uk/what-we-do/resources-and-publications/publications-library/still-running-3-early-findings-our-third-

[9] IBM. (2017) SPSS Statistics. [Online]. http://www-03.ibm.com/software/products/en/spss-statistics

Kellyann Stamp

DEVELOPMENT OF A NEUROADAPTIVE GAMING TECHNOLOGY TO DISTRACT FROM PAINFUL PROCEDURES

Kellyann Stamp [1], Chelsea Dobbins [1], Stephen Fairclough [2] and Helen Poole [2]

Department of Computer Science [1] and School of Natural Sciences and Psychology [2]
Liverpool John Moores University, Byrom Street, Liverpool, L3 3AF
E-mail address: K.Stamp@2012.LJMU.ac.uk, C.M.Dobbins@LJMU.ac.uk, S.Fairclough@LJMU.ac.uk, and H.M.Poole@ljmu.ac.uk

Abstract. Research shows that pain tolerance can be increased when a person is sufficiently distracted from painful stimuli. Video games are one of the most effective distractions that can be implemented, and adaptive games have been proven to provide a more efficient distraction than standard video games. This research is focused on creating a game that adapts to a player's attentional state, which we believe will lead to greater immersion, and theoretically, a stronger sense of immersion will provide a more sufficient distraction. To monitor the attentional states of the participants, functional Near Infrared Spectroscopy (fNIRS) equipment will be worn by the player, which will monitor the activity of the blood in the brain. We can use the results that the fNIRS equipment gathers to determine the level of concentration that a player is using, and then a biocybernetic loop (i.e. a loop which uses data from the brain to make changes in the game) can be used to adjust the game difficulty.

Keywords. Neuroadaptive, Gaming, Pain, Biocybernetic, fNIRS

1. Introduction

Distraction can increase pain tolerance by diverting attention away from the sensation of pain [1]. Research shows that active distractions, such as reading a book or playing a game, are more effective than passive distractions, such as watching the television, as they require a person to be actively involved in a task rather than just observing it [1]. In addition to this, adaptive games have been proven to be more effective sources of distraction than standard games [2] because the demand of the game is adapted to the skill level of the individual. This means that the skill of the user will not affect their ability to play through the game, and that even a novice user can experience the same level of immersion as an expert user. This is because the game will enable each user to progress at the same pace and complete the same tasks, as these tasks will be modified to suit the user. Although adaptive games are more effective than standard games, they still do not provide the most personal experience to each player, because they can only adapt to the users' skill level. A more efficient way of ensuring that the game is providing the most efficient distraction to each player would be to monitor the attentional state of a player, and then adapt the game in line with these states. A Biocybernetic loop can be used in this case to modify the difficulty level of the game in line with the brain readings that are gathered from the player.
The basis of this neuroadaptive prototype is that an adaptive game will allow a player to achieve goals in-game regardless of their level of skill, as the game will adapt in real time, enabling the player to enter the flow state more easily [3]. If the player is becoming overloaded then the game will become easier, and if the player appears to be bored then the game will increase in difficulty. Theoretically, this will create the most immersive game possible, which will distract the player from pain more than a standard game would.

2. Background

2.1 Concentration

To create a game that can successfully encourage immersion in a user, it is important to understand the concentration states that the brain experiences when a user is completing a task, and how these states are affected. The modified flow theory [4] states that there are four main states that the human brain can experience whilst it is

attempting to complete a task. These four states are apathy, boredom, flow and overload. The optimal state for the player to be in whilst completing a task is the flow state, which can also be referred to as 'being in the zone.' This state is ideal because the user is "*[acting] with total involvement*" [4]. To encourage a person to enter the flow state, the task that they are carrying out must be difficult enough to hold the attention of the user, but not so difficult that the user may lose concentration and give up the task. It is believed that whilst a person is in the flow state then they are less likely to notice external stimuli as much as they would if they were not in the flow state. If a player is focused on an efficient distraction, then we theorise that their pain tolerance will increase because they will be distracted from the painful stimuli.

2.2 Functional Near Infrared Spectroscopy (fNIRS)

In order to create a game that can adapt to the attentional state of a player, we must first be able to monitor this attentional state so that the game can adapt. This monitoring will be carried out using Functional Near Infrared Spectroscopy (fNIRS), which can monitor activity in the brain at a level that is comparable to fMRIs, but at a much cheaper price and in a much more convenient format [5][6].

During an fNIRS scan, near-infrared light is passed through the skull and received back into the system. The difference between the amount of light that is transmitted and received back allows us to understand how much of the light has been absorbed. The amount of light absorbed depends on the amount of oxygen that is bound to the haemoglobin module, which in turn can be used to determine a variety of different information from the brain, including attentional state [7]. The modified Beer-Lambert law is then used to determine the changes in the concentration of deoxygenated haemoglobin and oxygenated haemoglobin molecules, which will be the readings that enable changes in player concentration to be measured [8]. When neurons in the brain are activated, there is typically an increase of oxygenated haemoglobin and a decrease of deoxygenated haemoglobin, along with an increase in blood volume. These readings are what will be observed in order to determine a user's level of concentration – the activation of the neurons is what will be monitored, and then converted into attentional state boundaries within the biocybernetic loop.

2.3 Brain Computer Interface and the Biocybernetic Loop

A way of creating an adaptive game that can respond to a player's concentration level would be to employ Brain Computer Interface (BCI) techniques. BCI refers to platforms that rely on brain output in order to perform. There are two types of BCI that can be created, active and passive. Active BCI games require the conscious decision of the user to control the game, as the user must focus in a certain way to induce changes in the game. In a passive BCI game, users do not make deliberate physical changes to control the game or modify gameplay. In this instance, a passive loop will be used because an active loop may cause the user to lose the feeling of immersion, as they must focus on their own thoughts rather than the game. Signals that are read from the brain are used to modify the game, so that the game will make subtle adaptations without the conscious thought of the user. The changes will be subtle enough that the user does not notice them [9]. Brain Computer Interfaces are powered by a biocybernetic loop, as this is the way in which the feedback from the user is fed into the game so that changes can be implemented. The loop works by continuously sending data from the brain into a computer, which will filter and quantify the brain data. This data is then fed back into the game, so that the game can adapt itself in line with this information. This process continues to loop throughout gameplay to ensure that the game is always matched to the psychophysiological data [10].

3. Methods

The idea of creating an adaptive game is to increase the amount of time that the user spends in the flow state whilst they are completing a task. However, before a biocybernetic loop can be created, we must first gather data pertaining to desirable and undesirable player states: boredom, apathy, flow and overload. To gather brain data relating to these attentional states, a study has been undertaken that encourages participants to enter these states. 12 out of 20 participants have completed the study (3 female) with a mean age of 21. Participants in the study have played four difficulty levels of a racing game whilst wearing fNIRS equipment. These levels of easy, medium, hard and impossible demand have been established via pilot testing. The participants will play these four game conditions both with and without painful stimulus. The method used in this case to induce experimental pain is the Cold Pressor Test, wherein participants will submerge their foot in a container full of 2 degree water for a maximum of three minutes. This water is cold enough to induce pain in participants, however the participant is able to remove their foot from the water at any point.

During the study, participants will also experience the Cold Pressor without the distraction of the game, which will allow us to determine whether a distraction leads to a longer immersion in the Cold Pressor, and also which game condition leads to the longest Cold Pressor immersion. The gathering of fNIRS data in these three conditions (game alone, pain alone, game and pain in combination) will allow us to determine how the manipulation of game demand and experimental pain impacts activity in two areas of the cortex; the frontal cortex, which is sensitive to attentional processes, and the somatosensory cortex, which is part of the pain matrix.

Not only does this study enable us to gather this preliminary data that can be used to create a Biocybernetic loop, but it also enables us to examine the relationship between pain and distraction. When the participant submerges their foot in the cold pressor equipment, they are free to remove their foot whenever they consider themselves to be in too much pain to continue with the pain element of the study. Because we gather data from each participant based on immersion alone and an immersion with a distraction condition, we expect to see a longer average immersion time from the participants when they are playing the game with the cold pressor verses when they are experiencing the cold pressor on its own. We would also expect to see a longer immersion time when the participant is playing the medium or hard condition versus the easy or impossible condition, as these two conditions should encourage the participant to enter the flow state and therefore focus less on the pain that they may be experiencing. However, immersion is directly affected by the player's skill level. A player is less likely to experience immersion if they are unable to play the game properly, or if they find the game boring. For this reason, the Immersive Experience Questionnaire and the Dundee State Stress Questionnaire have been used to determine a player's level of immersion for each of the game conditions. In the event where the medium or hard level of the game do not encourage the longest Cold Pressor immersion time, we expect that the immersion time will be longest for the game condition which the participant rated as most immersive using these questionnaires. We expect that we will be able to use the results that will be gathered from this study in order to determine fNIRS readings for the states of boredom, apathy, flow and overload. These results can then be used within the biocybernetic loop to alter the game if any of the undesirable attentional states are recognised.

4. Results

Figure 1 shows fNIRS data from one participant. This figure indicates lower levels of oxygenated haemoglobin in the F1 area of the frontal cortex during a 'hard' level compared to a 'medium' level, which in turn indicates that the participant is concentrating less during the hard level.

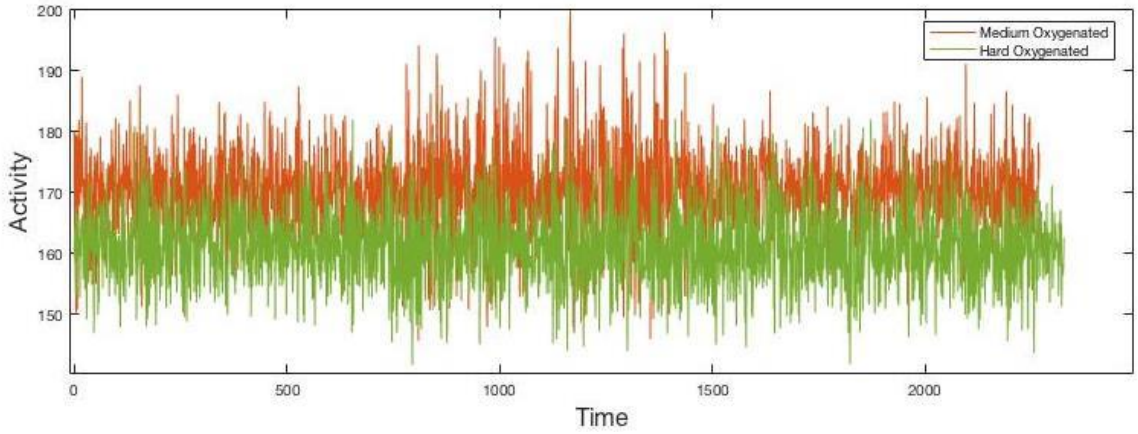

Figure 1: A comparative sample of raw fNIRS data comparing the oxygenated and deoxygenated blood levels during 'Hard' and 'Medium' level gameplay.

The higher levels of oxygenated haemoglobin in the medium level indicate more neurovascular coupling during this level compared to the hard level, which in turn indicates more brain activity. This participant also kept their foot inside the Cold Pressor for the entirety of the Medium game condition and was asked to remove their foot at the three-minute immersion limit, whereas the participant had previously removed their foot of their own accord and much earlier during all their previous immersions. These two results in conjunction show that a higher level of brain activity will encourage a higher pain tolerance.

5. Conclusion

Results from the study are encouraging and show that a distraction condition can increase the pain tolerance of a participant, and that different levels of game difficulty will also affect how effective the distraction is. Based on these initial results, another study will be undertaken, which will use a neuroadaptive game. We expect that the results of the next study will show a higher activation in the frontal cortex and a higher tolerance to pain when the participant is playing the neuroadaptive game versus a standard game. This is because the neuroadaptive game will enable the player to enter the flow state more easily as it is being modified in real-time to their state.

7. Further Work

The nature of fNIRS means head movement can cause the data to become noisy. For this reason, a Shimmer accelerometer has been used to record head movement. A heart rate monitor has also been used which will enable us to see whether the fluctuations that can been seen in the fNIRS readings can also be picked up in the heart rate readings. The next steps in beginning to develop the biocybernetic loop is to create a protocol that can be used to

filter all of this data to remove noise, so that this data can then be used in the creation of a biocybernetic loop. The final result will see this data being filtered and applied to the biocybernetic loop in real time.

7. References

[1] K. E. Weiss, L. M. Dahlquist, and K. Wohlheiter, "The effects of interactive and passive distraction on cold pressor pain in preschool-aged children," *J. Pediatr. Psychol.*, vol. 36, no. 7, pp. 816–826, 2011.

[2] H. S. Law E, Dahlquist LM, Still S, Weiss KE, Herbert LJ, Wohlheiter K, "Videogame distraction using virtual reality technology for children exeperiencing cold pressor pain: the role of cognitive processing," *J. Pediatr. Psychol.*, vol. 36, no. 1, pp. 84–94, 2011.

[3] W. K.A., "Interactive versus passive distraction for acute pain management in young children: the role of selective attention and development," *J. Pediatr. Psychol.*, vol. 38, no. 2, pp. 202–212, 2013.

[4] L. E. Nacke and C. A. Lindley, "Flow and Immersion in First-person Shooters: Measuring the Player's Gameplay Experience," *Proc. 2008 Conf. Futur. Play Res. Play. Share*, pp. 81–88, 2008.

[5] H. Neuroscience, A. R. Harrivel, D. H. Weissman, D. C. Noll, and S. J. Peltier, "Monitoring attentional state with fNIRS," vol. 7, no. December, pp. 1–10, 2013.

[6] K. Izzetoglu, S. Bunce, M. Izzetoglu, B. Onaral, and K. Pourrezaei, "fNIR spectroscopy as a measure of cognitive task load," *Proc. 25th Annu. Int. Conf. IEEE Eng. Med. Biol. Soc. (IEEE Cat. No.03CH37439)*, vol. 4, pp. 3431–3434, 2003.

[7] E. Olsson, G. Ahlsén, and M. Eriksson, "Skin-to-skin contact reduces near-infrared spectroscopy pain responses in premature infants during blood sampling," *Acta Paediatr. Int. J. Paediatr.*, vol. 105, no. 4, pp. 376–380, 2016.

[8] Z. Barati, P. A. Shewokis, M. Izzetoglu, R. Polikar, G. Mychaskiw, and K. Pourrezaei, "Hemodynamic response to repeated noxious cold pressor tests measured by functional near infrared spectroscopy on forehead," *Ann. Biomed. Eng.*, vol. 41, no. 2, pp. 223–237, 2013.

[9] M. Poel, F. Nijboer, E. L. Van Den Broek, S. Fairclough, and A. Nijholt, "Brain computer interfaces as intelligent sensors for enhancing human-computer interaction," *14th ACM Int. Conf. Multimodal Interact. ICMI 2012, Oct. 22, 2012 - Oct. 26, 2012*, pp. 379–382, 2012.

[10] J. R. Wolpaw, N. Birbaumer, W. J. Heetderks, D. J. McFarland, P. H. Peckham, G. Schalk, E. Donchin, L. A. Quatrano, C. J. Robinson, and T. M. Vaughan, "Brain-computer interface technology: A review of the first international meeting," *IEEE Trans. Rehabil. Eng.*, vol. 8, no. 2, pp. 164–173, 2000.

Jun Qi

Assessing Intensity Pattern of Lifelogging Physical Activity

Name of author(s): Jun Qi and Po Yang
School/Institute, Address: Department of Computer Sciences, Liverpool John Moores University, Liverpool, UK, L3 3AF
E-mail address: j.qi@2015.ljmu.ac.uk

Abstract. Lifelogging physical activity (PA) assessment is crucial to healthcare technologies and studies for the purpose of treatments and interventions of chronic diseases. Traditional lifelogging PA monitoring is conducted in non-naturalistic settings by means of wearable devices or mobile phones such as fixed placements, controlled durations or dedicated sensors. Although they achieved satisfactory outcomes for healthcare studies, the practicability become the key issues. Recent advance of mobile devices make lifelogging PA tracking for healthy or unhealthy individuals possible. However, owning to diverse physical characteristics, immaturity of PA recognition techniques, different settings from manufactories and a majority of uncertainties in real life, the results of PA measurement is leading to be inapplicable for PA pattern detection in a long range, especially hardly exploited in the wellbeing monitoring or behaviour changes. This paper investigates and compares uncertainties of existing mobile devices for individual's PA tracking. Irregular uncertainties (IU) are firstly removed by exploiting Ellipse fitting model, and then monthly density maps that contain regular uncertainties (RU) are constructed based on metabolic equivalents (METs) of different activity types. Five months of four subjects PA intensity changes using the mobile app tracker *Moves* [6] and *Google Fit* app on wearable device Samsung wear S2 are carried out from a mobile personalised healthcare platform MHA [7]. The result indicates that uncertainty of PA intensity monitored by mobile phone is 90% lower than wearable device, where the datasets tend to be further explored by healthcare/fitness studies. Whilst PA activity monitoring by mobile phone is still a challenging issue by far due to much more uncertainties than wearable devices.

Keywords. Physical activity, intensity pattern, ellipse fitting model, density map, mobile device.

1. Introduction

Lifelogging physical activity (PA) aims at capturing one's entire life using digital devices for health statues and wellness. Thus as a key role plays in a number of chronic diseases, its effectiveness and accuracy are critical to conduct personalised clinical diagnoses of treatments and preventions. Normally, PA assessment in clinics filed are mostly observed either through distributing several wearable sensors over one's body and training their sensory data with advanced machine learning algorithms, or capturing and analysing a series of images with wearable cameras. Both ways exhibits relatively accurate measures, however, their obtrusiveness, cost, battery life and storage capacity are the serious issues leading to the limitation of permanently applying to the completely natural environments.

Unfortunately though, due to the commercial perspective, nearly all of the popular wearable devices and mobile apps in the market focus more on personal fitness and exhibit a lack of compatibility and extensibility. Also, owing to the heterogeneity of connected devices and rapid

change of diverse life patterns in an IoT environment, lifelogging PA information captured by mobile devices usually contains much uncertainty. Effective validation of these high volume and multi-dimensional lifelogging PA data becomes an extremely difficult task. Traditional PA validation methods hardly deal with these scattered and heterogeneous data sets. In the existing literature, none is reported to successfully improve the accuracy of these wrapped PA data collected by mobile devices in a smart healthcare environment.

Our study in this paper attempts to take lifelogging PA as a target to explore the possibility of utilizing new techniques for investigating and comparing the feasibilities of customer device/app for lifelogging PA assessment in a smart healthcare environment. We first give a comprehensive review of existing life-logging PA measurement mobile devices, and identify regular (RU) and irregular (IU) uncertainties of these life-logging PA measures in a smart healthcare environment. We use Ellipse fitting model to remove RU, and make density map for each month with an individual's PA intensity using mobile phone and wearable device respectively. PA intensity of four subjects with two devices are analysed and compared from the mobile personalised healthcare platform MyHealthAvatar (MHA) [7] in our case study.

2. Uncertainty

Customer PA monitors like wearable devices and mobile phones have addressed some practical issues such as storage, battery life and cost, especially mobile apps which are often free. Nevertheless, PA recognition results offered by mobile devices are widely divergent as a result of different places being carried by different users such as pocket or handbags. Furthermore, the diverse life pattern of an individual person may cause huge indeterminateness, as they perform PA in varying ways owning to age, gender, weight, etc. Hence, a specific PA tracking model that fits one group of user may not fit another one [32]. In addition to that, some applications often automatically switch off themselves for energy efficiency which has contributed to missing data. In general, the uncertainties of lifelogging PA from customer devices here is divided into two types as our previous work investigated [5]:

Irregular Uncertainty (IU): randomly and accidently occurs in lifelogging PA data. The causes of these uncertainties include device malfunctions or faults, breakdown of a third party server, misuse of devices or sudden change of personal circumstance. The occurrence of IU will appreciably impact the efficiency and accuracy of assessing personal health. We have implemented Ellipse fitting model to remove IU in our previous work [5][3].

Regular Uncertainty (RU): frequently and persistently occurs in lifelogging PA data. The causes resulting in these uncertainties are mainly from some regular influencing issues, like intrinsic sensors' errors, differentiation of personal physical fitness and changes of environment. The occurrence of regular uncertainty in physical activity data is inevitable so that it is impossible to completely eliminate these uncertainties.

2.1 Handling with IU

The level of PA is assessed and represented by the number of steps walking per day or the distance walking per day. Current mobile devices enable measuring walking speed related information, like Daily Walking Speed. Therefore, our inspiration for managing the above two types of uncertainties is to build a 2D distribution of physical activity regarding two benchmarks: Daily Walking Steps (Steps) and Daily Walking Speed (Speed). Fig. 2 shows a typical raw data distribution. As we can see, some points exceed regular ranges, e.g., 17000 steps/ hour. We use Ellipse fitting model for the removal of IU, where the confidence interval between 95% and 98%. Details see our previous work [5][3].

2.2 Density map visualization

We also use a density map to construct longitudinal PA monitoring data distribution as our previous work [3]. Here we select (METs) and PA duration as the validation standard for the each PA intensity. In other words, the intensity of the activity is based on the amount MET × duration. Some typical intensity levels emerged for all the PA types of the mobile devices are presented in the table 1.

$$Intensity = \frac{ActivityDuration/hr \times MET/hr}{maxActivityDuration/hr \times MET/hr} \times pixel \qquad (4)$$

Where $ActivityDuration/hr \times MET/hr$ refers to intensity of the PA in each hour;
$ActivityDuration/hr \times MET/hr$ refers to maximum intensity value of the month;
In the density map, the vertical axis indicates 24 hours a day. While horizontal axis indicates days of each month from 1st to 30th or 31st. Image pixel ranges from 0 to 255, which means the image is in the grey level. PA intensity ranges from light colour to dark colour, where dark colour denotes very high intensity and vice versa. The white part in the map represents sedentary and uncertain patterns.

2.3 Feature extraction

To measure the dissimilarities of each monthly density map, we select six histogram features (mean, variance, skewness, kurtosis, energy and entropy) from the map. The mean, variance and skewness present the degree of average, discrete and asymmetrical distribution in a grayscale histogram, respectively. Kurtosis measures the relative peakness or flatness of the distribution to a normal distribution. Energy and entropy represent the average degree of gray distribution. We also select four texture features based on gray-level co-occurrence matrix (GLCM) which are contrast, correlation, energy and homogeneity. Contrast measures the local variations in the gray-level co-occurrence matrix. Correlation measures the joint probability occurrence of the specified pixel pairs. Energy provides the sum of squared elements in the GLCM. Also known as uniformity or the angular second moment. Homogeneity measures the closeness of the distribution of elements in the GLCM to the GLCM diagonal.

2.4 Distance measure and RU determination

In order to assess the subject's PA intensity state, Euclidean distance is adopted to measure the dissimilarity among density maps, as Eq. (3).

$$distance_{i,j} = \sqrt{\sum_{i=2,j=1}^{k}(x_{i,j} - x_{i-1,j})^2} \qquad (1)$$

Where *x* reprensts the vectors of extracted features. $x = [x_1 \dots x_k]$. The smaller the distance, the similar the two map images, and vice versa.

The validation dataset features four randomly selected healthy individuals using the mobile devices for 5 months. The subjects investigated are staff and research students at a university. They are working 6 to 8 hours in front of a computer every work day, whilst PA intensity and time are relatively stable each month.

3. Case study: uncertainty evaluation and comparisons

In this case study, we create four months density maps from the subject using *Moves* app on mobile phone and *Google Fit* app on Samsung Gear S2, respectively, with the datasets from July to October 2015. To measure the uncertainties of each month's PA intensity pattern, histogram and texture features are extracted from both devices. The subject used the mobile app *Moves* and *Google Fit* datasets are collected from the mobile personalised healthcare platform MHA [7].

3.1 Density maps dissimilarity evaluation from mobile phone

The subject in the case study is a female, 30 years old, working as a researcher at the university 7 hours (desk job), and working out 1.5 hours per working day. Four months PA intensity are represented as the density maps shown as figure 3 (b) from the mobile phone. Whilst figure 3 (c) shows the histogram features and texture features extracted from the maps, representing the PA intensity pattern dissimilarities among the four month using mobile phone. However, the subject's lifestyles are relatively stable, while as we can see from the dissimilarity measures, the trend line displays large distance changes, which proves that much uncertainty exists using the commercial products.

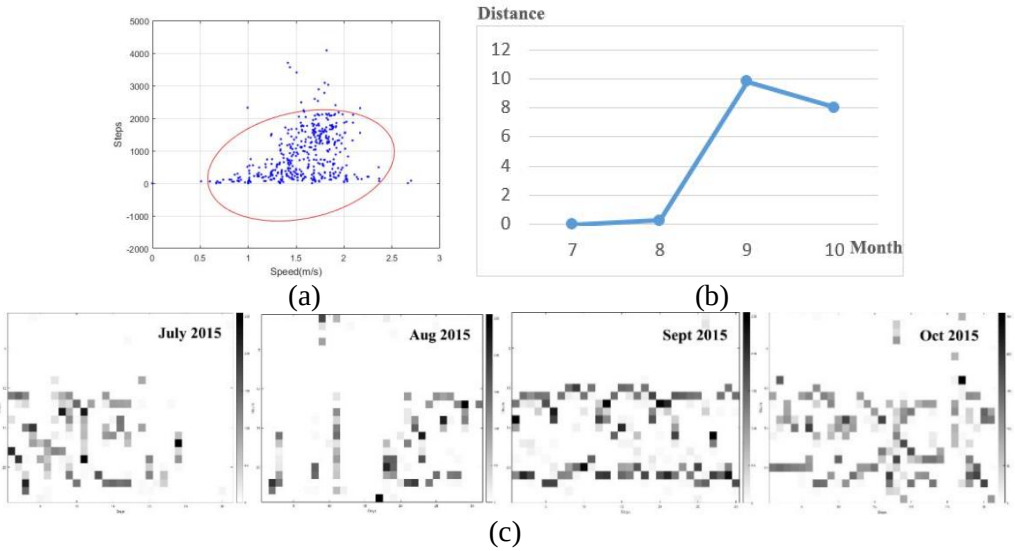

Figure 2. (a) Ellipse fitting model for IU removal of consecutive four months' of the subject's *Moves* dataset (c= 0.98) from mobile phone datasets (b) Density maps of four consecutive months' datasets from mobile phone dataset (c) histogram and texture features dissimilarity for four consecutive months' datasets from mobile phone dataset

3.2 PA Intensity pattern comparisons with wearable devices and mobile phone

The devices of mobile phone and wearable device usage of four subjects' PA intensity for consecutive five months are presented in figure 3. The subjects are staff and research students at university, spending 6 to 8 hours sitting in front of computer, so the lifestyles are relatively sedentary. Subject 1 has less fluctuations with mobile phone, while others show more uncertainties with both histogram and texture features. On the other hand, Compared with mobile phone PA tracker, the wearable device presents relatively more stable and less limit of fluctuations. As we can see in the figure 3, the fluctuation limit is 2.7 with wearable device, while mobile phone is up to 26, and thus the uncertainty distance among each month is bigger than the wearable device. the distance of wearable device is 90% lower than mobile phone, which presents more stable with less uncertainties in lifelogging PA monitoring. The key reason is the placement on human's body that the subject is able to take the band on the wrist all the time. Also, due to the battery and capacity saving mode, PA apps on mobile phones switch themselves off occasionally. The mobile device/sensor placement on human body is therefore attracting increasingly attentions in human physical activity research field in recent years [4].

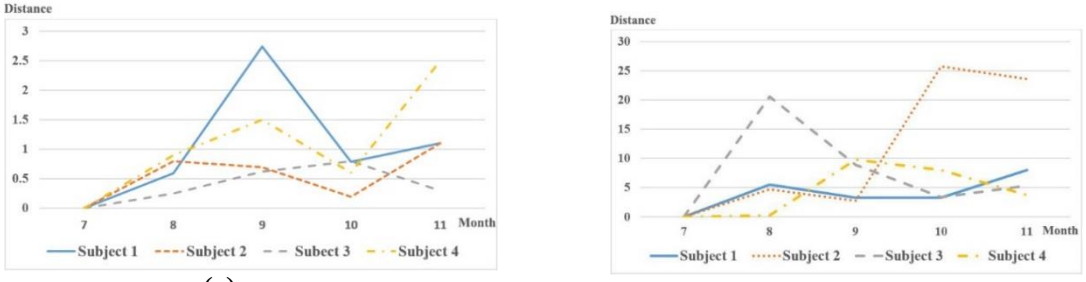

Figure 3. Four subjects' density map dissimilarities comparison of five months using (a) wearable device and (b) mobile phone from histogram and texture features

4. Conclusion and future work

Lifelogging physical activity (PA) monitoring and measurement is increasingly crucial task to the general public especially to the patients. Effectively assessing long term physical activities with mobile devices are becoming one of the most popular research areas in recent years. This paper

investigates existing commercial mobile PA trackers from a mobile personalised healthcare platform MHA [7] using *Moves* mobile app and *Google Fit* on Samsung Gear S2. We first use Ellipse fitting model to remove irregular uncertainties (IU), then density maps are created to represent monthly PA intensity visualisations. Histogram and texture features are extracted from the maps for measures of PA intensity dissimilarities. The results prove that commercial devices exist uncertainties due to a variety of reasons. While wearable devices exhibits more stable fluctuation than mobile phones which may further explored for healthcare studies.

References

[1] H.-L. Chan, S.-C. Fang, Y.-L. Ko, M.-A. Lin, H.-H. Huang, C.-H. Lin, Heart rate variability characterization in daily physical activities using wavelet analysis and multilayer fuzzy activity clustering., *IEEE Trans. Biomed. Eng.* 53 (2006) 133–139.

[2] Ó.D. Lara, A.J. Prez, M. a. Labrador, J.D. Posada, Centinela: A human activity recognition system based on acceleration and vital sign data, *Pervasive Mob. Comput.* 8 (2012) 717–729.

[3] J. Qi, P. Yang, M. Hanneghan, S. Tang, Neurocomputing Multiple density maps information fusion for effectively assessing intensity pattern of lifelogging physical activity, *Neurocomputing*. 220 (2017) 199–209.

[4] M. Shoaib, S. Bosch, O. Durmaz Incel, H. Scholten, P.J.M. Havinga, A Survey of Online Activity Recognition Using Mobile Phones, *Sensors.* 15 (2015) 2059–2085.

[5] P. Yang, M. Hanneghan, J. Qi, Z. Deng, F. Dong, D. Fan, Improving the Validity of Lifelogging Physical Activity Measures in an Internet of Things Environment, *2015 IEEE Int. Conf. Comput. Inf. Technol. Ubiquitous Comput. Commun. Dependable, Auton. Secur. Comput. Pervasive Intell. Comput*. (2015) 2309–2314.

[6] Moves, (n.d.). https://www.moves-app.com/ (accessed October 14, 2016).

[7] MHA, (n.d.). http://www.myhealthavatar.eu/ (accessed October 10, 2016)

Ibrahim Alobaidan

Build trust in the cloud computing - Isolation in Container based virtualisation

I Alobaidan and M Mackay
Department of computer sciences, Liverpool John Moores, University (LJMU), Liverpool, UK. I.M.Alobaidan@2012.ljmu.ac.uk and M.I.Mackey@ljmu.ac.uk

Abstract -- Cloud computing is revolutionizing IT ecosystems through offering scalable computing resources that are easy to configure, use and inter-connect. However, this model has always been viewed with some suspicion as it raises a wide range of security and privacy issues that need to be negotiated. This research focuses on the construction of a trust protocol in cloud computing to build a relationship between cloud service providers and cloud users. In particular, we address the rise of container-based virtualisation which has weak isolation compared to traditional VMs because of the shared use of the OS kernel and system components. Therefore, we will build a trust protocol to solve this weaker isolation whilst maintaining the performance and scalability of the approach. This paper proposes a security system to protect containers from other guests through the addition of a Role-based Access Control (RBAC) model and the provision of strict data protection and security.

Keywords—Cloud computing, Container isolation, RBAC, isolation benchmarking.

1. INTRODUCTION

Trust can be defined as a positive expectation towards the behaviour of another. In the context of cloud computing, the user's trust the intentions and actions of the cloud service provider (CSPs) with their personal data and information [1]. Trust in this context can be explained as believing in a promise that has been made by brands or technology [2]. People tend to lose trust in a system if they find that the information given to them is inaccurate. Furthermore, customers also needs some form of proof in order to believe the assertions made. For instance, CSPs need to show evidence to potential cloud users that their environment is secure and will protect the privacy of its users. This could be through the deployment of certified technologies or past performance for instance.

Trust is a critical issue in cloud computing because the remote, Internet-based nature of the service makes the user dependent on their provider for the effective running of their infrastructure. This includes the privacy and security of the data stored remotely, the integrity and robustness of the services running in the cloud, and the proper isolation of different tenant slices. The user must therefore trust the cloud provider assurances that all necessary security measures are being deployed and enforced to protect their assets within the cloud. On a technical level, this includes a range of security and network management systems and services such as end-to-end encryption, strong user authentication, robust virtualisation, and active infrastructure monitoring to name but a few. However, CSPs are not necessarily forthcoming regarding the configuration of their infrastructure and lack extensive third party auditing. Therefore, customers are often not sure whether they can identify a trustworthy cloud provider or not. Our work aims to identify solutions that would help to create a trust-based relationship between cloud service providers and cloud users.

One aspect that is especially critical for cloud computing is the need for isolation. Due to the shared tenancy, that is a central feature of virtualised infrastructures, providers need to enforce strong mechanisms to ensure that virtual services running on the same physical server do not interfere with or impede each other and that users cannot break out of their allocated virtual environment. Hypervisor based virtual machines typically provide a high degree of isolation and this abstraction enables the virtual machines to share hardware resource without interfering with other virtual machines. Intrusion, bugs, and viruses that compromise one virtual machine therefore cannot easily affect the other machines

due to this property [4]. However, a recent trend in cloud-based virtualisation is away from traditional 'full' virtual machines and towards containers [4]. These offer significant performance advantages due to the reduction in overheads through sharing a common system up to the OS kernel, but suffer from a resulting lack of isolation through more shared elements [4].

The remainder of this paper is organised as follows describe the isolation in the cloud, proposed approach which provide an overview about trust protocol model and the project testbed and conclusion.

2. ISOLATION IN THE CLOUD

In this section we will look in more detail at the issues of isolation in virtualised containers.

2.1 Isolation in containers

There are various merits that come with container-based technology. These merits are related to performance and efficiency in the execution of operations, as the level of abstraction occurs at the operating system which is better than virtualizing the whole hardware stack. Containers therefore share the same operating system kernel while offering root authorization as necessary [5]. Figure 1 show that the differences between hypervisor and container virtualisation.

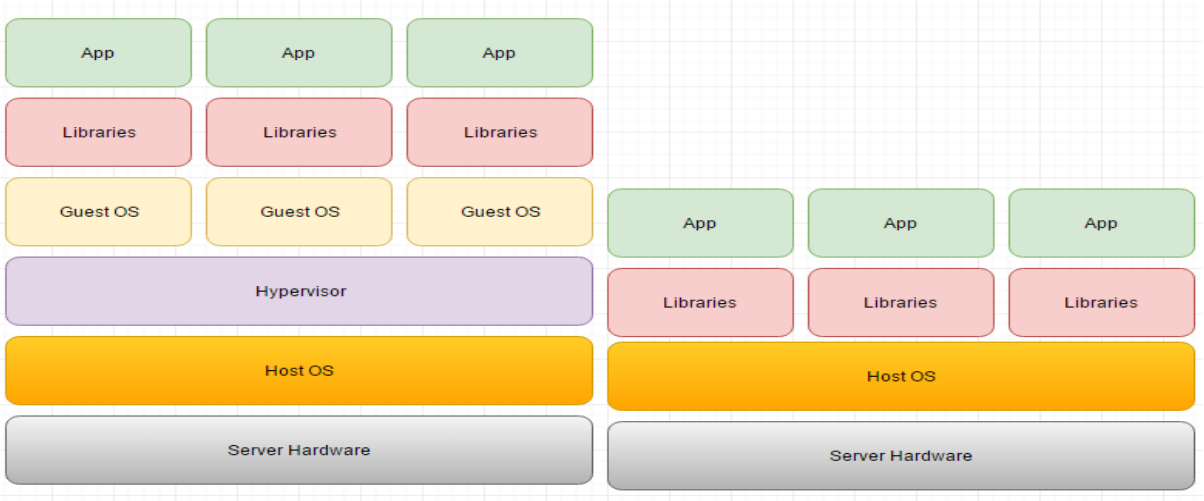

Figure 1: Hypervisor Vs Container.

Despite these merits, there are also downsides in using container-based technology. The weak isolation in containers is due to the sharing of components and an operating system kernel. Therefore, in the case of an attack or a flaw in the container, the magnitude is amplified because the attack can be propagated to the underlying operating system and consequently to the other containers. Container-based virtualisation relies on a customised kernel to enable sharing of operating system resources, thus, an application coupled with all its dependencies is deployed in a container which allows access to the kernel namespaces, policies, control groups, and even policies. This weak isolation through a common kernel allows installation of applications that may have system-level security measures and controls. If not checked well, they may contain malware or other malicious code that could spread to other containers thus compromising a whole system [5]. For instance, a bug, virus or intrusion could carry over to other containers because they share the same OS.

A recent study by IBM involved a comparison of isolation in Linux containers and full virtual machines [6]. The primary goal was to evaluate efficient methods of resource control using the two different methodologies. There was a comparison of traditional virtual machines and Linux containers when handling various workloads that were particularly CPU, memory, and network intensive to evaluate the level of resource isolation provided.

3. PROPOSED APPROACH

3.1 Trust protocol Model

To identify the solution that would help to create a trust based relationship between cloud service providers and cloud users, I have investigated the key elements to build trust in the cloud computing by focussing on addressing isolation in the container based virtualisation problem. Cloud service providers need to show evidence to cloud users show that the environment is secure and will protect the user's privacy. Therefore, the trust protocol helps to solve the weaker isolation issues and responsible for protect containers from other guests by using RBAC model.

We are developing a trust layer to address one of the key shortcomings in container-based virtualisation by using role based access control to isolate the guest VMs from each other. Role Based Access Control (RBAC) will be used as it relies on defining and assigning users to roles which includes system the permissions, as shown in figure 2. This method enables the individual user to perform a specific task in a specific container such as view, create, or modify a file. Roles are defined, for example, according to role, authority, and responsibility within the cloud user.

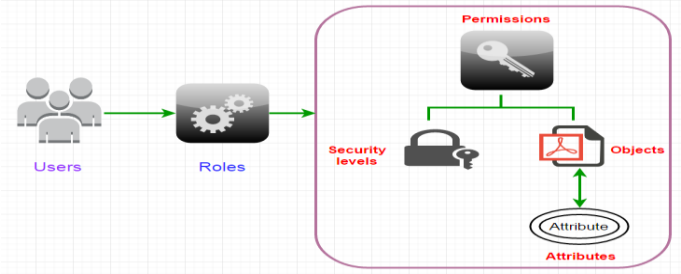

Figure 2: Trust protocol by using containers based virtualisation

We have created the first design that provides users with a higher degree of trust in cloud services in terms of data confidentiality, integrity and availability. Further, due to the centralized nature of data stored in cloud infrastructures, our proposed design would minimize data leakage and improve monitoring. Figure 3 shows the trust protocol design based on container-based virtualisation with RBAC. In this prototype, each container has Policy Decision Point (PDP), Policy Enforcement Point (PEP), Policy Database (PDB) and Policy Information Point (PIP). First, the PEPs in the container obtain information about an incoming user access request. Then, the PEP processes this and sends the information to the PDP for a decision. The PDP makes an access control determination according to it local policies or consults the PIP and PDB which can retrieve the attribute values related to the subject, resources and environment. Finally, the decision is relayed back to the PEP where it can be enforced.

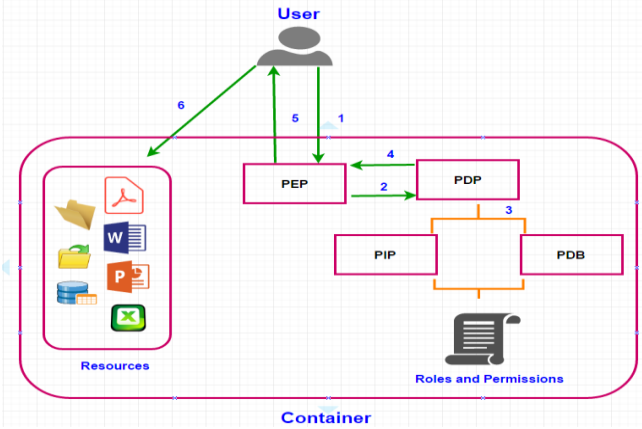

Figure 3: Trust model

Our RBAC model consists of independent systems in each part of the virtualised system so the containers do not rely on the host to make the decision. This means that a container can make its own decision about incoming access requests and the host can treat each container separately or according to a group policy. This will also help to minimise the delay in making decisions and reduce load on the host policy decision point. It will also improve availability and performance of the access control system, give the user greater visibility and confidence in their data integrity and therefore help to build trust.

A prototype of our trust protocol will be created using a Raspberry Pi Cloud in order to demonstrate a trustworthy, secure, and scalable cloud service in a practical environment. We aim to create a ‘data centre’ using up to 200 Raspberry pi nodes running Docker and Kubernetes containers. This will provide an excellent test bed for our work because, despite the limited performance of these devices, they will work in the same logical manner as a fully specified data centre and will demonstrate the same issues regarding isolation of users and services. Figure 4 show that **Software** Stack for RPi Cloud.

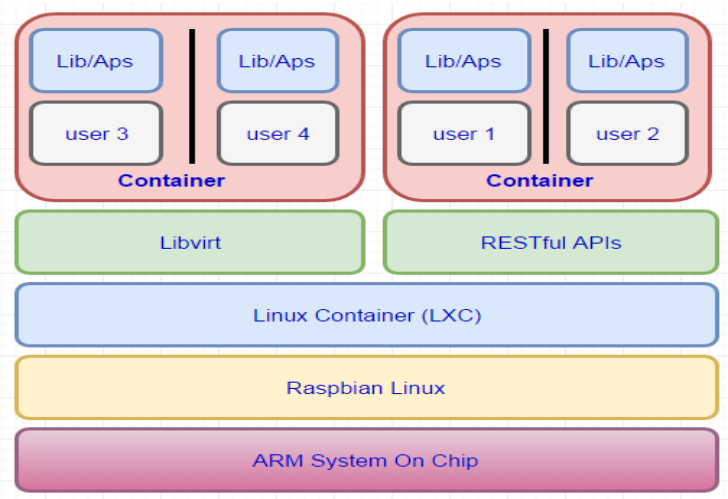

Figure 4: Software Stack for RPi Cloud [11].

4. CONCLUSION

In conclusion, therefore, we can say that container-based virtualisation does not provide a high level of isolation because it shares aspects of the OS kernel and components between all instances. This means that a user instance (and their data) is never truly secure and trustable and bugs, a virus, or other intrusions could carry over from one container to the other. Since this level of isolation is to some extent intrinsic to the approach, the issue of isolation in container virtualisation could instead be addressed by creating a trust layer using RBAC. Our model attempts to enforce isolation within each instance, as an individual user can only perform a specific task in a container according to role, authority, and responsibility assigned to that cloud user.

5. REFERENCES

[1] Pearson, S. 2012. Privacy, security and trust in cloud computing. *Computer Communications and Networks*, pp.3-42.

[2] Khan, K.M., & Malluhi, Q. 2010. Establishing trust in cloud computing. *IT Pro, Sept/Oct*: 20-26.

[3] Michael, B. 2009. In Cloud Shall We Trust? *IEEE Security & Privacy, Sept/Oct*: p. 3.

[4] Matthews, J. N., Hu, W., Hapuarachchi, M., Deshane, T., Dimatos, D., & Hamilton, G. (2015). Quantifying the Performance Isolation Properties of Virtualization Systems.

[5] Bettini, A. (2015). Vulnerability Exploitation in Docker Container Enviroments.

[6] W. F., Ferreira, A., & Rajamony, R. (2015). An Updated Performance Comparison of Virtual Machines and Linux Containers. IBM Research.

[7] Soltesz, S., Pötzl, H., Fiuczynski, M., Bavier, A., & Peterson, L. (2015). A Scalable, High-performance Alternative to Hypervisors. *Container-based OS Virtualization*.

[8] Anon. (2015). *Isolation*. Retrieved from Isolation Benchmark Suite: http://web2.clarkson.edu/class/cs644/isolation/design.html

[9] Xavier, M. G., Neves, M. V., & Rossi, F. D. (2015). Performance Evaluation of Container-based Virtualization for High-Performance Computing Environments.

[10] Muniz, J. (2015). *Penetration Testing with Raspberry Pi*. Birmingham: Packt Publishing.

[11] Tso, F.P., White, D.R., Jouet, S., Singer, J., & Pezaros, D.P. 2013. The Glasgow Raspberry Pi Cloud: A scale model for cloud computing infrastructures. In *Proceedings of IEEE 33rd International Conference on Distributed Computing Systems Workshops*, 8-11 July, Philadelphia (pp.108-112).

Ruqayah Al-Dahhan

Context-Aware Cloud-Based Access Control for the Internet of Things

Ruqayah R Al Dahhan, Qi Shi, Gyu Myoung Lee, and Kashif Kifayat
School of Computing and Mathematical Science, Liverpool John Moores University, Byrom Street, Liverpool, L3 3AF, UK
R.R.Aldahhan@2015.ljmu.ac.uk, Q.shi@ljmu.ac.uk, G.M.Lee@ljmu.ac.uk, K.Kifayat@ljmu.ac.uk

Abstract. Outsourcing data to some cloud servers enables a massive, flexible usage of cloud computing resources. However, various security concerns have been raised, due to hosting sensitive data on untrusted cloud. Access control is the first defensive line that forbids unauthorized access to the stored data. Moreover, access control on the untrusted cloud can be enforced using advanced cryptographic mechanisms. However, some challenges are still outstanding. These challenges are: 1) making dynamic decisions to grant access rights to the cloud resources and 2) solving the issue of the cryptographic access control systems that is considered as a performance killer. This issue is the revocation process. In this paper, we analyse some of the existing, related issues and propose a system that offers a solution to perform the revocation process without incurring heavy computation and communication overhead, particularly, if the revocation happens frequently. Currently, most of the revocation techniques require re-issuing many private keys for non-revoked users as well as re-encrypting the cipher-texts. In addition, unconstrained integration between the Internet of Things (IoT) and the cloud technologies will be provided to build a universal environment. This integration will be in a particular manner where dynamic context information can be extracted by IoT which is then used to improve the decision–making process enabling real-time access control. These proposed solutions will be useful to apply in many applications that need a secure, flexible, efficient access control system.

Keywords. Access control, revocation, context awareness.

1. Introduction

Merging the cloud computing and the internet of things (IoT) creates an essential, practical paradigm that serves a large number of applications. Where, IoT provides the dynamicity by interconnecting things/objects in a global, dynamic network. However, most of these interconnected things have limited computational power and storage. On the other hand, the cloud computing offers unlimited storage and powerful computation capabilities.

Outsourcing data to some cloud servers enables a massive, flexible usage of cloud computing resources. However, various security concerns have been raised, due to hosting sensitive data on untrusted cloud[1]. Access control is the first defensive line that forbids unauthorized access to the stored data. In addition, it is one of critical security mechanisms for data protection in cloud applications.

To ensure that an access control mechanism removes or at least eliminates the mentioned security concerns, attribute-based access control has been introduced. Moreover, to hide the data from the untrusted storage server, encrypted data is stored in cloud data servers[2]. In general, attributes are classified into two types: 1) non-temporal attributes with discrete attribute values (e.g. age, address, email, occupation, etc.), and 2) temporal attributes (e.g. interval, time, etc.).

Each cloud access control mechanism has crucial requirements which need to be supported. These requirements are described as follows:

1) The revocation process [3] : is an essential prerequisite of any cloud access control system. It means that a revoked user, after it has been revoked, will no longer have the previous assigned right for further data access and decryption of related cipher text/data.
2) The delegation of authority property.

3) The activity property (i.e., making decisions depends on the current situations).

The last two points are auxiliary requirements that enhance the performance of any access control system and provide more flexibility.

However, to the best of our knowledge, these requirements have not been efficiently achieved altogether in any of the existing systems. In terms of delegation, for example, in[4], the authors use a Hierarchical Attribute-set based encryption technique in which a delegation algorithm is efficiently applied. However, due to the hierarchical structure of the system, the cipher text size increases linearly with the number of attributes. To achieve effective and efficient access control, we need a model that fulfils all the above requirements.

In this paper, developing a flexible, active access control model based on context information gathered by the IoT technology is the proposed work. In particular, the revocation problem will be addressed by adopting a novel revocation approach which uses a cloud server to perform most of the required, heavy computations without trusting it. Also, a delegation property will be devised.

The rest of this paper is structured as follows. The literature review is presented in section 2 in which we classify some of the existing access control problems. The proposed system is presented in section 3. Finally, section 4 provides the conclusion and the future work.

2. Literature review

Some requirements and weaknesses in the existing systems are summarized as follows:

- To support any sufficient cloud access control system, some requirements need to be achieved. These requirements are revocation, activity and delegation properties. These requirements have not been efficiently achieved altogether in any of the existing systems.
- The attribute revocation is a critical issue that is difficult to manage in CP-ABE [5], particularly, in multi-authority systems. In addition, temporal attributes are not well handled by CP-ABE. So the adoption of CP-ABE requires additional refinements.
- Some requirements are needed in order to handle the revocation problem. These requirements are an instantaneous misbehaving user revocation process, collusion resistance, reducing the computation overhead, Backward Security, and Forward Security[6, 7].
- The shortcomings of the existing schemes include the cloud server being assumed trusted, the use of a lazy revocation process[8], updating all secret keys of the non-revoked users and re-encrypting cipher texts (i.e. high computation overheads)[9], revoking a limited number of users[10], or expanding the cipher text size.
- Some issues have not been addressed in any activated delegation process. These issues that have to be taken into account are key-delegation abuse, and revoking the delegated keys.
- Organizing the gathered information by IoT in a way that meets the system needs and utilizing contextual information to provide improved services to the system user, are the essential issues of any context-aware system[11].

3. The proposed system

Based on the challenges and drawbacks identified earlier, the general aim of this proposed system is to form a spontaneous coalition between the IoT and cloud in a particular way where IoT provides accurate, dynamic context information to the cloud which in turn improves decision-making for access to its resources. This aim will be serving a large number of applications, particularly, that have digital contents such as e-books, videos, games and so on. Where, it can be essential to find a mechanism that prevents them from being obtained by inappropriate users. This will be achieved by utilizing relevant contextual information such as locations and identities offered by IoT for the access control.

To achieve the goal of this proposal, some principles and fundamentals that related to the cloud access control have been studied. Attribute-based access control over encrypted data is known as an attribute-based encryption (ABE) technique. The major operations of the ABE are system initialization, key generation, encryption and decryption (illustrated in figure1) that use to control the access to data. The ABE has been chosen due to its ability to store data on an untrusted server which in turn benefits for significantly exploiting cloud resources.

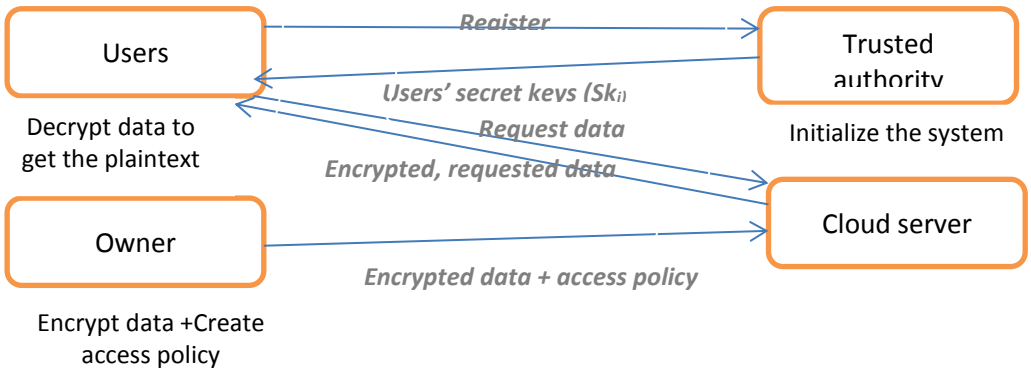

Figure1: The main operations of any cloud access control system

The design of the proposed system is divided into two stages. These stages are 1) designing an initial cloud oriented access control model including an algorithm to solve the revocation problem stated earlier, and 2) designing a model for collecting raw data using the IoT technology and extracting context-awareness information from the data, which is utilized to make access control decisions and activate necessary delegation properties. These two models will be integrated together to produce the complete framework proposed.

For the first stage, we have chosen the CP-ABE scheme of Balani and Ruj [12] to extend it with privacy preserving revocation that is needed to mitigate the burden of the revocation process on the owner, gain benefits from cloud computing resources, and build collusion-resistant systems. Where, the selected scheme has some weaknesses that have been identified, e.g. a limited number of users can only be revoked when the revocation process is performed. In addition, the decision-making ability of this scheme does not adapt to the contextual information changes. However, some desirable properties of the scheme led us to choose it.

To design a privacy preserving revocation system, a strategy of system design has been adopted. That is to delegate the primitive missions of any revocation process to the cloud without revealing any information about the data or users' access privileges. In contrast with the existing systems, our proposed system does not assume that the cloud can be trusted. To prevent the server from inferring any information of users' keys, the Boneh–Lynn–Shacham (BLS) signature technique has been chosen. This type of signature has the shortest length among signature schemes used in the traditional cryptographic systems. That is needed due to the bandwidth constraints of the environment and because of the efficiency requirements of any system that has a large number of users. As a result, the signature generation operation will be added to the operations of the ABE system. This operation will be executed by users as shown in figure2.

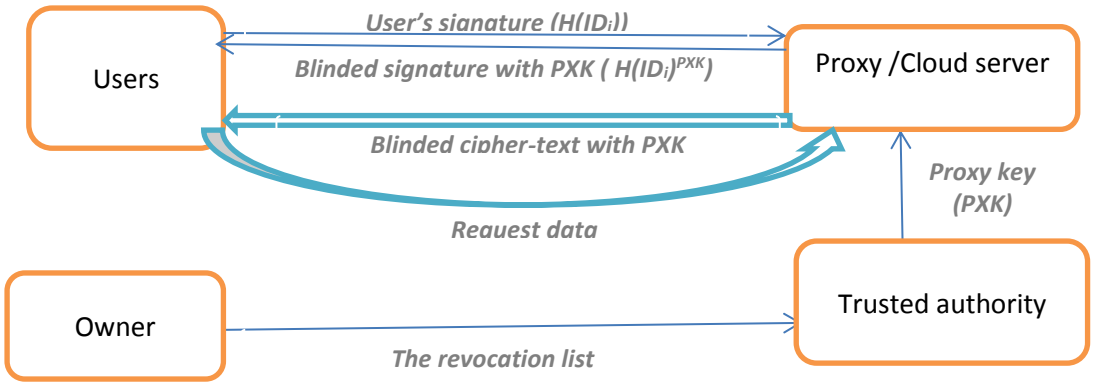

Figure2: the proposed privacy preserving revocation system

We have chosen a privacy preserving revocation process to make the system more confidential. Where, confidentiality is considered as a critical issue that has an effect on a decision of users or owners when they adopt cloud services. In addition, to build a collusion-resistant system, avoiding placing entire trust in a single designated entity (which is a server), has been under our considerations. Achieving privacy preserving revocation will not only eliminate the burden of owners from the expensive revocation task, but also mitigate their fear of leaking their outsourced data. However, the mentioned challenges have to be solved.

4. Conclusion and future work

In this paper, the major issues of the current systems such as revocation problem and the absence of active access control systems, have been identified. The proposed system is based on the integration of IoT and cloud computing to create an active access control system. This system grants adaptable access rights to users/clients depends on their current situations by utilising dynamic, relevant contextual information which is gathered by the IoT technology. The system will efficiently solve the revocation problem on an untrusted server as well as activating the delegation capability.

As a foundation of our future work, an initial cloud access control model can be built by developing our adopted system utilizing the techniques that we have selected and stated earlier. After that, a range of potential issues will be studied to start with the second stage of the system development. This stage consists of two steps which are designing a model for making access control decisions utilizing context-awareness information that is extracted by IoT technology and activating necessary delegation properties. These two models will be integrated together to produce the complete framework proposed. Finally the theoretical evaluations and experimental measurements of the system performance will be conducted to check the efficiency and security of the proposed scheme which in turn can reduce the data owner's workload if the revocation occurs frequently.

References

[1] D. Zissis and D. Lekkas, "Addressing cloud computing security issues," *Future Generation computer systems*, vol. 28, pp. 583-592, 2012.

[2] M. Ahmadi, M. Chizari, M. Eslami, M. J. Golkar, and M. Vali, "Access control and user authentication concerns in cloud computing environments," in *Telematics and Future Generation Networks (TAFGEN), 2015 1st International Conference on*, 2015, pp. 39-43.

[3] S. Ruj, "Attribute based access control in clouds: A survey," in *Signal Processing and Communications (SPCOM), 2014 International Conference on*, 2014, pp. 1-6.

[4] T. Radhika and S. Vasumathi Kannagi, "Survey on user revocation and fine grained access control of PHR in cloud using HASBE," *International Journal of Computer Science and Mobile Computing*, vol. 3, pp. 452-6, 2014.

[5] K. Yang, X. Jia, and K. Ren, "Attribute-based fine-grained access control with efficient revocation in cloud storage systems," in *Proceedings of the 8th ACM SIGSAC symposium on Information, computer and communications security*, 2013, pp. 523-528.

[6] M. Horváth, "Attribute-based encryption optimized for cloud computing," in *International Conference on Current Trends in Theory and Practice of Informatics*, 2015, pp. 566-577.

[7] C.-W. Liu, W.-F. Hsien, C. C. Yang, and M.-S. Hwang, "A Survey of Attribute-based Access Control with User Revocation in Cloud Data Storage," *IJ Network Security*, vol. 18, pp. 900-916, 2016.

[8] Z. Wan, J. e. Liu, and R. H. Deng, "HASBE: a hierarchical attribute-based solution for flexible and scalable access control in cloud computing," *IEEE transactions on information forensics and security*, vol. 7, pp. 743-754, 2012.

[9] K. Yang and X. Jia, "Expressive, efficient, and revocable data access control for multi-authority cloud storage," *IEEE transactions on parallel and distributed systems*, vol. 25, pp. 1735-1744, 2014.

[10] S. Jahid and N. Borisov, "Piratte: Proxy-based immediate revocation of attribute-based encryption," *arXiv preprint arXiv:1208.4877*, 2012.

[11] M. Giannikos, K. Kokoli, N. Fotiou, G. F. Marias, and G. C. Polyzos, "Towards secure and context-aware information lookup for the Internet of Things," in *Computing, Networking and Communications (ICNC), 2013 International Conference on*, 2013, pp. 632-636.

[12] N. Balani and S. Ruj, "Temporal access control with user revocation for cloud data," in *2014 IEEE 13th International Conference on Trust, Security and Privacy in Computing and Communications*, 2014, pp. 336-343.

Darren Conway

Understanding Nrf2 and NF-κB dynamics with mathematical modelling

D Conway [1], J Wardyn[2], Chris Sanderson[2], J Leedale[2] and S Webb[1]

[1] Department of Applied Mathematics, Liverpool John Moore's University, James Parsons Building Byrom Street, Liverpool, L3 3AF, UK

[2] Department of Cellular and Molecular Physiology, University of Liverpool, Crown Street, Liverpool L69 3BX, UK

Abstract

Reactive oxygen species (ROS), produced by oxidative stress, are a by-product of normal metabolism and play a role in the initiation, promotion, and malignant conversion of carcinogenesis through activation/suppression of redox-sensitive transcription factors. NF-E2-related factor 2 (Nrf2) encodes for antioxidant and general cytoprotective genes, while NF-κB (nuclear factor kappa-light-chain-enhancer of activated B cells) regulates the expression of pro-inflammatory genes. During low levels of oxidative stress, Nrf2 is activated and translocates to the nucleus where it transcribes its target genes preventing a further increase in ROS levels, thereby restoring oxidative modifications of affected proteins. However, at a certain threshold at which ROS levels threaten cellular viability, the NF-κB responses become activated, triggering an inflammatory response. The NF-κB and Nrf2 pathways are therefore at the core of protective cellular signalling and the imbalance between their activities has been linked to many inflammatory diseases, cancer and neurodegeneration. The central goal of this paper is to develop an *in silico* model that will provide a better understanding of how the two pathways interact. A stochastic petri net model containing both Nrf2 and NF- κB pathways was generated and the correlation between this computational data and experimental data provides confidence that the model predicts critical test points of contact between the two pathways. The model is therefore a tool that can be used to advance the discovery, development and clinical use of therapeutic drugs that will target oxidative stress in cases of chronic inflammation and disease.

1. Introduction

The Nrf2 Coding sequence first characterised by Yuet Wai Kan, who revealed Nrf2 was able to bind activator protein-1 (AP-1) and NEF-E2 tandem repeat concensus DNA sequence. The Nrf2 protein belongs to the Cap'n'Collar family of proteins (CNC) and to the subfamily of basic leucine zipper (bZIP) proteins (1,2). The transcriptional activity of the Nrf2 protein requires the formation of a heterodimer complex with another member of the bZIP subfamily- the small MAF (sMaf) proteins. This interaction facilitates binding to a *cis* regulatory DNA element called the Antioxidant Response Element (ARE), which is contained within the promoters of Nrf2 target genes (1,3). The key characteristic of this transcription factor is its very low basal activity and its stringent regulation, as the half-life of Nrf2 protein has been estimated to last only 10-30min (4). The stability of Nrf2 dramatically increases as a result of diverse stimuli including plant-derived phytochemicals and intracellular and extracellular stress factors, such as ultraviolet (UV) and gamma (or ionising) radiation, electrophiles,

pollution, inflammation and reactive oxidant species (ROS) (3,5). Expression levels of the Nrf2 protein are primarily controlled at a post-transcriptional level, through an interaction with proteins that trigger proteasome mediated degradation (6,7). The best understood negative regulator of Nrf2 is the Kelch-like ECH-associated protein (Keap1), which is an actin-bound zinc metalloprotein that acts as an E3-ligase, facilitating the attachment of ubiquitin chain to Nrf2 (8). Keap1 binds as a dimer to the Neh2 domain within Nrf2 forming bonds with the high affinity ETGE and low affinity DLG amino acid sequences. This interaction brings the Nrf2 protein into proximity with Cullin3 and Ring Box 1 (Rbx1), which then catalyse the process of ubiquitin attachment (**Figure 1**) (9). Keap1 is located mainly in the cytosol where it constantly sequesters Nrf2, thereby restricting basal Nrf2 activity to very low levels. An unusually high number of reactive cysteine (Cys) residues are encoded within Keap1 (27 Cys residues), makes it an extremely sensitive sensor of oxidative stress, with C151, C257, C273, C288 and C297 being especially sensitive to oxidation (3,10). The oxidation of thiols within Cys residues leads to the formation of disulphide bridges between cysteines, resulting in a conformational change in Keap1 protein structure, which in turn prevents the effective ubiquitination and degradation of Nrf2 (9,11).

Newly formed Nrf2 proteins will still bind to free Keap1 dimers. However as Keap1 becomes saturated, free Nrf2 is then allowed to enter the nucleus, where it will subsequently heterodimerise with sMaf and bind to ARE containing promoter sequences (**Figure 1**) (9). Therefore, antioxidant pathway activation will rely on Nrf2 protein synthesis to overcome the levels of Keap1, which are usually present in cells, at very low (near-saturated) levels (12).

The Keap1/Cull3/Rbx1 complex is extremely robust and efficient in restricting Nrf2 protein expression. However, several other negative regulators of Nrf2 protein expression have been described. The recently described GSK-3/β-TrCP axis exhibits a notable difference to Keap1-mediated inhibition (13). GSK-3 is active basally and requires priming phosphorylation of its targets, which then prompts further attachment of a phosphate group onto a serine or threonine residue. In the presence of glucose the insulin/Akt/PI3K pathway leads to GSK-3 phosphorylation at Ser9 (β isoform) and Ser21 (α isoform), which terminates its activity (14). Nrf2 is also a target for GSK-3 phosphorylation, on the Neh6 domain, facilitating docking of the β-TrCP E3 ubiquitin ligase and formation of the β-TrCP/Skp1/Cull1/Rbx1 complex, which like Keap1/Cull3/Rbx1 catalyses ubiquitination of Nrf2 and subsequent degradation(15,16). While Keap1 is thought to dominate the control of cytoplasmic Nrf2 levels, the GSK-3/β-TrCP axis is thought to be predominantly active in the nucleus, directing Nrf2 protein for nuclear proteasomal degradation (15).

Nrf2 controls the transcription of over 200 genes and depending on the tissue context, these genes have prominent roles in the maintenance of redox status and the generation of reducing equivalents, protein folding and degradation, cell metabolism, calcium homeostasis and drug metabolism (17,18).

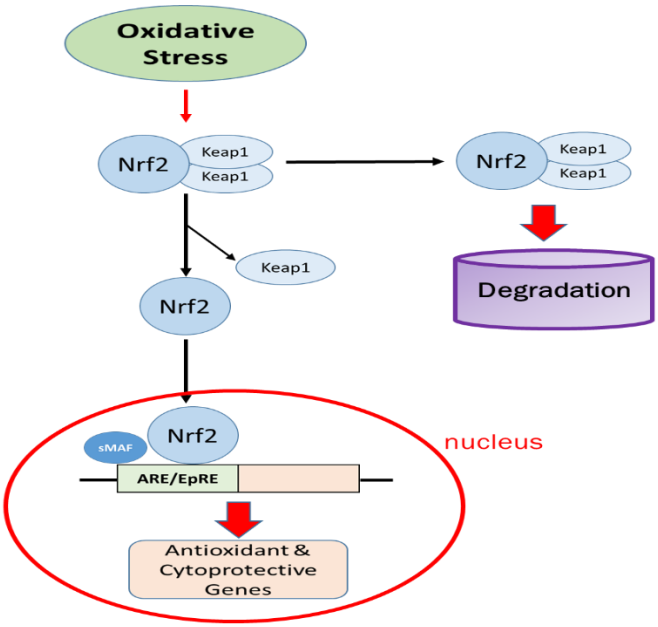

Figure 1. The Keap1-dependent Nrf2 regulation. Simple schematic diagram of the Nrf2 pathway. Nrf2 is sequestered by Keap1 under normal conditions and the complex closes allowing attachment of the ubiquitin chain. The Keap1 is then recycled and binds to another Nrf2 molecule. During oxidative stress, there is a modification of cysteine residues on Keap1 by oxidation or attachment of electrophilic compounds. The Keap1 is unable to form the closed complex and therefore catalyse the ubiquitin attachment. The newly made Nrf2 is then accumulated in the nuclear space and leads to ARE genes transcription.

The NF-κB transcription factor mediates immune responses to bacterial and viral infections, as well as initiates gene expression supporting inflammation, cell development, proliferation, anti-apoptotic pathways, oxidative metabolism and protection against UV radiation (19-21). NF-kB is actually a family of transcription factors including RelA (p65), RelB, c-rel, p50 and p52 subunits, which act as homo- or hetero-dimers (22). Only the p65, RelB and c-rel contain the transactivation domain required to drive transcription. The p50 and p52 subunits are detected basally in the nucleus of unstimulated cells and are thought to have an inhibitory effect on gene expression, by blocking DNA sequence availability (22,23). A complex network of protein interactions usually initiated by an extracellular stimuli (22,24) mediates NF-kB signalling. The NF-kB subunits form homo- and hetero-dimers through their Rel homology domains (RHD), which are also necessary for their dimerization, DNA binding and association with the IkBa inhibitor (22,24). The p65/p50 heterodimer is sequestered in the cytoplasm by association with IKBa, which obscures one out of two NLS and limits its nuclear entry (22,25,26). Importantly, NF-kB gene transcription is inducible by variety of stress stimuli and over 150 different factors have been identified as activators of NF-kB mediated gene expression: *e.g*. LPS, exotoxin B, muramyl peptide, viruses *e.g.* Hepatitis B, Adenovirus, Herpex Simplex Virus-1, HIV, cytokines, but also physical stress, UV radiation, shear stress, ischemia oxidative stress and environmental hazards (27,28). NF-κB plays a central role in the maintenance of the immune responses by initiating the genetic program designed to modulate the local environment and to attract the immune cells to the site of infection or injury. It mediates the expression of approximately 300 genes, including numerous cytokines and their receptors, anti-apoptotic genes and adhesion molecules (28,29).

TNFα is one of the best-studied cytokines and it is a potent activator of NF-kB-mediated gene expression, playing an important role in systemic inflammation and the induction of fever (30,31). It has pleiotropic effects as it can induce a range of cellular responses such as proliferation, chemotaxis, apoptosis and inflammation, as its downstream signalling triggers several molecular cascades (32).

Pro-inflammatory cytokines such as TNFα and IL-1β activate the canonical signalling cascade by

engaging the extracellular receptors and initiating a relay of intracellular phosphorylation events, which co-ordinate signalling and conditional cell responses (33). Activation of the TNFR1 receptor initiates the TRADD/RIP signalling cascade, which removes the phosphate group from the IKK kinases complex, comprised of the IKKα and IKKβ catalytic subunits and IKKγ (NF-κB essential modifier, NEMO) (**Figure 2**). IKK activation results in the phosphorylation of IKBα on Ser32 and Ser36 and parallel activation of several kinases, such as MAPK p38, JNK (22,24,32). Phosphorylation primes IKBα for interaction with the β-TrCP/Skp1/Cullin1 complex, which drives IKBα ubiquitination and proteasomal degradation, finally releasing the NF-κB subunits to the nucleus (34).
The entire signalling process from TNFR1 activation to κB transcription is very rapid, taking place within minutes. The activation of inflammatory gene transcription also initiates multiple negative feedback loops, which prevents the inflammatory signalling uncontrollably increasing. The IKBα protein is one of the earliest gene targets of NF-κB signalling, in response to TNFα cytokine. Shortly following translation, IκBα localises to the nucleus and removes p65 from the DNA, and sequesters it back into the cytoplasm (35). In addition, NF-κB also transcribes the deubiquitinating enzyme (DUB) A20, which terminates the signalling cascade upstream of the IKK complex by modification of the receptor interacting protein (RIP), which is essential for TNRF1 receptor signalling (**Figure 2**). The A20 protein removes Lys-63 chains from the RIP protein leading to Lys-48 ubiquitination and targeting for proteasomal degradation, leading to inactivation of the downstream phosphor-relay signalling (36,37). Therefore, both IKBα and A20 create safety loops terminate the signalling from the inflammatory signalling.

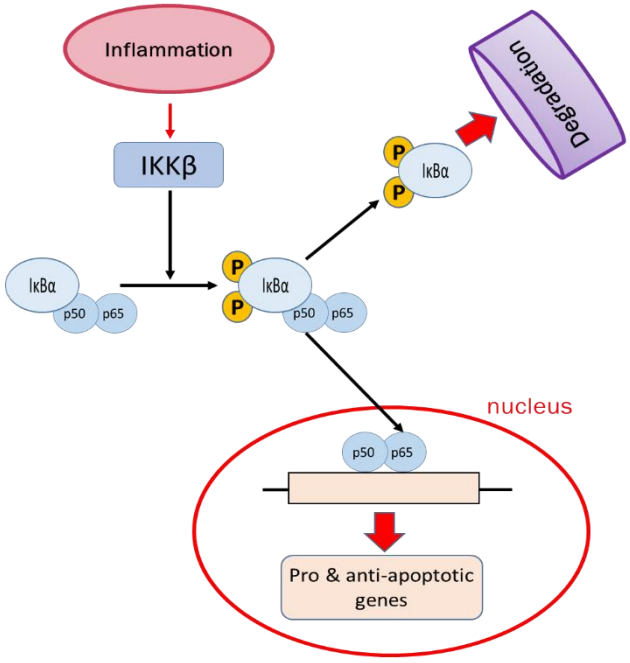

Figure 2 The Canonical and Non-Canonical NF-kB Pathways. Simple schematic diagram of the NFkB pathway. The canonical/classical pathway of NF-κB activation involves inflammation that triggers a downstream cascade of ubiquitination and phosphorylation events leading to nuclear occupancy of p65/p50 heterodimers. The p65/p50 dimer then translocates to the nucleus and mediates transcription of κB driven genes.

To simulate a perturbation, we used the firing of two time delayed places, TNF and CDDO, both shown on the signalling network in Figure 3. This perturbation is set at 50 time units to allow the simulated system to reach a steady state. The model has been minimised to only include functional parts. The inclusion and omission of pathway components was decided through reading literature detailing the

workings of both pathways. Three points were chosen to demonstrate the cross-talk between both pathways. These three components are: 1) Nrf2 gene transcription modifies NFkB preventing it from translocating into the nucleus, 2) NFkB gene transcription of Nrf2 and 3) keap-1 inhibition of IKK. In order to evaluate the accuracy of our stochastic model, we tested its simulation output against the experimental data results (Figure 4). Details of the experiments are given in the Materials and Methods sections.

2. Material & Methods

Our method models signal flow as the pattern of token accumulation and dissipation within places (proteins) over time in the Petri net. Transitions in the network represent directed protein interactions; each transition models the effect of a source protein on a target protein, transfection, production and decay. Through transition firings, the source can influence the number of tokens assigned to the target, called the token-count, thereby modelling the way that signals propagate through protein interactions in cellular signalling networks.

In order to overcome the issue of modelling reaction rates in the network, signalling dynamics are simulated by executing the signalling Petri net (SPN) for a set number of steps (called a run), each time beginning from some initial marking.

For each step, the individual signalling rates are simulated via generation of random orders of transition firings (interaction occurrences). When the results of a large enough number of runs are averaged together, we find that the series of token-counts correlate with experimentally measured changes in the activity levels of individual proteins in the underlying signalling network. In essence, the tokenized activity-levels computed by our method should be taken as abstract quantities whose changes over time correlate to changes that occur in the amounts of active proteins present in the cell. It is worth noting that some of the most widely used experimental techniques for protein quantification—western blots and microarrays—also yield results that are treated as indications, but not exact measurements, of protein activity-levels within the cell. In contrast, our method is designed to operate on tokenized models of signalling networks with the ultimate intent of predicting the activity-level changes of proteins in the underlying signalling network over time.

2.1 Cell Culture of SK-N-AS and BAC$^{Nrf2\text{-}Venus}$ Neuroblastoma Cell Lines

BAC$^{Nrf2\text{-}Venus}$ cells were generated previously by stable integration of bacterial artificial chromosome (BAC) encoding Nrf2-Venus fluorescent protein fusion into neuroblastoma SK-N-AS cells, at 2 copies per cell. The wild-type SK-N-AS and BAC$^{Nrf2\text{-}Venus}$ were maintained in supplemented MEM medium (1% P/S, 10% FBS(10270106), 1% Glutamax (2mM) and 1%NEAA (11140035)) in a humidified atmosphere at 37^{o}C, 5% CO_2 and passaged every 3-4 days when the cell monolayer reached 80-90% confluence. For subculture, the cells were washed twice with pre-warmed DPBS (w/o Ca^{2+} and Mg^{2+}) and 2ml of 0.25% Trypsin-EDTA (Life Technologies, 15090046) was added onto cells and placed to TC incubator ~2min to allow the cells to detach. The cells were collected by adding 8ml pre-warmed media and spun down for 3min at 200G. Cell media was then removed and pellet re-suspended in 10ml of fresh cell culture media and seeded onto desired flask/plate for further culture. The BAC$^{Nrf2\text{-}Venus}$ cells were used for up to 25 passages.

2.2 Transfections of Plasmids Encoding Fluorescent Fusion Proteins

Transient transfections were carried to introduce fluorescent protein fusions into target cells using Lipofectamine 2000 (Invitrogen) according to manufacturer's protocol. For transient expression of p65-DsRedXP construct of cells cultured in 35mm dish, 0.5µg of Maxi-prepped DNA stock was used alongside 0.5µl of Lipofectamine 2000 for imaging the next day.

2.3 Live Cell Imaging

For real-time imaging of live cells, cells were seeded onto the 1 or 4 compartment 35mm glass bottom dishes (Greiner Bio-One). The 4 compartments allowed imaging of 4 different experimental conditions in parallel. The imaging experiments were performed under humidified atmosphere, at 5% CO_2 and 37^{o}C on two imaging systems. The primary cells expressing plasmid encoded fluorescent protein fusions were imaged on the Zeiss Axiovert 5.10 (Zeiss Germany) confocal microscope using 40x oil immersion objective with numerical aperture (NA) of 1.4. The image acquisition on this system was coupled with autofocus Marco (Ellenberg lab, EMBL), which enabled maintenance of stable Z-plane position of the imaged cells, avoiding the problems of focal drifts that can occur during the long acquisition times. The LSM 7.80 (Zeiss, Germany) system was used for monitoring low expression of fluorescent proteins, as it has superior resolution and sensitivity of detection, using 40xoil immersion objective (1.4 NA) and LSM ZEN 2010 image acquisition software (Zeiss). In both systems the image acquisition was performed, using 512x512 pixel resolution, 7 scanning speed with the pinhole diameter adjusted to the fluorescence intensity of imaged samples.

2.4 Image Analysis

Image analysis post-acquisition was performed using Cell Tracker software Version 6.0 (www.dbbkgroup.org/celltracker/) (Shen *et al,* 2006). The nucleus was drawn manually and adjusted on every acquisition image, either manually or automatically by cell tracker software. The data was averaged and exported to Excel file format. It was normalized to the initial fluorescence levels and the noise was reduced by averaging the values using 3rd order moving average (three frame smoothing). The data from cell populations was averaged between independent experiments and error bars were plotted using standard deviation of the mean. The legends of the figures contain information about the biological replicated "n" and the total cell numbers analysed "c".

2.5 Fluorescence Cross Correlation Spectroscopy (FCCS)

The FCCS experiments were performed at University of Manchester with kind help from Dr. James Boyd (White lab). The data collection was performed using LSM 780 with confocor 3 mounted on Axio observer Z1 microscope using oil immersion 100x lens (N.A. 1.46) and using ZEN2010 software (Zeiss). The Venus and the mCherry fluorescence were excited using a 514nm laser and 561nm DPSS diode laser respectively. The pinhole was set to 1 airy unit and the laser power was typically set to 1% laser power, adjusted to avoid photobleaching and to maximize the count per minute (cpm) fluorescent signal to minimum 0.5 kHz value. The data collection protocols were previously described by Bacia *et al,* 2006; and were carried out 10x for 10s each and the fluorescence signal of mCherry and the Venus channels was then compared using first correlation and then cross-correlation logarithms using LSM ZEN 2010B FCS function. The data was then exported to MATLAB (Mathworks).

3. Results

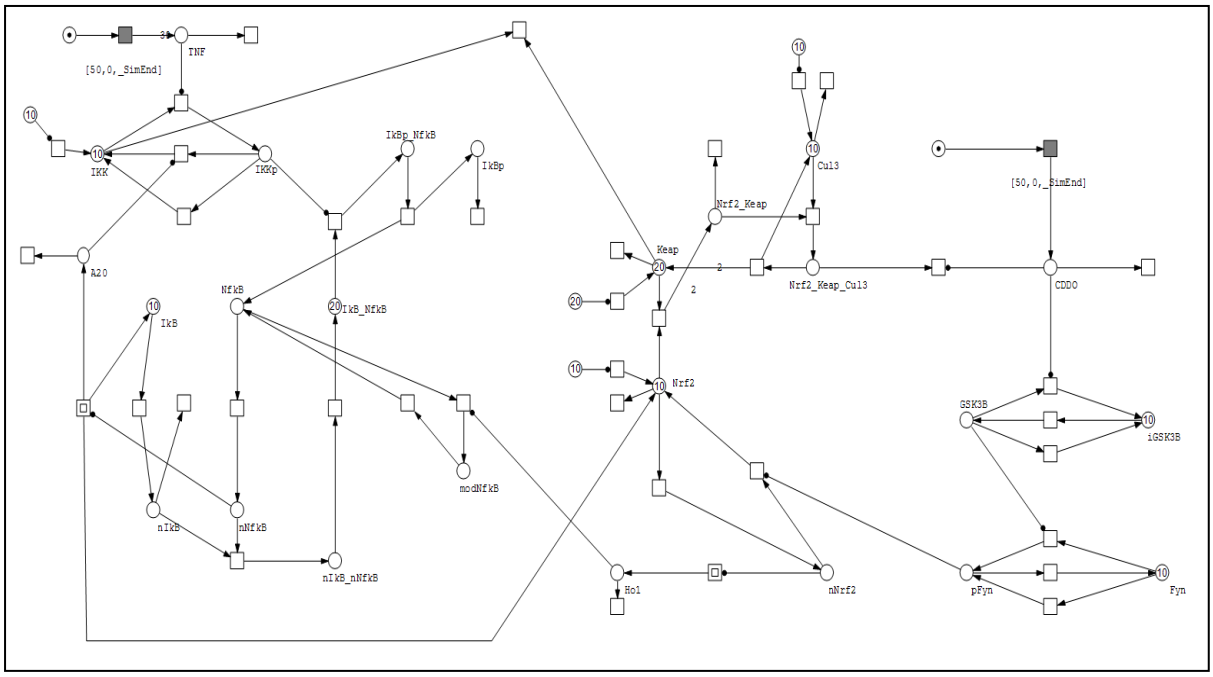

Figure 3 The Petri-Net model. Schematic outlay of the petri-net model. The model contains a simplified working version of the Nrf2 and NF-κB pathways and the interactions between both (nNF-κB/Nrf2, Keap-1/IKK, HO-1/NF-κB).

To validate our model and ensure that its output was accurate to what is seen *in-vivo*, the computational data was compared to the experimental results (Figure 4). CDDO-Me activates the Nrf2 pathway and mimics the effect of the cells response to oxidative stress. The introduction of CDDO-me *in-vivo* results in an increased peak of Nrf2 activity followed by smaller oscillations of Nrf2 activity before returning to a steady state level (Figure 4A – green). Similarly, NF-kB activity increases, in response to the administration of TNFα, giving of a singular large peak and several smaller oscillations before returning to its original steady state level. Comparatively, the same results can be seen from the output of our model (Figure 4B). When a run is fired in our model there is an increase in the activity of both NF-kB and Nrf2 levels followed by smaller peaks and a return to a base line level. This validation gives us confidence that the dynamics within our model are correct and the data obtained can be trusted.

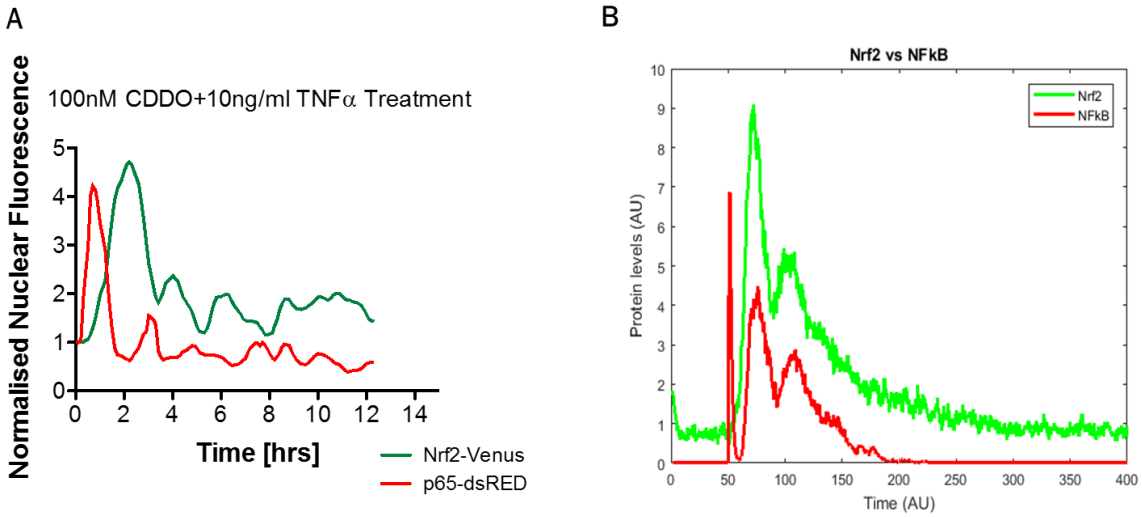

Figure 4 Qualitative validation of the petri-net model through comparison of experimental vs simulated data. (A) Co-administration of CDDO-Me and TNFα in BAC cells expressing p65-dsRED. Peaks in p65 nuclear levels (red) induce subsequent Nrf2 (green) accumulation. (B) Co-stimulation of CDDO-Me and TNFα by the model produce peaks in NF-κB levels that also lead to Nrf2 accumulation. The petri-net qualitatively represents Nrf2/NF-κB dynamics.

Next, the levels of NF-kB were altered by changing the multiplicity on the relevant edges from 1 to 2 and 4 (Figure 5). These changes were made to assess if the oscillatory behaviour shown by Nrf2 was driven by NF-kB. All 3 Nrf2 runs were plotted on the same graph to shown comparison. The original values were plotted in blue, the double NF-kB increase was plotted in red and the 4-fold increase was plotted in yellow. A graph for the NF-kB traces is also shown below. In the original Nrf2 trace, the initial peak is approximately 9 arbitrary units high. This initial peak then increases to approximately 16 and 25 arbitrary units respectively when NF-kB is doubled and quadrupled.
One of the biggest limiting factors in the Nrf2 pathway is keap-1. Therefore, it is important to show the effect of keap-1 on the dynamics of our model (Figure 6). The original trace (Figure 6A) is shown with a maximum Nrf2 peak of approximately 9 arbitrary units. The level of keap-1 in this simulation was 20 arbitrary units. To showcase the effect of keap-1 on Nrf2 activity, the amount of keap-1 was altered and plotted against the maximal peak of Nrf2 (Figure 6B). The obvious trend shown from the results is that a decrease in keap-1 leads to an increase in Nrf2 and vice-versa.

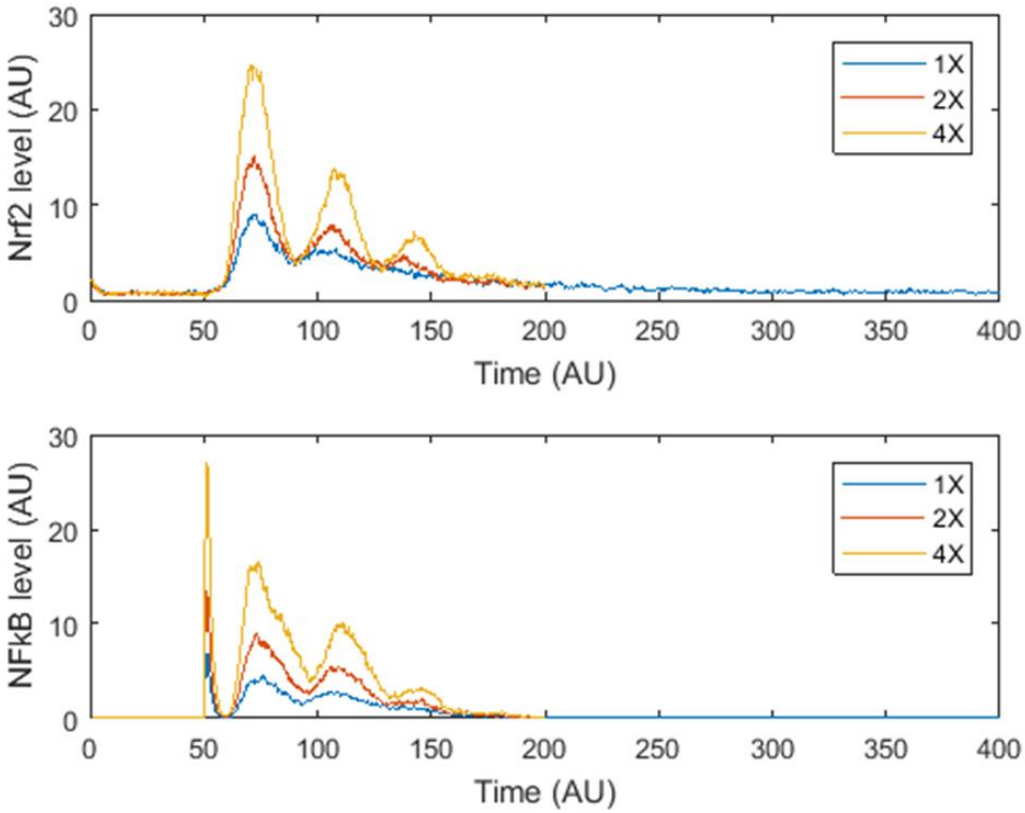

Figure 5 High levels of NF-κB expression promote oscillatory behaviour in Nrf2. (A) Plot showing Nrf2 levels when NfkB is constant (blue), increased 2 fold (red) and increased 4 fold (yellow). (B) Plot showing NFkB levels when NfkB is constant (blue), increased 2 fold (red) and increased 4 fold (yellow).

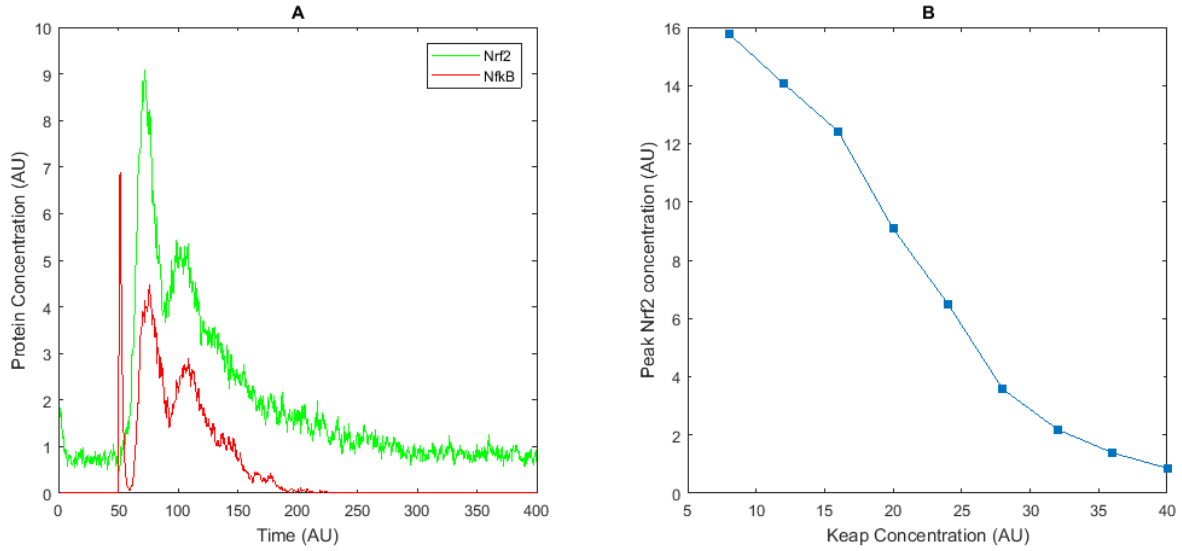

Figure 6 Changing Keap-1 levels alter network dynamics. (A) Initial plots of Nrf2 (green) and NF-κB (red) when co-stimulated by CDDO-Me and TNFα. (B) Decrease in both Nrf2 when keap-1 levels are increased.

4. Discussion

As can be seen in Figure 4, our method accurately predicts the dynamics between the Nrf2 and NFkB pathways. Once the scheduled transition fires in our model, there is a rapid increase in Nrf2 before both proteins oscillate to steady state. This result mimics the outcome of the experiment (Figure 4).

Figure 5 shows the effect of increasing NFkB levels on the system. It is clear to see that larger, smoother oscillations of Nrf2 are produced when NFkB is elevated. Without any change to NFkB, a singular peak is observed in the Nrf2 trace (Figure 5, blue). Subsequently, there are two and three peaks observed respectively when NFkB is doubled (Figure 5, red) and quadrupled (Figure 5, yellow). Also, the ratio between both proteins during these increases is maintained. Therefore, our model add weight to the hypothesis that NFkB drives Nrf2 dynamics.

The biggest limiting factor in the Nrf2 pathway is the presence of keap-1. To ensure our model accurately predicts what occur *in-vivo* keap-1 levels were fluctuated *in-silico* to observe the effect on Nrf2 levels (Figure 6). The simulations correctly conclude that increasing keap-1 levels leads to a decrease in Nrf2 activity and a decrease in keap-1 levels give rise to higher amounts of Nrf2. Thus, keap-1 has been shown to be crucial in the maintenance of Nrf2 levels and acts as the dominant mechanism of decay in our model.

Despite the complexity of the network dynamics, it was straightforward to find and integrate the connectivity information to build the model. However, although the information sources provided information on existing pathways, little was offered in the way of biochemical or kinetic detail. Thus, it is difficult to use the information in the literature to assemble a parameterised petri-net or ODE model. This further underlies the advantage of using our model as a way of quickly characterising the network dynamics of the pathways.

For simulations that will be compared to experimental results, it is important that the time units are considered. The time in our model is measured in arbitrary units, therefore, before comparing experimental results and predictions, it is necessary to attribute each time unit to a number of seconds, minutes or hours. This can be done by directly comparing the activity level of experimentally measured proteins at several time points in order to determine what time units correspond to the different sampled time points.

Another advantage to our model was the resilience of the overall behaviour of the network to changes in the initial states. This further reduces the need for experimental work prior to simulation. The next step is to create an ODE model using experimentally derived concentration values to predict the rates of production, transfection and decay in the Nrf2 pathway to provide even more quantitative insight into the dynamics that drive it.

Though our method's predictions will not be as accurate as the results returned by a correctly parameterized ODE, biologists using our method can derive information about a network's dynamic behaviour without having to conduct extensive experimentation and computationally expensive parameter estimation. This novel capability offers scientists the exciting prospect of being able to test hypotheses regarding signal propagation in silico. As a result, by using our method researchers can evaluate a wide array of network responses in order to determine the most promising experiments before even entering the laboratory.

5. References

(1) Hirotsu Y, Katsuoka F, Funayama R, Nagashima T, Nishida Y, Nakayama K, et al. Nrf2-MafG heterodimers contribute globally to antioxidant and metabolic networks. Nucleic Acids Res 2012 Nov 1;40(20):10228-10239.

(2) Jyrkkanen HK, Kuosmanen S, Heinaniemi M, Laitinen H, Kansanen E, Mella-Aho E, et al. Novel insights into the regulation of antioxidant-response-element-mediated gene expression by electrophiles: induction of the transcriptional repressor BACH1 by Nrf2. Biochem J 2011 Dec 1;440(2):167-174.
(3) Bryan HK, Olayanju A, Goldring CE, Park BK. The Nrf2 cell defence pathway: Keap1-dependent and -independent mechanisms of regulation. Biochem Pharmacol 2013 Mar 15;85(6):705-717.

(4) Bellezza I, Mierla AL, Minelli A. Nrf2 and NF-kappaB and Their Concerted Modulation in Cancer Pathogenesis and Progression. Cancers (Basel) 2010 Apr 13;2(2):483-497.

(5) Lee JM, Li J, Johnson DA, Stein TD, Kraft AD, Calkins MJ, et al. Nrf2, a multi-organ protector? FASEB J 2005 Jul;19(9):1061-1066.

(6) Suzuki T, Yamamoto M. Molecular basis of the Keap1-Nrf2 system. Free Radic Biol Med 2015 Nov;88(Pt B):93-100.

(7) Cuadrado A, Moreno-Murciano P, Pedraza-Chaverri J. The transcription factor Nrf2 as a new therapeutic target in Parkinson's disease. Expert Opin Ther Targets 2009 Mar;13(3):319-329.

(8) Ghosh M, Yang Y, Rothstein JD, Robinson MB. Nuclear factor-kappaB contributes to neuron-dependent induction of glutamate transporter-1 expression in astrocytes. J Neurosci 2011 Jun 22;31(25):9159-9169.

(9) Baird L, Lleres D, Swift S, Dinkova-Kostova AT. Regulatory flexibility in the Nrf2-mediated stress response is conferred by conformational cycling of the Keap1-Nrf2 protein complex. Proc Natl Acad Sci U S A 2013 Sep 17;110(38):15259-15264.

(10) Figiel I. Pro-inflammatory cytokine TNF-alpha as a neuroprotective agent in the brain. Acta Neurobiol Exp (Wars) 2008;68(4):526-534.

(11) Chiu J, Dawes IW. Redox control of cell proliferation. Trends Cell Biol 2012 Nov;22(11):592-601.

(12) Suzuki T, Shibata T, Takaya K, Shiraishi K, Kohno T, Kunitoh H, et al. Regulatory nexus of synthesis and degradation deciphers cellular Nrf2 expression levels. Mol Cell Biol 2013 Jun;33(12):2402-2412.

(13) Kim SW, Lee HK, Shin JH, Lee JK. Up-down regulation of HO-1 and iNOS gene expressions by ethyl pyruvate via recruiting p300 to Nrf2 and depriving It from p65. Free Radic Biol Med 2013 Dec;65:468-476.

(14) Lee J, Kim MS. The role of GSK3 in glucose homeostasis and the development of insulin resistance. Diabetes Res Clin Pract 2007 Sep;77 Suppl 1:S49-57.

(15) Chowdhry S, Zhang Y, McMahon M, Sutherland C, Cuadrado A, Hayes JD. Nrf2 is controlled by two distinct beta-TrCP recognition motifs in its Neh6 domain, one of which can be modulated by GSK-3 activity. Oncogene 2013 Aug 8;32(32):3765-3781.

(16) Rojo AI, Medina-Campos ON, Rada P, Zuniga-Toala A, Lopez-Gazcon A, Espada S, et al. Signaling pathways activated by the phytochemical nordihydroguaiaretic acid contribute to a Keap1-

independent regulation of Nrf2 stability: Role of glycogen synthase kinase-3. Free Radic Biol Med 2012 Jan 15;52(2):473-487.

(17) Thimmulappa RK, Mai KH, Srisuma S, Kensler TW, Yamamoto M, Biswal S. Identification of Nrf2-regulated genes induced by the chemopreventive agent sulforaphane by oligonucleotide microarray. Cancer Res 2002 Sep 15;62(18):5196-5203.

(18) Hayes JD, Dinkova-Kostova AT. The Nrf2 regulatory network provides an interface between redox and intermediary metabolism. Trends Biochem Sci 2014 Apr;39(4):199-218.

(19) Kaltschmidt B, Widera D, Kaltschmidt C. Signaling via NF-kappaB in the nervous system. Biochim Biophys Acta 2005 Sep 30;1745(3):287-299.

(20) Mauro C, Leow SC, Anso E, Rocha S, Thotakura AK, Tornatore L, et al. NF-kappaB controls energy homeostasis and metabolic adaptation by upregulating mitochondrial respiration. Nat Cell Biol 2011 Aug 28;13(10):1272-1279.

(21) Smale ST. Hierarchies of NF-kappaB target-gene regulation. Nat Immunol 2011 Jul 19;12(8):689-694.

(22) Hayden MS, Ghosh S. Shared principles in NF-kappaB signaling. Cell 2008 Feb 8;132(3):344-362.
(23) Zhong H, May MJ, Jimi E, Ghosh S. The phosphorylation status of nuclear NF-kappa B determines its association with CBP/p300 or HDAC-1. Mol Cell 2002 Mar;9(3):625-636.

(24) Perkins ND, Gilmore TD. Good cop, bad cop: the different faces of NF-kappaB. Cell Death Differ 2006 May;13(5):759-772.

(25) Mincheva-Tasheva S, Soler RM. NF-kappaB signaling pathways: role in nervous system physiology and pathology. Neuroscientist 2013 Apr;19(2):175-194.

(26) Li Q, Verma IM. NF-kappaB regulation in the immune system. Nat Rev Immunol 2002 Oct;2(10):725-734.

(27) Glass CK, Saijo K, Winner B, Marchetto MC, Gage FH. Mechanisms underlying inflammation in neurodegeneration. Cell 2010 Mar 19;140(6):918-934.

(28) Pahl HL. Activators and target genes of Rel/NF-kappaB transcription factors. Oncogene 1999 Nov 22;18(49):6853-6866.

(29) Turner DA, Paszek P, Woodcock DJ, Nelson DE, Horton CA, Wang Y, et al. Physiological levels of TNFalpha stimulation induce stochastic dynamics of NF-kappaB responses in single living cells. J Cell Sci 2010 Aug 15;123(Pt 16):2834-2843.

(30) Liu L, Chan C. The role of inflammasome in Alzheimer's disease. Ageing Res Rev 2014 May;15:6-15.

(31) Lee RE, Walker SR, Savery K, Frank DA, Gaudet S. Fold change of nuclear NF-kappaB determines TNF-induced transcription in single cells. Mol Cell 2014 Mar 20;53(6):867-879.

(32) Liu C, Cui G, Zhu M, Kang X, Guo H. Neuroinflammation in Alzheimer's disease: chemokines produced by astrocytes and chemokine receptors. Int J Clin Exp Pathol 2014 Dec 1;7(12):8342-8355.

(33) Sakurai H, Suzuki S, Kawasaki N, Nakano H, Okazaki T, Chino A, et al. Tumor necrosis factor-alpha-induced IKK phosphorylation of NF-kappaB p65 on serine 536 is mediated through the TRAF2, TRAF5, and TAK1 signaling pathway. J Biol Chem 2003 Sep 19;278(38):36916-36923.

(34) Winston JT, Strack P, Beer-Romero P, Chu CY, Elledge SJ, Harper JW. The SCFbeta-TRCP-ubiquitin ligase complex associates specifically with phosphorylated destruction motifs in IkappaBalpha and beta-catenin and stimulates IkappaBalpha ubiquitination in vitro. Genes Dev 1999 Feb 1;13(3):270-283.

(35) Bergqvist S, Alverdi V, Mengel B, Hoffmann A, Ghosh G, Komives EA. Kinetic enhancement of NF-kappaBxDNA dissociation by IkappaBalpha. Proc Natl Acad Sci U S A 2009 Nov 17;106(46):19328-19333.

(36) Chen J, Chen ZJ. Regulation of NF-kappaB by ubiquitination. Curr Opin Immunol 2013 Feb;25(1):4-12.

(37) Wertz IE, O'Rourke KM, Zhou H, Eby M, Aravind L, Seshagiri S, et al. De-ubiquitination and ubiquitin ligase domains of A20 downregulate NF-kappaB signalling. Nature 2004 Aug 5;430(7000):694-699.

Ameer Jebur

Development of an Experimental and Numerical Study for Piles Penetrated in Soil

Ameer A. Jebur, William. Atherton, Rafid. Alkhaddar and Ed. Loffill
Liverpool John Moores University, Faculty of Engineering and Technology, Department of Civil Engineering, Peter Jost Enterprise Centre, Byrom Street, L3 3AF ,Liverpool, UK.
A.A.Jebur@2015.ljmu.ac.uk; W.Atherton@ljmu.ac.uk; R.M.Alkhaddar@ljmu.ac.uk
E.Loffill@ljmu.ac.uk

Abstract: The targets of this technical note were to examine the pile bearing capacity penetrated in sand soils and to develop a predictive model for pile-load settlement using a new computational intelligence (CI) approach. A series of the experimental pile load tests were conducted on precast concrete model piles to investigate the ultimate pile bearing capacity, settlement and to provide accurate database to establish the model, thereby making the current in situ pile load test unnecessary. The program of testing comprised three piles of aspect ratios of 12, 17 and 25 to explore the behavior of rigid and flexible piles. Furthermore, evolutionary artificial neural networks (ANNs) based on a new Levenberg-Marquardt (LM) algorithm was adopted to achieve the desired goal. Moreover, the model piles were penetrated in a calibration chamber in two different sand relative densities, loose and medium. Five inputs model parameters (pile length, applied load, pile flexural rigidity, pile aspect ratio and sand-pile angle of internal friction) were considered to play a key role on the pile bearing capacity and the associated settlement and were set to be the output parameters. Finally, the results revealed that the optimal model of the Levenberg-Marquardt (LM) algorithm has the ability to simulate the pile bearing capacity with root mean square error, RMSE and correlation coefficient, R of 0.047 and 0.988 respectively.

Keywords: computational intelligence, Levenberg-Marquardt, cohesion less soil, sand relative density, pile-bearing capacity

1. Introduction

Pile foundations are slender structural elements, commonly used as load transferring systems and soil settlement controls at sites where there are inadequate sub-soil layers. Pile bearing capacity and associated settlement play a key role in the design of pile foundations [1]. It has been demonstrated by Das [2] that pile bearing capacity can be determined by dividing the ultimate applied load by a certain safety factor, depending on the strength of the structure and its serviceability. Associated settlement can be attributed as a consequence of an increase in effective stress, resulting in elastic compression and a reduction in soil volume in the effective stress zone [3].

In conventional procedures, pile settlement can be determined by dividing the sub-soil layers into sections. The total summation of the compression in soil layers is equal to the settlement [4, 5]. Uncertainties associated with a range of factors i.e. soil stress history, nonlinear relationships between soil stress-strain and stress distribution due to sampling, have been cited as barriers to accurately determining pile settlement [6]. Because of these difficulties, there has recently been in increase in the number of experimental and numerical studies concerning pile bearing capacity [7]. However, for simplification purposes and by necessity, several hypotheses associated with the significant parameters that govern pile settlement, have been assumed. This has resulted in the fact that the majority of current

approaches fail to achieve the required levels of accuracy with respect to pile settlement [8].
Despite many investigations highlighting the use of artificial neural networks (ANNs) to simulate pile bearing capacity and settlement, to date, there are still specific gaps in the subject knowledge. Comprehensive experimental tests evaluating the bearing capacity of concrete model piles, driven in three different sand densities, carried out to create an accurate database to develop and verify a new Levenberg-Marquardt (LM) algorithm to predict pile load-settlement response, would be a breakthrough in deep foundation research.

2. Methodology

2.1. Artificial neural network (ANN) model

Artificial neural networks are data driven computing methods, which, more specifically, can be applied when the relationship between model input and output parameters are nonlinear [3]. ANNs consider three processing layers or nodes; namely, an input layer, one or more hidden layer(s) and an output layer [9]. Those layers form the ANN means of learning and detailing the patterns controlling the dataset that the network is constructed with. It is worth pointing out that the objective of the hidden layer is to transform the model input parameters into the output layer, multiplied by connection weights and any bias either added or subtracted. This computational intelligence (CI) approach has been cited as a versatile and efficient computational tool, which successfully solves problems that may be difficult to tackle using numerical approaches. The multi-layer back propagation (MLBP) method developed by Rumelhart, Hinton [10], is the most robust and popular process to train the network in many fields of engineering and sciences [9]. In this study, the Levenberg-Marquardt (LM) algorithm was trained using the (MLBP) with training parameters.

3. Results and discussion

The ANN was trained using the Levenberg-Marquardt (LM) MATLAB algorithm version R2017a, as it is a more reliable and a faster approach than all other artificial neural approaches [11]. To include full details about the LM algorithm is beyond the scope of this study but can be found in Hagan, Demuth [12]. The mean square error (MSE) function was identified to measure the model performance with an error goal set at 0. The TANSIG transfer function (TF) was utilised between layer one and two, while the PURELIN transfer function was used to interconnect layer two and three as shown in Eqs. 1 and 2, and as recommended by Alizadeh, Najjari [13]. The experimental dataset, a total of 254 data points, was randomly divided into three subsets, composed of 70% training (178 data points), 15% testing (38 data points) and 15% validation (38 data points). After training the ANN network, the results revealed that the optimum ANN model consisted of three layers; the input layer, one hidden layer with 10 neurons and an output layer. This training process normally ends when the error value is sufficiently small enough [14]. It can also be seen that the training process stopped to avoid overfitting once the cross-validation error started to increase. The variation in error gradient. The error histogram graph (EHG) has been presented in Fig. 3 to obtain additional verification of network performance. EHG can give an indication of outliers and data features where the fit is significantly poorer than the majority of the rest of the data [15].

3.1. Evaluation of the robustness of the ANN model

The results of the experimental load-settlement tests and the predicted ANN based outputs are discussed in this section. The testing program consisted of three piles with slenderness ratios (lc/d) of 12, 17 and 25 with diameters of 40mm to examine the behaviour of rigid and flexible piles. In total, 254 points recorded the experimental pile load test data using a P3 strain indicator. The Levenberg-Marquardt (LM) algorithm was utilized to train the network based on MATLAB, version (R2017a). Figs. 2 and 3 show the distributions of the axial versus predicted load carrying capacity. A load cell (type DBBSM) was placed within the mechanism of the applied load to measure the load at each increment. In addition, two displacement transducers (LVDTs), with 50mm travel, were used to measure the pile settlement at each load increment. Plastic mechanisms in the soil surrounding the pile is the leading

cause for the non-linearity of the load-settlement curve; as the applied load increases, the pile response shows nonlinearity until reaching a maximum capacity at 10% pile diameter, as reported by EN 1997-1 (2004). There was an excellent fit between the proposed LM training algorithm and targeted values, with a correlation coefficient of 0.99008 for all data, which confirms the fact that the LM training algorithm is a superior method.

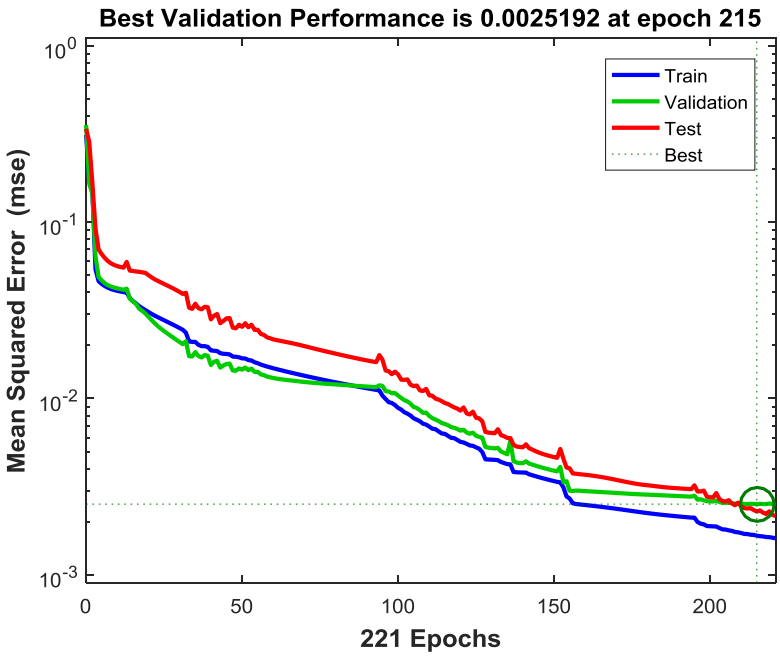

Figure. 1: Graph presenting the optimum mean square error (MSE) selected during the training process.

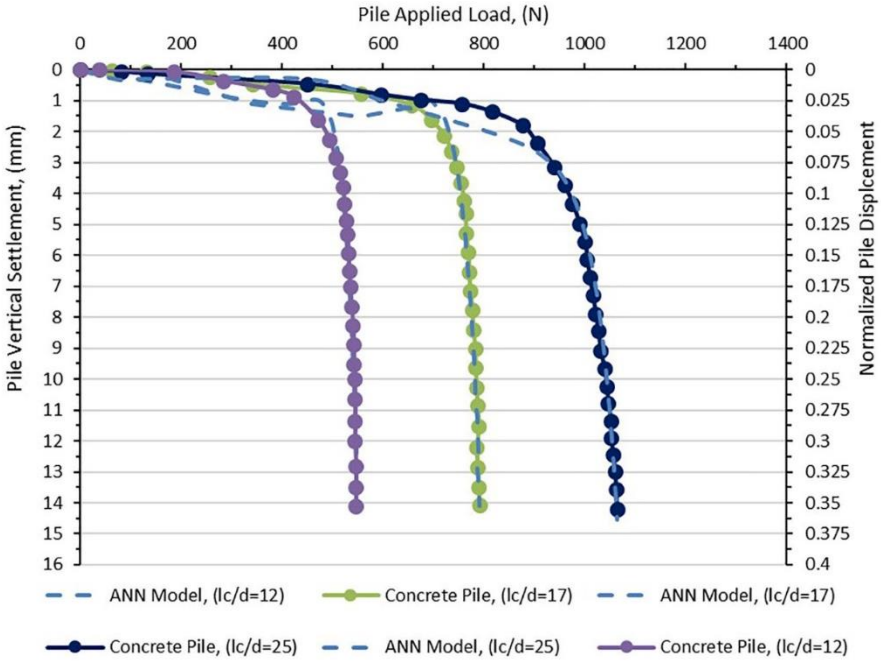

Figure. 2: Profiles of measured versus predicted pile load tests for model piles embedded in loose sand.

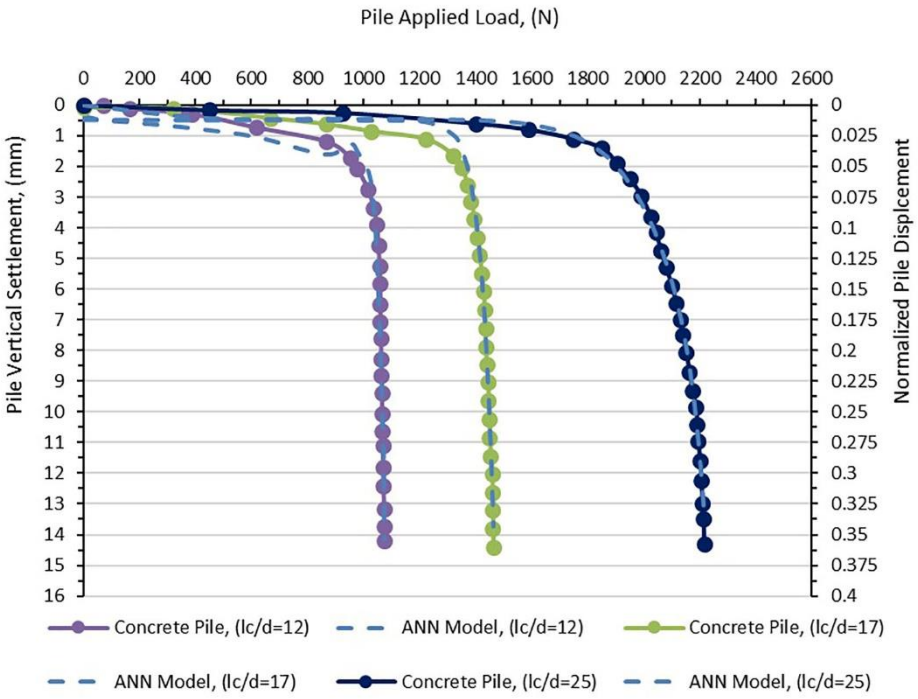

Figure. 3: Profiles of measured versus predicted pile load tests for model piles embedded in medium sand.

Lastly, the performance of the LM algorithm was also examined graphically, as demonstrated in Fig. 4. The testing dataset has been utlised to plot a regression calibration curve between fitted versus predicted values, with a 95% confidence interval (CI). Significant agreement can be observed between the measured versus predicted values, with a root mean square error (RMSE) and correlation coefficent (R) of 0.0478 and 0.988, which also confirms that ANN, based on the Levenberg-Marquardt (LM) MATLAB training algorithm, can successfully reproduce the results of the experimental pile settlement with high accuracy.

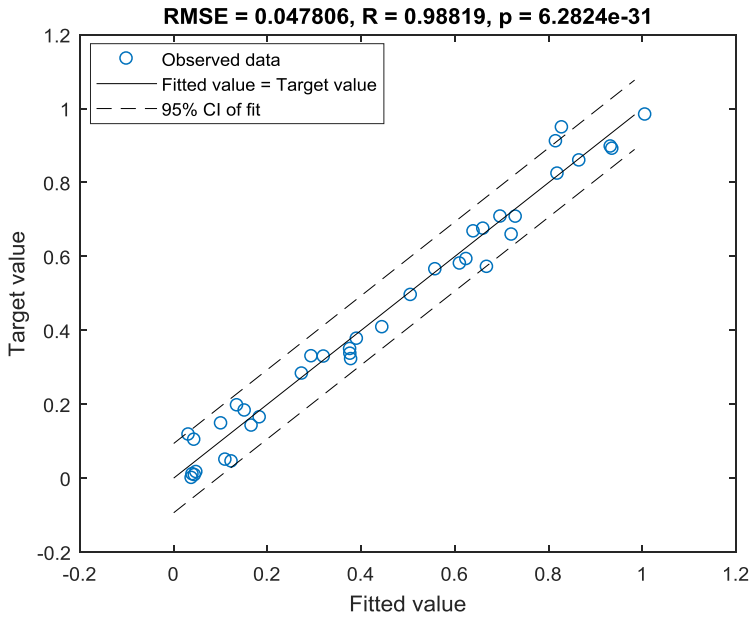

Figure. 4: Profiles of fitted versus observed settlement for the testing dataset with 10 neurons at a 95% confidence interval (CI).

4. Concluding remarks

In conclusion, based on the results of the graphical comparison of pile carrying capacity and the regression calibration curve, the proposed algorithm can be used as an efficient data-driven approach to accurately model pile settlement with a root mean square error (RMSE), correlation coefficient (R) and mean absolute error (MAE) of 0.050192, 0.98819 and 0.0025192, respectively. One of the advantages of the proposed method is that pile settlement can be successfully simulated using the proposed LM algorithm with five input parameters that can be easily determined without the need to run expensive and time consuming tests such as in situ pile-load tests, cone penetration tests (CPT) and standard penetration tests (SPT).

Acknowledgements
The first author would like to show his gratitude to Dr. William Atherton and Prof. Rafid Al Khaddar for their guidance and to the technical staff from Liverpool John Moores University, UK, who provided insight and expertise of great assistance for the current study.

References

[1] Feng Q, Kong Q, Song G. Damage detection of concrete piles subject to typical damage types based on stress wave measurement using embedded smart aggregates transducers. Measurement 88 (2016) 2016:pp. 345–52.
[2] Das BM. Principles of Foundation Engineering. United State of America: Global Engineering; Nelson Education LTD, pp. 896.; 2015.
[3] Nejad FP, Jaksa MB, Kakhi M, McCabe BA. Prediction o fpile settlement using artificial neuralnetworks based on standard penetration test data. j ComputGeotech. 2009;36(7):pp. 1125-33.
[4] Fang HY. Foundation engineering handbook. New Delhi, India: CBS Publishers and Distributors. 2001.
[5] Tomlinson MJ. Pile Design and Construction. London, U.K: Sixth Edution, E & FN Spon, 588.; 2014.
[6] Shahin MA, Maier HR, Jaksa MB. Predicting settlements of shallow foundations using artificial neural networks. Journal of Geotech Geoenviron Eng ASCE. 2002;128(9):pp. 785–93.
[7] Xu L-Y, Cai F, Wang G-X, Ugai K. Nonlinear analysis of laterally loaded single piles in sand using modified strain wedge model. Computers and Geotechnics. 2013;51:pp. 60-71.
[8] Poulos HG. Common procedures for foundation settlement analysis-Are they adequate? In:. Proc 8th Australia New Zealand conf on geomechanics, Hobart;. 1999:pp. 3-25.
[9] Bashar T. Pipe pilesetup:Databaseandpredictionmodelusingartificial neural network. Soils andFoundations. 2013;53(4):pp. 607-15.
[10] Rumelhart DE, Hinton GE, Williams RJ. Learning internal representation by error propagation, In: Rumelhart, D.E., McClelland, J.L. (Eds.), Parallel Distributed Processing. MIT Press, Cambridge. 1986:pp. 318-62.
[11] Jeong D-I, Kim Y-O. Rainfall-runoff models using artificial neural networks for ensemble stream flow prediction. Hydrol Process 19(19). 2005:pp. 3819–35.
[12] Hagan MT, Demuth HB, Beale MH, Jesús OD. Neural Network Design1996.
[13] Alizadeh B, Najjari S, Kadkhodaie-Ilkhchi A. Artificial neural network modeling and cluster analysis for organic facies and burial history estimation using well log data: A case study of the South Pars Gas Field, Persian Gulf, Iran. Computers & Geosciences (45). 2012:pp. 261-9.
[14] Yadav AK, Malik H, Chandel SS. Selection of most relevant input parameters using WEKA for artificial neural network based solar radiation prediction models. Renewable and Sustainable Energy Reviews, (31). 2014:pp. 509-19.
[15] Abdellatif M, AthertoN W, Alkhaddar R, Osman Y. Flood risk assessment for urban water system in a changing climate using artificial neural network. J, Nat Hazards, 79. 2015:pp. 1059–77.

Alaa Abbas

An innovative method for the construction of a separate sewer system in narrow streets in UK and EU cities

(Oral)

Alaa Abbas [1], Felicite Ruddock[2], Rafid Alkhaddar[3], Glynn Rothwell[4] and Robert Andoh[5]

[1] Postgraduate Research Student, Liverpool John Moores University, Department of Civil Engineering, Henry Cotton Building, 15-21 Webster Street, Liverpool, L3 2ET, UK, A.H.Abbas@2015.ljmu.ac.uk

[2] Programme Leader, Department of Civil Engineering, Liverpool John Moores University, Peter Jost Centre, Byrom Street, Liverpool L3 3AF, UK, F.M.Ruddock@ljmu.ac.uk.

[3]Professor of Water and Environmental Engineering and Head of the Department of Civil Engineering , Liverpool John Moores University, The Peter Jost Centre, Byrom Street, Liverpool, L3 3AF, UK, R.M.Alkhaddar@ljmu.ac.uk

[4]Dr.Glynn Rothwell, Department of Maritime and Mechanical Engineering, Liverpool John Moores University, Byrom Street, Liverpool, L3 3AF, UK,G.Rothwell@ljmu.ac.uk

[5]Professor Robert Andoh, CEO and President of AWD Consult Inc. 32 Vista Drive, South Portland, ME 04106, USA, bandoh@awdconsult.com

Abstract

Sewer systems that convey both sanitary sewage and stormwater through a single pipe are referred to as combined sewer systems. This system diverts all flows exceeding the design capacity to the receiving watercourses in heavy rain events. Therefore, environmental regulations limit the use of this system and separate sewer systems are currently used in all new developments. However, the UK, most other European, and other countries usually have narrow streets occupied by a complex network of infrastructure services. About 70% of sewer systems in the UK and Europe are combined systems. Finding a space in which to place another two sets of pipes (in a separate sewer system) is therefore challenging. This research investigates a design which is capable of overcoming this challenge by a modified system for the sewer networks. The system includes a proposed new design for the manhole shape, which will allow the storm flow and the foul flow to pass through the same manhole without mixing and allows using one trench to set two pipelines. This will bring economic advantages by decreasing construction cost by about 30% plus extra protection for the environment by separating sewage from stormwater, decrease footprint by 16% and construction time by 18%.

Keywords: Combined, design, separate sewer system, storm, urban drainage.

1. Introduction

The sewer system is the networks of pipes used to drain the stormwater caused by wet weather and the sewage from urban areas. Two systems are mainly used; the old one is the combined sewer, which uses a single pipe to convey both sanitary sewage and stormwater through a single pipe. The newer one is a separate sewer system, in which two sets of pipes are used, one just to drain the cleaner stormwater runoff to the nearest watercourse (river, lake, etc.) while the second set of pipes collects and conveys the sewage water to a Waste Water Treatment Plant (WWTP).

The combined sewer system has been used widely and efficiently in the past because it is a simple system, as one pipe is designed to carry the sewage water flow through dry weather in addition to stormwater following wet weather. For that reason, the diameter of the pipe is designed to be able carry both sewage and stormwater flows and the WWTP is designed to have a capacity about three times the dry weather sewage flow. This system makes up about 70% of the sewer system in the UK and in many EU countries such as Germany, France, and Belgium(Read and Vickridge 1997). The large size of pipe with little flow through dry season causes that suspended solid settles as sediment at the bottom of the pipe and in wet weather, the storm flows help to remove these sedimentations from the pipes, many hydraulic and pollution problems associated with this phenomena. Expansion of urban areas and the increase of impermeable areas have put more pressure on the sewer system by increasing the quantity of stormwater flow, making the combined sewer system unable to convey all the flow to the WWTP in a short period to avoid flooding. The combined sewage system is designed to release untreated overflows to watercourses through a Combined Sewer Overflow (CSO) to keep the hydraulic load at a manageable level (Brombach 2005).

The separate sewer systems have been designed to address the harmful environmental impact of combined sewer system and avoiding flooding by increasing the capability of the stormwater drainage system to convey runoff caused by heavy rain to nearest watercourses, via separate pipelines (Butler and Davis 2011). The advantage of this system over the combined sewer system is regarding environmental protection as it does not discharge wastewater directly into the watercourse Table 1 (Eriksson et al. 2007). However, a separate sewer system occupies more space and is more expensive than the combined system and its use is dependant on environmental regulation to overcome the pollution challenges that caused by CSO. This resulted in limitation of the use of combined sewer systems, except as limited extensions or replacements for existing combined systems (Bizier 2007).

Table 1. Advantages of Combined and Separate Sewer Systems

Separate System	Combined System
➢ Expensive ➢ Less pollution effects on watercourse ➢ Additional space is required to accommodate both pipes	➢ Lower costs for pipe construction ➢ High pollution level through heavy rain time on watercourses ➢ The space occupied by the single pipe is smaller

2. Innovation in sewer system design

The new technologies available today for the design, manufacture, maintenance and inspection of sewer systems have urged designers to revisit traditional urban drainage management with an innovative outlook. The EPA implemented a project, which has provided an overview of many recent works on sewer systems. Innovative system designs identified in the EPA study include using Real-Time Control, Vacuum sewer technology and retrofit such as a sustainable drainage system (SUDS) or Best Management Practice (BMP) (United States Environmental Protection Agency 2007). The American Society of Civil Engineers (ASCE) conducted a study to separate the combined sewers in three cities in the US by using pressure tubing to pump the sewage from houses and suspend it in the existing combined sewer system, which has been used to convey stormwater only. A Feasiblity study of this project showed that the cost of the separation work is expensive compared with the traditional separate system because the high initial cost of integrating house units with a new pressure separate system (Jones 2006).

Cembrano (2004) and Polaskova et al. (2006) have presented attempts to decrease the discharge from

CSOs to the receiving watercourses by optimising the sewerage systems through a complex system that includes pressure pipes and additional storage tanks fitted with controller systems. This solution increased the storage capacity of the sewer system but it is still an expensive solution. (Wang et al. 2013) found that retrofitting into the urban environment by intercepting runoff through green areas is economical and protects the environment. They used three green infrastructure models: bioretention basins (vegetated basins), green roofs, and permeable pavement); their studies showed that employing green infrastructure will reduce runoff quantity, minimise peak stormwater flows, and improve runoff quality., However, this solution needs larger open areas for it to work. Andoh et al. (2005) found that it is better to find solutions in the upstream parts of the system rather than the downstream portions. His research focuses on installing inlet flow restrictors in catchment basins and using these to limit inflow to the hydraulic capacity of the existing combined sewer system.

This research proposes an innovative method for laying a separate sewer system using one trench to set up the storm pipe and sanitary pipe, one on top of the other. It is intended that this will bring economic advantages plus extra protection for the environment, decrease the footprint and construction time, and make it possible to lay this separate sewer system even in the narrow streets that most of the UK and European cities have.

3. Innovative design of sewer system

The UK and most other European countries usually have narrow streets, occupied by a complex network of infrastructure services such as potable water, electricity, communication and gas lines. Finding a space in which to place another two sets of pipes (in a typical separate sewer system) is a challenge, but this proposed design is capable of overcoming this problem.

The manhole is the main element of a sewer network; it is a structure used to gain access to the sewer for inspection and maintenance. Manholes have witnessed improvement over time in the materials used; old manholes were built of brick, and then significant developments were made by using concrete and using precast materials. However, corrosion of concrete by H_2S means that the industry has to coat the inner surface of the manhole or use newly developed materials such as fiberglass and polyethylene instead (Hughes 2009). The manhole's location should provide easy access, and they should be sited at every change of alignment or gradient and wherever there is a change in the size of a sewer, and in addition at reasonable intervals for inspection and maintenance normally between (50 -100) meters. The typical design of a manhole is circular with a range of diameters between 1 to 1.8 m

Figure 1 shows a typical manhole design.

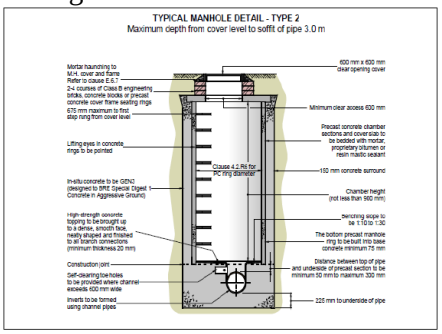

Figure 1. Typical design of a sanitary manhole (Defra 2011)

This research presents a new design for geometry of manhole integrating a storm and sanitary system in one combined structure and keeping the separate function. The system is designed to ensure that no mixing of stormwater and sewage will take place Figure 2a&b provides details for the separation technique. The sewerage pipe extends below the external manhole and ends at the internal manhole, while the storm pipe ends at the external manhole and then the flow makes a half circle around the inner foul manhole.

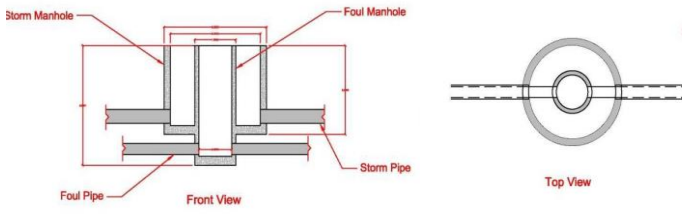

(a) (b)

Figure 2 a & b. New shape for storm/sanitary manhole

This design allows the use of one trench to accommodate the two separate pipes one over the other (storm on the top and sanitary pipe at the bottom) Figure 3 demonstrates the new method of laying pipes.

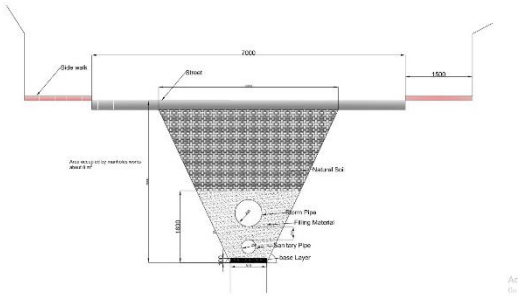

Figure 3. A new method for laying a separate pipeline system.

4. Feasibility Analysis

In order to evaluate the economic advantages of the new sewer system, one case study has been selected to apply the traditional separate sewer system in one case and the innovative separate sewer system in other. The following hypothesis and assumptions were created, based on industry standards and literature review as shown in Table 2.

Table 2. Design parameters proposed to calculate initial cost and construction time

	Traditional Separate Sewer System	**Innovative Separate sewer system**
Initial cover depth	1 meter	1 meter
Pipes diameters	Storm water pipe of 250 mm foul water pipe of 150 mm	Storm water pipe of 250 mm foul water pipe of 150 mm
Slope of pipe	1/pipe diameter	1/pipe diameter
Trench's side slope angle	45º	45º
Trench's width (w) and depth (d) relationship	W=1.33d+200 (in mm)	W=1.33d+200 (in mm)
Rate of excavating production	120 cubic metres per day	120 cubic metres per day
Estimate cost of excavation and laying	100 US$ per meter	85 US$ per meter

The cost of pipe laying includes excavation cost and excludes pipe material. The cost model proposed by (Maurer et al. 2010) is depended in design 200 meters length sewer line using both methods to compare the cost, time and occupied area. Figure 4. shows there is a 30% cost reduction for digging

and laying the new design due to the narrower trenches required compared to the traditional method and Figure 5 demonstrates the new method uses 16% less road surface. The time factor is important when constructing a sewer network as it is related with the nuisance that infrastructure construction causes to local businesses and community, the new system reduces the total installation time by 18% as shown in Figure 6.

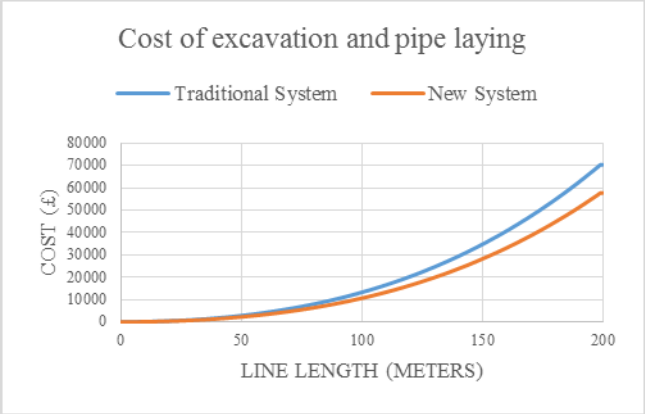

Figure 4. Comparison of the Digging and Laying Costs

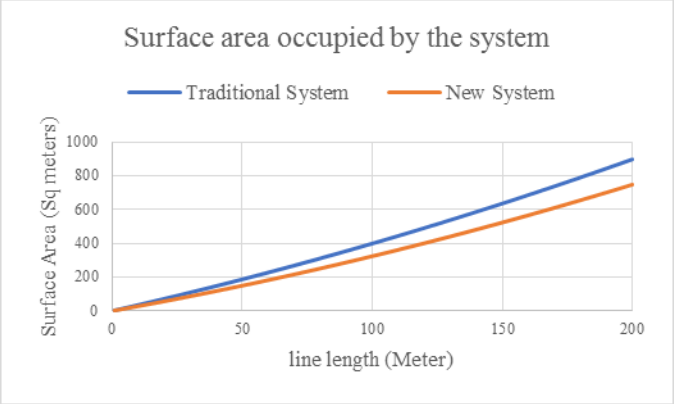

Figure 5. Comparison of the surface area occupied by each system

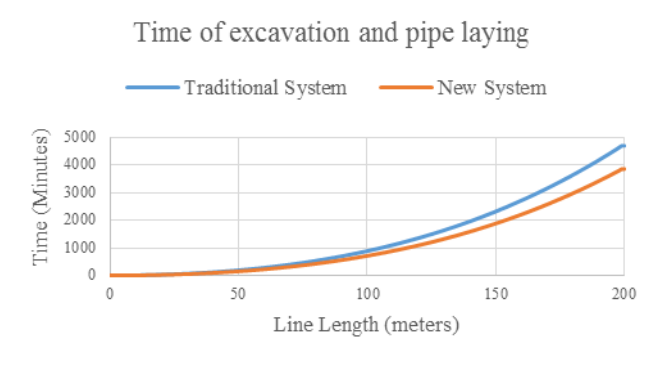

Figure 6. Comparison of the Construction Times

CONCLUSION

Due to the rapid expansion of urban cities and developments during the industrial era, communities have become more conscious of the necessity of disposing of the sewage generated by human activities and draining the storm water resulting from rainfall outside cities to avoid flooding and hygienic effects. It is clear that the traditional combined sewer system is no longer used in a development area, and the

traditional separate sewer system has high initial cost makes it not attractive to authorities and has a limited use in narrow streets which is prevalent in the UK and EU cities. The innovative separate system proposed in this research merges the advantages of combined and separate sewer systems into one modified system, which complies with the regulatory requirements of the 21st century, decreases the initial cost and protects the environment. The new design makes it possible to install separate sewer systems even in narrow streets which is very challenging when using the traditional system.

Refrences

Andoh, R. Y. G., Stephenson, A. J., and Collins, P. (2005). "Approaches to urban drainage systems management for the 21st century." *National Hydrology Seminar*.

Bizier, P. (2007). *Gravity Sanitary Sewer Design and Construction*, American Society of Civil Engineers, USA

Brombach, H., Weiss, G. & Fuchs, S., (2005). "A new database on urban runoff pollution: comparison of separate and combined sewer systems." *Water Science & Technology*, 51(2), 9.

Butler, D., and Davis, J. W. (2011). *Urban drainage*, London.

Cembrano, G. (2004). "Optimal control of urban drainage systems. A case study." *Control Engineering Practice*, 12(1), 1-9.

Defra (2011). "National Build Standards Design and Construction of new gravity foul sewers and lateral drains " *Water Industry Act 1991 Section 106B, Flood and Water Management Act 2010 Section 42*, Department for Environment Food and Rural Affairs, UK, 36.

Eriksson, E., Baun, A., Mikkelsen, P. S., and Ledin, A. (2007). "Risk assessment of xenobiotics in stormwater discharged to Harrestrup Å, Denmark." *Desalination*, 215(1-3), 187-197.

Hughes, J. B. (2009). *Manhole Inspection and Rehabilitation*, American Society of Civil Engineers ASCE, Reston, Va.

Jones, J. E. (2006). "ASCE Combined Sewer Separation Project Progress." *Great Works on Urban Water Resources (1962-2001)*, 73-88.

Polaskova, K., Hlavinek, P., and Haloun, R. (2006). "Integrated approach for protection of an urban catchment area." *Desalination*, 188(1-3), 51-59.

Read, G. F., and Vickridge, I. G. (1997). *Sewers : rehabilitation and new construction : repair and renovation*, London : Arnold.

United States Environmental Protection Agency, E. (2007). "Innovation and Research for Water Infrastructure for the 21st Century."USA, 80.

Wang, R., Eckelman, M. J., and Zimmerman, J. B. (2013). "Consequential Environmental and Economic Life Cycle Assessment of Green and Gray Stormwater Infrastructures for Combined Sewer Systems." *Environmental Science & Technology*, 47(19), 11189-11198.

Mikel Zabaleta

Dual Three-phase PM Generator Parameter Identification using Experimental and Simulated System Responses

Mikel Zabaleta
School of Engineering, Technology and Maritime Operations, LJMU
E-mail address: m.zabaleta@2014.ljmu.ac.uk

Abstract. The paper describes a procedure to identify the dq inductances of an electric machine, which is here applied to a dual three-phase PM machine. A hybrid simulation/experimental approach is utilised. A power converter is used to force step current transients and the responses are recorded. These are then fed into a combined parameter estimation/ simulation model, which yields at the output the machine parameters that provide the best fit of the simulation results to the experimental responses. The machine used in the testing is a 150kW generator.

Keywords. Six-phase machine, parameter estimation, multiphase machine modelling, model identification.

1. Introduction

Due to the rapid development of the power electronics in the second half of the twentieth century, a strong research effort has been put into the modelling of electrical machines. Once the models are made available, the importance of having the correct parameters becomes paramount when accurate representation of the real machine's behaviour is required. The main parameters affecting the dynamic behaviour of the machine are those related to the flux linkages (d- and q-axis inductances and permanent magnet's flux). Estimating the flux linkages in a machine is usually a complicated task since these depend on the stator currents and on the magnetic saturation. If sensor-less or predictive control is considered, the values of the machine's parameters are of key importance [1].

Numerous methods for estimating synchronous machine parameters are available in the literature. Among them, the standstill frequency response (SSFR) is one of the most widely used ([2] and [3]) for parameter identification in large synchronous machines. This method allows to obtain the machine's parameters by applying a certain perturbation signal (voltage) to the machine's terminals and then analysing the response (currents). In [4], SSFR method is applied to a permanent magnet machine using a dc step signal as the perturbation. In general, using SSFR requires positioning of the rotor of the machine in certain predetermined positions precisely in order to obtain the dq decoupled parameters and, usually, magnetic saturation is not taken into account.

In [5], an offline parameter identification procedure is described and applied to a permanent magnet machine. It introduces the currents as inputs and uses the stator voltages as optimised outputs. In this way, the outputs can be expressed as linear equations regarding the tuned parameters, thus allowing to use linear optimisers. This requires a machine model built with currents as inputs and voltages as outputs (voltage source model) which makes it very difficult to integrate it with a power converter (that is usually modelled as a voltage source).

In [6], several simulation models to identify the machine's parameters are presented. In this case, the machine model is developed as a current source (voltages as inputs, currents as outputs). However, the identified parameters are very sensitive to the model errors such as discretization, resolution of the PWM, etc.

Work in [7] uses the recursive least squares (RLS) algorithm to estimate the machine's parameters online. A set of several gains need to be tuned in order to obtain a good convergence of the estimation process. This makes it complex for implementation in real situations as a convergence failure may directly affect the operation of the converter.

The research described here is focused on developing an offline parameter identification procedure that allows to infer the main machine's parameters (*dq* inductances) during the commissioning of a combined converter/machine set. For this purpose, a simulation model is developed and a series of tests are performed to gather experimental data to correlate the simulation model output with. With the experimental data, an iterative parameter sweep algorithm is applied yielding the values that best fit the experimental data.

2. Machine Model

The simulation platform for electromagnetic transient simulations (EMT) within Ingeteam is Matlab's SimPower Systems. SimPower Systems® does not provide a built-in model for multiple three-phase winding machines within the model library. This led to the development of a model for such machines within the SimPower Systems environment. The model was constructed following the vector space decomposition (VSD) equations in the synchronously rotating frame [8]. The model is very flexible and highly configurable, allowing for different spatial phase shift angles between first phases of the three-phase sets (0^o for double three-phase, 30^o for asymmetrical six-phase and 60^o for symmetrical six-phase topologies).

3. Control Electronics Model

As the control hardware used in the test rig is the real hardware used in Ingeteam's converters, its modelling is not a trivial issue. This is so since it includes a considerable number of lags and delays (due to the real hardware implementation) that may affect the dynamic performance.

As a consequence of this, and in order to have flexibility of the algorithm development and validation, a simplified model for the control electronics has been developed. Ingeteam's original model represents not only the DSP, but also FPGAs and PLC logics, which makes the simulations extremely complex and computationally very demanding. The simplified simulation model includes all the components that affect the dynamic behaviour of the current loops (such as measuring filters, modulation strategy, computational delays, etc.), but omits other issues, which have minor or negligible effect (such as the task manager, internal mailboxes, field-bus communications, FPGA-built ultimate protections, etc.). Additionally, Ingeteam's original model includes some routines and checks during the initial stages of the simulation (such as dc-link precharging, transformer energization and machine's pole position detection) that increase the required simulation time. These initialisation routines have been eliminated providing the model with already known initialisation values. All these considerations enormously simplify the simulation model allowing a faster programming and debugging.

4. Experimental Rig Description

The test bench used for this research is the test rig used by the Ingeteam to emulate the behaviour of offshore wind converters. In order to obtain realistic results, the rig includes not only the machines and the converters to be tested, but also a control cabinet emulating the wind turbine's PLC. In this way, the wind turbine behaviour can be reproduced taking into account every single intervening device. The general overview of the test rig can be seen in Figure 1.

The test rig has three machine arrangements to cater for the three electrical machines already used in wind turbines (i.e. electrically excited synchronous machine, asynchronous machine and permanent magnet machine). Each of the machine arrangements consist of a 150kW dc machine that acts as a motor regulating the rotational speed and the ac machine arranged in a back-to-back configuration, as seen in Figure 2a.

For the purpose of this work, and to cover the situations where double three-phase machines are used, the original three-phase permanent magnet machine of the test rig was replaced by a new one that can accommodate different stator winding configurations.

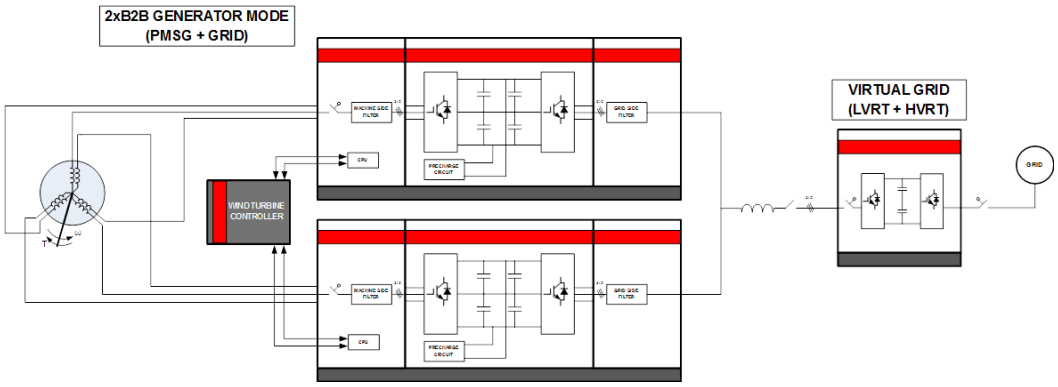

Figure 1 Test-bench overview.

(a) (b)

Figure 2 Electrical machine arrangement (a) and conversion line (b).

The test rig also includes two 150kW, 690V conversion lines (Figure 2b), each of which is constituted by two three-level NPC converters arranged in back-to-back configuration. Additionally, the grid side of the test rig can be connected directly to a real stiff grid (by means of a configurable inductance to simulate different grid impedances) or can be connected to a virtual grid emulator. This device is a power converter that can simulate any grid condition such as frequency drifts, low and high voltage conditions, symmetric and asymmetric voltage sags and surges, etc. Each of the three-phase windings of the permanent magnet machine is connected to a conversion line. The conversion lines are equipped with the same controllers as in the converters for real-world applications, so that the results obtained here can be directly extrapolated to the real scenarios. For further details of the test bench, please see [9].

5. Comparison of Simulation and Experimental Results

In what follows, all the simulations and experimental results share the same controller settings regarding sampling time (625 us) and switching frequency (800Hz).

With the initial parameters given by the machine manufacturer, the response shown in (Figure 3a) was obtained. As can be seen, the differences in the responses are quite significant, both in terms of dynamic and steady state performance.

In order to obtain the machine parameters that best match the experimental response, an optimization procedure was developed. It consists of an iterative algorithm that continuously varies the selected machine parameters (*Lls*, *Lmd* and *Lmq* in this case, which stand for the stator leakage inductance and mutual inductances along *dq* axes).

After the optimisation, the same simulation as the one shown in Figure 3a was repeated yielding now a much better fitting of the simulation to the experimental data (Figure 3b). This indicates that the actual machine parameters and those obtained by the identification are equal for all practical purposes. Additionally, the machine model developed is also validated as the dynamic response is the same as that of the actual machine once the parameters are properly set.

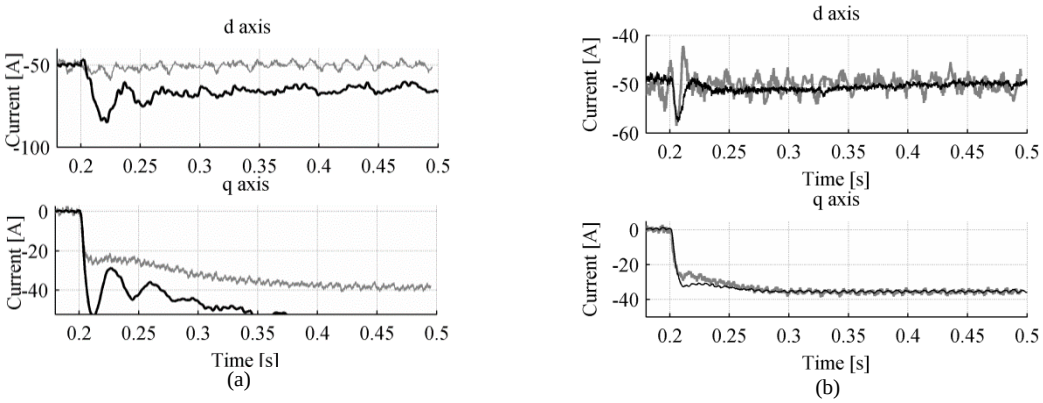

Figure 3 Simulated (black) and experimental (grey) response to -35A current step in the *q*-axis. The top picture shows the *d*-axis current and the bottom one the *q*-axis current. (a) is with the manufacturer's parameters and (b) is with the identified parameters.

6. Conclusions

A procedure to correlate the dynamic response of a permanent magnet machine yielded by a simulation model and by an actual machine is presented. It has been applied to a system with the real control and acquisition hardware (thus increasing the modelling complexity) and has been proved to be effective. The procedure consists of a series of modified simulation models that allow comparing the responses obtained from simulation with those from the real machine. Once the comparison between the responses is obtained, an iterative algorithm is run, which varies different parameters in the simulation model and aims to obtain as close as possible response to the experimental one.

7. References

[1] S. Bolognani, M. Zigliotto and K. Unterkofler, "On-line parameter commissioning in sensorless PMSM drives," Proc. International Symposium on Industrial Electronics, Guimaraes, Portugal, 1997, pp. 480-484.

[2] IEEE Draft Guide for Test Procedures for Synchronous Machines Part I - Acceptance and Performance Testing; Part II - Test Procedures and Parameter Determination for Dynamic Analysis, IEEE Unapproved Draft Std P115/D2, Jun 2009.

[3] K. M. Rahman and S. Hiti, "Identification of machine parameters of a synchronous motor," IEEE Trans. on Industry Applications, vol. 41, no. 2, pp. 557-565, 2005.

[4] S. Weisgerber, A. Proca and A. Keyhani, "Estimation of permanent magnet motor parameters," Conf. Rec. IEEE Industry Application Society Annual Meeting, New Orleans, USA, 1997, pp. 29-34.

[5] A. Zentai and T. Daboczi, "Offline parameter estimation of permanent magnet sychronous machines by means of LS optimization," Proc. IEEE/SICE International Symposium on System Integration, Nagoya, Japan, 2008, pp. 36-41.

[6] H. Kubo and Y. Tadano, "Parameter estimation of PMSM driven by PWM inverter based on discrete dynamic model," Proc. Annual Conference of the IEEE Industrial Electronics Society (IECON), Florence, Italy, 2016, 2873-2878.

[7] S. J. Underwood and I. Husain, "Online parameter estimation and adaptive control of permanent-magnet synchronous machines," IEEE Trans. on Industrial Electronics, vol. 57, no. 7, pp. 2435-2443, 2010.

[8] E. Levi, "Multiphase electric machines for variable-speed applications," IEEE Trans. on Industrial Electronics, vol. 55, no. 5, pp. 1893-1909, 2008.

[9] M. Zubiaga, I. Larrazabal, D. Madariaga, J. Aguirrezabal, I. Zubimendi, G. Nuñez, I. Garin, E. Burguete and M. Zabaleta, "Low scale grid emulator test bench for in-house validation of high power converters oriented to offshore," Proc. WindEurope Summit 2016, Hamburg, Germany, 2016.

Hayder Shandara

Modelling of permanent deformation in reinforced cold flexible pavements using three dimensional simulations

H K Shanbara[1,3], F Ruddock[2] and W Atherton[2]

[1] PhD Student, Department of civil engineering, Liverpool John Moores University, Liverpool, UK, h.k.shanbara@2014.ljmu.ac.uk
[2] Department of civil engineering / Liverpool John Moores University, Liverpool, UK.
[3] Lecturer, Al-Muthanna University, Al-Muthanna, Iraq.

Abstract. Flexible pavements failure often occurs due to excessive permanent deformation (rutting) as a result of the undesirable environmental conditions and heavy traffic under repeated wheel loads. The currently used design procedure of flexible pavements presumes that the pavement response to these undesirable conditions is elastic, whereas the viscoelastic, viscoplastic and plastic pavement behaviours are not properly considered. Therefore, the quality of asphalt mixtures is one of the essential factors that affects flexible pavements performance to resist the deformations. The development of such pavements performance has been considered valuable by reinforcing asphalt mixture. In this study, a three-dimensional finite element model was developed, using ABAQUS software to investigate the effect of repeated wheel load condition on rutting formation and pavements response. This model assumes that the pavement material response to the applied load is viscoelastic. In addition, the model is focused on the prediction of the contribution of natural and synthetic fibres in the surface course of cold bituminous emulsion mixture (CBEM) to develop the tensile and shear strength of flexible pavements in terms of rutting resistance. The results show that the behaviour of flexible pavements structure is improved when the quality of CBEMs was enhanced using these fibres.

Keywords. Cold bituminous emulsion mixture, finite element modelling.

1. Introduction

Due to high traffic volume and undesirable environmental conditions, flexible pavements deteriorate with time and several pavement failures are observed [1]. Rutting (permanent deformation) is a common and widespread mode of pavement failures and one of the main causes for the overall deterioration in flexible pavements, especially in hot climate regions, and the service and the performance quality of such pavements descend because of depression of the pavement surface. In hot climatic areas, rutting often occurs when heavy and slow traffic loads are applied onto pavements surface. The shear and tensile stresses in pavement materials become critical due to the high stresses concentration underneath the vehicle tyres. Therefore, asphalt pavements behave as a ductile material and, hence, the risk of sudden depression on the pavement surface increases. This may result in both functional and structural failures, thus causing significant safety concerns (hydroplaning and vehicle dynamics) to motorists.

The consequence of rutting is a quick deterioration of flexible pavements if the cause of the problem is not perfect considered at the design stage. In pavements maintenance, laying a new overlay or design new flexible pavements can be conducted using hot mix asphalt (HMA) or cold mix asphalt (CMA) mixtures. Cold bituminous emulsion mixture (CBEM) is one of the common types of CMA. Although HMA provides higher performance than CMA [2], CMAs are used because of achieving cost-effective with minimum negative impact on the environment. Both economic and environmental benefits could be gained by eliminating the need to heat huge amount of aggregates and asphalt compere to the

conventional HMA [3]. However, CMA has been considered as an inferior mixture in terms of the shear and tensile strength, mechanical properties and long curing time [4 and 5]. Several techniques have been applied to improve the performance of such mixtures and to mitigate the development of pavement deformation under specific conditions. Examples of such strategies: increasing the HMA or CMA overlay thickness; using additives; using waste materials as filler replacements; and reinforcing the flexible pavements. These techniques have been accompanied by experimental and field testing, as well as mechanistic and empirical design methods in order to evaluate their performance [6]. When reinforcement materials, such as natural and synthetic fibres, are used, the performance of asphalt mixtures could be better than that mixture using conventional materials [7]. The fibre-reinforced HMA mixtures enhance pavement's strength, bonding and durability [8]. It is strongly affected by type, content, diameter, length and surface texture of fibres [9 and 10]. These factors should be also considered when fibers are added to CMA mixtures. The use of natural and synthetic fibres technology in reinforcing cold mixtures to moderate the impact of high stresses have been identified as the optimal solutions to mitigate the pavements damaging potential [11]. The effect of transportation vehicle axle repetitions on the structural performance of flexible pavement surfacing material and the use of different temperatures for the routing of the transportation vehicles have been identified as the key areas based on minimum road maintenance need. Structural performance in this context refers to the surface rutting due to moving vehicles.

The ability to predict the amount of rutting or permanent deformation in flexible pavements is an important aspect of pavements design. A successful mechanistic pavement model is crucial to maximize the service life of the pavement without need for long lasting maintenance. The overall objective of this study is therefore to develop a three dimensional finite element model to simulate the dynamic response of flexible pavements with cold mix, natural and synthetic fibres, different temperatures, and load repetitions, and also with consideration of the viscoelastic characteristic of flexible pavement materials. Flexible pavements have both elastic behaviour of aggregate and viscous behaviour of bitumen [12]. Therefore, asphalt mixtures are viscoelastic materials that its behaviour depends on the time rate of stresses and strains in the asphalt layer . A general finite element program, ABAQUS, was used for this purpose. Also, this study is undertaken to evaluate the effect of natural and synthetic fibres as a reinforcement material on rutting in CMA. In order to validate the efficiency of the model, the predicted results were compared to accurately measured in laboratory data.

2. Classical rutting prediction approach

Classic attempts to model rutting analysis are concentrated on protecting the under layers. At the top of the subgrade layer, the vertical stress and strain are limited to control the permanent deformation of the whole pavement structure and also restricted the tensile stress and strain at the bottom of the lowest bituminous layer to control fatigue cracks [13]. A classic model of rutting prediction utilized in road pavement analysis is given in [13] :

$$N_f = 1.077 \times 10^{18} \, (10^{-6} \div \varepsilon_v)^{4.4843} \quad (1)$$

Where:
Nf : applied load (kN).
εv : vertical compressive strain at the top of subgrade layer.

Nowadays, comprehensive researches have been carried out using different laboratory test methods such as wheel tracking test, creep test, complex (dynamic) modulus test and triaxial test, combined with contributions from investigations of pavement field rutting [13]. It was noticed that rutting failure was not solely occurring in subgrade layer or other under layers but also can be as a result of bituminous mixture problems. Consequently, it has become obvious that in accurate road pavement design procedure, the cumulative permanent deformation in all pavement layers must be considered.

Three model types have been used to compute permanent deformation in flexible pavement: empirical, mechanistic empirical and fully mechanistic. The empirical model is the simplest mathematical form fitted to controlled field data depending on regression equations. Properties of materials and site

conditions are not included in this type of modelling whilst specific applications, for instance performance predictions in system of road pavement management are commonly used. The main purpose of this model is to evaluate future performance based only on the recorded deformation history. The mechanistic empirical model is designed based on a combination of predictions of simple mechanistic response (usually using theory of elasticity) with empirical equations which are calibrated by experimental tests. The computed mechanistic response is utilized as input in the empirical model to predict actual performance, such as rutting and cracking. The effect of traffic loading and environmental conditions can be involved. Throughout application, the model mechanistic response is obtained during a pavement structural analysis. The linear elastic theory is usually used for its formulation and fast computer analysis.

Fully mechanistic models to compute or predict permanent deformation also use a structural analysis program to show the effect of the stresses and strains in the road pavement structure due to the influence of loading time (frequency) and temperature. The different characteristics of material behaviour are represented using constitutive models to directly predict rutting, cracking and other types of damage. With the most important points of these models, the effect of various load conditions, for example loading time, value and temperature can be simply evaluated and incorporated into these models. Because of capabilities of mechanistic models to predict road pavement distresses, there is no need for empirical functions. However, constitutive mechanistic models are complex and have some difficulties in calibration and execution. Very limited researches have been carried out to fulfil mechanistic models to predict behaviour of asphalt mixtures.

3. Finite element model development

Different techniques are available to predict flexible pavements deformation such as multilayer elastic theory, boundary element methods, analytical methods, hybrid methods, finite difference methods and finite element methods (FEM). Currently, FEM has been successfully used for flexible pavements performance analysis and has been proven suitable for application to the complex behaviour of the composite pavement materials. Furthermore, using three-dimensional (3D) finite element models can solve all problems that can not be solved with two-dimensional (2D) models under repeated loading. Therefore, in this study, a 3D finite element model has been adopted for analysis to simulate the natural and synthetic fibres reinforced CMA mixtures. In addition, this model considers viscoelastic pavement properties, moving load application to properly characterize the time, rate, and temperature dependent responses of bituminous layer.

The commercial finite element software ABAQUS was used to build this model to evaluate the change in pavement response properties due to different fibres bonding conditions. The ABAQUS program has been widely used in various researches to model the hot mix asphalt pavements system since the variety of modelling capability including the viscoelastic materials behavior under the repeated load but none has been simulated CMA.

4. Results

Figures 1 and 2 present comparisons between the measured and predicted rutting under the wheel path on the surface of the pavements with different temperatures. It can be clearly observed that there is a good agreement on rut depth measurements between the model and the test.

5. Conclusion

In this research, the use of the three-dimensional finite element simulations in estimating pavement's rutting was discussed. The processes of choosing and optimizing the suitable meshes are investigated. The process for implementing a finite element model which considers the viscoelastic material behaviour, pavement boundary and load geometry were described.

In particular, the following items were concluded:

- According to obtained results, the model provided can properly predict rutting behaviour in cold mix asphalt of various types of reinforcing materials.
- Results show that the natural and synthetic fibres have positive effects on mechanical behaviour of asphalt mixtures.
- The ordinary cold mixtures exhibited less resistance to the rutting than reinforced mixtures with glass and coir fibres.

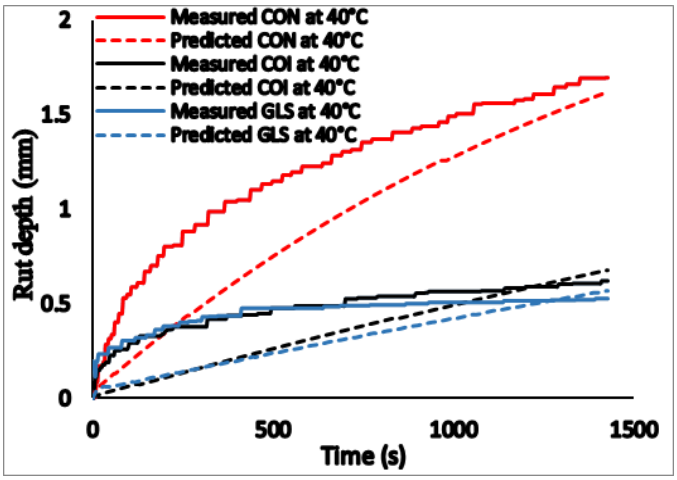

Figure 1. Measured and predicted CBEMs rutting at 40°C.

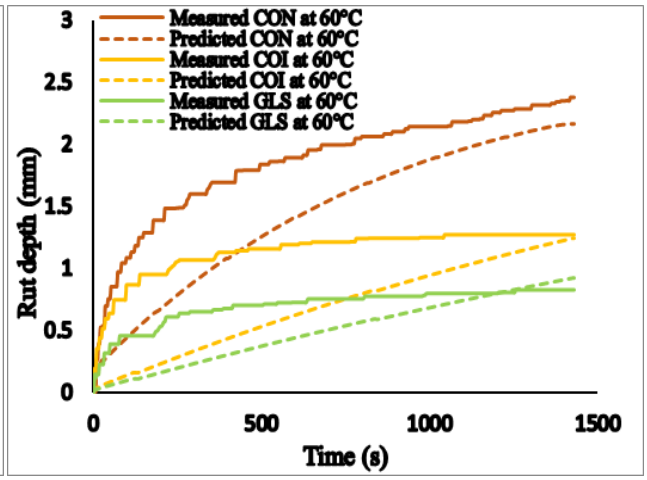

Figure 2. Measured and predicted CBEMs rutting at 60°C.

Acknowledgements

The first author wishes to express his sincere gratitude to the Itaqi Ministry of Higher Education and Scientific Research and Al-Muthanna University in Iraq for providing the financial support. The authors also thank David Jobling-Purser, Steve Joyce, Neil Turner and Richard Lavery who helped the authors a lot to complete this study.

References

[1] Chazallon, C., Koval, G., Hornych, P., Allou, F. & Mouhoubi, S. (2009) Modelling of rutting of two flexible pavements with the shakedown theory and the finite element method. *Computers and Geotechnics*, 36**,** 798-809.

[2] Dong, Q., Huang, B. & Zhao, S. (2013) Field and laboratory evaluation of winter season pavement pothole patching materials. *International Journal of Pavement Engineering*, 15**,** 279-289.

[3] Dulaimi, A., Al Nageim, H., Ruddock, F. & Seton, L. (2016) New developments with cold asphalt concrete binder course mixtures containing binary blended cementitious filler (BBCF). *Construction and Building Materials*, 124**,** 414-423.

[4] Thanaya, I. N. A., Zoorob, S. E. & Forth, J. P. (2009) A laboratory study on cold-mix, cold-lay emulsion mixtures. *Proceedings of the Institution of Civil Engineers - Transport*, 162**,** 47-55.

[5] Al-Busaltan, S., Al Nageim, H., Atherton, W. & Sharples, G. (2012) Green Bituminous Asphalt relevant for highway and airfield pavement. *Construction and Building Materials*, 31**,** 243-250.

[6] Ghauch, Z. G. & Abou-Jaoude, G. G. (2013) Strain response of hot-mix asphalt overlays in jointed plain concrete pavements due to reflective cracking. *Computers & Structures*, 124**,** 38-46.

[7] Shanbara, H. K., Ruddock, F. & Atherton, W. (2016) Rutting Prediction of a Reinforced Cold Bituminous Emulsion Mixture using Finite Element Modelling. *Procedia Engineering*, 164**,** 222-229.

[8] Ye, Q., Wu, S. & Li, N. (2009) Investigation of the dynamic and fatigue properties of fiber-modified asphalt mixtures. *International Journal of Fatigue*, 31**,** 1598-1602.

[9] Chen, H., Xu, Q., Chen, S. & Zhang, Z. (2009) Evaluation and design of fiber-reinforced asphalt mixtures. *Materials & Design*, 30**,** 2595-2603.

[10] Abtahi, S. M., Sheikhzadeh, M. & Hejazi, S. M. (2010) Fiber-reinforced asphalt-concrete – A review. *Construction and Building Materials*, 24**,** 871-877.

[11] Abiola, O. S., Kupolati, W. K., Sadiku, E. R. & Ndambuki, J. M. (2014) Utilisation of natural fibre as modifier in bituminous mixes: A review. *Construction and Building Materials*, 54**,** 305-312

[12] Saltan, M. & Sezgin, H. (2007) Hybrid neural network and finite element modeling of sub-base layer material properties in flexible pavements. *Materials & Design*, 28**,** 1725-1730.

[13] Uzarowski, L., *The Development of Asphalt Mix Creep Parameters and Finite Element Modeling of Asphalt Rutting*, in *Civil Engineering*. 2006, University of Waterloo.

Luna Salh

Microwave Plasma Effect on Adhesion Promotion in Fibre Cementitious Composites

L Salh, D Lee, A Shaw and P French

Built Environment and Sustainable Technologies Research Centre (BEST),

Liverpool John Moores University, Byrom Street, Liverpool,

L3 3AF, UK

l.salh@2013.ljmu.ac.uk, D.Y.Lee@ljmu.ac.uk, A.Shaw@ljmu.ac.uk, P.French@ljmu.ac.uk

Abstract: It is well known that interface in composites plays an important role in composite properties. This study involved in an investigation of the effect of microwave plasma on improving the pull-out load of fibres in cement mortar. Three different types of fibres including polypropylene, glass and basalt fibre were selected to perform plasma treatments. Argon gas was used as plasma activation gas with a flow rate of 3, 2 and 1 letter/min. Also, three different treatment duration were investigated: 5, 10 and 15 minutes per each side of each fibre. The distance from the plasma source kept constant at 100mm. Tinius Olsen machine H25KS was used to perform single fibre pull-out test. The results indicated that surface modification of fibres by microwave plasma contributed to higher fibre pull-out load.
Keywords: Fibre reinforced concrete (FRC), plasma treatment, pull-out test. Interfacial transition zone (ITZ)

1. Introduction

Concrete is a very well-known construction material that is most used around the world. It is very strong in compression. However, concrete is weak in tension and has a very low energy absorption capacity. An effective way to improve the tensile strength of concrete is by adding different fractions of fibres. During the past few decades, the concrete construction field has seen a growing interest in the advantages that fibre reinforcement has to offer such as high ductility and sufficient durability. The most common type of fibres used for reinforcing concrete is steel, polymer, glass and carbon fibre (Kizilkanat et al., 2014).

Fibre reinforced concrete FRC is cementing concrete reinforced mixture with more or less randomly distributed small fibres. In the FRC, a number of small fibres are dispersed and distributed randomly in the concrete at the time of mixing, and thus improve concrete properties in all directions. It is an effective way to increase toughness, shock resistance and resistance to plastic shrinkage cracking of the mortar. These fibres have many benefits; they can improve the structural strength to reduce the heavy steel reinforcement requirement. The freeze-thaw resistance of the concrete is improved. The durability of the concrete is improved to reduce the crack width.

As a result of adding fibres to concrete, a significant post-cracking behaviour improvement was reported. In the other hand fibres lead to the reduction in compressive strength, workability and a phenomenon called fibre balling was reported by a number of researchers (Suksawang and Mirmiran, 2014) (Wafa, 1990) (Rao et al., 2013) (MacDonald et al., 2009). Therefore, in this research study, an attempt to overcome those drawbacks of adding fibres was made by using microwave plasma.

Plasma is the fourth state of matter. It can be considered as a gaseous mixture of negatively charged

electrons and highly charged positive ions being created by heating a gas or by subjecting a gas to a strong electromagnetic field. Plasma particles lead to chemical and physical interactions between the plasma and the treated substrate surface. These interactions depend on so many factors, such as plasma condition, type of the used gas, power, pressure and distance from the flame and treatment duration.
Plasma is used widely in both scientific studies and industrial applications such as medical, food, textile, automotive, etc.
Although plasma is widely used in so many different industries, its application and benefits till date are poorly realised in the field of civil engineering. Therefore, in this research study, the effect of microwave plasma on the enhancement of the properties of fibre reinforced concrete has been investigated.
The enhancement of the interfacial transsition zone (ITZ) between the cement matrix and the plasma treated reinforcement fibres is caused by both physical and chemical modifications. The physical modifications can be achieved by surface roughening of the fibres, producing a larger surface area for bonding. Thus, the friction between the matrix and the fibre is increased. The chemical modification is included in the implantation of active polar groups on the surface of the fibre, reducing the surface energy of the fibre. Thus, the chemical bonding between the matrix and the fibre is enhanced.
According to the differences in gas temperature, plasma can be divided into:

- High-temperature plasma: When the gas temperature is higher than 10^6 K. This type representing the majority of our universe.
- Low-temperature plasma: When the gas temperature is lower than 10^6 K. This type is more prevalent on Earth. It can be further divided into (1) hot plasma, when the gas temperature higher than 1000 K. Such as lightning, electrical arc, and other high-power discharges; and (2) cold plasma, when the gas temperature is lower than 1000 K. Such as various glow discharges at low pressure.

2. Experimental Work

2.1. Materials

Macro synthetic Durus S400 fibre provided by Sika UK with thickness with the length of 55mm was used. The fibre has a melting point of 160°c. Alkali resistance macro synthetic glass fibre provided by Oscrete UK was used. The fibres were random in size and length ranging between 37 to 67 mm. Organic basalt fibre provided by MagmaTech UK was used. Basalt fibre is a new type of fibre which is introduced to the use in the construction fields a few years ago. The length of basalt fibre was 25mm.
Araldite glue and Aluminium plates of dimension 20x35 mm was used. Plastic disposable pipes of the diameter of 20mm and height of 50mm were used as a mortar mould for the pull-out tests. Plastic discs of 20mm in diameter and 1 mm thick with a slot in one diameter were used to indicate the centre of the specimens.

2.2. Plasma Treatments

Marconi 10mhz-20MHz microwave test set 6200A was used as a signal generator. TMD microwave amplifier (PTC6441 TWTA 500w 2.5-7.5 GHz). The PTC6441 travelling wave tube amplifier is helping to produce microwave plasma.
Microwave plasma with the frequency of 5.8 GHz and power of -16.00 dBm was used as shown in Figure 1. The technicians in Liverpool John Moores University's workshop created a fibre holder as shown in the figure. Argon gas provided by BOC was used as a plasma activation gas.
Polypropylene, glass and basalt fibres were treated with three different flow rates as 3, 2 and letter/min. for each fibre and each flow rate, three treatment durations of 5, 10 and 15 min/side were investigated. The treated fibres were wrapped in Aluminium foil, labelled and transferred to the concrete laboratory for the purpose of pull-out specimens preparations. For each parameter, three identical fibres were treated.

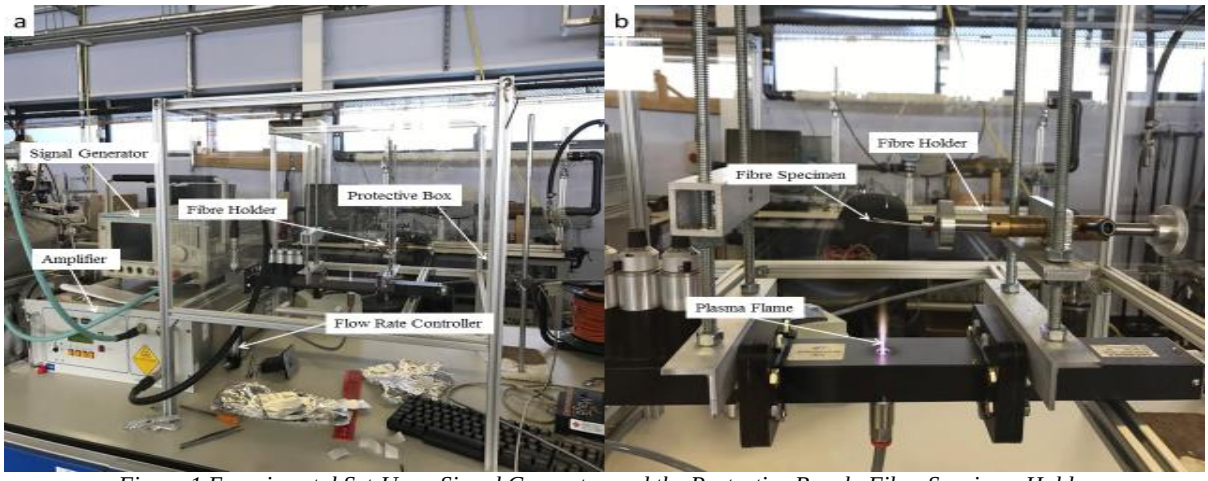

Figure 1 Experimental Set-Up a. Signal Generator and the Protective Box, b. Fibre Specimen Holder

2.3. Pull-Out Test

Cement mortar specimens were fabricated using Portland cement, sand and tap water from university's tap. The mix ratio of 1:1.5:0.5 for cement: sand: water. The raw material was mixed by hand until a homogenous mix obtained. Thereafter plastic moulds of 20mm in diameter and 50mm in high was used. Prior to hardening, the treated fibres are vertically inserted in the centre of the mortar specimens with the help of the plastic discs created earlier. The upper part of each fibre wrapped in Aluminium foil. The specimens labelled as indications to their groups and kept in the laboratory for 24 hours. After 24 hours the plastic discs were removed and the specimens cured in the plastic container contained water to a specific level to ensure that the specimens are not submerged completely. The container covered for 28 days.

The embedment length for the fibres kept as 10mm for the glass and the basalt fibre, and 15mm for the polypropylene fibre.

The pull-out test was modified according to the size and shape of the mortar moulds. A steel cage was fabricated to secure the pull-out specimens. The specimen and the cage were mounted on the grip of the testing machine, while the fibre glued between two 20x 35 mm Aluminium plates to be pulled out by the testing machine. The rate of the machine was set to a displacement of 1mm/min. The machine plotted the force-extension curve.

3. Results and Conclusion

The investigation is aimed to increase the adhesion between the fibres and the cement matrix in an attempt to improve the interfacial transition zone (ITZ). Figure 2 shows the comparison between the maximum pull-out load for treated and untreated. Figure 2 a. shows the maximum pull-out load of fibres glued to two Aluminium plates. For polypropylene fibres and improvement of 11.42% of the pull-out load was observed when the fibres treated with the flow rate of 3 l/min for 10 min/side. For the glass fibre, the maximum pull-out load increased from 135.11N for untreated fibres to 245.67N when the fibres treated with 3 l/min for 5 min/side. Similar to the basalt fibre a significant increase was observed up to 35% when the fibres treated with a flow rate of 3 l/min for 10 min/side.

Figure 2 b, c and d show the maximum experimental pull-out load for fibres treated with 3, 2 and 1 l/min respectively in cement mortar. The maximum pull-out load of polypropylene fibre was found to be with the fibre treatment of 2 l/min for 5 min/side when an increase of 20.41% recorded. For the pull-out force in glass fibre specimens, an increase of 40.7% compared to untreated fibres was recorded. A remarkable improvement for basalt fibres was recorded to be 50.83% for fibres treated with 2 l/min for 10 min/side compared to untreated fibres.

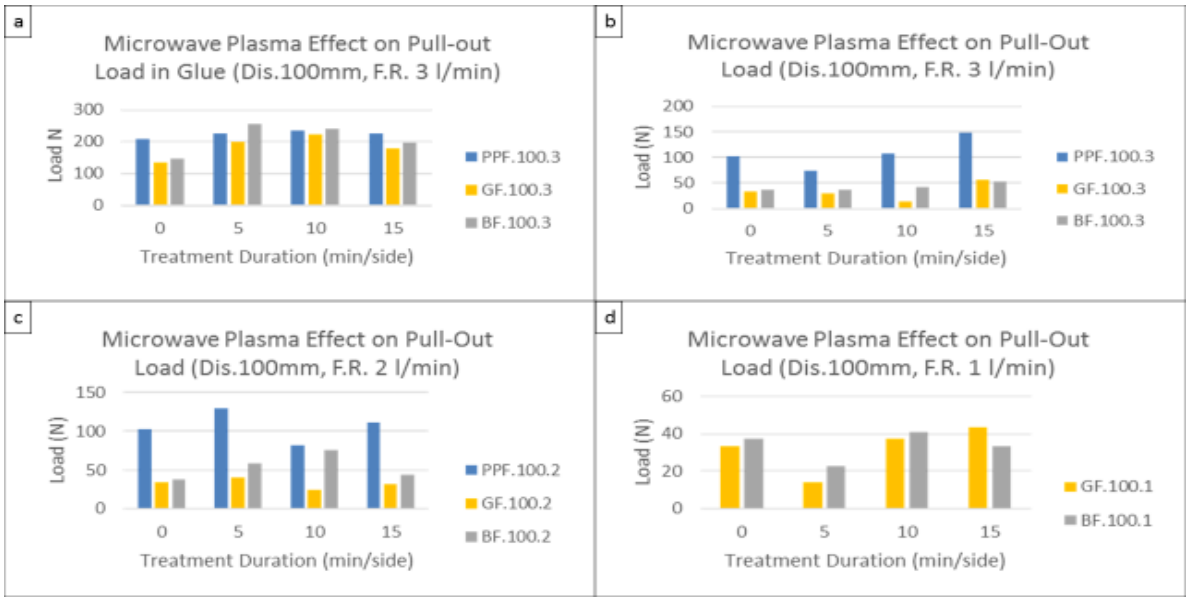

Figure 2 Experimental Results a. Pull-out Load in the Glue, b. Pull-out Load in Cement Mortar Flow Rate 3 l/min, c. Pull-out Load with Flow Rate 2 l/min, d. Pull-out Load with Flow Rate 1 l/min

References

Kizilkanat, A. B., Kabay, N., Akyüncü, V. & Erdoğan, G. 2014. Basalt Fibers And Mechanical Properties Of Basalt Fiber Reinforced Concrete. *Bazalt Lİfler Ve Bazalt Lİflİ Betonlarin MekanİK Özellİklerİ.,* 32**,** pp. 444-452.

Macdonald, C. N., Ballou, M. L. & Biddle, D. T. Case Histories Using Synthetic Fibre Reinforced Concrete. Shotcrete for Underground Support XI, 2009.

Rao, K. S., Kumar, S. R. & Narayana, A. L. 2013. Comparision of Performance of Standard Concrete and Fibre Reinforced Standard Concrete Exposed to Elevated Temperatures. *American Journal of Engineering Research (AJER),* 02**,** PP. 20-26.

Suksawang, N. & Mirmiran, A. 2014. Use of Fibre Reinforced Concrete for Concrete Pavement Slab Replacement. Florida Department of Transportation: Florida International University and Florida Institude of Technology.

Wafa, F. F. 1990. Properties and Applications of Fibre Reinforced Concrete. *Engineering Science King Abdulaziz University*, 2**,** PP. 49-63.

Ali El-Hajaji

Salt production by evaporation ponds from brine disposed from distillation plants (MED)

Ali Elhajaji[1] & Rafid Al Khaddar[2]

[1]Liverpool John Moores University, School of the Built Environment, The Peter Jost Centre, Byrom Street, Liverpool, L3 3AF, UK; T:+44(0)1512314149; F: +44(0)1512312815; email: A.H.ElHajaji@2012.ljmu.ac.uk
[2]Liverpool John Moores University, School of the Built Environment, The Peter Jost Centre, Byrom Street, Liverpool, L3 3AF, UK; T: +44(0)151 231 2809; F: +44(0)1512312815; email: r.m.alkhaddar@ ljmu.ac.uk

Abstract

Considering the parity between natural evaporation and traditional salt works, there is a strong argument to adopt an integrated approach for the solution of brine disposal management from thermal desalination plants. Therefore, this paper has aimed to support the use of evaporation ponds as opposed to traditional salt works, to recover minerals and NaCl (halite) from brine, with particular reference to ZWPD in Libya, located on the southern Mediterranean coast. The work also pave the way for further development of mineral salt exploitation from the brine disposed from thermal distillation plants. The investigation results indicated that the EDS spectrum of the salt crystals sample exhibited two highly intense peaks of Na^+ and Cl^- at 41.38% and 25.05% of the total wt% respectively, in contrast with low intense peaks of Mg^{2+} and Si at 5.06% and 0.28% of the total wt% respectively. Meanwhile, O_2 represented only about 28.22% of the total wt% and the absence of other chemical elements shows that salt crystal samples have good purity and a homogeneous crystallographic structure. The crude of NaCl salt produced from the evaporation ponds ranged between grade 1, 2 and 3 with purity reaching 80.73% and moisture 0.52% compared to conventional methods of salt production. On the other side, laboratory and fieldwork experiments indicated the actual the possibility of a further exploitation of such saturated brine has been experimentally analysed by laboratory tests in order to produce high purity of NaCl to be commercialised in the food and industries.

Keywords: Thermal Desalination Plants, Zwuarah Desalination Plant (ZWDP), Brine

1. Introduction

In both scenarios (reverse osmosis and thermal desalination technologies), the water produced has a higher salinity concentration than the source water. In cases of reverse osmosis and thermal desalination, the brine discharged contains chemical residues of antiscalants, while the by-products of biocides and antifoaming agents are present in brine discharged from thermal desalination plants. A low concentration of metals results from the corrosion phenomenon at different levels in both reject streams (Lattemann and Höpner, 2008). The average dose of antifoam agent injected into the make-up seawater is 0.1mg/l (Darwish et al., 2013), while the maximum dose of antiscalants agent is 2 ppm in thermal desalination plants (Abdulgader and Mustafe, 1998). Neither of these commercial chemical additives

pose any threat to the environment or food grade products (Cipollina et al., 2012). The seawater intake is also chlorinated with typical doses 0.5–2 mg/l of active Cl_2 (Darwish et al., 2013). Because of the extended process within each evaporator and a high temperature, any residual effects of the brine discharge are minimal due to high dilution following reaction within the evaporation units (Cipollina et al., 2012). However, there is an impact on sensitive ecosystems and the marine environment because of high salinity and continuous disposal (Lattemann and Höpner, 2008; Medeazza, 2005). During the desalination process, there are various concentrations of salts and minerals found in brine including SO_4^{2-}, Cl^-, Na^+, Ca^{2+}, Mg^{2+}, K^+, Fe^{2-} and Cu^{2+} (Abdulsalam et al., 2016). Considering the parity between natural evaporation and traditional salt works, there is a strong argument to adopt an integrated approach for the solution of brine disposal management from thermal desalination plants. Therefore, this paper aims to support the use of evaporation ponds as opposed to traditional salt works, to recover minerals and NaCl (halite) from brine, with particular reference to ZWPD in Libya, located on the southern Mediterranean coast.

2. Study Site and Evaporation Ponds Installation

An experiment was carried out in July 2014 to construct ten evaporation ponds next to the outlet of Zwuarah distillation plant. These ponds are located in the north-western side of the city of Tripoli (Latitude 32°53'420" N and longitude 12°10'578" E) (**figure.1**). They are shaped as irregular rectangles with dimensions of (5m) width, (4.5m) long and (0.25m) deep. The total area of whole evaporation ponds is about ($225m^2$). The depth of the brine in each pond was approximately (0.07-0.1m). A volume of 15.75 m^3 of brine from the evaporator of ZWDP for ponds was used to carry out the experiments.

Figure 1: Site of study and Evaporation Ponds Installation.

3. Sampling and Data Collection

3.1. Brine Samples, SEM and EDX Analysis

The bulk element concentrations of chloride (mgl^{-1}), calcium (mgl^{-1}), magnesium (mgl^{-1}), sodium (mgl^{-1}), potassium (mgl^{-1}), sulfate (mgl^{-1}) and salinity (mgl^{-1}) were analysed in the Lab of ZWDP using Hach methods 2013 for water, wastewater and seawater and the mass of these elements (gr) was calculated for the brine sample collected from the evaporator of ZWDP. In addition, five brine samples were collected from the evaporation ponds and analysed up to the salt crystallization stage (Halite) over five weeks at different salinity percentages (%). Additionally, the weight percentages (%) of element concentrations were calculated to be compared with the quantified results obtained from scanning electron microscopy equipped with energy dispersive X-ray analysis (SEM-EDX) which allows only quantitative determination of the total soluble salt content in the salt crystal (Halite). The percentage of Halite (NaCl) purity and moisture was also determined and the total salt harvested from the ponds was weighed. Sample of dried salt crystals were attached to aluminium studs with carbon glue to a sputter

coated with gold to overcome the problem of charging during scanning electron microscopy SEM analysis. The stud was loaded into an FEI Inspect SEM with an Oxford Instrument INCA analysis system. Conditions were 10kV; magnified at 43x, 117x and 154x with image scale 2mm, 1mm and 500µm respectively to determine salt shape. The weight percentages (wt%) of chemical elements in the salt sample were carried out by energy dispersion of X-Ray spectroscopy (EDX) coupled with scanning electron microscopy (SEM) analysis. The salt sample was uncoated to remove the gold from the results and 20 kV voltages were used at image scale 1mm with magnification 117x. Data was processed with Sem Quant Software to identify and quantify the elemental constituents of the salt sample and five essential chemical elements were found in the salt sample.

4. Results and Discussion

The outcomes of the total weight percentages (wt%) calculated from the concentrations of ions by titration using Hach methods for the brine and salt sampled during five weeks at different percentages of salinity level indicated that, the wt% of the salt is primarily influenced by Na^+ and Cl^- at the fifth week alongside other elements such as Mg^{2+} and $SO4^{2-}$. There was a significant increase in wt% of Cl^-, Ca^{2+}, Mg^{2+}, Na^+, K^+ and $SO4^{2-}$ up to the fourth week, followed by a notable decrease in wt% in the fifth week. The observed variation can be attributed to the gypsum crystallization at this stage which revealed fluctuations of salinity level. At salinity level 7.7%, the wt% of extracted chemical elements of Cl^-, Ca^{2+}, Mg^{2+}, Na^+, K^+ and $SO4^{2-}$ varied between 4.26%, 0.03%, 0.25%, 1.59%, 0.07% and 0.37% respectively, while at salinity level 9.7%, the wt% of extracted chemical elements of Cl^-, Ca^{2+}, Mg^{2+}, Na^+, K^+ and $SO4^{2-}$ varied between 5.36%, 0.04%, 0.37%, 2.02%, 0.08% and 0.51% respectively, whereas at salinity level 19.2% the wt% of extracted chemical elements of Cl^-, Ca^{2+}, Mg^{2+}, Na^+, K^+ and $SO4^{2-}$ varied between 10.65%, 0.06%, 0.98%, 7.15%, 0.27% and 1.03% respectively, while, at salinity level 38.5% the wt% of extracted chemical elements of Cl^-, Ca^{2+}, Mg^{2+}, Na^+, K^+ and $SO4^{2-}$ varied between 21.33%, 0.12%, 2.48%, 18.98%, 0.7% and 8.51% respectively. At salinity level 0.9% the wt% of extracted chemical elements of Cl^-, Mg^{2+}, Na^+, and $SO4^{2-}$ varied between 0.5%, 0.02%, 0.32%, 0.01% respectively, however Ca^{2+} and K^+ did not exist at this level of salinity, which is possibly due to crystallization of salt (NaCl) of a purity reaching 80.73% with moisture 0.52%. The results of the analysed brine samples from the evaporation pond showed considerable variation in the ions composition which maybe attributed to high salinity levels due to intense evaporation taking place in the ponds that were not detected in the analysis. SEM/EDS analysis was performed on the salt crystal samples to determine their crystallographic structure and to identify wt% of the chemical elements present in the salt crystal samples. The investigation results indicated that the EDS spectrum of the salt crystals sample exhibited two highly intense peaks of Na^+ and Cl^- at 41.38% and 25.05% of the total wt% respectively, in contrast with low intense peaks of Mg^{2+} and Si at 5.06% and 0.28% of the total wt% respectively. Meanwhile, O_2 represented only about 28.22% of the total wt% and the absence of other chemical elements shows that salt crystal samples have good purity with a homogeneous crystallographic structure (**figure 2)**. Addala et al., 2013 also supported the notion that the significant intensities of peaks indicate high crystalline quality. The crude salt produced from the evaporation ponds indicated a strong presence of Na^+ and Cl^- alongside other impurities present in small but significant quantities. This is in accordance with a study by Kasedde, (2013), who recorded an average proportion of halite (NaCl) in grade 1 as 92%, 64% in grade 2 and 65% in grade 3 for the salt production from salt works. Hence from the present investigation, the result of the mineralogical analysis of the salt by EDS analysis indicate that the salt yield crude from the evaporation ponds ranged between grad 1, 2 and 3 compared to conventional method of salt production. On the other side, that result indicate that the concentration of toxic trace metals or elements in the salt harvested from the experimental study not exist. Therefore, the outcomes reveals that the NaCl produced from the brine disposed from distillation plants can be commercialised in the food and industries sectors. The outcomes of the experimental fieldwork in the evaporation ponds revealed that a volume of brine of 15.75 m^3 produces about 309 kg of salt within an area of 255m^2 and depth variance of 0.07-0.1m, thus demonstrating that by increasing the outlying area and the volume of brine, it is likely to instigate salt production. Consequently, as ZWDP disposed about 26,666.7 $m^3day^{-1}$of the brine, it is anticipated that about

523,175.261kgday^{-1} could be extracted in the form of salt. More than 30% of the total global production of sodium chloride (table salt) is derived from solar evaporation ponds (Ahmed et al., 2009). According to the prices obtained from leading industrial websites, such as (www.Alibaba.com) the current market price for sea salt (sodium chloride) with a purity of 99% ranges between US $ 50-100/ tonne, and high quality food grade pool sodium chloride ranges between US $340-360. Another website (www.econmist.com) was also used to investigate the current market price of the lowest grade of gritting salt for de-icing roads. According to this website, the value of salt per tonne ranges between $ 40-50 in America and Britain. Another study by Abdulsalam et al., 2016 was also used to investigate the price of different minerals showing that the price of sodium and magnesium ranges between US $ 350 - US $ 2,410 respectively. The recovery of such salt or minerals can generate significant revenues annually for Libya resulting in major investment across public and private sectors, particularly within the environmental and economic infrastructure. This is because the geographical location is eminently suitable for the evaporation ponds as it has a mild, dry temperature and high annual evaporation rates, combined with minimal land costs and availability.

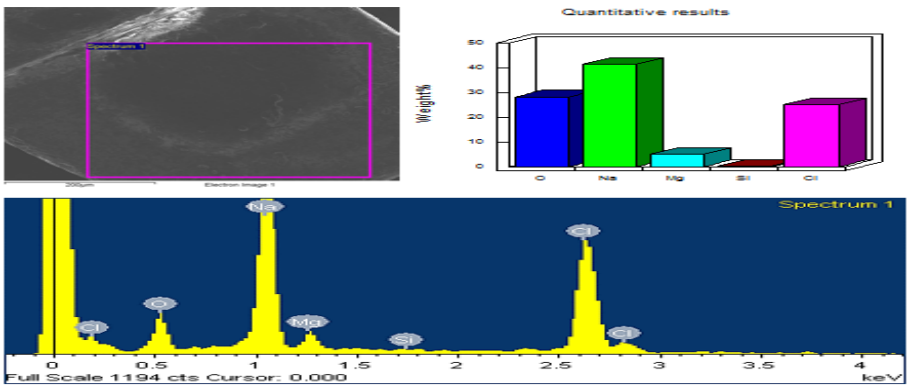

Figure 2: EDX Analysis of Salt crystal Harvested of Evaporation Ponds.

5. Conclusion

According to our experimental work, this study has revealed that the best way to recover salt and minerals for domestic, commercial and industrial use, an integrated cycle that utilizes a distillation plant with evaporation ponds is undoubtedly the best method, in terms of production, cost and efficacy, in contrast with more conventional salt extraction methods. Furthermore, the quality of the end-product shows a huge potential for further development and investment by building more desalination plants on the Libyan coastline. It also paves the way for further investment and development of an eco-friendly venture that will ultimately propagate further economic growth for Libya, while providing further work opportunities.

6. References

Abdulgader. A and Mustafe. G. (1998) *Performance evaluation of Belgard EV2050 at al-Aziza reheat plant, Research and Development Centre, Saline Water Conversation Corporation*; *Technical Report No. TR-3808/EVP96004*, October. pp. 1786- 1804

Abdulsalam. A, Mohamed. T and Ahsan. A. (2016) An integrated technique using solar and evaporation ponds for effective brine disposal management, *Sustainable Energy*, v.1 (1), January.pp.1-12

Addala. S, Bouhdjer. L, Chala. A, Bouhdjar. A,Halimi.O, Boudine. B, Sebais. M. (2013) Structural and optical properties of a NaCl single crystal doped with CuO nanocrystals, *Science and Technology*, March, v.22 (9), pp.1-5.

Cipollina. A, Misseri. A, Staiti. G, Galia. A. Micale. G and Scialdone. O. (2012) Integrated production of fresh water, sea salt and magnesium from seawater, *Desalination and Water Treatment*, v.49 (3), May. pp. 390–403

Darwish. M, Hassabou. A and Shomar. B. (2013) Using Seawater Reverse Osmosis (SWRO) desalting system for less environmental impacts in Qatar, Desalination, v.309 (1), Junary.pp.113-124
Kasedde. H. (2013) *Characterization of Raw Materials for salt Extraction from Lake Katwe, Uganda,* 1-35, MSc. Thesis, KTH, Royal Institute of Technology, Stockholm University, Sweden.
Lattemann. S and Höpner. T. (2008) Environmental impact and impact assessment of seawater desalination, *Desalination*, v.220 (3), March, pp.1-15
Medeazza. G. (2005) "Direct" and socially-induced environmental impacts of desalination, *Desalination*, v. 185 (3), November, pp.57-70

Ilaria Frau

Real-time assessment of zinc-polluted water using optical, electrical and microwave techniques

I Frau[1], O Korostynska[1], A Mason[2,3] and P Byrne[4]
[1]Built Environment and Sustainable Technologies (BEST) Reseach Institute, Department of Civil Engineering, Faculty of Engineering and Technology, Liverpool John Moores University, Liverpool, L3 3AF, UK.
[2]Animalia, Norwegian Meat and Poultry Centre, PO Box Økern, 0513 Oslo, Norway
[3]Built Environment and Sustainable Technologies (BEST) Reseach Institute, Department of Built Environment, Faculty of Engineering and Technology, Liverpool John Moores University, Liverpool, L3 3AF, UK.
[4]School of Natural Sciences and Psychology, Faculty of Science, Liverpool John Moores University, Liverpool, L3 3AF, UK.
E-mail address: I.frau@2016.ljmu.ac.uk

Abstract. Metal pollution in the aquatic environment has attracted global attention, especially due to the dispersion of trace metals in freshwater surrounding abandoned mining areas. This paper reports the experimental procedure used for continuously detecting changes in the concentration of zinc in water using three methodologies based on electromagnetic (EM) waves: UV-Vis spectrophotometer, for measuring absorbance; LCR (inductance, L, capacitance, C, resistance, R) meter, for capacitance and resistance measurements; and a novel microwave sensor method which permits to detect the reflected power (S_{11}). With this last methodology, two planar sensors were used: interdigitated electrode (IDE) pattern on polytetrafluoroethylene (PFTE) substrate, and the same kind of sensor functionalised with bismuth (III) oxide coating. Spectra signals, as reflected power, were analysed in the MHz - GHz frequency range. Results show that the signals were dependent on the type and concentration of present metal with $R^2 = 0.9942$, $R^2 = 0.999$, $R^2 = 9903$, $R^2 = 0,997$, $R^2 = 9992$ respectively for absorbance, capacitance, resistance and reflected power measured with uncoated and coated IDE sensors. In conclusion, this novel sensing system could be a cost-effective alternative for detecting metal pollution in-situ, and in real-time.

Keywords. Water quality monitoring, zinc pollution, microwave sensing system, bismuth oxide thick film, planar IDE sensors

1. Introduction

Despite the importance of mineral resources for human progress, mineral extraction has caused global environmental problems, especially for the dispersion of heavy metals (zinc, lead, cadmium, copper) which cannot be degraded or destroyed by micro-organisms. Therefore they persist in the environment and can enter the body through the air, food, and water causing long-term health effects [1].

In UK mining regions, zinc (Zn) is the most presented trace metal in surface waters and is a worldwide environmental health concern. Nowadays, it is difficult to characterise and prioritise remediation strategy in polluted mining areas [2]. The methods for evaluating the state of Zn polluted areas suffer many limitations, particularly those related to the use of laboratory-based analysis, which typically excludes the possibility for online pollution monitoring and detection of unexpected pollution events (e. g. those caused by flooding)[3]. Recent legislative drivers in Europe require new sensing systems able to distinguish abnormal changes from normal variations, which in turn creates the need for low-cost continuous monitoring technologies and to guarantee an

immediate response to detect events [4]. Much progress has been made over the past 30 years in the formulation of predictive, preventative and remedial technologies to limit the impact of mine water pollution on water bodies. A number of approaches (e.g. voltammetric sensors [5]) make use of environmentally-friendly bismuth (Bi) - based electrodes. Bi films are increasingly replacing the mercury devices (highly hazardous), which have long proved to be suitable for the sensitive detection of heavy metals [6].

A novel technique capable of meeting this current demand is a novel microwave sensor method developed by the authors [7]. In an effort to combine the benefits of both microwave technology and the application of Bi nanoparticles films, this experiment exposes a thick film coating printed on a planar IDE sensor for detecting zinc concentration in natural water.

This paper considers the feasibility of using a microwave sensing approach by comparing it with more commonly used UV-Vis and impedance-based measurements. The remainder of the paper documents the experimental procedure and setup, in addition to the results and obtained using these three methodologies based on EM waves.

2. Experimental procedure

2.1. Thick-film preparation

Two IDE sensors were functionalised by screen-printing a paste mixture based on bismuth oxide as the principal material. Bismuth (III) oxide powder 90-210 nm particle size, (Sigma-Aldrich 637017) was used for creating a thick film paste using screen-printing. 92.5 wt. % bismuth (III) oxide nanopowders were mixed with 7.5 wt. % of a polymer (PVB) binder, namely Butvar B98 in solid form, and a suitable amount of ethylene glycol butyl ether (solvent) to form the paste. These two components work as a matrix for developing the correct consistency of the paste to be printed with a manual screen printer (Super Primex) over the planar sensors (Fig. 1 a). The thickness of the Bismuth oxide thick film was increased by multiple screen-printing, with the two sensors having 4 and 6 layers printed. The thickness was measured using a surface profiler (Taylor Hobson - Form Talysurf 120), resulting in 40 and 60 µm respectively for 4 and 6 layers. Every time the sensors were screen-printed twice, they were placed in an oven at 170º C for 1 hour to evaporate the alcohol.

2.2. Sample preparation

Five samples of zinc solutions at different concentrations (0, 1, 10, 50, 100 mg/L) were prepared by dissolving a defined volume of Zn 1000 ppm ICP standard solution certified (Sigma-Aldrich 18562) in deionised water.

2.3. Electromagnetic measurements

Five samples containing zinc are analysed with a UV-Vis spectrophotometer, a programmable LCR meter and microwave spectroscopy. The UV-Vis absorption spectrum can be considered an optical signature. The absorbance of samples was analysed by measuring approx. 3.5 mL of the zinc solutions in plastic cuvettes and analysed with UV-Vis Spectrophotometer (Jenway 7315) at the wavelength range 200 - 1000 nm. Capacitance and resistance were measured using a HAMEG impedance analyser configured with a bespoke coaxial probe at the frequency range between 20 Hz and 200 kHz for the impedance range from 1 to 25 Ω. For this measure, 400 µL of sample volume were used and five repetitions were performed for each sample.

The principle of using microwave spectroscopy is based on the interaction of radio frequencies and microwaves with the solution under examination [8] which permit detection of changes in the spectra at specific frequencies related to the presence and concentration of zinc.

In this experimental, three gold eight-pair IDE pattern printed on planar PTFE substrates were used: one sensor was uncoated and the other two were functionalized as described earlier.

The microwave IDE sensors are connected to a Rohde and Schwarz ZVA 2.4 VNA (Vector Network Analyser) via a coaxial cable (Fig. 1 b). Molex edge mount connectors were used in this work and SMA type connectors. All the equipment was specified for 50 Ω impedance. The VNA used a one-port configuration to enable S_{11} measurement, which permits measurement of the power reflected from the planar sensors which operating in the MHz-GHz frequency range (10 MHz – 15 GHz, 60,000 discrete points). The interaction between zinc solutions and excitation of the sensors at radio wave or microwave frequencies emits an electromagnetic field, which uniquely interacts with the solutions presented to the sensor to enable determination of composition and concentration.

For each measurement (n=5 for each concentration), 400 µL of zinc solution is dispensed onto the sensor using a pipette, with the solution held in place by a well-manufactured holder specifically for these sensors.

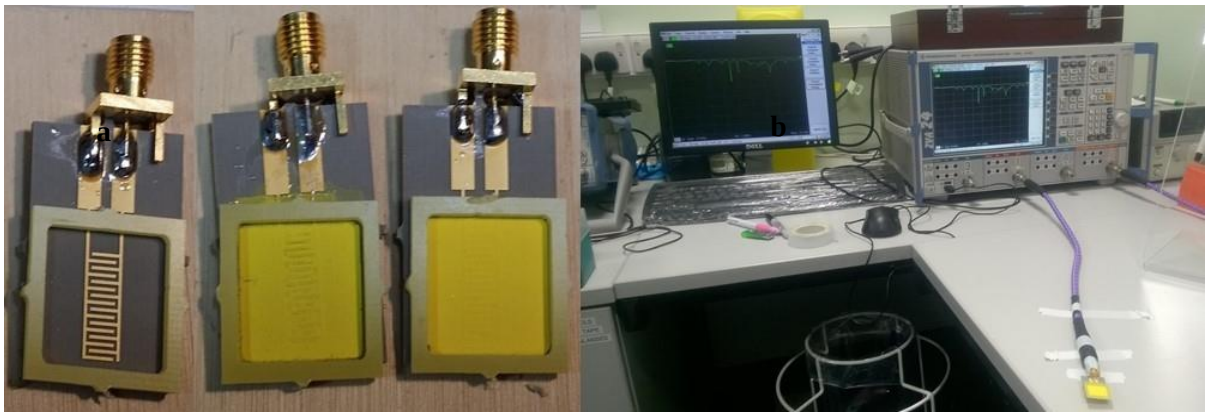

a b

Figure 3 (a) Planar gold eight-pair IDE sensors on PTFE substrate (from left: uncoated sensor and with 4 and 6 layers of bismuth oxide coating). (b) Experimental setup: Vector Network Analyser with a coaxial cable to a planar sensor with bismuth oxide coating.

4. Results and Discussion

Results obtained measuring zinc solution with the techniques previously described are summarised in table 1, which shows R^2, sensitivity (for each 1 mg/L of zinc concentration) and RSD (relative standard deviation).

Table 1 Summary of statistical features obtained for optical, electrical and microwave measurements of zinc water samples.

Properties		**R^2**	**Sensitivity[a]**	**RSD (%)**
Absorbance (at 305 nm)		0.9942	0.0026	1.5 %
Capacitance (at 250 Hz)		0.999	5 nF	2.5 %
Resistance (at 500 Hz)		0.9997	66.84 Ω	2.5 %
Reflected power (S_{11}) - uncoated IDE sensor	at 502 MHz	0.9903	0.0341 dBm	0.6 %
	at 2.46 GHz (peak)	0.978	0.0624 dBm	1.1 %
Reflected power (S_{11}) – functionalised IDE sensor (4 layers, 40 µm)	at 502 MHz	0.9905	0.0341 dBm	1.3 %
	at 2.51 GHz (peak)	0.9865	0.0519 dBm	2.1 %
Reflected power (S_{11}) – functionalied IDE sensor (6 layers, 60 µm)	at 599 MHz	0.9992	0.0283 dBm	1.8 %
	at 2.56 GHz (peak)	0.9372	0.0596 dBm	2.8 %

[a]for every 1 mg/l change of zinc concentration

The change in the optical absorption in the UV-Vis range is related to the increasing concentration of Zinc. There is a linear trend at 305 nm, with $R^2 = 0.9942$ obtained for the 5-point calibration curve. Similarly, the LCR measurements show a good linear correlation with zinc concentration at 250 Hz, with $R^2 = 0.999$. Otherwise, the resistance and zinc concentration are correlated with a power trend with $R^2 = 0.9997$.

The response for the microwave technique demonstrates a shift in signal amplitude, which corresponds with the different concentrations of zinc tested. It is noted also that the sensor output returned to its baseline (air) output when samples were removed and the sensor rinsed and allowed to dry. This indicates that they are reliable and reusable. During the measurements, significant pronounced resonant peak shifts were noticed once the different concentrations of zinc samples were placed in contact with the sensor pattern. This shift was more pronounced when samples had a higher concentration of Zn. This is clearly visible in several parts of the spectrum, in particular between 100 MHz and 4 GHz (figure 2, left side).

There is a similarity between the results obtained with the uncoated sensor and the functionalised sensors. The output of functionalised IDE sensor with bismuth oxide thick film (60 µm) is shown in

figure 2. A small frequency shift toward higher frequencies is observed: with the uncoated sensor the peak is set at 2.46 GHz; with the functionalised sensor (40 µm) at 2.51; and with the functionalised sensor (60 µm) at 2.56 GHz (figure 2 left side). This is due to the increasing of the thickness and the consequent change of the dielectric constant. Figure 2 (right side) shows two frequencies (599 MHz and 2.56 GHz) at which good correlations (R^2 = 0.9992 and R^2 = 0.9372) with zinc concentration and sensor output occur, using 6-layer bismuth coated sensor.

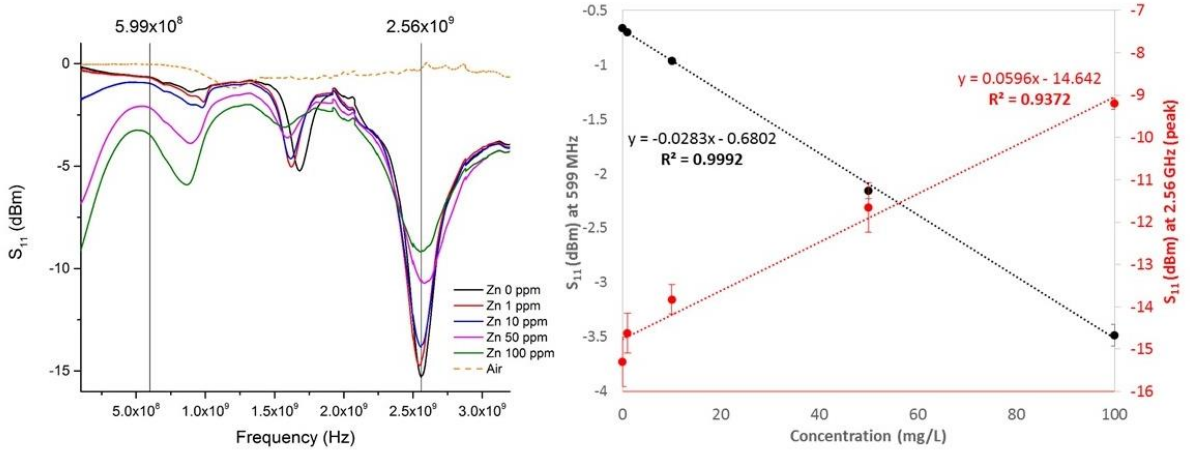

Figure 4 On the left, it is shown the average microwave data captured over a range of frequencies (between 100 MHz and 3.2 GHz) for air and each zinc standard solution measured with a functionalised IDE sensor with 6 layers of bismuth oxide coating (60 µm); two specific frequencies, namely 599 MHz and 2.56 GHz (peak), are evidenced and described on the right with a linear correlation, demonstrating a good correlation between reflected power (S_{11}) and zinc concentration.

5. Conclusion

This paper communicates the experimental results of using planar type microwave sensors for real-time determination of metal concentrations, in particular, zinc. A comprehensive set of complementary experiments using optical, electric and microwave detection methods confirm the potential of this novel sensing approach as an alternative method of metal pollution monitoring in abandoned mining area. Planar sensors were functionalised with different layers of bismuth (III) oxide. The results demonstrate that the uncoated and functionalised sensors return comparable performance (R^2 = 0.992) to alternative techniques, namely optical spectroscopy (R^2 = 0.9942), capacitance (R^2 = 0.999) and resistance (R^2 = 0.9758).

This experiment adds weight to the body of evidence supporting the notion that microwave spectrometry is an attractive option for water quality analysis with minimal operational cost. It could offer the ability to monitor and report water quality over large and remote geographical areas for both in-situ and real-time monitoring and will be able to provide an early warning system for pollution events. Further work is in progress to expand and progress toward realisation of this concept.

Acknowledgments

The authors gratefully acknowledge the support of Liverpool John Moores University, Faculty of Engineering and Technology PhD Scholarship Programme, which allowed this research to be undertaken.

References

[1] X. Zhang, L. Yang, Y. Li, H. Li, W. Wang, and B. Ye, "Impacts of lead/zinc mining and smelting on the environment and human health in China," *Environmental Monitoring and Assessment*, vol. **184**, pp. 2261-2273, 2012.

[2] P. Byrne, P. J. Wood, and I. Reid, "The Impairment of River Systems by Metal Mine Contamination: A Review Including Remediation Options," *Critical Reviews in Environmental Science and Technology*, vol. **42**, pp. 2017-2077, 2012/10/01 2012.

[3] O. Korostynska, A. Mason, and A. I. Al-Shamma'a, "Monitoring Pollutants in Wastewater: Traditional Lab Based versus Modern Real-Time Approaches," in *Smart Sensors for Real-Time Water*

Quality Monitoring, S. C. Mukhopadhyay and A. Mason, Eds., ed Berlin, Heidelberg: Springer Berlin Heidelberg, 2013, pp. 1-24.
[4] W. Brack, V. Dulio, M. Ågerstrand, I. Allan, R. Altenburger, M. Brinkmann, *et al.*, "Towards the review of the European Union Water Framework management of chemical contamination in European surface water resources," *Science of The Total Environment*, vol. **576**, pp. 720-737, 1/15/ 2017.
[5] V. Rehacek, I. Hotovy, and M. Vojs, "Bismuth film voltammetric sensor on pyrolyzed photoresist/alumina support for determination of heavy metals," *Electroanalysis*, vol. **26**, pp. 898-903, 2014.
[6] P. Niu, C. Fernández-Sánchez, M. Gich, C. Ayora, and A. Roig, "Electroanalytical Assessment of Heavy Metals in Waters with Bismuth Nanoparticle-Porous Carbon Paste Electrodes," in *Electrochimica Acta* vol. **165**, ed, 2015, pp. 155-161.
[7] O. Korostynska, A. Mason, and A. I. Al-Shamma'a, "Flexible microwave sensors for real-time analysis of water contaminants," *Journal of Electromagnetic Waves and Applications*, vol. **27**, pp. 2075-89, / 2013.
[8] A. Mason, B. Abdullah, M. Muradov, O. Korostynska, A. Al-Shamma'a, S. G. Bjarnadottir, *et al.*, "Theoretical Basis and Application for Measuring Pork Loin Drip Loss Using Microwave Spectroscopy," *Sensors (14248220)*, vol. **16**, pp. 1-13, 2016.

Islem Megdiche

A review of ultra-high performance fibre reinforced concrete

Islem Megdiche[1], William Atherton[1], Clare Harris[1] and Glynn Rothwell[2]
Department of Civil Engineering[1]
Department of Maritime and Mechanical Engineering[2]
Liverpool John Moores University,
Liverpool,
L3 2ET
I.Megdiche@2015.ljmu.ac.uk

Abstract
In the oil and gas industry, storage tanks are usually surrounded by a secondary containment called bund wall. The purpose of a bund wall is to contain any spillage from the storage tank in the event of failure. Currently, the existing bund walls fail to withstand the impact of the fluid in the case of a total failure of a storage tank. Most bund walls are constructed from reinforced concrete (RC) designed to withstand the hydrostatic pressure only. Therefore, in this research, a new design is proposed by using Ultra High Performance Fibre Reinforced Concrete (UHPFRC) since it was proven that adding fibres to concrete improve its impact strength making in suitable to use when dynamic loads are involved. In this paper, a literature review is given on the fibre reinforced concrete, mainly relating to how it was developed over the years, its constituents, preparation and its hardened mechanical properties.
Keywords. Bund wall, fibre reinforced concrete, dynamic loads.

1. Introduction

The development of UHPFRC dates back to the 1930's when the French engineer Eugène Freyssinet conducted research to improve the compressive strength of concrete by pressing it during setting. Other researchers continued to enhance the mechanical properties of concrete and during the 1970's, they considered using vacuum mixing and high pressure at high temperature in order to reduce the porosity of hardened Portland cement paste. Subsequent advances in the field were linked to the use of plasticizers and pozzolanic admixtures such as silica fume during the 1980's. As a result, two very compacted materials were developed which were Macro-Defect-Free cement (MDF) and Densified Silica Fume (DSF). These two materials were very brittle which led to the inclusion of fibres to improve the ductility of the concrete. During the 1990's, researchers started adding fibres to high strength concrete which improved the mechanical properties of the concrete, especially with the development of new plasticizers based on polycarboxylate ethers (Hassan, 2013).
Since its inception, UHPFRC was used in many applications. The first of which was a footbridge in Sherbrooke, Canada that was built in 1997 (Habel et al., 2008). Subsequently, many footbridges were built worldwide such as the Footbridge of Peace in South Korea, the Sakata Mirai and Yokemuri footbridges in Japan, to name but a few. Additionally, UHPFRC is used in the construction of highway bridge applications such as the Bourg-les-Valence bridges in France, the Shepherds Creek bridges in Australia, etc. Moreover, UHPFRC is incorporated in durability applications such as in the Cattenom nuclear power plant in France where more than 2000 pre-stressed elements made of UHPFRC were used for the exchange body of the cooling system of the tower.
The main advantage that UHPFRC brings is the enhanced mechanical properties, which are higher compressive, tensile and flexural strength in addition to a higher Modulus of Elasticity. Additionally, UHPFRC is a light material compared to plain concrete and reinforced concrete, which can lead to significant savings in dead load thus saving in transport costs, material consumption together with faster

fabrication. However, there are limitations related to the use of UHPFRC, mainly its high cost compared to the standard concrete. According to the study of Cousins et al., (2008), it has been reported that the price of UHPFRC ranges from \$1829/m^3 to \$ 2222/m^3. The storage of the UHPFRC for at least 48 hours and applying heat treatment add to its initial cost. Furthermore, another limitation lies in the lack of design codes for structural applications (Hassan, 2013).

2. Constituents of UHPFRC

In this section, a brief description of the constituents of UHPFRC is given. These constituents are cement, aggregate, supplementary materials, superplasticizers, water and fibres.

2.1. *Cement*

Typically, UHPFRC contains between 700 - 1000kg/m^3 of cement which is twice the amount of cement for a conventional concrete. UHPFRC has a very low water to cement ratio therefore it is recommended to use Portland cement with low C_3S and low C_3A because of their low water demand. Types of cement that have been successfully used are CEM I 42.5, CEM II 52.5 and CEM III/B (Hassan, 2013).

2.2. *Aggregate*

According to Hassan, (2013), coarse aggregates have been replaced by fine aggregates to improve the compaction and reduce the permeability. Generally, the most suitable material is silica sand because of its fineness and high quartz content. Being rich in quartz helps the silica sand to react with $Ca(OH)_2$ from the hydration of cement to form calcium silicate which increases the strength of UHPFRC.

2.3. Supplementary cementitious materials

Supplementary cementitious materials are added to the mix in order to enhance the strength, durability and workability. Furthermore, they significantly reduce CO_2 emissions caused by the production of cement. Those materials include silica fume (SF), ground granulated blast furnace slag (GGBFS) and pulverised fuel ash (Hassan, 2013).

2.4. Superplasticizer

Superplasticizers are chemical additives that tend to reduce the water to cement ratio and produce a flowing concrete. Superplasticizers allow dispersing of the cement and silica fume particles and aid fibre distribution, which improve the mechanical properties significantly. For UHPFRC, the water to cement ratio is about 0.2, which is a low value. Types of superplasticizer include naphthalene sulfonate, melamine sulfonate and polycarboxylate polymer in liquid and powder forms. The polycarboxylate polymer in liquid form is the most common (Hassan, 2013).

2.5. Water

Water is an important ingredient in the mixture. Clean tap water is generally used for UHPFRC, as any organic contents tends to retard the setting and hardening (Hassan, 2013).

2.6. Fibres

Fibres constitute the main component of UHPFRC. They are available in many types of material such as steel, glass fibre, carbon fibre, aramid fibre, basalt fibre, polypropylene and polyethylene. However, the most common material used for UHPFRC is steel. The inclusion of steel fibres significantly improves the tensile behaviour as the fibres carry all the tension force once the matrix has cracked. Ideally, the optimum content of fibres is about 2% (Hassan, 2013).

3. Production of UHPFRC

There are three main phases to prepare a UHPFRC mix which are mixing, casting and curing. They are explained in details in this section.

3.1. Mixing

The first phase in preparing UHPFRC is to mix all the constituents together. Firstly, dry ingredients, which are cement, aggregate and supplementary cementitious materials, are mixed for 1 - 5 minutes.

Then, water and superplasticizers are added to the dry mix to transform it into a cement paste. This takes 5 - 10 minutes. Finally, steel fibres are added to the mix with care given to the dispersion of the fibres. A good mix is where fibres are evenly dispersed which is achieved by adding fibres very slowly. This process takes approximately 5 minutes (Ma et al. 2004).

3.2. Casting

The second phase to prepare UHPFRC is to cast the mix. The process is similar to casting plain concrete except that care has to be given to the direction of placing as this was reported to be crucial. It has been demonstrated that placing UHPFRC in the longitudinal direction of the specimen yields higher flexural strength compared to when it is placed transversely (Hassan, 2013).

3.3. Curing

The third and last phase is curing. According to the recommendations, members have to be cured at ambient temperature for 24 hours from initial settings (Graybeal, 2005). After demoulding, a thermal treatment is applied to the UHPFRC in order to allow the concrete to strengthen faster, to delay shrinkage and creep effects and to improve the durability.

4. Mechanical Properties

In this section, the mechanical properties of UHPFRC are explored in terms of compressive behaviour and tensile behaviour.

4.1. Compressive behaviour

The compressive behaviour is characterised by the compressive strength, the Elastic Modulus and the Poisson's Ratio. It has been reported by that for UHPFRC, the compressive strength is greater than 150MPa while it is less than 40MPa for normal concrete. The compressive strength depends significantly on the mix composition, type and duration of curing. In the UK, compression tests are carried out using 100mm and 150mm cube specimens. There are many standards that give guidelines on how the compression test is performed but the most recognised is BS-EN 12390-3.

The Elastic Modulus of UHPFRC ranges between 50 to 60GPa. It is higher compared to ordinary concrete where the Elastic Modulus ranges between 29 to 36GPa. It has been shown that the Elasticity Modulus depends highly on the curing regime. There are numerous standards and recommendations on how to determine the Modulus of Elasticity from a compression test such as (BS 1881-121 1983, BFUP AFGC 2002 and ASTM C469-02 2002).

Poisson's Ratio is an important parameter, particularly for civil engineering applications. For a plain concrete, this value is from 0.16 to 0.22 while for a UHPFRC, it ranges from 0.13 to 0.25. Generally, a value of 0.2 is admitted. Poisson's Ratio can be determined through compression and tensile testing or through non-destructive testing techniques (Hassan, 2013).

4.2. *Tensile Behaviour*

The tensile behaviour of UHPFRC is far much enhanced compared to plain concrete, which is in fact the main advantage of UHPFRC. The tensile behaviour is characterised by an elastic stage followed by a hardening stage where the micro cracks appears and the tensile strength and deformation keep increasing. The third stage is called strain softening, where a rapid deformation and a loss of strength occur. Tensile behaviour of UHPFRC is determined experimentally through direct and indirect tests. It has been reported that test methods yield variable values of tensile strength. The highest value reported ranges from 8 to 13.5MPa (Hassan, 2013)

5. Conclusion

The use of UHPFRC is a promising solution that was used in many applications ranging from highways to bridges. Particularly, in case of bund walls subjected to dynamic loads, the replacement of plain or reinforced concrete with UHPFRC would tend to mitigate the aftereffects of catastrophic failure since it was reported that UHPFRC has good impact resistance properties. In this paper, a review of UHPFRC has been given that included the development of UHPFRC over the years, its advantages, limitations, constituents, its production and its mechanical properties.

Acknowledgments
The authors would like to thank Liverpool John Moores University for the continuing financial support of this project.

References

Cousins, T. Roberts-Wollmann, C. & Sotelino, E. 2008. *UHPC deck panels for rapid bridge construction and long term durability*. Proceedings of the International Symposium on Ultra High Performance Concrete. Kassel, Germany. Kassel University Press GmbH, 699-705.

Graybeal, B. A. 2005. *Characterization of the behavior of ultra-high performance concrete*. PhD, University of Maryland**,** 360.

Habel, K.Charron, J. P.Braike, S.Hooton, R. D.Gauvreau, P. & Massicotte, B. 2008. *Ultra-high performance fibre reinforced concrete mix design in central Canada*. Canadian Journal of Civil Engineering, 35**,** 217-24.

Hassan, Aram Mohammad Tariq (2013) *Performance Fibre Reinforced Concrete for Highway Bridge Applications.* Ph.D. thesis, University of Liverpool.

Ma, J. Dehn, F. Tue, N. Orgass, M. & Schmidt, D. 2004. *Comparative investigations on ultra-high performance concrete with and without coarse aggregates.* Proceedings of the International Symposium on Ultra High Performance Concrete. Kassel, Germany. Kassel University Press GmbH, 205-12.

Goran Omer

Development of an electromagnetic sensor as an NDT method to assess the integrity of marine structures

G S Omer,M Riley,A Shaw,b Atherton,P Kot, M Magomed, J D Cullen
Built Environment and Sustainable Technologies research Centre (BEST), Liverpool John Moores University, Byrom Street, Liverpool, L3 3AF, UK
g.s.omer@2015.ljmu.ac.uk,M.L.Riley@ljmu.ac.uk,A.Shaw@ljmu.ac.uk, W.Atherton@ljmu.ac.uk, P.Kot@ljmu.ac.uk, M.Muradov@ljmu.ac.uk, J.D.Cullen@ljmu.ac.uk.

Abstract:

The main aim is to construct a novel Non –destructive electromagnetic (EM) wave sensor to determine the conditions of concrete structure, which may be affected by carbonation and chloride. More specifically focusing on structures in the marine environment and on highway structures. The specific objectives of the research investigate the feasibility of using sweeped electromagnetic waves and NDT method used to detect failure in concrete structures, analyse and evaluate the reinforcement materials. Examples include type and size of steel-reinforced concrete, evaluation of the concrete mixture for the types of aggregate gradation, and impact of different testing temperature. An initial preliminary experiment was undertaken to identify a curing process and drying process of UK mix ratio with limestone concrete type. The test of two concrete slabs was made for curing period of over 28 days by using EM wave and horn antenna. Two concrete slabs of size (250x250x60mm) were tested; one of them submerged in tap water and the other submerged in the Rock Salt water (NaCl) for over 28 days. The S-parameter measurements were recorded for both samples every 15 minutes during 28 days. The results demonstrated a noticeable change in EM signature, affected by absorbed amount of tap water and salt water in the concrete slab during curing period. Both samples remained untouched during the experimental work and factors contributing such as light and temperature remained constant during the test procedure. In conclusion, preliminary experiments prove that the electromagnetic waves at the frequency ranges between 2 and 13 GHz can be used to identify the concrete damage by penetrating water and chloride in real time measurements and in a non-destructive manner.

Key words: Electromagnetic wave; Horn Antenna; Microwaves; Concrete slab; Chloride

Introduction and background:

Reinforcement corrosion caused by the presence of chloride ions in the neighbourhood of the re-bars has been identified as one of the major causes of deterioration of concrete structures. The chlorides could find their way to concrete either as part of constituent materials when sea sand is used, or, by gradual permeation and diffusion as in the case of marine structures, or, cases where de-icing salts used to melt away snow on highways. Thus, determination of chloride content in a concrete structure is an important part of periodic non-destructive testing

carried out for structures identified to be vulnerable to chloride induced reinforcement corrosion [1]. In many concrete structures, chloride content caused reinforcement corrosion in the neighbourhood of the reinforcing bars is not almost contained from the beginning. In many concrete structures damaged by reinforcement corrosion caused by the present of chloride ions, chloride content around the reinforcing bar has reached sufficient chloride ions caused reinforcement corrosion by gradual permeation and diffusion from a surface of concrete as in the case of marine structures or, cases where de-icing salts are used to melt away snow on highways concrete mainly becomes contaminated due to chloride ions present in marine water or snow and ice. Then the process of deterioration of the corrosion continues based on the availability of moisture, oxygen and carbon dioxide and the presence of chloride ions in the concrete [2].

Carbonation occurs when carbon dioxide from the air enters the concrete and reacts with hydroxides, such as calcium hydroxide, to form carbonates. In the reaction with calcium hydroxide, calcium carbonate is produced: $Ca(OH)2 + CO2 \rightarrow CaCO3 + H2O$ [3].Then this response decreases the concrete pH to as low as 8.5, at the level that the passive film on the steel is not steady. In good-quality concrete carbonation, the process is usually slow; it has been estimated that carbonation will proceed at a rate of up to 0.04 inches per year. Concrete structures in marine environments such as bridge substructure elements come directly under the exposure category[4]. Three areas of concrete structures in marine environments can be distinguished regarding corrosion: the submerged zone (always below seawater), the splash and tidal zone (Intermittently wet and dry) and the atmospheric zone (well above mean high tide and infrequently wetted)[5].

Microwaves have been identified as being sensitive to moisture content. For non-destructive testing, many applications for moisture determination use the microwave method. In the microwave technique, valuable information about the permittivity of the sample [4] is known. As water has high a microwave frequency compared to dry materials, it is easily measured using the technique. Other apparatus able to measure moisture content can be destructive for building fabrics such as bricks, concrete, blocks, plaster, etc., as they require additional drilling into the wall to take a sample of the content. Furthermore, these types of methods provide inexact results. The Compton provides enhanced results scattering of gamma ray's method [6].

Moreover, it is even more essential for inspection methods to spread electromagnetic (EM) waves through the structure and determine building fabric failures, such as concrete flat roof membrane failure, marine structures. Research has been undertaken in developing a novel method that would use EM waves to resolve the problems mentioned above. Different ranges of EM waves were used for testing as well as horn antennae, which will be used to identify the best parameters to provide accurate measurements [7].

Methodology and Results:

At present, most of the highway concrete structures and marine structures getting damaged during the high chloride and carbonations reduces the pH level of the concrete when oxygen, chlorides, and moisture all penetrate the concrete, because of they are build exposed to the sea water and spreading de-icing salt in the winter time on the highway. The developing of novelty of using Microwave spectroscopy to determine the chloride and carbonations of the concrete structure in real time and in non-destructive manner. The horn antenna will assist to identify the location of the reinforcement in the concrete structures. Horn antenna has been design to be able to carry out many measurements without being worried with its displacement. The sensor frame had two calibrated displacement transducers attached, which assist clarification of the distance between the antenna and the surface of the concrete sample. A final displacement transducer was located between the antennas to calculate their angle. In addition, the sensor designed operates in frequency ranges between (1.5 to 18 GHz) and the measurements were provided by s-parameters namely S_{11} or S_{21}.The design sensor as shown in figure 1. The following figure 2 and 3 shows the full experiment setup during the sample test.

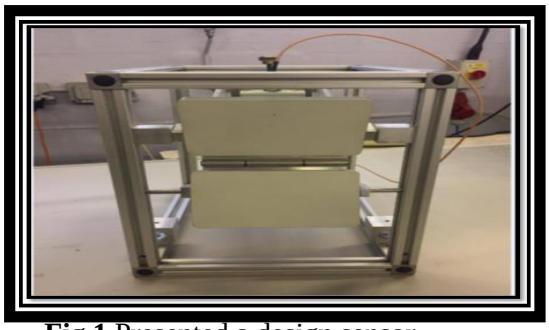

Fig.1 Presented a design sensor.

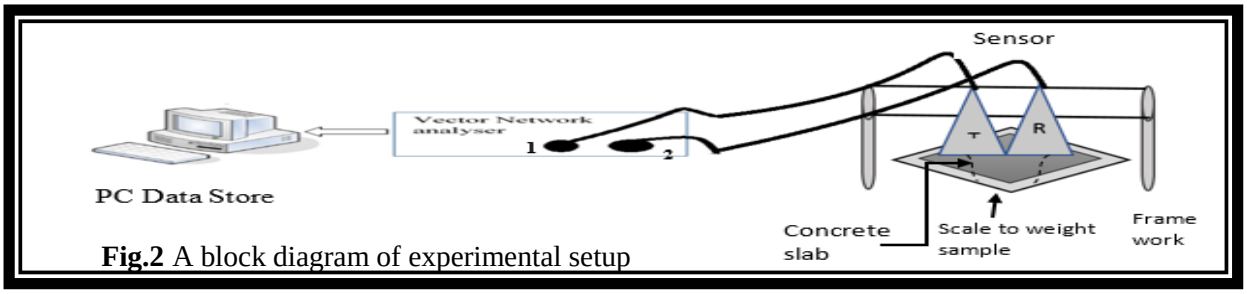

Fig.2 A block diagram of experimental setup

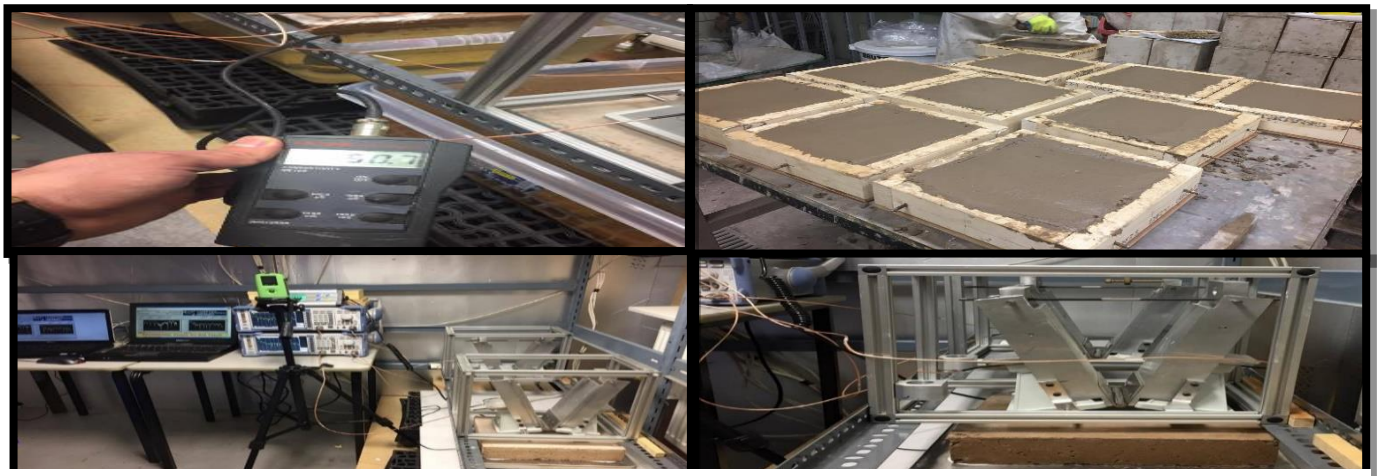

Fig. 3 Preliminary experiment setup of the drying process of concrete sample for over 72 hours.

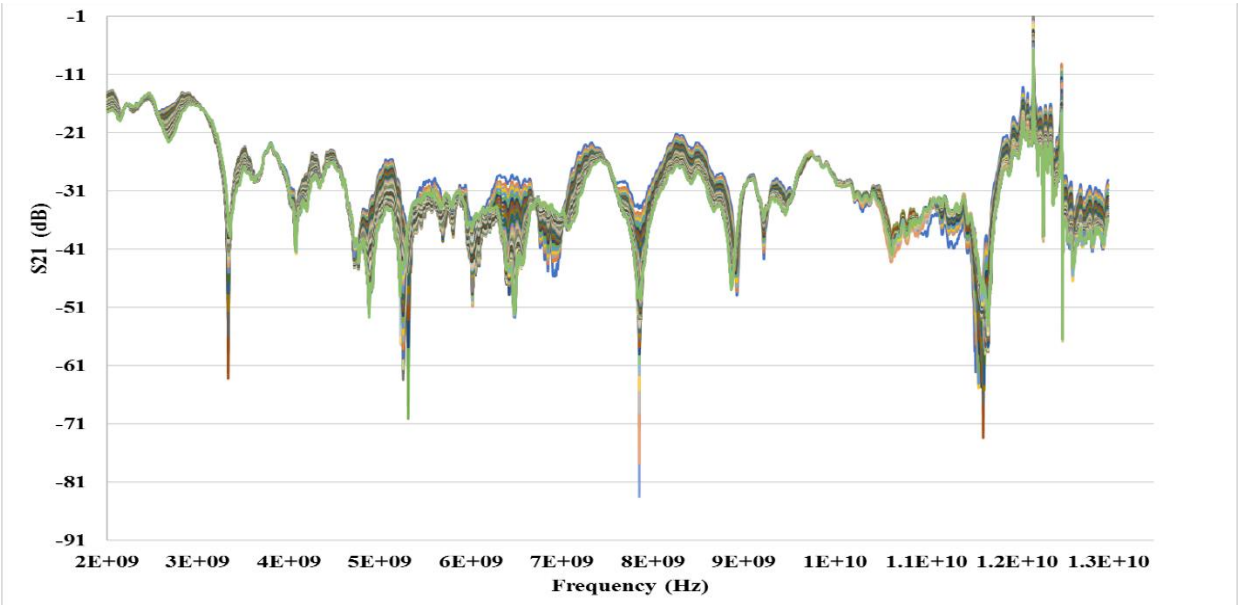

Fig.4 UK concrete mix ratio with limestone drying process over 72 hours

Figure 4 shows the S21 measurements of the concrete cube taken everyone minutes during 72 hours. It can be seen that there are a noticeable change in EM signature. The changes are supposed to be caused by the decreasing amount of salt water in the concrete cubes.

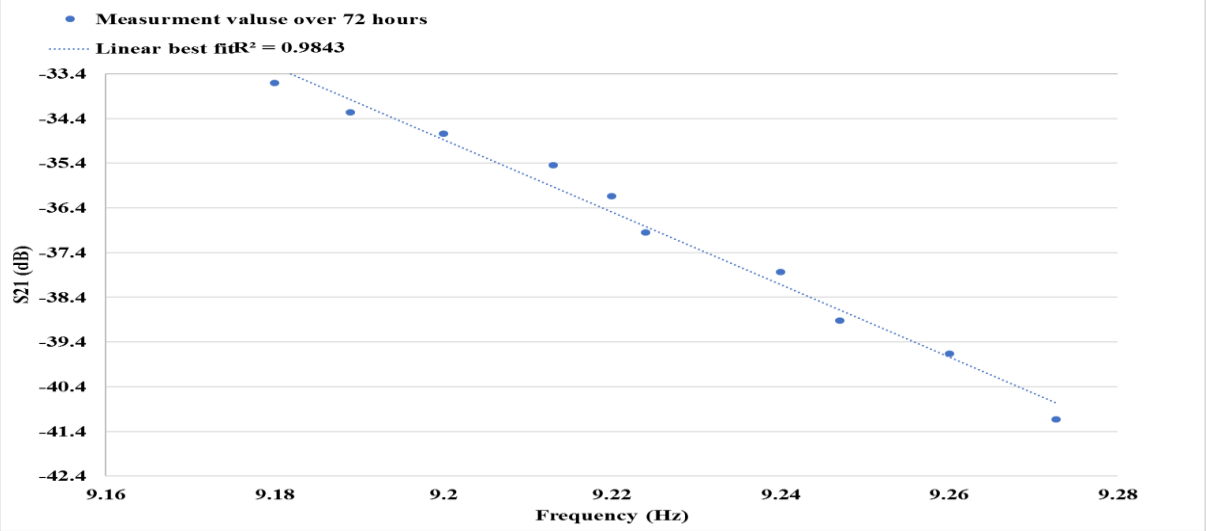

Fig.5 Linear best fit (R^2=0.98)

Figure 5 shows the linear best fit at 6.83GHz over 72 hours weight loss. R^2=0.98 which is the reasonable accurate results for correlations between S_{21} parameter and chloride and moisture loss in concrete slab.

Conclusions and Future work: Preliminary experiments provide capable results that the electromagnetic waves at frequency ranges between (1.5 to 13.0GHz) can be used to investigate chloride content in marine concrete structures in real time measurement's and in non-destructive manner. Future work will test concrete structures, by exiting method and comparing it with the innovative technology method and do some more experiment test at different temperature conditions.

References:

1. Spitzlei, M., *Choosing a Method for Measuring youir Materials Moisture content*, in *Article*. 2002. p. 1-9.
2. Zhou, Y., et al., *Carbonation-Induced and Chloride-Induced Corrosion in Reinforced Concrete Structures.* Journal of Materials in Civil Engineering, 2015. **27**(9): p. 04014245.
3. Bioubakhsh, S., *The penetration of chloride in concrete subject to wetting and drying*, in *Faculty of the Built Environment*. 2011, Univerity College London: UCL (University College London). p. 355.
4. Verma, S.K., S.S. Bhadauria, and S. Akhtar, *Review of Nondestructive Testing Methods for Condition Monitoring of Concrete Structures.* Journal of Construction Engineering, 2013. **2013**: p. 1-11.
5. Humphreys, M., et al., *Strategies for Minimising the Whole of Life Cycle Cost of Reinforced Concrete Brodge Exposed to Aggressive Environments.* Report, 2008: p. 1-12.
6. Bucuresu, D., *NON- destructive measurment of Moisture in Building Materials by Compton Scattering og Gamma Rays.* 2011. **63**(1): p. 61-75.
7. Bavusi, M., et al., *Electromagnetic Sensing Techniques for Non-Destructive Diagnosis of Civil Engineering Structures.* 2012.

Khalid Hashim

Influence of interaction between organic matter and dyes on the performance of electrocoagulation units- Experimental, economic, and statistical approach

Khalid S. Hashim [1,2], Andy Shaw[1], Rafid Alkhaddar[1], Montserrat Ortoneda Pedrola[1], and David Phipps[1]

[1] Department of Civil Engineering, Liverpool John Moores University, UK.

[2] Department of Environment Engineering, Babylon University, Iraq.

Abstract

A comprehensive study has been carried out to assess the influence of organic matter (ethylenediaminetetraacetic acid (EDTA)) on the removal of industrial dyes (methylene blue as a model dye) from water using the electrocoagulation (EC) method. This includes an investigation of the influence organic matter on dye removal from water using a flow column EC cell (FCEC), the preliminary operating cost and energy consumption of the FCEC. Additionally, this study includes measurement of the produced amount of hydrogen gas (H_2) from FCER, and an SEM (scanning electron microscopy) investigation of the influence of the EC process on the morphology of the surface of the aluminium electrodes. A statistical analysis was conducted to compare the influence of key operational parameters, such as initial pH, electrolysing time, and current density on dye removal.

The results obtained showed that the presence of 50 mg/L of EDTA increased the residual dye concentration by 0.8 mg/L, and increased the operating cost by 9%. Additionally, it was found that FCER emits, during the removal of methylene blue dye, 0.005 mole of H_2 gas. Statistically, the influence of operating parameters on MB dye removal followed the order: EDTA> CD > IED > pH. The obtained SEM images showed a large number dents on anode's surface due to the production of aluminium hydroxides.

Keywords: organic matter, methylene blue dye, electrocoagulation, statistical analysis.

1. Introduction

The textile industry plays a central role in the European economy as it accommodates 267,000 companies and about 6.3% of the European employers in 2008 (Lotito *et al.*, 2014). Additionally, it accounted for about 3.6% of the EU-27 manufacturing in terms of value added.
However, the textile industry produces huge volumes of heavily polluted wastewater, due to the high consumption of huge quantities of water and chemicals, which in turn represents a serious environmental issue (Bechtold *et al.*, 2006). For instance, it has been reported that the textile industry requires 0.1 - 0.2 m^3 of water to produce 1 kg of products, which in turn results in thousands cubic meters of dyes containing wastewater (Lotito *et al.*, 2014; Joshi and Mhatre, 2015). Moreover, textile companies annually consumed, on a global scale, bout 700000 tons of 1000 different kinds of dyes and pigments, about 12 to 45 % of this vast amount of dyes will be discharged to the water bodies (De Jager *et al.*, 2014; Sharma *et al.*, 2016). Discharging this dyes containing wastewater into the water bodies creates undesirable colours and odours (Fu *et al.*, 2010); limits sun light penetration that

seriously damages the aquatic life (Santos and Boaventura, 2015); and decreases the concentration of the dissolved oxygen (Firmino *et al.*, 2010). Furthermore, decomposition products of azo dyes are carcinogenic and have long half-time life, for instance, the hydrolysed dye RB-19 has a half-time life of 46 years at pH of 7 and temperature of 25 ^{0}C (Firmino *et al.*, 2010; Gole and Gogate, 2014; Joshi and Mhatre, 2015).

Therefore, a wide spectrum of treatment methods were used to remove dyes from water, such as reverse osmosis, filtration, aerobic and anaerobic degradation, and chemical oxidation (Mahmoud *et al.*, 2012; Gole and Gogate, 2014). However, most these conventional treatment techniques are not efficient to remove azo dyes (Aşçı *et al.*, 2015; Hayat *et al.*, 2015). More importantly, using some of these conventional techniques to remove azo dyes results in the formation of carcinogenic compounds (Aravind *et al.*, 2016), for instance, biological reduction of azo dyes under anaerobic conditions leads to cleave the nitrogen double bonds resulting in formation of aromatic amines, which categorised as carcinogens (Lourenço *et al.*, 2015).

In consideration of the environmentally negative impacts of the wastewater of the textile industry and the drawbacks of the conventional treatment techniques, there is a serious need for efficient, cost-effective, and environmentally friendly treatment method. In this context, a number of separated or integrated treatment methods were recently suggested and applied to treat the effluents of the textile industries, such adsorption by treated char (Mahmoud *et al.*, 2012), nano-filtration (Ong *et al.*, 2014), membrane bioreactor-ultrafiltration (De Jager *et al.*, 2014), and electrocoagulation (Vidal *et al.*, 2016). Amongst these new techniques, electrocoagulation method (EC) received a wide interest over the last few years as it poses solely advantages, for instance it can simultaneously remove different pollutants at relatively short treatment time, reduce the sludge volume, and it eliminates the need chemical additives (Safari *et al.*, 2015; Elabbas *et al.*, 2016). Additionally, the production of hydrogen gas during the performance of the EC units, which can be collected and reused as eco-friendly fuel (Lakshmi *et al.*, 2013). However, the performance of this method is highly influenced by several operating parameters such as the as the chemistry of the solution being treated, initial pH, and gap between electrodes (Wan *et al.*, 2011; Hashim *et al.*, 2015).

In this context, this study has been devoted to investigate the presence of organic matter on the performance of the EC units in terms of dye removal and energy consumption. In this investigation, methylene blue dye (MB dye) was chosen as the model dye because it is a hazard and toxic substance that causes skin irritation, permanent eye injury to the eyes, and its degradation forms toxic compounds (Golder *et al.*, 2005; Mahmoud *et al.*, 2013; Asghari *et al.*, 2012; Riyanto and Mawazi, 2015). The molecular structure of MB dye is shown in Figure (1).

2. Experimental

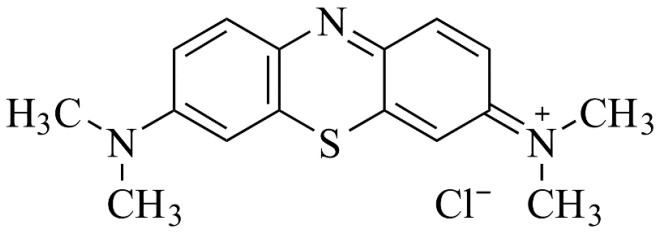

Figure (1): Molecular structure of MB dye, (Samide *et al.*, 2014)

2.1. Material and methods

Synthetic drinking water stock solution, 100 mg/l, used in the present study was prepared using deionised water and MB dye supplied by Sigma Aldrich. Samples with less MB dye concentrations (10 to 25), diluted from this stock solution, were treated at different current densities (1 to 3 mA/cm^2), initial pHs (4 to 8), and inter-electrodes distances (5, 10, and 15 mm). The initial pH value was

adjusted to the desire level by using 1 M HCl or 1 M NaOH solutions, while the current density was driven from a DC rectifier (HQ Power; Model: PS 3010, 0-10 A, 0–30 V). Water conductivity was kept constant at 0.32 µS/cm using a proper amount of NaCl. A Hanna meter (Model: HI 98130) was used to measure both water conductivity and pH values.
After the optimisation of the influence of the mentioned key operating parameters, the influence organic matter on dye removal was investigated by electrolysing EDTA-MB dye compound containing water samples.
To prepare EDTA-MB dye compound, 50 mg of EDTA were added to 1000 mL of pre-prepared MB dye stock solution (with MB dye concentration of 15 mg/L) and stirred for 5 min to ensure a homogenous distribution of contents; then stored (refrigerated) for the next use. EDTA-MB dye compound containing solution was electrolysed under the optimum operating conditions that obtained from MB dye removal experiments (i.e., for 30 min at a CD of 2 mA/cm^2 , initial pH of 6, and IED of 5 mm). It is noteworthy to mention that EDTA has been selected as an OM because it is widely used in different industrial and domestic applications (such as detergents, painting, fertilisers, printed circuit boards, herbicides, and photography and surface treatment industries); thus, it highly expected to find EDTA in industrial effluents (Lin *et al.*, 2015; Babay *et al.*, 2001).
The progress of MB dye removal was monitored by collecting 10 mL samples from the reactor at 5 min intervals during the course of experiments. These samples were filtered with 0.45 µm filters (supplied by Sigma-Aldrich) to remove undesirable solids; then the residual concentration of MB dye in filtrate was measured using a Hach Lange spectrophotometer (Model DR 2800). All experiments were carried out at room temperature (20 ±1^{0}C).
Dye removal efficiency (RE %) was determined as follows:

$$RE\% = \frac{C_0 - C}{C} \times 100\% \quad \textbf{(1)}$$

Where C_0 and C are the influent and effluent concentrations of MB dye, in mg/L, respectively. While, the energy consumption (E) was determined using the following formula (Un *et al.*, 2013b):

$$E = \frac{I * V * T}{Vol.} \quad \textbf{(2)}$$

Where *E* is the electrical energy consumption (kWh/m^3), *I* is the current (A), *V* is the potential (V), *t* is the electrolysis time (hrs), and *Vol.* is the volume of solution (m^3).
Statistically, the influence of each individual operating parameter on dye removal is measured by determining its Beta value. The latter is a measure of how strongly each parameter influences the modelling of removal process (Tabachnick and Fidell, 2001; Pallant, 2005; Field, 2008). The higher the absolute beta value is, the stronger the influence of the parameter (Pallant, 2005). In this study, SPSS-23 package was used to analyse the obtained data.

2.2. EC reactor

The decolourisation process was conducted using a new cylindrical EC reactor (figure 2). This new EC reactor uses a perforated-plate flow column to enhance water mixing process that increase the collision rate between coagulants and pollutants, which in turn enhances the removal efficiency. Hashim *et al.* (2015) presented more details about this reactor.

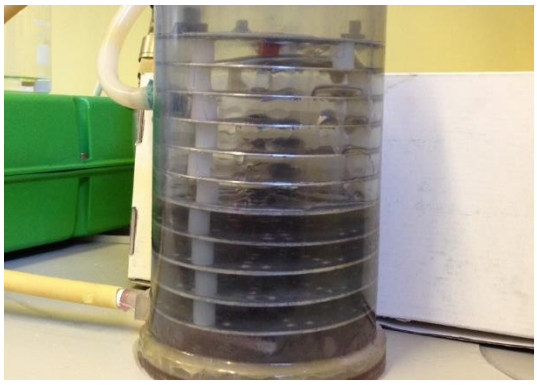

Figure 5: *The new EC reactor.*

3. Results and discussion

3.1 Influence of initial pH on dye removal

pH is used as a measure of hydrogen ions' concentration (H^+), and it can be calculated by the negative logarithm of the concentration of H^+ ions (Lim, 2006). This parameter significantly influences the performance of EC units as it governs the speciation of aluminium hydroxides (Emamjomeh and Sivakumar, 2009; García-García *et al.*, 2015).

To investigate the influence of the initial pH on MB dye removal, sets of batch experiments were commenced by adjusting the initial pH of synthetic water samples to the required value (from 4 to 8) using 1 M HCl or 1 M NaOH solutions. While the initial MB dye concentration, current density (CD), and inter-electrodes distance (IED) were kept constant at 15 mg/L, 2 mA/cm^2, and 1 mm respectively. Figure 2 shows that, after 20 minutes of electrolysis, the residual MB dye concentration decreased gradually as the initial pH increased from 4 to 7 to reach its minimum level, about 0.5 mg/l, at a pH of 7. Then, an increase was observed as the initial pH increased from 7 to 8. This change of MB dye removal with the initial pH could be mainly attributed to the predominant species of aluminium, where in alkaline and acidic conditions; the prevailing species have low adsorption capacity. While, in the neutral or slight alkaline range of pH, the predominant species have high adsorption capacity (Ghosh *et al.*, 2008a; Emamjomeh and Sivakumar, 2009; Un *et al.*, 2013a).

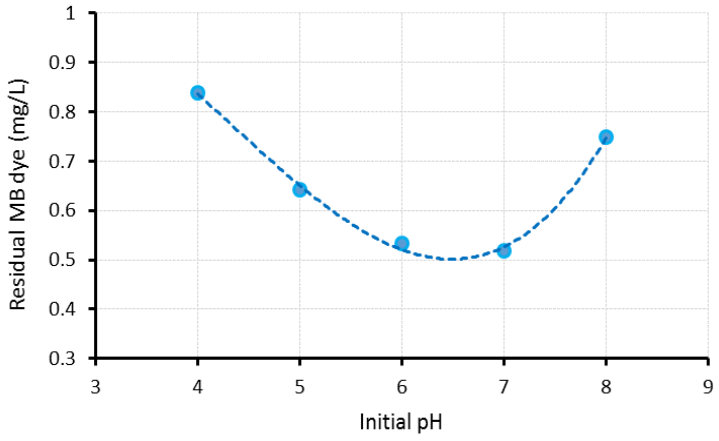

Figure 6: *Effect of initial pH on MB dye removal.*

Thus, in the current project, the rest of the experiments were carried out at an initial pH of 7.

3.2 Influence of inter-electrodes distance (IED) on dye removal

To explore the influence of the IED on MB dye removal efficiency, several synthetic water samples containing 15 mg/L of MB dye were electrolysed at different IEDs (5, 10, and 15 mm). The electrocoagulation experiments were carried out at constant water flow rate of 1 L/h, initial pH of 7,

and CD of 2 mA/cm^2. The obtained results, Figure 3-A, indicated that the wider the IED was, the lower the removal efficiency was. For instance, after 30 min of electrolysing, the residual MB dye concentration increased from about 0.5 to 0.85 mg/L as the IED increased from 5 to 20 mm respectively.

This behaviour could be attributed to two reasons, firstly; increasing electrodes spacing promotes the formation the metallic anodic film that reduces melting rate of the anode, which in turn slow down the removal rate (MAMERI *et al.*, 1998; Ghosh *et al.*, 2008b). Secondly, widening the gap between the electrodes results in decreasing the electrostatic attraction force that decreases flocs formation, and consequently reduces removal efficiency (Khandegar and Saroha, 2013).
In addition, the energy consumption of the EC cells is significantly influenced by the IED as the latter determines the ohmic potential drop of the EC unit (Ghosh *et al.*, 2008b; Un *et al.*, 2013b).
Thus, the influence of the IED on energy consumption, in the present study, was explored by electrolysing synthetic water samples containing 15 mg/L of MB dye at three different IEDs (5, 15, and 20 mm) while the CD, and initial pH were kept constant at 2 mA/cm^2, and 7 respectively.
The obtained results indicated that the energy consumption increased as the IED increased, Figure 3-B. It can be seen that the energy consumption increased from 6.3 kW.h/m^3 at IED of 5 mm to about 12.1 kW.h/m^3 at IED of 15 mm. This could be explained, as mentioned before, by the decrease of water conductivity as the IED increased, which increases the energy consumption. Furthermore, widening the IED promotes the growth of the metallic film on the surface of anode, which in turn increases the energy consumption (Ghosh *et al.*, 2008b).

3.3. Influence of the current density (CD) on dye removal

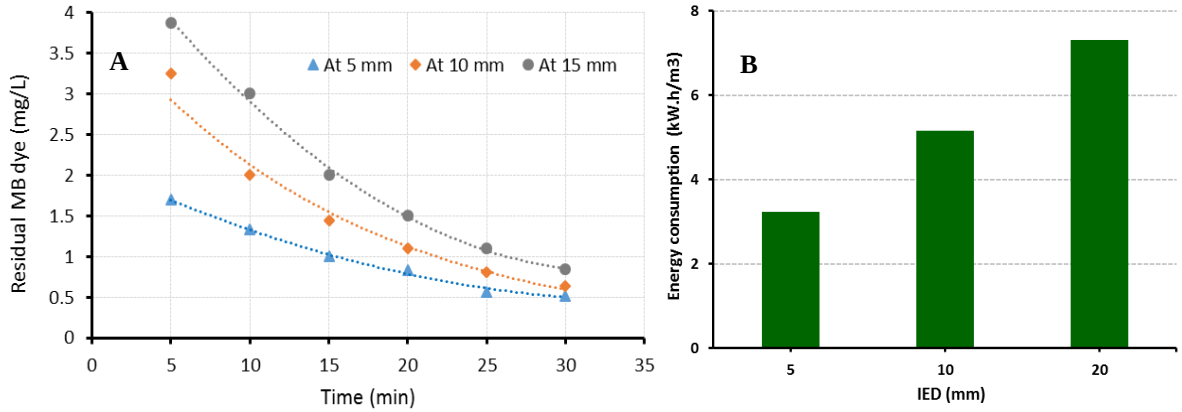

Figure 7: *Influence of the IED on: A) the removal of MB dye, B) energy consumption.*

Faraday's Law (Eq. 3) highlights a fact that the CD highly influences the coagulant dosage and the removal efficiency in consequence.

$$X = \frac{(I)(t)(m)}{(Z)(F)} \quad (3)$$

X is the released coagulants from the anode (g), *I* the applied current in amperes, *t* electrolysis time (second), *M* is the molecular weight (26.98 g/mol), *Z* the number of electron, and *F* is Faraday's constant (96487 C/mol).
Moreover, the CD determines other parameters that can influence the performance of the EC units such as the floc's growth and size and generation rate of bubbles (Un *et al.*, 2009; Gao *et al.*, 2010; Phadke, 2014).
The influence of CD on iron removal was investigated by the electrolysis of several 15 mg/L MB dye containing water samples at different CDs (1, 2, and 3 mA/cm^2), when the initial pH, and IED were kept constant at 7 and 5 mm, respectively.
The obtained results, Figure 4-(A), indicated that the higher CD was, the more rapid the MB dye removal was. Where, it can be seen from this figure that, after 30 min of electrolysis, the residual MB dye concentration decreased from 0.64 to 0.2 mg/L as the CD increased from 1 to 3 mA/cm^2,

respectively. This could be attributed, according to Faraday's Law, to the fact that the dissolved coagulants increased as the CD increased. As the coagulants increased, the number of available active sites increased correspondingly, and enhanced MB dye removal as a consequence (Zhu *et al.*, 2007; Chaturvedi and Dave, 2012).
However, Figure 4-(B) shows that when CD increased from 1to 3 mA/cm^2, the energy consumption significantly increased from 1.32 to 6.65 kWh/m^3, respectively.
Thus, in this investigation, it might be reasonable to infer that the CD of 2 mA/cm^2 is the best value to commence the rest of experiments.
According to the results obtained from the previous part of the current study, the best MB dye removal efficiency , using the new EC reactor, could be achieved at a CD of 2 mA/cm^2 , initial pH of 6, IED of 5 mm, and treatment time of 30 min. Thus, these values will be used to investigate the

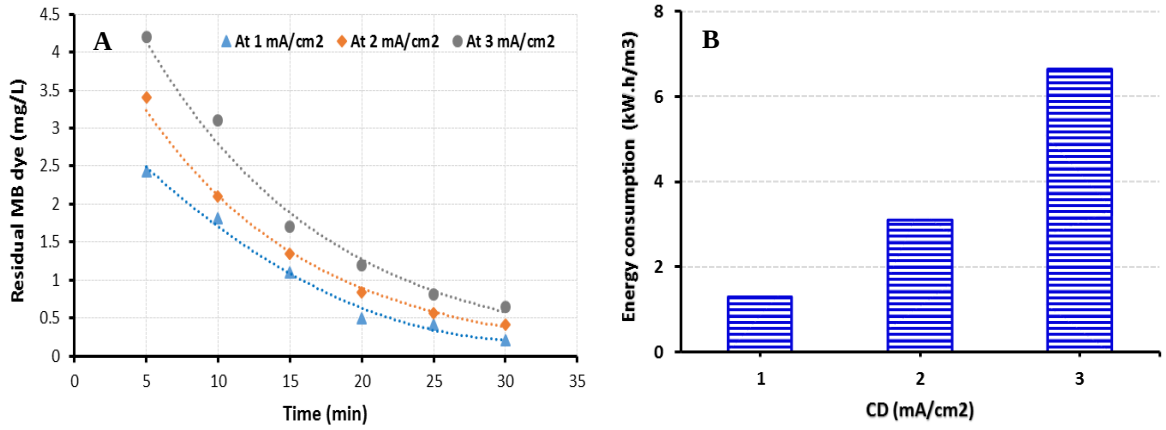

Figure 8: *Effects of CD on: (A) MB dye removal, (B) Energy consumption.*

influence of organic matter on MB dye removal from water.

3.4. Influence of organic matter (OM) on dye removal

This part of the study is a central phase as it deals with the experimental proving of the existence of the targeted problem, which is the influence of OM on industrial dyes removal by the EC method.
To investigate the influence of OM on dye removal, EDTA-MB dye compound containing solution was electrolysed under the optimum operating conditions that obtained from MB dye removal experiments (i.e., for 30 min at a CD of 2 mA/cm^2 , initial pH of 6, and IED of 5 mm).
Figure 5 represents experimental evidence on the significant influence of OM on the ability of the EC units to remove industrial dyes from water, where, it can be clearly seen from this figure that the residual MB dye concentration increased from 0.5 to 1.3 mg/L as the concentration of EDTA increased from 0 to 50 mg/L, respectively. Furthermore, it was noticed that adding 50 mg/L of EDTA increased the energy consumption by 7%.

The negative influence of EDTA on removal efficiency could be attributed mainly to the ability of EDTA to compete for active adsorption sites on flocs, decreasing the removal of the targeted pollutants (Matilainen *et al.*, 2010; Mohora *et al.*, 2014). Additionally, OM promotes the growth of the passive oxide film on the anode that decreases the number of the liberated ions, and consequently minimises the removal efficiency (Khandegar and Saroha, 2013; Mohora *et al.*, 2014).

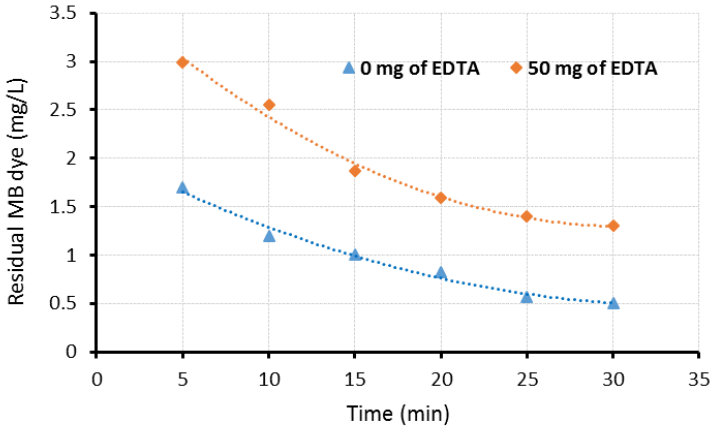

Figure 9: *Influence of OM (EDTA) on MB dye removal.*

3.5. Operating cost (OC)

Operating cost is an essential parameter in any treatment method as it determines the applicability of that method. The operating cost for MB dye removal from water has been calculated according to the unit prices of the Iraqi market in December 2016 (2.5 pence/kWh of electricity, and 1.53$/kg of aluminium).

The magnitude of the consumed energy, according to Eq. 2, was 3.3 kWh/m^3. While, the consumed amount of material of electrodes was calculated using Faraday's Law (Eq. 3).

$$X = \frac{(I)(t)(m)}{(Z)(F)} \quad (3)$$

X is the released coagulants from the anode (g), *I* the applied current in amperes, *t* electrolysis time (second), *M* is the molecular weight (26.98 g/mol), *Z* the number of electron, and *F* is Faraday's constant (96487 C/mol).

Then, the minimum cost for MB dye removal has been calculated according to the following equation (Kobya *et al.*, 2009; Ozyonar and Karagozoglu, 2011):

$$OC = C_{energy} + C_{electrode} \quad (4)$$

Where C_{energy} (kWh/m^3), and $C_{electrode}$ (kg of Al /m^3) are the consumed quantities of energy and material of electrodes per cubic meter of water.

The results obtained from this preliminary economic study indicated that the presence of OM increased the operating cost for MB dye removal from 0.2 to about 2.2 US $/m^3.

3.6. Estimating the produced hydrogen gas and the yieldable energy from this gas

The quantification of H_2 gas emission from the FCER, during the electrolysis of iron containing water, was carried out using the following formula (Phalakornkule *et al.*, 2010):

$$Q_{H_2} = \frac{CD \,.\, A \,.\, t \,.\, H}{F} \quad (5)$$

Where, Q_{H_2}, CD, A, t, H, and F are the quantity of the emitted amount of H_2 gas (mole), applied current density in (A/m^2), effective surface area of electrodes (m^2), treatment time (sec), number of hydrogen molecules (1/2), and Faraday's constant (96,500), respectively.

According to the results obtained from experimental work, the required electrolysis time to remove 15 mg/L of MB dye from water, at CD of 2 mA/cm^2, is about 30 min. Therefore, the produced amount of H_2 gas is:

$$Q_{H_2} = \frac{2 * 0.0284 * 30 * 60 * 0.5}{96500} = 0.0053 \text{ mole}$$

In fact, according to these results, the harvested amount of H_2 gas from filed-scale EC plants could be used to generate a considerable amount of energy.

3.7. Scanning electron microscopy characterisation of electrodes

In order to investigate the influence of the EC process on the morphology of anode surface, SEM images of aluminium anode, before and after EC process, were obtained. The generated images, indicated that the virgin anode surface was uniform and homogenous except small scratches (Figure 6-(A)), which could have happened due to mechanical handling of metal during electrode shaping process. Figure 6-(B) shows the same anode after a series of EC experiments. The anode surface became inhomogeneous, with several dents. This could be attributed to the consumption of anode material at the active sites where the anode dissolution results in the generation of aluminium hydroxides (coagulation ions) (Ahlawat *et al.*, 2008; Vasudevan *et al.*, 2012).

3.8. Statistical analysis of the influence of each operating parameter.

As it has been mentioned before, the statistical significance of each operating parameter determines whether this parameter exerts an important or negligible influence on the removal process.

Beta values for the studied parameters have been calculated in order to measure how strongly each

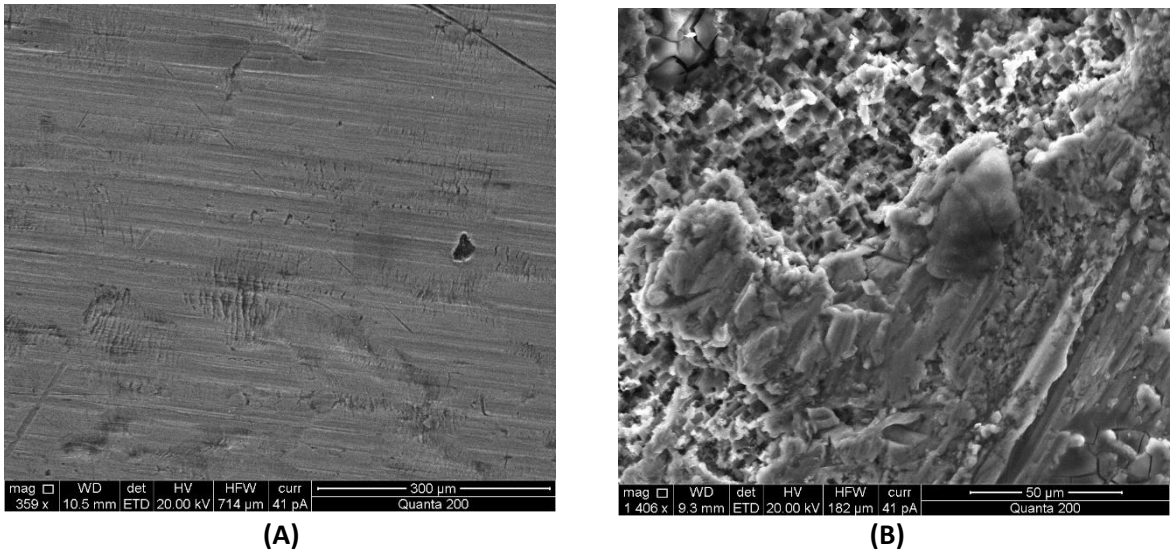

Figure 10: *SEM images of aluminium anode, (A) before EC process, and (B) After EC process*

parameter influences MB dye removal. Results obtained showed that the influence of the studied operating parameters followed the order: EDTA > CD > IED > pH.

4. Conclusion

The current study was commenced to show that the presence of OM significantly influences the performance of EC cells in terms of industrial dye removal from water. In this study, a new EC reactor, FCER, has been applied to remove MB dye from water, in the presence of EDTA as OM,

taking into consideration the influence of key operating parameters. The obtained results showed that MB dye removal is reversely proportional to the presence of OM, and the magnitude of IED. Contrarily, the coagulants produced from the sacrificial anode is proportional to combination of both CD and electrolysis duration, which enhances MB dye removal. In addition, it was found that the EC process generates a considerable amount of H_2 gas that could be used as an eco-friendly fuel in different applications.

Statistically, it has been found that the EDTA concentration plays the highest influence on MB dye removal, while the initial pH has the lowest influence on dye removal.

For future work, the new EC reactor should be used to remove other pollutants, such as arsenic and nitrate, from water and wastewater. Additionally, an SEM investigation should be carried out to characterise the produced sludge from this new reactor, which will further enlighten on the reactions taken place.

References

Ahlawat, R., Srivastava, V. C., Mall, I. D.and Sinha, S. 2008. Investigation of the Electrocoagulation Treatment of Cotton Blue Dye Solution using Aluminium Electrodes. *CLEAN - Soil, Air, Water,* 36**,** 863-869.

Aravind, P., Subramanyan, V., Ferro, S.and Gopalakrishnan, R. 2016. Eco-friendly and facile integrated biological-cum-photo assisted electrooxidation process for degradation of textile wastewater. *Water Res,* 93**,** 230-41.

Aşçı, Y., Demirtas, E. A., Iscen, C. F.and Anagun, A. S. 2015. A statistical experimental design to determine the azo dye decolorization and degradation by the heterogeneous fenton process. *Fresenius Environmental Bulletin,* 24**,** 3717-3726.

Asghari, A., Kamalabadi, M.and Farzinia, H. 2012. Electrochemical Removal of Methylene Blue from Aqueous Solutions Using Taguchi Experimental Design. *Chemical and biochemical engineering quarterly* 26**,** 145-154.

Babay, P. A., Emilio, C. A., Ferreyra, R. E., Gautier, E. A., Gettar, R. T.and Litter, M. I. 2001. Kinetics and mechanisms of EDTA photocatalytic degradation with TiO2 under different experimental conditions. *International Journal of Photoenergy,* 3**,** 193-199.

Bechtold, T., Burtscher, E.and Hung, Y.-T. 2006. Treatment of Textile Wastes. In: Wang, L.K., Hung, Y-T., Lo, H.H., Yapijakis, C., Handbook of Industrial and Hazardous Wastes Treatment, Second Ed. Marcel Dekker Inc., New York, pp. 400-440.

Chaturvedi, S.and Dave, P. N. 2012. Removal of iron for safe drinking water. *Desalination,* 303**,** 1-11.

De Jager, D., Sheldon, M. S.and Edwards, W. 2014. Colour removal from textile wastewater using a pilot-scale dual-stage MBR and subsequent RO system. *Separation and Purification Technology,* 135**,** 135-144.

Elabbas, S., Ouazzani, N., Mandi, L., Berrekhis, F., Perdicakis, M., Pontvianne, S., Pons, M. N., Lapicque, F.and Leclerc, J. P. 2016. Treatment of highly concentrated tannery wastewater using electrocoagulation: Influence of the quality of aluminium used for the electrode. *J Hazard Mater*.

Emamjomeh, M. M.and Sivakumar, M. 2009. Fluoride removal by a continuous flow electrocoagulation reactor. *J Environ Manage,* 90**,** 1204-12.

Field, A. 2008. *Multiple regression using SPSS. Research Methods in Psychology,* C8057, pp.1-11.

Firmino, P. I., Da Silva, M. E., Cervantes, F. J.and Dos Santos, A. B. 2010. Colour removal of dyes from synthetic and real textile wastewaters in one- and two-stage anaerobic systems. *Bioresour Technol,* 101**,** 7773-9.

Fu, J., Wen, T., Wang, Q., Zhang, X. W., Zeng, Q. F., An, S. Q.and Zhu, H. L. 2010. Degradation of Active Brilliant Red X-3B by a microwave discharge electrodeless lamp in the presence of activated carbon. *Environ Technol,* 31**,** 771-9.

Gao, S., Yang, J., Tian, J., Ma, F., Tu, G.and Du, M. 2010. Electro-coagulation-flotation process for algae removal. *J Hazard Mater,* 177**,** 336-43.

García-García, A., Martínez-Miranda, V., Martínez-Cienfuegos, I. G., Almazán-Sánchez, P. T., Castañeda-Juárez, M.and Linares-Hernández, I. 2015. Industrial wastewater treatment by electrocoagulation–electrooxidation processes powered by solar cells. *Fuel,* 149**,** 46-54.

Ghosh, D., H. Solankiand Purkait, M. K. 2008a. Removal of Fe(II) from tap water by electrocoagulation technique. *J Hazard Mater,* 155**,** 135-43.
Ghosh, D., Solanki, H.and Purkait, M. K. 2008b. Removal of Fe(II) from tap water by electrocoagulation technique. *J Hazard Mater,* 155**,** 135-43.
Golder, A. K., Hridaya, N., Samanta, A. N.and Ray, S. 2005. Electrocoagulation of methylene blue and eosin yellowish using mild steel electrodes. *J Hazard Mater,* 127**,** 134-40.
Gole, V. L.and Gogate, P. R. 2014. Degradation of brilliant green dye using combined treatment strategies based on different irradiations. *Separation and Purification Technology,* 133**,** 212-220.
Hashim, K. S., Shaw, A., Alkhaddar, R.and Montserrat, O. P., 2015. An innovative use of flow columns in electrocoagulation reactor to enhance the water mixing process. *12th International Post-Graduate Research Conference*. Salford University, UK.
Hayat, H., Mahmood, Q., Pervez, A., Bhatti, Z. A.and Baig, S. A. 2015. Comparative decolorization of dyes in textile wastewater using biological and chemical treatment. *Separation and Purification Technology,* 154**,** 149-153.
Joshi, P. A.and Mhatre, K. J. 2015. Microbial efficiency to degrade Carbol fuchsin and Malachite green dyes. *Advances in Applied Science Research,* 6**,** 85-88.
Khandegar, V.and Saroha, A. K. 2013. Electrocoagulation for the treatment of textile industry effluent--a review. *J Environ Manage,* 128**,** 949-63.
Kobya, M., Demirbas, E.and Akyol, A. 2009. Electrochemical treatment and operating cost analysis of textile wastewater using sacrificial iron electrodes. *Water Sci Technol,* 60**,** 2261-70.
Lakshmi, J., Sozhan, G.and Vasudevan, S. 2013. Recovery of hydrogen and removal of nitrate from water by electrocoagulation process. *Environ Sci Pollut Res,* 20**,** 2184-2192.
Lim, K. F. 2006. Negative pH Does Exist. *Journal of Chemical Education,* 83**,** 1465.
Lin, Q., Pan, H., Yao, K., Pan, Y.and Long, W. 2015. Competitive removal of Cu-EDTA and Ni-EDTA via microwave-enhanced Fenton oxidation with hydroxide precipitation. *Water Sci Technol,* 72**,** 1184-90.
Lotito, A. M., De Sanctis, M., Di Iaconi, C.and Bergna, G. 2014. Textile wastewater treatment: aerobic granular sludge vs activated sludge systems. *Water Res,* 54**,** 337-46.
Lourenço, N. D., Franca, R. D. G., Moreira, M. A., Gil, F. N., Viegas, C. A.and Pinheiro, H. M. 2015. Comparing aerobic granular sludge and flocculent sequencing batch reactor technologies for textile wastewater treatment. *Biochemical Engineering Journal,* 104**,** 57-63.
Mahmoud, D. K., Salleh, M. a. M., Karim, W. a. W. A., Idris, A.and Abidin, Z. Z. 2012. Batch adsorption of basic dye using acid treated kenaf fibre char: Equilibrium, kinetic and thermodynamic studies. *Chemical Engineering Journal,* 181-182**,** 449-457.
Mahmoud, M. S., Farah, J. Y.and Farrag, T. E. 2013. Enhanced removal of Methylene Blue by electrocoagulation using iron electrodes. *Egyptian Journal of Petroleum,* 22**,** 211-216.
Mameri, N., Yeddou, A. R., Lounici, H., Belhocine, D., Grib, H.and Bariou, B. 1998. Defluoridation of septentrional Sahara water of north Africa by electrocoagulation process using bipolar aluminum electrodes. *Water Research,* 32**,** 1604-1612.
Matilainen, A., Vepsalainen, M.and Sillanpaa, M. 2010. Natural organic matter removal by coagulation during drinking water treatment: a review. *Adv Colloid Interface Sci,* 159**,** 189-97.
Mohora, E., Rončević, S., Agbaba, J., Tubić, A., Mitić, M., Klašnja, M.and Dalmacija, B. 2014. Removal of arsenic from groundwater rich in natural organic matter (NOM) by continuous electrocoagulation/flocculation (ECF). *Separation and Purification Technology,* 136**,** 150-156.
Ong, Y. K., Li, F. Y., Sun, S.-P., Zhao, B.-W., Liang, C.-Z.and Chung, T.-S. 2014. Nanofiltration hollow fiber membranes for textile wastewater treatment: Lab-scale and pilot-scale studies. *Chemical Engineering Science,* 114**,** 51-57.
Ozyonar, F.and Karagozoglu, B. 2011. Operating Cost Analysis and Treatment of Domestic Wastewater by Electrocoagulation Using Aluminum Electrodes. *Polish J. of Environ. Stud,* 20**,** 173-179.
Pallant, J. 2005. *SPSS SURVIVAL MANUAL,* Australia, Allen & Unwin.

Phadke, A. 2014. *Iron removal using electro- coagulation followed by floating bead bed filtration.* MSc thesis, Louisiana State University and Agricultural and Mechanical College.
Phalakornkule, C., Sukkasem, P.and Mutchimsattha, C. 2010. Hydrogen recovery from the electrocoagulation treatment of dye-containing wastewater. *International Journal of Hydrogen Energy,* 35**,** 10934-10943.
Riyantoand Mawazi, M. 2015. Electrochemical Degradation of Methylen Blue Using Carbon Composite Electrode (C-PVC) in Sodium Chloride. *IOSR Journal of Applied Chemistry,* 8**,** 31-40.
Safari, S., Azadi Aghdam, M.and Kariminia, H. R. 2015. Electrocoagulation for COD and diesel removal from oily wastewater. *International Journal of Environmental Science and Technology,* 13**,** 231-242.
Samide, A., Tutunaru, B., Tigae, C., Efrem, R., Moanţă, A.and Drăgoi, M. 2014. Removal Of Methylene Blue And Methyl Blue From Wastewater By Electrochemical Degrada. *Environment Protection Engineering,* 40.
Santos, S. C.and Boaventura, R. A. 2015. Treatment of a simulated textile wastewater in a sequencing batch reactor (SBR) with addition of a low-cost adsorbent. *J Hazard Mater,* 291**,** 74-82.
Sharma, S., Kaushal, J.and Mahajan, P. 2016. Adsorption of textile dyes by plant biomass-a review. *International Journal of Advanced Technology in Engineering and Science,* 4.
Tabachnick, B. G.and Fidell, L. S. 2001. *Using Multivariate Statistics,* Boston, Allyn and Bacon.
Un, U. T., Koparal, A. S.and Bakir Ogutveren, U. 2009. Electrocoagulation of vegetable oil refinery wastewater using aluminum electrodes. *J Environ Manage,* 90**,** 428-33.
Un, U. T., Koparal, A. S.and Bakir Ogutveren, U. 2013a. Fluoride removal from water and wastewater with a bach cylindrical electrode using electrocoagulation. *Chemical Engineering Journal,* 223**,** 110-115.
Un, U. T., Koparal, A. S.and Ogutveren, U. B. 2013b. Fluoride removal from water and wastewater with a bach cylindrical electrode using electrocoagulation. *Chemical Engineering Journal,* 223**,** 110-115.
Vasudevan, S., Lakshmi, J.and Sozhan, G. 2012. Optimization of electrocoagulation process for the simultaneous removal of mercury, lead, and nickel from contaminated water. *Environ Sci Pollut Res,* 19**,** 2734–2744.
Vidal, J., Villegas, L., Peralta-Hernandez, J. M.and Salazar Gonzalez, R. 2016. Removal of Acid Black 194 dye from water by electrocoagulation with aluminum anode. *J Environ Sci Health A Tox Hazard Subst Environ Eng,* 51**,** 289-96.
Wan, W., Pepping, T. J., Banerji, T., Chaudhari, S.and Giammar, D. E. 2011. Effects of water chemistry on arsenic removal from drinking water by electrocoagulation. *Water Res,* 45**,** 384-92.
Zhu, J., Zhao, H.and Ni, J. 2007. Fluoride distribution in electrocoagulation defluoridation process. *Separation and Purification Technology,* 56**,** 184-191.

Keyur Joshi

Detection of adulteration in milk products using electromagnetic wave sensors

K H Joshi*, A Shaw, A Mason, O Korostynska and A Al-Shamma'a

Built Environment and Sustainable Technologies (BEST) Research Institute,
Department of Built Environment,
Liverpool John Moores University,
Liverpool,
L3 2ET
*K.H.Joshi@2014.ljmu.ac.uk

Abstract: This article introduces a novel approach for detecting the adulteration of milk products by using electromagnetic wave sensors. Microwave spectroscopy was carried out on milk samples to determine presence of foreign particles, other than its normal constituents. The experiments were performed for primarily found contaminants like pesticides, residue detergents and added water as a form of adulterants. Urea is one such natural constituent of milk which can be present up to the extent of 70 mg per 100 ml (700 ppm) in milk. Any higher level than that is a form of adulteration, done to make the life span of milk product longer than usual. This extra amount is dangerous for health and therefore it becomes important to determine the level of such adulterants present within milk. Spectral signatures were recorded, for data analysis, using Vector Network Analyser for various samples of milk spiked with varying amount of adulterant. This database is then analysed to determine the overall quality of given milk products with respect to adulteration. The results achieved through this methodology are promising. This technique attempts to resolve the limitations of milk quality testing schemes being employed currently in practice to give quality monitoring system which is real-time, less costly, and less complex than the other existing standards. With further optimization in the design of this type of sensors and their selectivity, this system, in situ, has the potential to be applied at certain levels of milk supply chain hierarchy - specifically for milk quality inspection.

Key Words *- adulteration, data analysis, electromagnetic wave sensors, microwave spectroscopy, milk quality inspection, real-time, resonator, spectral signatures, urea, vector network analyser.*

1. Introduction

In this paper, a novel technique to determine the adulteration, in milk, using electromagnetic (EM) wave sensors is demonstrated. Milk adulteration can cause consumers to contract food borne diseases when adulterated milk or such affected milk products are consumed [1]. The detection of adulteration, of any form, is essential part of milk quality monitoring and control process. There are several forms of milk adulteration, both unintentional and deliberate forms, which can be fatal if not identified, and lead to health deterioration or food poisoning. Some contaminants can enter into the dairy chain through the stage of milk processing and packaging or via melamine (intentional) means of adulteration done for the purpose of achieving commercial gains [2]. The adulterants ranging from water, carbonates/bi-carbonates, starch, gelatine up to urea etc. have been reported to be a prevalent practices of melamine adulteration of milk in India [3]. Some of these adulterants are very harmful to human health, such as urea or even polluted water as reported in many developing countries.

In this article, the analytical study is made based on the experiments carried out to detect urea content, in milk, as main adulterant. Urea can be naturally available in milk up to 700 ppm (i.e. 70mg per 100ml)

The test which uses para-dimethylamino benzaldehyde (DMAB), was used for estimation of urea in milk after precipitation of milk proteins with the help of trichloroacetic acid (TCA). Following section shows the detailed methodology, in steps, that is used as a benchmark standard to validate the results achieved through microwave spectroscopy. The results achieved here using a non-invasive, low-profile portable, electromagnetic wave resonator sensor are promising and discussed at the end of this paper.

2. Methodology

2.1. Making the Reagents

2.1.1. p-Dimethyl Amino Benzaldehyde (DMAB) solution. 1.6 g DMAB was dissolved in 100 ml ethyl alcohol and then 10 ml concentrate Hydrochloric (HCl) acid was added. This reagent is stable for 1 month. New standard curve was prepared with each new batch of reagent as per required.

2.1.2. Phosphate buffer pH 7.0. 3.403 g anhydrous potassium dihydrogen orthophosphate (KH_2PO_4) and 4.355 g anhydrous dipotassium monohydrogen orthophosphate (K_2HPO_4) were dissolved separately in 100 ml of deionized water. These solutions were, then combined and, diluted to 1 liter with deionized water. If the pH of the solution is not 7.0 at this point then it has to be adjusted by adding more K_2HPO_4 (if the pH is lower than 7) or by adding KH_2PO_4 (if the pH is higher than 7). Add either of the two by small parts and mix the volume before pH testing, as required.

2.1.3. Trichloroacetic Acid (TCA), 24% w/v. Freshly prepared, 24.0 g TCA was dissolved in deionized water and volume made up to 100 ml.

2.1.4. Urea standard stock solution 5 mg/ml. 5 ± 0.001 g urea (analytical grade) was dissolved and diluted with 1 liter of deionized water. This can be adjusted to required volume.

2.2. Procedure

2.2.1. Preparation of standard curve. Take a stand for 20 tubes, for 10 + 1 + 8 tubes (10 - for preparation of calibration solutions, 1 - for blank samples, 8 - milk samples). In 10 test tubes for calibration solutions, add necessary volume phosphate buffer and necessary volume of urea solution, as specified in table 1.

Table 1: Sample making for standard curve

Test-tube number	Urea solution (5 g/l) volume, ml	Buffer solution, ml
1	0.04	4.96
2	0.08	4.92
3	0.12	4.88
4	0.16	4.84
5	0.2	4.8
6	0.24	4.76
7	0.28	4.72
8	0.32	4.68
9	0.36	4.64
10	0.4	4.6

*2.2.2. Preparing milk samples***.**

- 10% w/v skim-milk standard solution was prepared, as per the instructions from data sheet of product bought from Sigma Aldrich. Hence, 10 grams of skim milk powder was dissolved in deionized water (solvent), making the final volume of solution up to 100ml.
- Then 8-point milk samples were prepared with varying urea concentrations. This was achieved by spiking each of 8 milk samples under test with increasing amount of Urea in the orders of 0mg (0ppm), 2mg (200ppm), 4mg (400ppm), 6mg (600ppm), 8mg(800ppm), 10mg(1000ppm), 12mg (1200ppm) and 14mg (1400ppm) per 10ml of milk obtained through skim milk powder standard solution. This enables to test the sensor ability to detect urea in the milk samples.

  We can do this by volumetric sample making starting from highest concentration of 1400 ppm and then using equation $C_1V_1=C_2V_2$ full sample making table 2 can be prepared. For the stock

solution of urea, first make 28 mg Urea/20 ml milk solution. The volumetric sample making allows for higher accuracy than other methods, due to using only one reference solution and making others from that. These samples then were undergone centrifugation at 4000 rpm for 50 minutes. Each obtained sample was than filtered using Whatman grade 42 filter paper (without nitrogen) and funnels. 5 ml of filtrate of each sample was then added in separate 8 test tubes**.**

Table 2: Milk sample making with 8-point urea concentrations

Tube number (Urea)/10ml	Milk solution, ml	Urea stock solution (28 mg/ 20 ml Milk), ml
1 (0mg)	10	0
2 (2mg)	8.5715	1.4285
3 (4mg)	7.1430	2.8570
4 (6mg)	5.7145	4.2855
5 (8mg)	4.2855	5.7145
6 (10mg)	2.8570	7.1430
7 (12mg)	1.4285	8.5715
8 (14mg)	0	10

2.2.3. Preparing of blank sample. 5 ml of buffer solution was added in 1 test-tube.

2.2.4. Adding of colored reagent. When tubes with calibration solutions, blank sample and milk samples filtrate was ready, 5 ml of DMAB solution was added in each of the 19 test-tubes. Test-tubes were thoroughly shaken and let stand for 10 minutes at room temperature.

2.3. Spectrophotometry estimation.

First cuvette (cell) for blank sample was measured as a reference (zero) point in the spectrophotometer, at 420nm wavelength, and then one by one cuvettes for each calibration solution and then for each milk sample were measured. Measure each calibration solution.

3. Data analysis.

Figure 1 shows the standard curve achieved using above method. Figure 2 identifies 8-point milk samples with varying concentrations of urea with reference to the same standard curve.

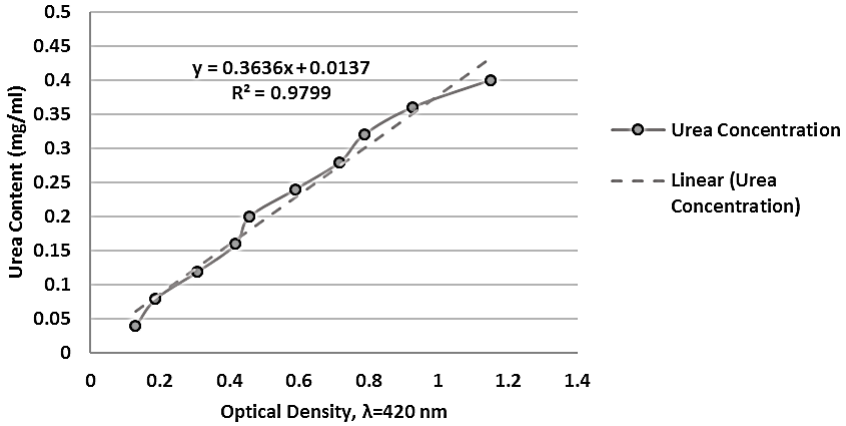

Figure 1. Standard curve using urea and buffer solution samples in spectrophotometer

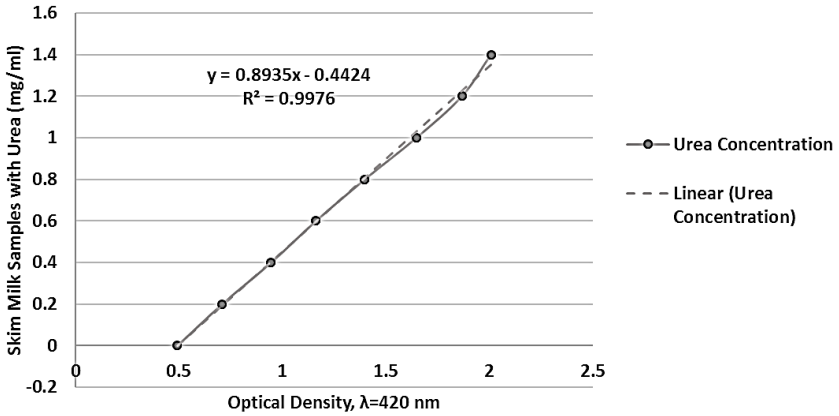

Figure 2. Milk samples spiked with urea detected in spectrophotometer

4. Results using EM wave sensor.

Figure 3 illustrates measurement setup with DC motor pump that circulates milk sample between two wings of resonator sensor connected to VNA, whereas figure 4 demonstrates the scattering parameter S_{21} (dBm) vs. urea content (mg/ml) graph. It can be seen from the plots of figure 4 that, using EM wave spectroscopy linear correlation of up to 96.18% was achieved, at 8.5678 GHz frequency. Total 5 repetitions were made for each measurement for given 8-point of urea samples, at room temperature.

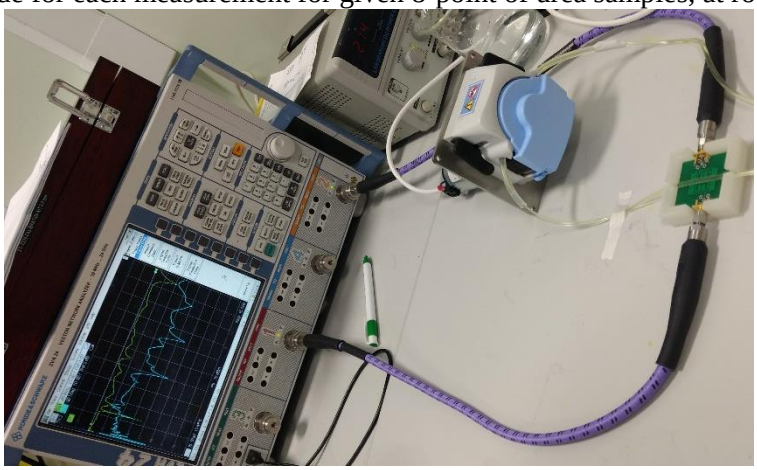
Figure 3. Experimental setup of urea detection in milk using EM wave sensor

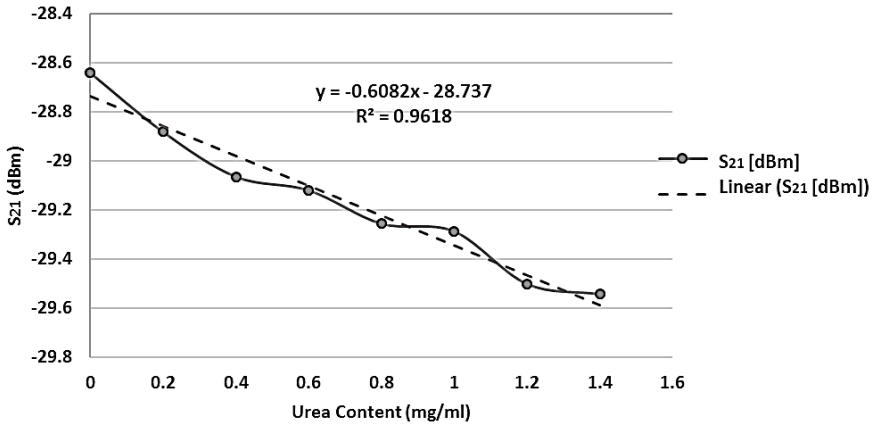

Figure 4. Milk samples spiked with urea detected through microwave spectroscopy

5. Conclusion.

The results achieved here demonstrate that the proposed novel technique, using EM wave sensor has shown quite promising results and has the potential to replace the robust existing methodologies, which are tedious, complex, and costlier than the proposed technique overall. Authors have also demonstrated

spoilage due to bacteria adulteration in their other publication. Hence, this method can incorporate more than one objectives of determining quality of milk products using EM wave sensors. This can aid into high quality of adulteration control in milk, with real-time operation along with content testing.

References

[1] K. H. Joshi, A. Mason, O. Korostynska, and A. Al-Shamma'a, "Milk Quality Monitoring Using Electromagnetic Wave Sensors," in *Sensors for Everyday Life: Environmental and Food Engineering*, Smart Sens., vol. 23, S. C. Mukhopadhyay, O. A. Postolache, K. P. Jayasundera, and A. K. Swain, Eds. Springer International Publishing AG, 2017, pp. 121–134.

[2] M. Kenny, "Safety and Quality," in *Milk and Dairy Products in Human Nutrition*, E. Muehlhoff, A. Bennett, and D. McMahon, Eds. Rome: FAO Publications, 2013, pp. 243–273.

[3] S. G. Bhandare and V. S. Waskar, "Food safety management for Indian Dairy Industry," *Indian Dairym.*, vol. 62, no. 6, pp. 42–46, 2010.

Layth Kraidi

Analysing the Critical Risk Factors in Oil and Gas Pipeline Projects in Iraq

L Kraidi [1, 2], R Shah [1], W Matipa, [1] and F Borthwick [1]
[1] Department of the Built Environment, Faculty of Engineering and Technology, Liverpool John Moores University, Byrom Street Campus, Liverpool. L3 3AF
[2] PhD Student, Henry Cotton Building, 15-21 Webster Street, Liverpool, L3 2ET, UK. Email: L.A.Kraidi@2016.ljmu.ac.uk

Abstract. Oil and gas pipeline projects (OGPPs) are involving a vast range of problems which cause risk existing management system more challenging, particularly in the current and insecure global environment. Corrosion, design defects, material ageing, poor quality, misuse, geological disasters and third party disruption are examples of key risks that were resulting casualties and severe loss of property. Additionally, surprise and horrible terrorism and sabotage attacks are adding more complexity in managing the safety of OGPPs in developing countries with low levels of security. Hence, a new holistic risk management framework will be established in this paper for managing these risks in more comprehensive and systematic way; and to reduce the loss of life and property. An extensive literature review and quantitative research approach are conducted in this research to identify and analyse OGPPs critical risk factors worldwide. Based on the literature's findings, a questionnaire survey is distributed to rank the risk factors in OGPPs in Iraq. Research data is analysed by using a descriptive statistical method, and the results are presented in a table. The risk factors are ranked regarding their degree of influence on the pipeline. The current research's findings will be used as inputs to develop a computer-based model of risk management system useful in oil and gas pipe line projects.

Keywords. Oil and gas pipeline projects (OGPPs); pipeline safety; risk factors; probability; severity; ranking; and risk management framework.

1. Introduction

Oil and gas projects are risky because of the immense magnitude of variables, challenges, and also annoying and unexpected issues [2]. Oil and gas projects' problems are needing for more efficient ways of working that encompass the integration of people, processes, and technology [4]. The pipeline has become one of the safest and effective ways for oil and gas transportation. However; the accidents would happen during the transportation because of different causes such as corrosion, design defects, material ageing, poor quality, misuse, geological disasters and third party disruption; and these accidents are resulting casualties and severe loss of property [6]. Moreover, the unsafe and insecure global environments are making risk management more complex. For these reasons; the implemented risk management has to be comprehensive, holistic and systematic in order to identify and analyse the pipelines' risk factors; and to achieve the project objectives [8, 12]. As well as, the historical records are valuable sources of information for risk management studies [11]. After an in-depth review of the literature, it was found that most of the studies about OGPPs risk management are mainly at the local scale, and few studies have assessed more than one region. The developing

countries with low levels of security like Iraq have different situations compared to safe countries. This difference is due to internal wars and terrorist organisations that often make malicious terrorist attacks on OGPPs. Additionally, there is an absence of data records and proper knowledge on implementing such risk-controlling methods in these areas. So, it is significant to study the risk of OGPPs to provide the necessary date; and to analyse the associated risk factors to avoid the loss of life and wealth.

2. Research Aim

The challenging idea in this research is to develop a systematic risk management approach depending on a new holistic risk management framework (RMF). The RMF aims to support in identifying, analysing and ranking OGPPs risk factors in more comprehensive and systematic way. OGPPs stockholders could use this framework to improve pipeline risk management during the project's stages.

3. Research Methodology

Risk management is based on the premise that the risks are identifiable because defending a system from unknown events is almost impossible [3]. This paper's step-by-step risk management approach and a proposed framework for risk management system is presented in (figure 1). At the beginning, a comprehensive literature review is done to identify, understand and analyse the critical risk factors associated with OGPPs worldwide [5, 7, 9, 10, and 13]. Based on the literature's findings, thirty risk factors have been identified and conducted with an online survey to analysis the factors' probability and severity in Iraq. The factors have been analysed regarding their degree of probability, severity and index on a scale from 5 to 1. Where 5 means the heights probability, severity or index, while 1 mean the less. A descriptive statistical analysis method is used to calculate these factors' probability, severity and index values. The factors have ranked regarding their consequences on the projects. Table 1 shows the identified risk factors; risk factors types; and the factors' probability, severity and index values.

4. Proposed Risk Management Framework

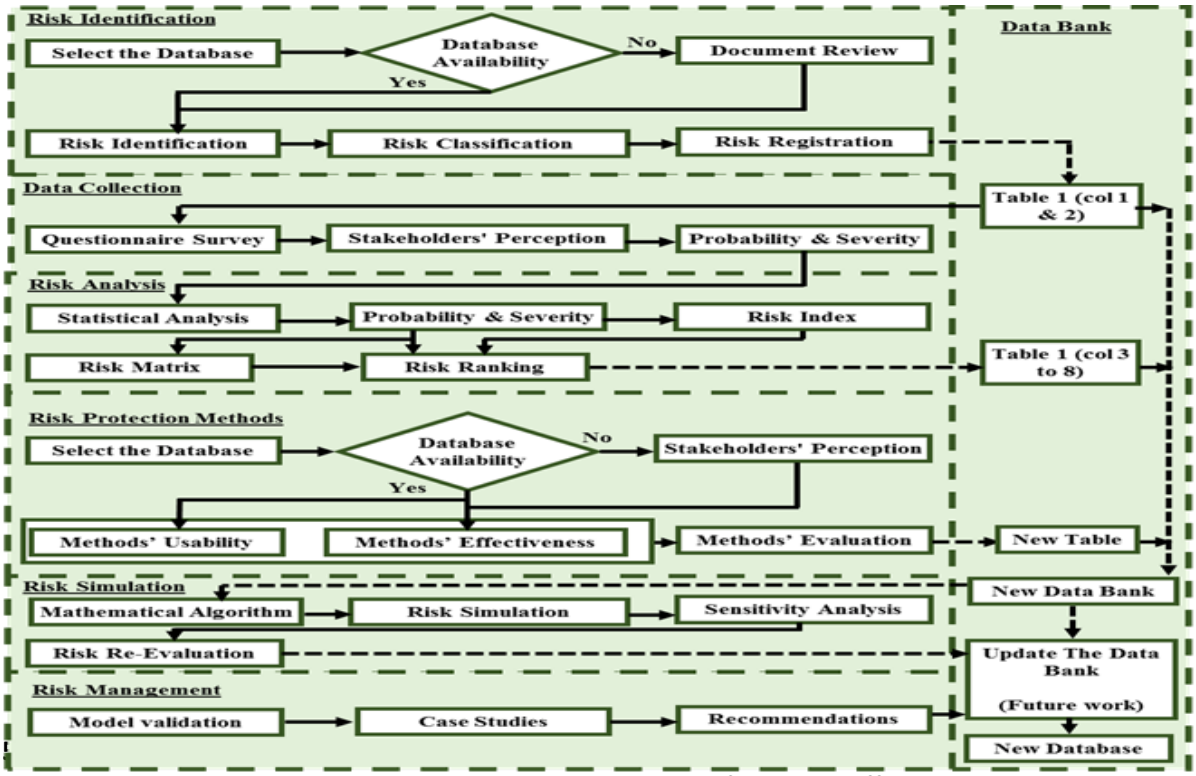

Figure 1 Risk Management Framework (RMF) [1, 8 and 9].

The research is started with analysing the critical OGPPs risk factors in different countries and different situations to provide a proper knowledge abut OGPPs and to make the research's results

suitable and applicable to many countries and to overcome the crucial problem of the shortage of available data and historical records in developing countries such as Iraq. Then OGPPs are evaluated and analysed through an online semi-structured questionnaire and descriptive statistical analysis by using (SPSS 23). The statistical analysis results are presented in (table 1).

Table 1 Risk factors, factors' type, probability, severity, index and ranking.

Risk Factors (1)	Risk Type (2)	RP		RS		RI	
		Mean [b] (3)	Ranking (4)	Mean [b] (5)	Ranking (6)	Index [c] (7)	Ranking (8)
Terrorism and sabotage	Security and Social	4.044	1	4.522	1	3.658	1
Corruption	Rules and Regulation	4	2	4.322	2	3.458	2
Thieves	Security and Social	3.744	3	4.106	4	3.074	3
Geographical location like 'Hot-Zones'	Pipeline location	3.739	4	4.106	5	3.070	4
The law does not apply to saboteurs	Rules and Regulation	3.628	12	4.172	3	3.027	5
Corrosion and lack of protection against it	Operational	3.711	6	3.956	6	2.936	6
Improper safety regulations	HSE	3.7	7	3.928	8	2.907	7
Public's low legal and moral awareness	Security and Social	3.717	5	3.844	11	2.858	8
Improper inspection and maintenance	HSE	3.656	10	3.906	9	2.856	9
Weak ability to identify and monitor the threats	Operational	3.656	11	3.883	10	2.839	10
Stakeholders are not paying proper attention	Rules and Regulation	3.567	18	3.956	7	2.822	11
Lack of proper training	Rules and Regulation	3.611	16	3.750	13	2.708	12
Sabotage opportunities arising due to the exposed pipeline.	HSE	3.672	8	3.678	16	2.701	13
Limited warning signs	HSE	3.617	15	3.667	17	2.652	14
Shortage of IT services and modern equipment	Operational	3.672	9	3.611	19	2.652	15
Lack of historical and risk registration	Rules and Regulation	3.578	17	3.706	15	2.652	16
The pipeline is easy to access	Pipeline location	3.617	14	3.661	18	2.648	17
Few researchers are dealing with this problem	Rules and Regulation	3.622	13	3.583	20	2.596	18
Design, construction and material defects	Operational	3.322	22	3.817	12	2.536	19
Conflicts over land ownership	Pipeline location	3.483	19	3.578	21	2.492	20
Threats to staff	Security and Social	3.322	21	3.711	14	2.466	21
Socio-political factors such as poverty and education level	Security and Social	3.45	20	3.400	24	2.346	22
Operational errors	Operational	3.078	24	3.567	22	2.196	23
Inadequate risk management	HSE	3.217	23	3.356	25	2.159	24
Leakage of sensitive information	Security and Social	2.972	25	3.489	23	2.074	25
Geological risks such as groundwater and landslides	Pipeline location	2.733	26	3.189	26	1.743	26
Natural disasters and weather conditions	HSE	2.628	27	3.033	27	1.594	27
Vehicle accidents	Pipeline location	2.428	28	2.700	29	1.311	28
Hacker attacks on the operating or control system	Operational	2.228	29	2.911	28	1.297	29
Animal accidents	Pipeline location	1.872	30	2.028	30	0.759	30

Where $RP\ is\ Risk\ Probability$, $RS\ is\ Risk\ Severity$, $RI\ is\ Risk\ Index$ and ($RI = RP \times RS/5$)

6. Conclusion

OGPPs are complex and risky and suffering a vast range of problems. Furthermore, risk management challenges are increasing daily due to the terrorism and sabotage attacks in the troubled countries. Common OGPPs risk factors have been identified based on a comprehensive review of the pipeline failure causes worldwide. The probability and severity of 30 risk factors have been calculated based on the statistical analysis results of a questionnaire survey with a total of 180 successful respondents. The RI for each factor was calculated to rank the risk factors concerning their degree of influence on the pipeline. Risk factors ranking indicates that terrorism and sabotage acts, corruption, hot-zones and the law is not applied to saboteurs are the risks that have the highest impact on the pipeline. On the other hand, geological hazards, natural disasters and weather conditions, vehicle accidents, hacker attacks and animal accidents are the factors with the least impact. Furthermore, the prioritised risk factors showed an essential need to understand the profile of third party disruption in Iraqi OGPPs in

order to mitigate and limit damage to pipelines. Scientifically, OGPPs stakeholders could use this paper's discoveries (such as provided in tables 1 and figure 1) as a database and risk evaluation tool through the stages of a pipeline project, and for monitoring and prioritising risks during design, re-design, construction, operation, inspection and maintenance activities.

7. Future work

The presented results in the paper are the research's first stage findings. Correspondingly, these numerical results will be adopted to develop a new computer-based model for OGPPs risk management during the next research stages. A mathematical algorithm and simulation software(s) will be used to simulate the risk factors. The will be developed model will be evaluated by running case studies in OGPPs in Iraq.

8. References

1. Fang, C. and Marle, F., 2012. A simulation-based risk network model for decision support in project risk management. Decision Support Systems, 52(3), pp.635-644.
2. Hokstad, P., Utne, I.B. and Vatn, J., 2012. Risk and interdependencies in critical infrastructures. Springer *Chapters*, *5*, pp.49-94
3. Labaka, L., Hernantes, J. & Sarriegi, J. M. 2016. A holistic framework for building critical infrastructure resilience. Technological Forecasting and Social Change, 103, 21-33.
4. Lameda, L, R., Van Den Berg & Gijsbert, F. Integration is about people, paper SPE 123352, presented SPE Digital Energy Conference and Exhibition, Houston, Texas, USA, 7-8 April 2009.
5. Li, H., Sun, R., Lee, W.-J., Dong, K. & Guo, R. 2016. Assessing Risk in Chinese Shale Gas Investments Abroad: Modelling and Policy Recommendations. Sustainability, 8, 708.
6. Liu, J., Li, L., Hou, T., Wu, X. & Zhou, Q. 2016. Study on Security Angle of Gas Pipeline Elbow Based on Stress Analysis Method. The Open Civil Engineering Journal, 10, 133-140.
7. Nnadi, U., El-Hassan, Z., Smyth, D. & Mooney, J. 2014. Lack of proper safety management systems in Nigeria oil and gas pipelines. IChemE Institution of Chemical Engineers, 237, 27 - 34.
8. Mubin, S. & Manna, A. 2013. Innovative Approach to Risk Analysis and Management of Oil and Gas Sector EPC Contracts from a Contractor's Perspective. Journal of Business & Economics, 5, 149-170.
9. Mubin, S. and G. Mubin (2008). Risk analysis for construction and operation of gas pipeline projects in Pakistan. Pak. J. Engg. & Appl. Sci. Vol 2(Jan), 22-37.
10. Rowland, A. 2011. GIS-based prediction of pipeline third-party interference using hybrid multivariate statistical analysis. PhD, Newcastle University
11. Ruijsscher, T. 2016. Improving risk identification on large infrastructure projects. Master Thesis, University of Twente.
12. Zhao, X. & Singhaputtangkul, N. 2016. Effects of Firm Characteristics on Enterprise Risk Management: Case Study of Chinese Construction Firms Operating in Singapore. Journal of Management in Engineering, 32, 05016008.
13. Srivastava, A. & Gupta, J. P. 2010. New methodologies for security risk assessment of oil and gas industry. Process Safety and Environmental Protection, 88, 407-412.

Kah Hou Teng

NUMERICAL INVESTIGATION ON USING AN ELECTROMAGNETIC WAVE SENSOR TO DETECT WATER HARDNESS IN WATER COOLING SYSTEM INDUSTRY

K.H. Teng[1, 2,*], Shaw A[1], M. Ateeq[3], Al-Shamma'a A[1], S.N. Kazi[2], B. T. Chew[2]

[1] Department of Build Environment, Faculty of Engineering & Technology, Liverpool John Moores University, Liverpool, L3 3AF, United Kingdom
[2] Department of Mechanical, Faculty of Engineering, University of Malaya, 50603 Kuala Lumpur, Malaysia
[3]Low Carbon Eco-Innovatory, Faculty of Engineering & Technology, Liverpool John Moores University, Liverpool, L3 3AF, United Kingdom

Abstract

Numerical study of using novel electromagnetic wave technique to detect water hardness concentration has been presented in this paper. Simulation is powerful and efficient engineering methods which allows for a quick and accurate prediction of various engineering problems. The RF module is used in this research to predict and design electromagnetic wave propagation and resonance effects of a guided wave to detect water hardness concentration in term of frequency domain, eigenfrequency and mode analysis. A cylindrical cavity resonator is simulated and designed in the electric field of fundamental mode (TM_{010}). With the finite volume method, the three-dimensional governing equations were discretized. Boundary conditions for the simulation were the cavity materials as aluminum, two ports which include transmitting and receiving port, and assumption of vacuum inside the cavity. The designed model was success to simulate a fundamental mode and extract S_{21} transmission signal within 2.1 GHz – 2.8 GHz regions. The signal spectrum under effects of port selection technique and dielectric properties of different water concentration were studied. It is observed that the linear reduction of magnitude in frequency domain when concentration increase. The numerical results were validated closely by the experimental available data. Hence, conclusion of the available COMSOL simulation package is capable of providing acceptable data for microwave research.

Keywords: Numerical and experimental, electromagnetic wave technique, water hardness concentration, signal spectrum, eigenfrequency, frequency domain

Nomenclature

RF	Radio Frequency
TM_{010}	Fundamental operation mode for Transverse Magnetic
S_{21}	Transmission coefficient
H	magnetic field intensity
E	electric field intensity
B	magnetic flux density
D	electric flux density or electric displacement
J	current density
P	electric charge density
Q	quality factor

1. Introduction

Water is a universal solvent which is easy to handle, save to consume, widely available and inexpensive in most industrialized regions [1]. Moreover, water is an efficient heat transfer medium compared to other materials, especially air, and could dissolve most of the substances come into contact. These unique properties of water make it ideal for an application of cooling water in the industry [2]. However, it causes an unwanted side effect for industrial applications. The water hardness concentration in cooling systems due to the dissolved ions

may exceed in relation to the solubility of some minerals such as calcium carbonate and calcium sulphate and deposit an insulated layer within the pipes and on the system surfaces [3]. This problem significantly reduces the overall performance of the cooling tower/ system and requires regular maintenance to restore the desired performance for the process it serves [4].
Recently, electromagnetic wave sensing technology have been developing rapidly and successfully used as a sensing method for various industrial applications including solution concentrations. Therefore, product designs of suitable sensor such as dimension, materials, etc. for specific application become a challenge for engineers and researchers. Simulation is a very useful and powerful tool to analyze, design, and operate complex systems [5]. By making use of software prototypes before committing to any actual design or experimental resources can significantly reduce the project costs saving thousands, even hundreds of thousands of dollars. The simulated models enable validation of the experiment hypotheses and can describe how the systems will perform in a real-world application without substantially investing on an experimental trial whose outputs is unknown. In addition, it is a cost-effective mean of exploring new processes, without having to resort to pilot programs. It could reduce project timescales as well because of the ease with which specific parameters can be varied for different sets of experiments depending on the desired outputs. Simulation provides a way of better understanding the system and helps to produce high quality results faster. Moreover, it is an efficient communication tool, showing how an operation works while stimulating creative thinking about how it can be improved.
Electromagnetic wave sensing technology is an innovative, novel, non-invasive and on-line monitoring technique with a high potential to monitor water quality and subsequently performance of the cooling system . In a laboratory environment, it uses a vector network analyzer to measure scattering parameter (S-parameter) to determine concentration of target chemicals. A simulation is conducted in this paper to assist the design of a suitable microwave cavity resonator and to examine the feasibility of it for an industrial application.

2. Electromagnetic Waves

2.1 Water hardness properties

In this experimental investigation, the relative permittivity of water with varying hardness was determined experimentally. A cylindrical microwave cavity resonator designed work along with the experimental setup. It was fabricated from aluminum and has 4 parts (the top, body and two ports to launch microwave inside the cavity). Sample solution was prepared in low-loss quartz tube (outer diameter of 15mm) with thin wall and inserted in the middle of cavity as in Figure 1. Simulation model was constructed similar to experimental cavity design by assign aluminum as the cavity material and polyvinyl chloride as tube material. Material properties are investigated at a constant temperature, i.e. 25 ± 1°C. All the experiments results were assigned as user define input into simulation package to achieve reliable results.

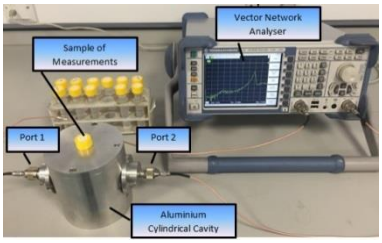

Figure 1: Microwave cavity resonator measurement system used in experiment

3 Numerical simulation

3.1 Model Geometry

RF module in COMSOL Multipyhsics 5.1 has been used to investigate the eigenfrequency inside a cylindrical cavity and response signal spectrum in a frequency domain to simulate the effect of hardness concentration. Figure 2 shows the model of the cavity used in this study. The cylindrical cavity has a

radius of 4.5cm and a height of 10cm.

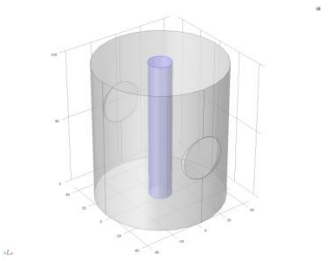

Figure 2: Model schematic of the cylindrical cavity

3.2 Material assignment and boundary condition

The wall was assigned an aluminum material and two ports were placed opposite to each other on both sides of the cavity (for transmission and reception of a signal). Impedance wall boundary was assigned as a perfect conductor to the aluminum wall as resistance to electromagnetic wave and has a perfect reflection within the cavity. The working cooling fluid temperature ranges in industrial was around 25 °C .Therefore, the temperature of 298 K (25 °C) was maintained within the cavity and measuring samples for this experiments. The samples used in this study were pure water and different concentrations of water hardness. Boundary conditions of the simulation setup are illustrated in Figure 3.

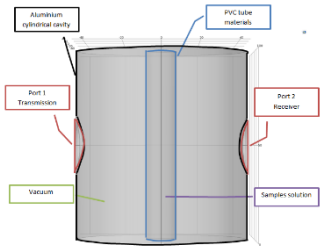

Figure 3: Boundary conditions for the analysed model

4 Numerical Procedure

In order to solve the partial differential equations governing the propagation of electromagnetic field inside a cavity resonator, an RF simulation module in COMSOL Multiphysics was used with user defined properties physical properties of samples. These included properties such as relative permeability, relative permittivity, electric conductivity and temperature.

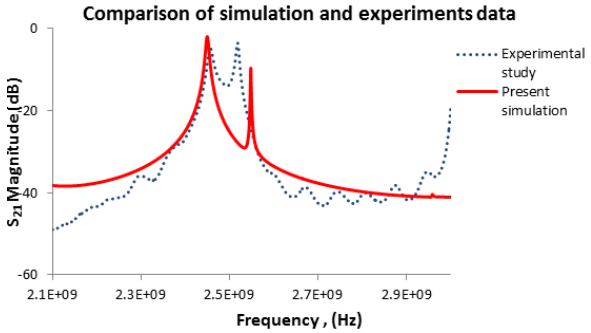

Figure 4: Comparison of simulated frequency spectrum data with experimental frequency spectrum data

Figure 4 shows the difference of the frequency spectrum between the experimental and simulation measurements. It is clearly demonstrated that the simulated S_{21} magnitude in empty cavity was relatively larger than the experimental S_{21} magnitude. This difference could be explained by the way the ports are modelled and the ideal simulation environments in comparison to the experimental measurements where there is a possibility of instrumentation errors during the experiment such as power dissipation in the coaxial cables, vacuum inside the cavity, etc. Based on the amount of difference in the results it can be concluded that the simulated and experimental measurements are comparable in terms

of their accuracy when an electromagnetic wave is propagated inside the designed cavity.

5 Results and Discussion

5.1 Effect of the water hardness on the signal spectrum

Figure 5 shows the effect of the concentration of calcium hardness on the S_{21} output signal where an input microwave power of 1mW rms (0 dBm) and the frequency range of 2.2–2.8 GHz was used. The results present a clear distinction in the amplitude of the signals with change in the sample hardness concentration. The amplitude of the spectrum for the higher concentration samples yields relatively a larger magnitude in comparison to the lower concentration. The observed phenomena can be explained as the result of the increased activity of soluble ionic compounds in the solution. The atoms absorb the EM wave and perturbs it . As a result, combination of higher quantity of different states atom will settle into an excited state with higher energy state.

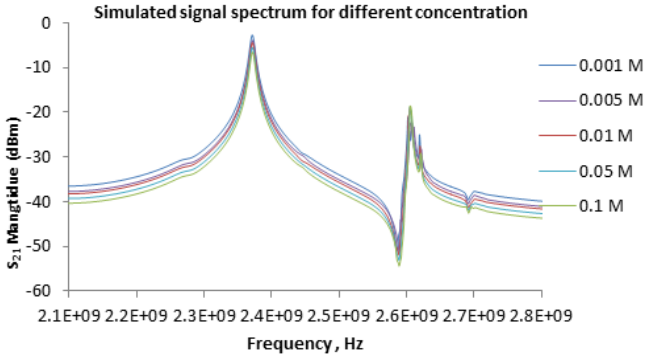

Figure 5: S_{21} spectrum analysis for different hardness concentrations in the solution

6 Conclusion

A numerical investigation on the eigenfrequency and different water hardness concentration were successfully performed. A range of frequency from 2.2 GHz to 2.8GHz with 4000 data points and 5 different calcium concentrations were considered in this numerical study. COMSOL Multiphysics simulation packages, RF module functions based on a finite element method and Maxwell equations model was used for simulations. The simulations setup was benchmarked against conducted experimental results. The simulated data have been evaluated and the results indicated close resemblances to the experimental results. In conclusion, COMSOL Multiphysics simulation package is efficient and reliable to simulate an EM wave model for the prediction of chemical compound across range of industries.

References

1. Rogers, P., R. De Silva, and R. Bhatia, *Water is an economic good: How to use prices to promote equity, efficiency, and sustainability.* Water policy, 2002. **4**(1): p. 1-17.
2. Teng, K., et al., *Fouling mitigation on heat exchanger surfaces by EDTA-treated MWCNT-based water nanofluids.* Journal of the Taiwan Institute of Chemical Engineers, 2016. **60**: p. 445-452.
3. Kazi, S.N., et al., *Study of mineral fouling mitigation on heat exchanger surface.* Desalination, 2015. **367**: p. 248-254.
4. Smaïli, F., V.S. Vassiliadis, and D.I. Wilson, *Mitigation of Fouling in Refinery Heat Exchanger Networks by Optimal Management of Cleaning*. Energy & Fuels, 2001. **15**(5): p. 1038-1056.
5. Kyoya, A. and M. Omiya. *Electromagnetic simulations and numerical models for an accurate prediction of indoor radio wave propagation in an office environment*. in *2016 IEEE International Conference on Computational Electromagnetics (ICCEM)*. 2016.

Isabel Atkinson

Solutions and recommendations for the reverse of high street decline through the application of national and global sustainability strategies

Isabel Atkinson and Dr Vida Maliene
Department of the Built Environment, Liverpool John Moores University, Byrom Street, L3 3AF
I.J.Atkinson@2008.ljmu.ac.uk and V.Maliene@ljmu.ac.uk

Abstract. Existing literature reports the vulnerability of many high streets to factors such as evolving consumer behaviour/preference, competition from alternative forms of retail, changing economic conditions and the costs associated with occupying high street units. Previous research highlights the affect that high street decline can have on local economies, the local environment and local social issues. Over the course of the last 7 years a number of government initiatives and incentives have been implemented, however, reports suggest that these interventions have produced mixed results. This research has involved the formulation of a comprehensive set of criteria which influence the success and sustainability of high streets. Through the use of surveys, data has been obtained from planning professionals and the residents of selected case study areas. The data will inform the application of Multiple Criteria Decision Making methods in order to compare case studies and identify the best alternative. The results will inform recommendations and enable the creation of a final complex model for successful and sustainable high streets.

Keywords. High street decline. Sustainable communities. Multiple Criteria Decision Making methods.

1. Introduction

Existing literature reports the vulnerability of many high streets to factors such as evolving consumer behaviour/preference, competition from alternative forms of retail, changing economic conditions and the costs associated with occupying high street units. Since 2010 the government has introduced a number of initiatives in an attempt to counteract the decline of struggling high streets. These interventions have included the Portas Review [1] and subsequent pilots, the High Street Innovation Fund and the High Street Renewal Fund. Such initiatives have together provided approximately £18 million of financial support [2], however reports suggest that these interventions have produced mixed results [3-4], indicating that further work is required to better inform and support stakeholders to improve the success and sustainability of their local high streets.

2. Definition of high street

According to the Oxford English Dictionary a high street is *"the main street of a town, especially as the traditional site for most shops, banks, and other businesses"*.
The term 'high street' is often used to refer the central retail area, or main commercial streets, of large urban centres [5]. However, the term is also often used to refer to small suburban shopping parades and the core commercial hubs of smaller towns and villages. The broad use of the term can therefore cause much confusion and debate. For the purpose of this research one size of high street – the large town centre - has been the focus of the investigation.

3. Factors contributing to decline

Key factors which have influenced the performance of retail centres over the last 50 years include: advances in modern technology and transportation; the growth in out-of-town retail centres offering

free parking, a range of leisure facilities, close proximity to major highways, cheap rent and built-for-purpose units etc.; the growth in online retail offering convenience, choice, lower prices and reduced overheads for retailers etc.; and the ever changing demands and preferences of the consumer.

4. High street decline and sustainable communities

Existing literature highlights the implications that a declining high street can have on ambitions for sustainable development. Decline can lead to store closures which in turn can lead to job losses and a reduction in the amount of money entering a local economy [6]. Additionally, the physical maintenance of buildings may decline if left unoccupied [7] which can attract anti-social behaviour and criminal activity. As the choice of shops and services decrease and the physical environment deteriorates, visitor perceptions of a high street can change [8] and consumers with the means to travel to competing centres will often choose to do so, therefore increasing car use [9]. Those left behind, due to social or economic disadvantages (e.g. the elderly, disabled and people with limited financial means), may then become marginalised, paying higher prices for goods due to a lack of choice and competition [10-13].

5. Criteria influencing the success and sustainability of high streets

A review of existing literature has enabled the identification of the criteria and sub-criteria which are considered to influence the success and sustainability of high streets; these are presented in table 1.

Table 1. Criteria and sub-criteria which influence the success and sustainability of high streets

Criteria	**Physical fabric**	**Movement**	**Exchange**
Sub-criteria	Streets Signage Buildings Trees and landscape Public open space Infrastructure Design	Pedestrian pavements/walkways Cycling facilities Public transport Parking facilities Goods/service vehicles Traffic management	Social space Economic space Political space Cultural space Community space
Criteria	**Real estate**	**Psychology**	**Safety and security**
Sub-criteria	Retail Entertainment Work places Civic venues Residential Health and social facilities	Identity/ image Experience Atmosphere	Actual crime Perceived crime CCTV and security presence Street lighting
Criteria	**Management**	**Environmental protection**	**Economic viability**
Sub-criteria	Town centre management team Partnership/stakeholder involvement Marketing Digital connectivity/internet presence	Environmental initiatives/ carbon reduction schemes Environmentally sustainable materials Waste management and recycling schemes	Commercial rent Business rates Trading hours Complementary daytime, evening and night-time economies

6. Aim and objectives

6.1 Research aim

The aim of this study is to establish a complex model for successful and sustainable high streets.

6.2 Objectives

1 To critically analyse the trends of traditional high streets from 1800 to present day.

2 To evaluate the UK and EU policy framework with regard to sustainable development and retail centres.
3 To analyse the best practice cases of sustainable high streets.
4 To establish a comprehensive set of criteria which influence the success and sustainability of high streets.
5 To validate the identified criteria through surveys completed by planning professionals from across England.
6 To conduct resident surveys in the case study areas in order to recognise the local community's opinions and needs.
7 To establish recommendations to encourage successful and sustainable high streets in the case study areas.
8 To establish a complex model for successful and sustainable high streets.

7. Methodology

Eight case study towns (presented in table 2) have been selected for investigation. The towns represent successful and declining examples of large town centres in England.

Table 2. Case study towns selected for investigation

Successful case study towns	Basingstoke South-East	Corby East-Midlands	Rotherham South Yorkshire	Shrewsbury West-Midlands
Declining Case study towns	Birkenhead North-West	Gosport South-East	Great Yarmouth East Anglia	Southport North-West

Multiple Criteria Decision Making (MCDM) methods have been selected for use in this study due to their ability to assess decision making problems comprising multiple, and often conflicting, criteria [14-16]. Two surveys have been conducted. The first survey has been completed by professionals working in planning and other related fields. This survey sought to identify the relative importance of the criteria listed in table 1. A second survey, completed by the residents of the town centres presented in table 2, has obtained data which will enable the towns to be assessed against one another based on the criteria (which will be weighted with reference to the relative importance established from the professionals' survey). A handful of the most appropriate MCDM methods will be applied in order to assess the town centres. The results of each method will be compared and analysed in order to establish the final model. The findings will enable the formulation of recommendations to support more successful and sustainable high streets.

8. Conclusion

Both surveys were open for a period of six months and have recently closed. Data analysis is therefore currently in the early stages. It is anticipated that the final model will assist key stakeholders (e.g. local authorities, local communities and local businesses) in identifying improvements which will produce the greatest impact in terms of the improved success and sustainability of their local high streets. The model will also provide an assessment tool for high street performance which will act as an alternative to existing measures which have been criticised for being too retail centric [17-18], too heavily focused on economic factors and lacking recognition of evening and night-time economies [18].
It is expected that the research will provide a valuable contribution to literature regarding retail centres, high street decline and sustainable communities. Furthermore, the study will add to the body of literature regarding the application of MCDM methods.

9. References

[1] Portas M, 2011 *The Portas Review: An independent review into the future of our high streets*. (London; BIS)
[2] DCLG and ATCM 2014 *Celebrating the great British high street*. Available from:

http://thegreatbritishhighstreet.co.uk/pdf/GBHS-Celebrating-The-GB-High-Street.pdf?2 [Accessed 07/04/2016]
[3] BBC 2013 *Portas High streets still struggling one year on.* Available from: http://www.bbc.co.uk/news/business-22693403 [Accessed 07/04/2016]
[4] BBC 2013 *High street retail fund 'barely touched'*. Available from: http://www.bbc.co.uk/news/business-21775773 [Accessed 07/04/2016]
[5] Carmona M, 2015 London's local high streets: The problems, potential and complexities of mixed street corridors. *Progress in Planning*. **100** 1-84.
[6] Hart C, Grazyna S and Cadogan J W, 2013 Conceptualising town centre image and the consumer experience. *Journal of Marketing Management*. **29**(15-16) 1753-1781.
[7] Department of the Environment Inner City Directorate 1989 *Improving Inner City Shopping Centres: An Evaluation of Urban Programme Funded Schemes in the West Midlands*. (London: HMSO)
[8] Mullis K. and Kim M, 2011 Factors determining inshopping in rural US communities: Consumers' and retailers' perceptions. *International Journal of Retail and Distribution Management*. **39**(5) 326–345
[9] Whysall P, 2011 Managing decline in inner city retail centres: from case study to conceptualization. *Local Economy.* **26**(1) 3-17
[10] Bromley R and Thomas C, 1993 The retail revolution, the carless shopper and disadvantage. *Transactions of Institute of British Geographers*. **18**(2) 222–236.
[11] Bromley R and Thomas C, 1995 Small town shopping decline: Dependence and inconvenience for the disadvantaged. *International Review of Retail, Distribution and Consumer Research.* **5**(4) 433–456
[12] Westlake T 1993 The disadvantaged consumer: Problems and policies. In: Bromley R and Thomas C. (Eds.) *Retail change: Contemporary issues*. (London: UCL Press) p. 172–191
[13] Williams P and Hubbard P, 2001 Who is disadvantaged? Retail change and social exclusion. The International Review of Retail. *Distribution and Consumer Research*. **11**(3) 267–286.
[14] Zanakis S, Solomon A, Wishart N and Dublish S, 1998 Multi-attribute decision making: a simulation comparison of select methods. *European Journal of Operations Research*. **107**(3) 507–529.
[15] Zeleny M 1982 *Multiple criteria decision making*. (New York: McGraw-Hill)
[16] Belton V and Stewart T 2002 *Multiple criteria decision analysis: an integrated approach*. (Boston: Kluwer Academic Publications)
[17] Griffiths S Vaughan L Haklay M Jones C E 2008 The sustainable suburban high street: a review of themes and approaches. *Geography Compass*. **2**(4) 1155-1188.
[18] Coca-Stefaniak A 2013 *Successful Town Centres – developing effective strategies. ATCM/GFirst Report*. Available from: https://www.atcm.org/policy_practice/tools_dir/successful_town_centres__developing_effective_strategies [Accessed: 17th February 2017].

Atiyah Atiyah

Developing a consensus marine pilot's reliability index (MPRI) by weighting and prioritising criterion using the Delphi technique and a fuzzy analytical hierarchy process

Atiyah A. Atiyah, Zaili Yang, Christos Kontovas and Farhan Saeed
School of Engineering, Technology and Maritime Operations, Liverpool John Moores University Liverpool, Byrom Street, L3 3AF, UK
E-mail address: a.a.atiyah@2013.ljmu.ac.uk

Abstract. The economy is significantly growing worldwide, and 80% of the world's trade (by volume) moves through seaports. However, the growth in global trades has led to a significant growth in marine accidents due to ship/port interface or human involvement. Moreover, a marine pilot conducts a pilotage operation in a dynamic working environment with variable operational objectives and priorities. Thus, a proper understanding of a variety of key factors influencing a pilot's reliability is vital in all the high-risk industries including marine and maritime industries. This study aims to develop a quantitative marine pilot's reliability assessment tool, known as the Marine Pilot's Reliability Index, which will help the decision-makers to identify the effects of these factors on pilot's reliability. Although human reliability has been investigated in different disciplines, there is no consensus on the selected criteria. Therefore, to integrate and examine the feasibility of the selected criteria, the Delphi Technique will be first used. This will allow developing a consensus regarding the reliability index for a marine pilot. Secondly, a Fuzzy Analytical Hierarchy Process approach will be used to rank the importance of each identified criterion. An illustrative example is given to explain the process of integrating and weighting the selected criteria based on the selected methodological process.

Keywords: Human reliability; Maritime safety; Delphi technique; FAHP

1. Introduction

During the last century, the world's economy has grown significantly and 80% of the world's goods by volume are now transported by sea through ports. This increase in volume has seen a subsequent increase in marine accidents, which mainly occur within the confines of the seaport (Oltedal and McArthur, 2011). Accident investigation shows that there has been a significant increase in marine accidents within the last century, and these accidents have mainly occurred during the ship/port interface (Hsu, 2012) under the guidance of a human element called a 'marine pilot'.

The human element has been identified as a major critical factor for most operational failures. Between 60 and 96% of incidents with serious consequences reported by different well-known high-risk industries, such as aviation, nuclear, maritime and health care, have been attributed to human error. It is essential to understand the influence of a variety of key factors on human reliability in all the high-risk industries, with marine and maritime being no exceptions. Therefore, this investigation aims at developing a marine pilot's reliability index (MPRI), which can effectively enable the decision-makers to identify the most critical situations leading to incorrect actions.

To achieve this goal, an intensive literature review has been carried out to stipulate the main dominant factors influencing a marine pilot's reliability during port pilotage operations. It is worth mentioning that previous studies have focused on factors influencing the operator's reliability in different disciplines independently, such as non-technical skills, technical proficiency and human fatigue. This approach does not effectively mitigate human error, as evidenced by the continuous existence of this factor. Moreover, these studies have not identified the degree of correlation between factors as one set. Therefore, this investigation will integrate the aforementioned factors that challenge operators' reliability during pilotage operation as one set. This will be followed by developing the MPRI to enable

the decision-makers to identify the risks to pilots' performance associated with these factors.
Thus, the objective from this investigation is to develop a marine pilot reliability index (MPRI) as an assessment tool that aims to assess the reliability of a marine pilot during pilotage operations, by investigating the current pilotage practice after analysing empirical data from this study. Moreover, the identified criteria will be examined using the Delphi technique to test the usefulness and the applicability of the proposed criteria for developing the MPRI. This will be followed by assigning the weight of importance to each agreed criterion resulting from Delphi using a fuzzy analytical hierarchy process (FAHP). Finally, an example of how the Delphi technique works in eliciting experts' opinions will be given, followed by weighting the importance of each criterion.

2. Literature review

In every dynamic working environment, team reliability is vital and requires operators to be continually monitoring situations and adjusting their decisions accordingly (Rouse et al., 1992). Decision-making is a central process in all organisations, and a successful operation requires an exceptionally reliable team. For a team conducting a pilotage operation, variation in the decision-making process can be expected, due to the dissimilarity of operators' responsibilities (Rouse et al., 1992). Thus the International Maritime Organisation (IMO) recognised the significant role that pilots play when adopting assembly resolution A.159 (ES.IV), 'recommendation on pilotage', in 1968: that it is vital to employ a qualified pilot in a port's approaches and other port areas where local knowledge of the port, language and regulations is required (IMPA, 2017).
An operator's expertise can be built through a set of technical competencies and personal physical abilities, working in conjunction with an additional set of competencies referred to as non-technical skills (NTS). NTS comprises both interpersonal and cognitive skills. Interpersonal skills, including mental and communicative skills, are applied during social interactions between team members, while cognitive skills are the capabilities and mental skills that are used to process and obtain knowledge. These skills are highly dependent on levels of personal fatigue, personal fitness and strength (Hetherington, Flin and Mearns, 2006). Studies have shown that an operator's mental capacity is significantly affected when facing a high mental workload. In addition, according to Ramin et al., (2012), the American Bureau of Shipping (ABS) guidance has stated essential factors that are significant for overall organisational safety when selecting operators for a task as follows:
1. Knowledge, skills and abilities that are shaped through an individual's basic knowledge, general training and experience.
2. Maritime-specific training and abilities, such as certificate and licences, and other maritime-related specific skills, such as vessel or offshore installation-specific skills and abilities.
3. Physical characteristics of an operator, such as stature, shoulder breadth, height, functional reach, overhead reach and weight.
4. Physical strength; capabilities and limitations, such as resistance to and freedom from fatigue; visual activity; physical fitness and endurance; acute or chronic illness; and substance dependency.
5. Psychological and mental characteristics, such as individual risk perception, risk tolerance and resistance to psychological stress.
Therefore, a generic MPRI assessment model is proposed, as shown in Appendix 1. The model consists of three levels. Level 1, the goal, is to develop a marine pilot reliability index (MPRI) within port pilotage operations. Level 2 consists of four main factors that are directly involved in shaping an operator's performance within an operation. Within each individual main factor, sub-factors, which shape out the main factor, are presented in Level 3. In the last level, a proposed index for each sub-factor is presented, with the aim of helping to point out the influencing factors in detail. These indices will help the decision-makers to predict the development of an error atmosphere in ample time and to take further action.

3. The proposed methodology

In this research, we aim to integrate, examine the feasibility of and rank the importance of the selected criteria using two different decision-making techniques, the Delphi technique and the fuzzy analytical hierarchy process.

3.1 Delphi technique

The Delphi method is a structural process (Keeney et al., 2001), built upon a number of sequential

questionnaires sent out in a form of rounds, and aiming to acquire consensus opinions among a group of experts with respect to that particular study (Linstone and Turoff, 1975; Kennedy, 2004). Delphi has been used since 1963 as an effective means of collecting and soliciting expert judgments where its main objective is to address an incomplete state of knowledge, or where there is a lack of agreement on an issue that must achieve a consensus state among a group of experts (Powell, 2003) for developing a conceptual framework. It has been used widely as a principal method to support decision- and policy-makers in planning and predicting the future (Pill, 1971; Landeta, 2006). Therefore, the Delphi technique cannot be used without establishing an expert panel (Powell, 2003), where every expert will be given a set of structured questionnaires in a form of rounds until a consensus among the expert panel is achieved. The minimum number of rounds is two, and this extends until a consensus is achieved. An illustrative example is given, as shown in Section 4. The experts are asked to give their opinions using five Likert scales. In this research, a consensus among variables is achieved when the median of that criterion reaches 3.75/5 or more and the inter-quartile range (IQR) falls within the third quartile or 1.25 and less. This means that if the median of a particular criterion is FOUR and the IQR is ONE, then the criterion is considered for the framework. However, if the median is less than 3.75 and the IQR is equal to or more than 1.25, this means the criterion is not a consensus. In the second round, every expert is given the median and the IQR resulting from the first round, and the criterion's operational definition is reformed. This process will give the experts the chance to reconsider their answers. If, in the second round, the criterion again does not reach a consensus, additional third and up to fourth rounds are applied following the same process as the second round, until a consensus is achieved. However, if in the fourth round this criterion still does not reach a consensus, then this criterion will be removed, as it is agreed by experts as not being important for developing the framework. The remaining criteria will then be ranked according to their importance using the FAHP technique.

3.2 Fuzzy analytical hierarchy process (FAHP)

The AHP has been counted as one of the most powerful methods used to express fuzzy information derived from a rational scale known as a membership function since 1977, when it was invented by Saaty. The main objective of the AHP is to derive the degree of importance in terms of weight for a set of operational activities (Saaty, 2008). The importance of an activity can be arbitrated depending on several criteria. These criteria might be dependent on all other operational stages, as they might be devised to fulfil the activity. This is a multi-criteria decision-making (MCDM) approach, which can be used for solving complex decisions and problems built in a hierarchical form that contain a multi-level – namely, objectives, criteria and alternatives. This hierarchal structure helps the analyst to provide the decision-makers who are conducting a multi-pairwise comparison with a tool to observe the influence of an element that significantly affects the operation in a hierarchal model. As per Saaty (2008), there are four main steps for structuring an AHP model:

a. Selection of criteria.
b. Evaluation of the relative importance of these criteria using pairwise comparisons.
c. Evaluation of each alternative relative to each other on the basis of each selection criteria, using the pairwise comparison technique.
d. Combination of the ratings acquired in steps 2 and 3 to obtain an overall relative rating for each alternative.

4. Illustrative example

As an example, the researcher gives out a questionnaire to obtain agreement among selected criteria that have been identified through the literature. Table 1 represents the identified reliability indicator, the number of rounds conducted and the actions according to the median and IQR obtained.

Table1. Delphi technique results.

Reliability Indicator	R1 (n=15)		R2 (n=15)		R3 (n=15)		R4 (n=15)		Action
	M	IQR	M	IQR	M	IQR	M	IQR	
Decision making	4	1	5	1	5	0	5	0	Remain
Situation awareness	4	1	4	1	4	0	5	0	Remain
Communication skills	3*	1	3*	1	3*	2*	3*	2*	Removed
Teamwork and leadership	3*	2*	4	1	4	1	5	0	Remain

(R1, R2, R3 and R4 represent the number of rounds; M represents the median; IQR represents the inter-quartile range; n represents the number of participants, where here there are 15; * means that this criterion has not reached a consensus and needs to be reconsidered.)

After examining criteria using the Delphi technique, and dropping criteria not considered important in this study, an FAHP technique is used to evaluate the relative importance and rank the above criteria based on their importance, as shown in Table 2:

Table 2. Criteria's relative weight of importance and ranking.

Reliability Indicator	Relative Weight	Ranking
Decision making	0.4553	1
Situation awareness	0.3221	2
Teamwork and leadership	0.2226	3

5. Conclusion

This study aims to identify the dominant factors that impact on an operator's reliability, in order to develop the MPRI. Due to the incomplete state of knowledge for developing the reliability index, which has a lack of agreement with reference to its development, this research employs the Delphi technique to elicit factors that are linked to an operator's reliability, followed by assigning the weight of importance to every identified factor. Although this study has begun data collection, after being granted ethical approval, it remains at the first stage (on round one). This is the reason for giving an illustrative example at this stage. However, the feasibility of using this technique has been proved, along with its effectiveness across different scholars. Therefore, we expect its successful achievement for developing a novel MPRI for the maritime industry.

6. References

Hetherington, C., Flin, R. and Mearns, K. (2006) 'Safety in shipping: The human element', *Journal of safety research*, 37(4), 401-411.

Hsu, W.-K. K. (2012), "Ports' service attributes for ship navigation safety", *Safety Science*, 50(2), 244-252.

International Maritime Pilots Association (IMPA) (2004), "International Maritime Organisation (IMO)". Available at *http://www.impahq.org/admin/resources/a960en-1.pdf* [Accessed: 05 April 2017]

Keeney, S., Hasson, F. and McKenna, H. P. (2001) 'A critical review of the Delphi technique as a research methodology for nursing', *International journal of nursing studies*, 38(2), 195-200.

Kennedy, H. P. (2004) 'Enhancing Delphi research: methods and results', *Journal of advanced nursing*, 45(5), 504-511.

Landeta, J. (2006) 'Current validity of the Delphi method in social sciences', *Technological Forecasting and Social Change*, 73(5), 467-482.

Linstone, H. A. and Turoff, M. (1975) *The Delphi method: Techniques and applications*, Addison-Wesley Reading, MA.

Oltedal, H. a. M., DP (2011) 'Reporting practices in merchant shipping, and the identification of influencing factors', *Safety Science*, 49(2), 331-338.

Pill, J. (1971) 'The Delphi method: substance, context, a critique and an annotated bibliography', *Socio-Economic Planning Sciences*, 5(1), 57-71.

Powell, C. (2003) 'The Delphi technique: myths and realities', *Journal of advanced nursing*, 41(4), 376-382.

Riahi, R., Bonsall, S., Jenkinson, I. and Wang, J. (2012), "A seafarer's reliability assessment incorporating subjective judgements", *Proceedings of the Institution of Mechanical Engineers, Part M: Journal of Engineering for the Maritime Environment*, **226(4),** 313-334.

Rouse, W. B., Cannon-Bowers, J. A. and Salas, E. (1992) 'The role of mental models in team performance in complex systems', *Systems, Man and Cybernetics, IEEE Transactions on*, 22(6), 1296-1308.

Saaty, T. L. (2008) 'Decision making with the analytic hierarchy process', *International journal of services sciences*, 1(1), 83-98.

7. Appendices

Appendix 1: A generic MPRI assessment model

Level 1	Level 2	Level 3	Factors shaping Level 3
The goal	Shaping factors	Sub-factors	Sub-factor Index
Marine Pilot Reliability Index (MPRI)	1. Technical Proficiency	1.1. Qualification	A set of competences (educational level, licences and certifications that exhibit his/her achievement in order to comply with the minimum work-related knowledge required to carry out certain duties
		1.2. Specific Training	A set of compulsory or additional work-related courses and refreshment that required maintaining the minimum operational standard
		1.3. Working Experience	The accumulation of knowledge or skills that gained over time as a pilot
	2. Human Fatigue	2.1. Working Hours	The number of working hours per day or the time of the day when the operator is carrying out his/her duty
		2.2. Work Stresses	Commercial and economical stresses, management stresses, work-related demand, high-level of traffic, management style, etc.
		2.3. Working Environment	Physical working environment, ergonomic design, the status of the operative environment.
	3. Non-Technical Skills	3.1. Decision-Making	Encompasses a set of structural sequence that includes defining and diagnosis problem, generating options, assessing risks and option selection through different available alternatives followed by an outcome review.
		3.2. Situation Awareness	Is a perception of elements in the current situation through information gathering, followed by assessing the significance of the gathered information from different resources to form a clear picture to implement procedure for current operational even, and finally implementing a necessary action to avoid unfavourable event.
		3.3. Communication Skills	Is the ability of a member to regulate, control, motivate, express feelings and convey information to other team members involved in an operation
		3.4. Teamwork and Leadership	Is the way that you can establish a clear two-way of communication, openness to criticism, empathy towards cultural diversity, capable of motivating people and developing a community atmosphere, coping with an operator's limitations, being a key team player
	4. Fitness and Strength	4.1. Operator Age	As an operator gains work-related experience, he/she is getting older. Operator age can indicate how the performance of an experienced operator changes over time. As a result, a reduction in physical capacities and coordination, flexibility, strength, and power can be expected when getting older.
		4.2. Health Issue	It has been identified as a factor that strongly associated with accidents at sea. It can be a result of the nature of work, geographical location, stresses at work, prolonged working hours, commercial pressure and organisational culture as well as a historic family illness.
		4.3. Body Strength	As a pilot, you are required to maintain a high level of body strength, as you need to climb a ladder from time to another followed by a high level of cognitive demand to guide the ship safely during pilotage operation. Any reduction on body strength will affect your ability to carry the operation safely.

Thomas Leiblein

Pre-test and validation criteria for qualitative data collection in a two-stage explorative study on *Legionella* prevention in water systems in hospitals

T W Leiblein[1,*], M Tucker[1], M Ashall[1], R Al Khaddar[1], S Lee[2], C Gollnisch[3] and S Hofer[4]

[1] Liverpool John Moores University, Faculty of Engineering and Technology, Department of the Built Environment, Byrom Street, Liverpool L3 3AF, United Kingdom

[2] Leegionella Ltd., Registered Office, 5 Ribblesdale Place, Preston PR1 8BZ, United Kingdom

[3] Hygieneinspektionsstelle für Trinkwassersysteme, Hauptring 35, 04519 Rackwitz, Germany

[4] Zurich University of Applied Sciences, Department Life Sciences and Facility Management, Institute of Facility Management, Campus Gruental / RA, 8820 Waedenswil, Switzerland

[*] Corresponding author: T.W.Leiblein@2014.ljmu.ac.uk

Abstract. This paper is part of an ongoing PhD research project, which systematically uncovers the situation of *Legionella* prevention in water systems in healthcare organisations in three different countries. The aim of the overall research project is to work out a framework for Facility Management (FM). The discipline Facility Management (FM) is present in healthcare and operates within a range of regulations specific to a country. According to the International Facility Management Association (IFMA) an organisation has to take precautions to manage risks properly. Healthcare facilities (i.e. hospitals) can be part of an FM portfolio. The complexity of hospitals is made up of the organisational structure as well as of technical and competitive service demands of different stakeholders. Those people in duty are serving for a delineated process of *Legionella* prevention in water systems. One element of the research project is to reflect this process by a two-stage exploratory research design. Data collection is carried out in two successive phases to strategically gather information for characterising case studies. Pretest and validation criteria of the data collection instruments and procedures were considered necessary elements for an appropriate research methodology. Field research is initiated by an open and inductive first phase (experts' interviews) and followed by a questionnaire study including further groups of stakeholders. Pretest elements and validation criteria improved the quality of primary data collected, enabling the adjustment of questions during field work. Furthermore contentual reflection together with experts from different professional fields and from different countries was an

important step to validate information. This work is part of an ongoing PhD research project and explains elements of applied methodology procedures.

Keywords. Built Environment, Hospital, Water system, Risk Management, *Legionella*

1. Introduction

Legionella is representing a potentially pathogenic bacterium, which may be found in water systems. In the hospital environment there exist different types of water systems. The complex and interdisciplinary healthcare (HC) setting employs several stakeholders providing water hygiene. Duties and responsibilities towards third parties need to be fulfilled in respect of *Legionella* detection and prevention of water systems. Among the stakeholders there might be Facility Managers (FM) and Facility Services (FS) staff. Their responsibilities at managerial and lower levels include risk management applied to maintenance, monitoring, assessment and prevention of contamination of water systems by *Legionella* [1]. Essentially the stakeholders' roles and duties need to be evident to manage tasks properly.

The aim of an ongoing research project is to systematically reveal the present situation of *Legionella* prevention in water systems in selected HC organisations in different countries. The project seeks to develop a 'reference system' (framework) guiding those responsible in HC organisations to identify, understand and properly take action for prevention [2]. The research considers stakeholder theory, business research methods, process and quality theory and definitions. Methodology, operationalisation and specific analysis patterns are described elsewhere [3]. The research project takes a FM perspective considering FM and FS related aspects of business organisation, processes and legal aspects [4]. Four dimensions were identified to build the frame of the research project. They had been characterised during an initial literature review. The dimensions are: *Legionella*, hospital, risk management and FM / built environment [5]. The present paper aims at providing insights on specific methodology characteristics, which are applied during the research project and aim at improving data collection quality. This research project considers the different national context of three countries, namely the United Kingdom (UK), Switzerland (CH) and Germany (GER). It requires the management of field data collection in accordance with the underlying research study design.

2. Methodology and Approach

FM is a Management discipline. As research intends to provide a practical framework as output, it is necessary to include and consider aspects people responsible are confronted with. In order to strategically gather information during the field work process, model descriptions help understand and serve as a solid fundament giving orientation throughout the research process. For that, already existing models, theories, definitions and modes of action were applied and transformed into the own research context [2, 3, 5-9]. Together they represent the reference scheme upon which the final research output will be built up, eventually providing a framework for FM. Appropriate data collection instruments and data collection procedures are seen necessary elements for research methodology and data collection procedures. They are described elsewhere [3]. Figure 1 shows the two stages of the 'exploratory sequential design', according to Creswell and Plano Clark's [10] prototypes of major mixed methods research designs.

2.1. Two stages of data collection

Data collection and analysis will be carried out by two consecutive phases. Field work is initiated

by stage I and realised through semi-structured interviews with gatekeepers to the organisation. The subsequent stage II is realised through a questionnaire study including further groups of stakeholders. These groups are identified during stage I. They are different process owners providing water safety and *Legionella* prevention.

2.2. Two focuses of measuring units

The units of measure are defined by 'process identification' and 'stakeholder identification' delivering information about the participating organisation's state [3]. It will ascertain how risk assessment is organised and reflect routines of monitoring, documentation and collaboration of stakeholders working for a common process chain of *Legionella* prevention in water systems of hospitals.

2.3. Three loops for validation and reliability

Additionally, field work contains three loops (figure 1). Loops 1-3 align desk work findings with practical relevance, validate conformity of procedures and transfer the points of view of organisations operating. By sharing and receiving knowledge through attending scientific conferences, research platforms and the professional network, the dialogue between scientific work and practitioners is provided continuously.

During loop 1 it was tested whether or not the perspective and the practical relevance from the FM/FS is represented in the study design and in the operationalisation process. The loop was also designed to get into dialogue with experts from different fields serving for *Legionella* prevention in water systems. Activities during a final workshop with an independent, reliable and experienced expert on drinking water hygiene reviewed, discussed and aligned desk work outcomes. It yielded a thorough strategy for field work activities [2, 5, 6]. Some basic questions scrutinise:

- The independency of collaborators in case of doing a risk assessment.
- Qualification level of staff.
- Historical facts on the building (age of pipework systems).
- Water usage / contexts of consumption.

Furthermore loop 1 helped identifying the correct interviewee (functions), who represent the Heads of Estates and Facilities (UK), Water Safety Team members (UK), members of the hygiene commission (CH, GER) and heads of technical systems, maintenance or operations (CH, GER).

Loop 2 characterises as a Swiss pre-study on residential homes for elderly people, another FM in HC setting [7]. The procedure and extent of an extensive questionnaire study was tested involving duty holders. The initial questionnaire included five different categories of questions. The total amount of items (questions) had to be reduced as a result of this study. Furthermore it suggests taking a closer focus on questions on how the organisational structure and the awareness of duty holders characterises. As confirmed in loop 1 the identification of process owners and the main characteristics of national statutory and normative requirements are essential being recognised by the organisation.

Risk management routines from practitioners of the organisation suggest another focus on the organisation structure, the duty holders and their general awareness on water hygiene.

Loop 3 represents a pre-test in the hospital setting and allowed for final adjustments to be applied to the entire sample. In loop 3 the confirmation of the identified different groups of duty holders was seen most important. A final collection of the functions of people involved in the process of water safety (process owners of *Legionella* prevention), which are termed variant from organisation to organisation, vary in different countries or represent combined responsibilities, will aid the interpretation and discussion of the final analysis of stakeholder views (knowledge sharing, collaboration, regulatory clarity, awareness about potential risks, definition and attitude to a suggested process chain on *Legionella* prevention and water hygiene).

All three loops presented here represent important steps to validate reliable information.

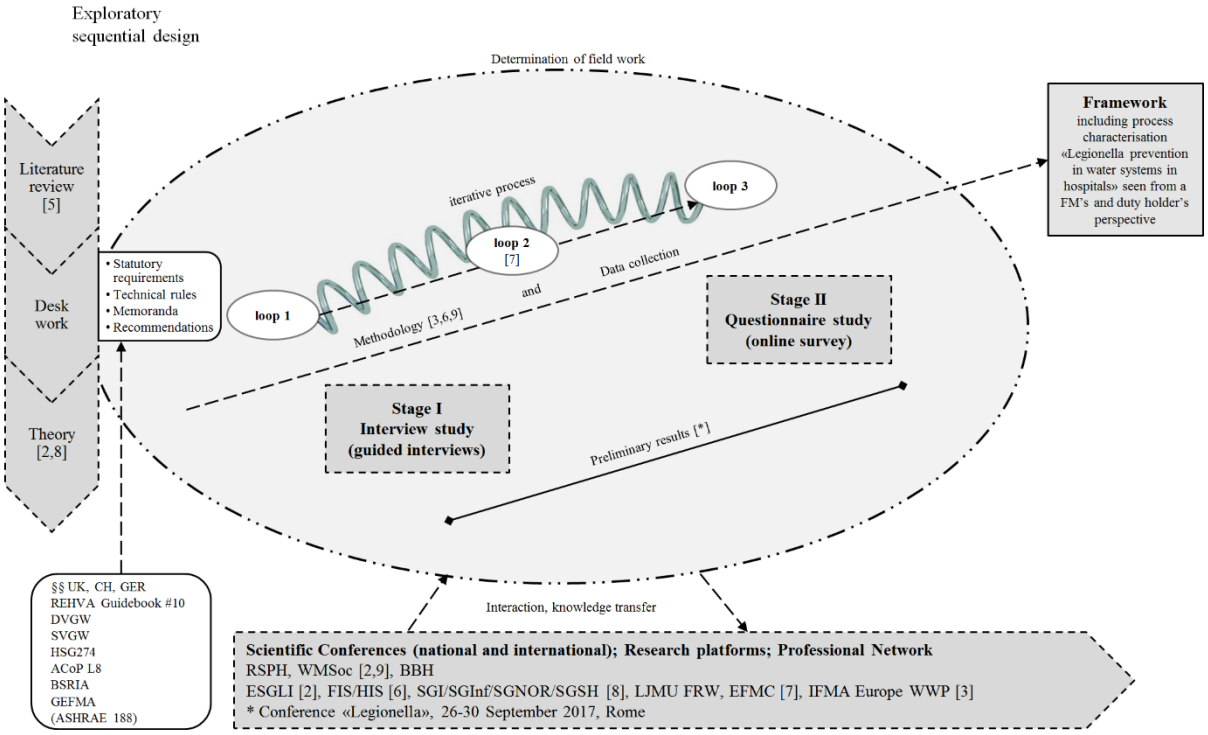

Figure 11. ***Two-stage research design for studying*** **Legionella** ***prevention in water systems in hospitals.***

3. Findings

Lists of questions of relevance for both stages during research had been discussed with experts on water hygiene and facility management. Initial questions emerged from desk work. Additionally, ideas of collecting data relevant to practitioners and strategies of accessing interview partners / organisations for the purpose of recruiting developed during the ongoing process and were tested. In order to continuously scrutinise and improve the research design and in order to align procedures with scientific methodologies, three loops co-assist methodology adjustment and the data collection process as well (figure 1). These three iterative steps validating the data collection process during field work allowed for improving the quality of primary data by:

- Contentual reflection together with experts from different professional fields and from different countries.
- Enabling the adjustment of questions during field work (replacement/shifting perspectives).
- Specification (e.g. correct wording / use technical terms; stakeholder identification).
- Focusing on essential information.
- Reducing the total amount of items (questions).

4. Discussion

The complexity of the study design revealing the issue of water hygiene in hospital settings is not limited to a specific country. And it is not limited to *Legionella* prevention alone with specific (national) demands in terms of legislation or standards. But a common challenge is the number of protagonists being involved in the process (‘Research project design and contextual framework’ [5]). In organisations which oriented by the WHO water safety plan processes seem to be existent,

but unfortunately are not described anywhere in scientific literature for FM in HC. It is only through the empirically justified logic of an appropriate reference system that evidence-providing elements can be identified, accessed, described and shared in a comprehensible manner. But for that the organisations must gain access to their practices. Perceived barriers during recruiting organisations to participate in the study may be ascribed to the sensitive topic of water hygiene within the sensitive context of healthcare. With respect to recent publications on the liability of duty holders [11, 12] this research project becomes even more relevant to people responsible. It raises awareness and helps understanding a common and interdisciplinary process of *Legionella* prevention of water systems in hospitals.

5. Conclusion

In terms of risk management, water safety and hygiene, there is a certain demand that research be seen from an FM and FS perspective. The complexity of potential risks, causes and liability may be closely connected with the country, legislation, environment, building, technical system, organisation, comprehension, awareness and, hence, the people. The research project will contribute to an understanding of the process of *Legionella* prevention in water systems of HC facilities. It is for this reason that the proposed methodological approach was selected, combining principles of stakeholder theory and business research with case study research. In practice, a framework is a simplification of a certain reality translated into a scheme. In order to achieve this goal, it is essential that a central process and the process owners be identified. Decision-making in the hospital environment is essentially based on facts. With the final result of a framework at the end of the research project, FM and FS people responsible in HC organisations obtain a meaningful instrument. This can be used as a management tool and will be formed with respect to a process-oriented perspective, issuing an organisation's protection goal of 'infection prevention'. The framework could help those responsible to reflect on their missions throughout the organisation and adjust (strategic) planning where seen necessary.

6. References

[1] Spagnolo AM, Cristina ML, Casini B, Perdelli F. Legionella pneumophila in healthcare facilities. Reviews in Medical Microbiology. 2013;24:70-80.
[2] Leiblein TW, Tucker M, Ashall M, Lee SB, Gollnisch C, Hofer S. Duty holders for *Legionella* prevention in healthcare organisations: The implications for Facility Management. Poster at ESGLI Conference, 3rd Annual Scientific Conference, London, 16.-17.09.2015, Poster No. 4/P45. Waterline - Journal of the Water Management Society. 2015:36.
[3] Leiblein TW, Tucker M, Hofer S. Methodology characteristics of a 'FM in healthcare' field study on risk management of Legionella in water systems. Conference proceedings of IFMA WWP Europe 2017, 29 May - 1 June. 2017:13 pages. In press 2017.
[4] Hungenberg H. Strategisches Management in Unternehmen: Ziele – Prozesse – Verfahren Wiesbaden: Springer Fachmedien; 2014.
[5] Leiblein TW, Tucker M, Ashall M, Lee S, Gollnisch C, Hofer S. Legionella and risk management in hospitals - A bibliographic research methodology for people responsible for built environments and facility management. International Journal of Hygiene and Environmental Health. 2016;219(8):890–7.
[6] Leiblein TW, Tucker M, Ashall M, Lee S, Gollnisch C, Hofer S. Methodological approach of assessing present state of technical processes in hospitals regarding risk management of Legionella in UK, GER and CH. Abstracts of Federation of Infection Societies (FIS) Annual Conference and the 10th Healthcare Infection Society (HIS) International Conference 2016, 6-8 November 2016, Edinburgh. Journal of Hospital Infection. 2016;94(Supplement 1):S87-8.

[7] Leiblein TW, Füchslin HP, Keserue HA, Tucker M, Hofer S. Risk management of water systems in residential homes: The ‘process’ of Legionella prevention. In: Susanne Balslev Nielsen, Per Anker Jensen, Rikke B, editors. Research papers for EuroFM´s 16th research symposium, EFMC2017, 25-28 April 2017 in Madrid, Spain. Lyngby: Polyteknisk Forlag; 2017. p. 78-90.
[8] Leiblein TW, Hofer S. Legionella in Hospitals: Duties, responsible and integrated Risk Management: A study on the role of Facility Management (FM) in cooperation with other people in charge. Swiss Medical Forum Supplementum 63 ad Swiss Medical Forum 2015 Annual Conference 2015 of SGI/SGInf/SGNOR/SGSH. 2015(36):147.
[9] Leiblein TW, Tucker M, Ashall M, Al Khaddar R, Hofer S. Risk Management - Hygiene and Legionella in water systems in hospitals: Relevance for Facility Management and Facility Services. Waterline - The Journal of the Water Management Society. 2016;Winter 2016-17:8-10.
[10] Creswell JW, Plano Clark VL. Designing and Constructing Mixed Methods Research. 2nd ed. Los Angeles, Washington D.C.: SAGE Publications Inc.; 2011.
[11] Gollnisch L-P, Gollnisch C. Praktische und juristische Aspekte der TrinkwV mit dem Schwerpunkt Legionellen an den Beispielen Festlegung Probenahmestellen, Probenentnahme und Gefährdungsanalyse. Der Hygieneinspektor - Zeitschrift des Bundesverbandes der Hygieneinspektoren. 2016;06/2016:35-46.
[12] Anonymous. Basildon Hospital fined over Legionnaires' disease deaths. BBC News. 2013 04 September 2013.

Jonathan Davies

The role of the hot circumgalactic medium in galaxy formation

Jonathan Davies, Robert Crain and Ian McCarthy
Astrophysics Research Institute, Liverpool John Moores University, 146 Brownlow Hill, Liverpool, L3 5RF
Email: j.j.davies@2016.ljmu.ac.uk

Abstract: The cold dark matter model of cosmological structure formation predicts the existence of thermodynamically multi-phase and dynamically complex reservoirs of gas that surround galaxies. This circumgalactic medium (CGM) interfaces the complex astrophysics of galaxies with the relatively simple gravitational evolution of diffuse intergalactic gas. It is now recognised that the CGM is not only a source of fuel for on-going star formation, but also the 'dumping ground' where violent outflows of gas from galaxies end up. Such outflows are powered by violent phenomena such as stellar explosions and the growth of black holes, and encode information about the evolution of the galaxy. Next generation, multi-billion dollar satellites are now under development to study the hot (10^6 K) component of the CGM via its X-ray 'glow', and exploitation of their data will require detailed modelling and theoretical interpretation. We have therefore coupled plasma emission models to the state-of-the-art EAGLE simulations of galaxy formation, enabling us to apply "X-ray vision" to a model of the gaseous Universe. We can now examine the physical conditions of the hot CGM, and study its origin and evolution over billions of years of cosmic history. The simulations also provide us with a "digital laboratory" within which to examine the influence of astrophysical processes on the state of the hot CGM. We are in the process of exploiting our tools to develop detailed predictions for the capabilities of the Athena and XRS-Lynx satellites, under development by the European Space Agency and NASA, respectively.

Keywords: galaxy formation, galaxy evolution, cosmological simulations

1. Introduction

The presence of hot, diffuse gas surrounding galaxies is a universal prediction of galaxy formation models. Detailed computer simulations of the formation of galaxies suggest that a significant fraction of the gas they accrete arrives supersonically, and shock-heats to form a quasi-hydrostatic corona, or circumgalactic medium (CGM) that envelopes the galaxy. The hot CGM of galaxies similar to own Milky Way is expected to exhibit temperatures of 10^6 K, making it luminous at X-ray wavelengths and potentially detectable with space-borne instrumentation.

Direct observation of the CGM is tantalising, since this gas interfaces relatively quiescent intergalactic gas with the turbulent and poorly understood gas within galaxies. The hot CGM is a potential source of fuel for ongoing star formation in galaxies, and its physical properties, such as its density and temperature structure, encode a record of the galaxy's formation history. Its enrichment with heavy elements, nucleosynthesised by massive stars, also sheds light on the nature of the violent feedback processes that regulate the galaxy's growth. The hot CGM may in fact prove to be the dominant reservoir of all atomic matter, including the

heavy elements from which life derives, in the present-day Universe. Study of the hot CGM therefore an exciting new astrophysical frontier.

Characterisation of the hot CGM remains inconclusive however. Luminosities inferred from X-ray observations are factors of 10-100 lower than predicted by simple analytical models such as those of White & Frenk (1991), rendering detailed study beyond the capabilities of the current generation of instrumentation. There is also controversy with regards to the origin of the hot gas, with the prevailing interpretation being that the emission is a signature of feedback-driven outflows, rather than gravitational accretion. These puzzles have fostered the development of a new generation of multi-

billion dollar satellites such as Athena (ESA) and XRS-Lynx (NASA), but these are scheduled to begin operations from 2030 onwards.

In advance of the advent of these facilities, we can study the hot CGM using cosmological simulations. Doing this now makes it possible to guide the design process of the instrumentation aboard these observatories. Cosmological simulations self-consistently calculate complex structure and dynamics of the CGM, following these quantities over billions of years. Analysis of the previous generation of cosmological simulations (e.g. GIMIC, Crain *et al.* 2010) highlighted the shortcomings of simple analytic models, demonstrating that the feedback processes that regulate the growth of galaxies also have a significant impact on the structure of the CGM, ejecting hot gas from the CGM and thus reducing its X-ray luminosity, potentially reconciling galaxy formation theory with X-ray observations.

The realism of cosmological simulations has improved markedly in recent years, with the EAGLE simulations (Schaye *et al.* 2015; Crain *et al.* 2015) representing the current state-of-the-art. EAGLE has been carefully calibrated to reproduce the observed properties of galaxies in the local Universe, affording unprecedented confidence in the fidelity of its predictions of the characteristics of the CGM. We are investigating the nature of the hot CGM of EAGLE galaxies in detail, and have already found significant differences with respect to the previous generation of simulations. Here, we demonstrate the role of baryonic processes in modifying the luminosity of the hot CGM relative to simple analytic models, and discuss the origin of the hot CGM of EAGLE galaxies.

2. Methods

To study the X-ray properties of hot gas in the simulation, we require a physical model which, given the temperature and chemical composition of the gas, will specify how much energy is emitted. To this end, we obtain spectral energy distributions from the Astrophysical Plasma Emission Code (APEC, Smith *et al.* 2001) which, when integrated over some appropriate passband, gives tabulated volumetric cooling functions L (in units of erg cm^3 s^{-1}) as a function of gas temperature for 11 elements (H, He, C, N, O, Ne, Mg, Si, Ca, S, Fe). The left panel of Figure 1 shows the cooling functions for the 0.5-2.0 keV passband, to which X-ray satellites are sensitive. These cooling functions can then be 'painted' onto fluid gas elements in simulations, giving their X-ray luminosity via $L_X = n_e\, n_H\, V\, \mathrm{L}$, where n_e and n_H are the number densities in

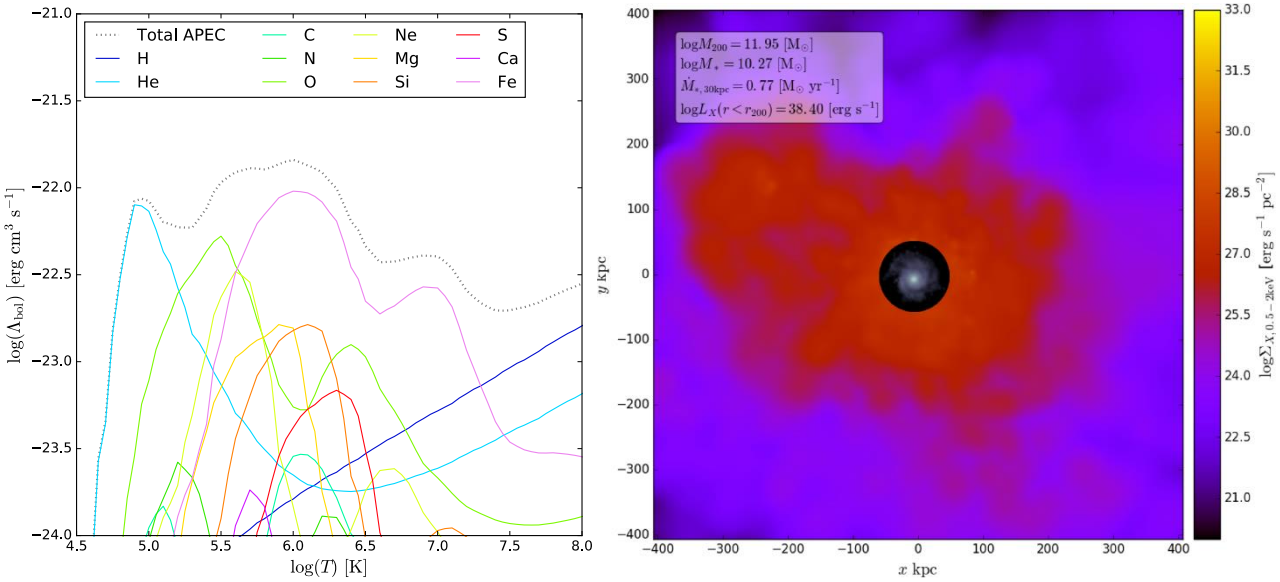

Figure 1. *Left panel:* The dotted line shows the bolometric cooling function as a function of temperature obtained from APEC at the solar abundances of Anders & Grevesse (1989). Coloured lines show contributions from individual elements. *Right panel:* An example X-ray surface density plot of an EAGLE galaxy, with the stellar component of the galaxy shown inset to demonstrate the spatial extent of the hot CGM.

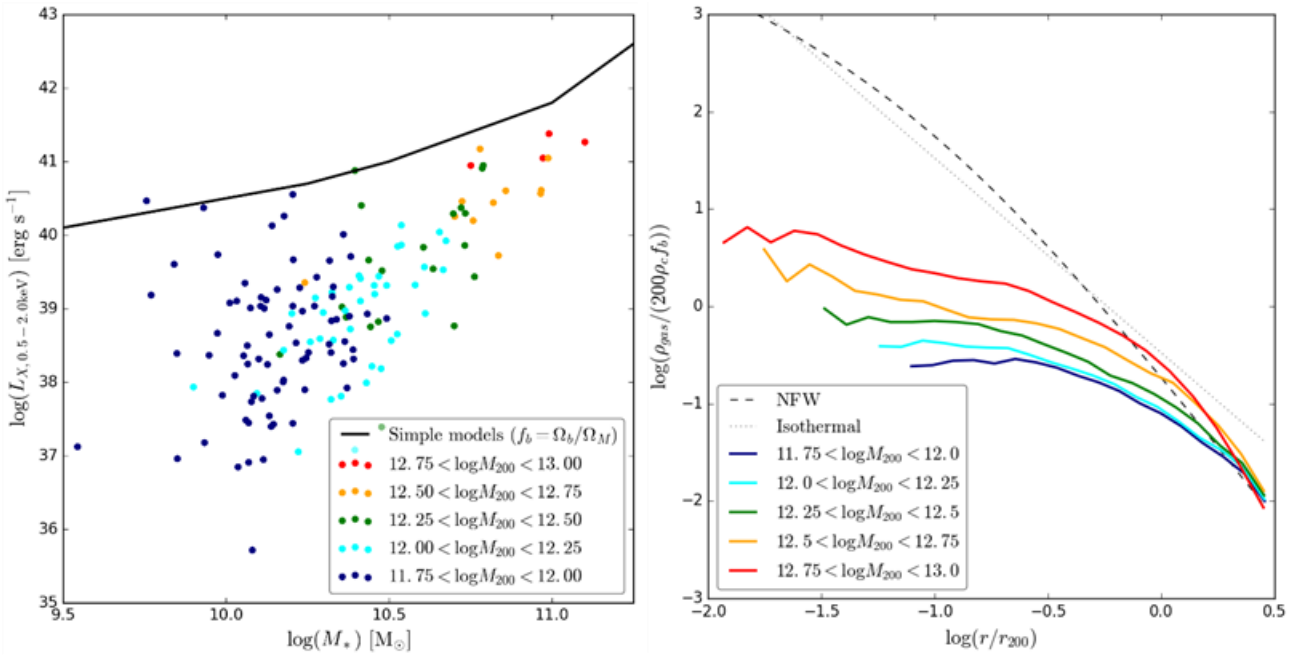

Figure 2. *Left panel:* The 0.5-2.0 keV soft X-ray luminosities of isolated galaxies in the Ref-L0050N0752 EAGLE simulation, as a function of stellar mass. The expected luminosities from analytical models are shown as a black line. *Right panel:* stacked density profiles of the galaxies in the left panel, with the densities normalised to the critical density and the radial distance normalised to the virial radius r_{200}.

and V is the volume associated with the fluid element. Note that at the typical temperatures of the hot CGM (10^6 K), the cooling is dominated by emission from heavy elements, such as oxygen and iron. It is therefore crucial to derive predictions from simulations, such as EAGLE, that track the synthesis and transport of these elements.

3. Results

To illustrate the use of our pipeline, we show in the right panel of Figure 1 an X-ray surface brightness map of the hot CGM associated with a Milky Way-like EAGLE galaxy. For reference, the stellar component of the galaxy is shown inset. The visual morphology for the halo is clearly complex, highlighting the necessity of approaching this problem with 3D numerical simulations. The left panel of Figure 2 shows the total 0.5 – 2.0 keV X-ray luminosity of the CGM as a function of its host galaxy's stellar mass. Symbols are coloured by the total dynamical mass of the system. The luminosity predicted by simple analytic models is shown as a black line, and is a factor of 10-100 greater than found in EAGLE.

The origin of this discrepancy is made clear in the right panel of Figure 2, in which we show the median 'stacked' radial density profile of the hot CGM, for galaxies categorised into five bins of dynamical mass. The central density of the hot CGM is strongly suppressed relative to the analytic profiles (shown as solid and dashed black lines) typically assumed by simple models, with the greatest suppression exhibited by the least massive galaxies. This suppression is a consequence of star formation and ejective feedback, the latter driven by massive stars and growing black holes.

Simulations enable us to monitor the evolution of the hot CGM over billions of years of cosmic evolution, and elucidate its origin. In the left panel of Figure 3 we plot, as a function of the dynamical mass of the galaxy, the fraction of its X-ray luminous mass contributed by

fluid elements ejected (by feedback) from within the galaxy in the last 0.5 Gyr. This gas contributes little to the mass of the hot CGM, indicating that most of the gas is sourced from intergalactic accretion. The ejected gas is not representative of the hot CGM, because it is preferentially enriched with heavy elements nucleosynthesised by massive stars, enhancing its X-ray luminosity. In the right panel of Figure 3, we plot the fraction of the total luminosity contributed by ejected gas, and find that it can, particularly

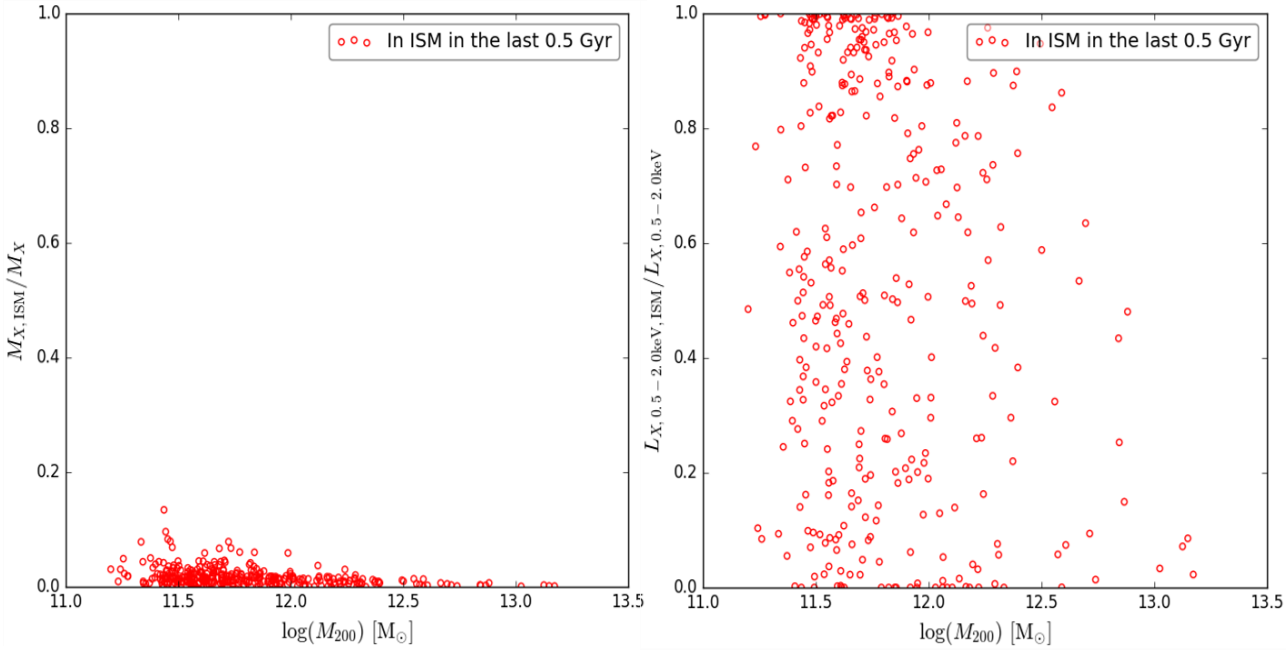

Figure 3. *Left panel:* The fraction of the X-ray luminous gas mass within r_{200} that has been in the interstellar medium of the central galaxy within the last 0.5 Gyr. *Right panel:* The fraction of the total luminosity within r_{200} that comes from this ISM-recycled gas. The halos plotted are for isolated galaxies in the Ref-L0050N0752 simulation.

in low-mass systems, dominate the luminosity of the hot CGM. This highlights the danger of inferring conclusions from simple models, and motivates the interpretation of observations by like-for-like comparisons with detailed, state-of-the-art numerical models.

4. Conclusions

In this paper, we have explored how coupling advanced plasma models to state-of-the-art cosmological simulations such as EAGLE can offer insight into how astrophysical processes such as star formation and feedback-driven winds from massive stars, supernovae and growing black holes can profoundly affect the baryon content and X-ray properties of the hot CGM. We have also demonstrated that caution should be used when assuming that the hot CGM is made up of gas driven out of the ISM by winds (as one would naïvely infer from X-ray observations) as in our simulations this gas contributes disproportionately to the luminosity. This highlights the vital importance of theoretical galaxy formation models and

large-scale simulations in guiding our interpretation of new data from the next generation of X-ray satellites. The results presented here will be expanded upon in an upcoming publication, in which we will characterise the hot CGM and probe its dynamics in more detail. In the future, we will begin generating realistic mock observations of the CGM using EAGLE galaxies, which together with our theoretical predictions, will help guide the design and development of the next generation of space-borne satellites.

5. References

Crain, R. A. *et al.*, 2010, MNRAS **407**(3), pp. 1403-1422
Crain, R. A. *et al.*, 2015, MNRAS **450**(2), pp. 1937-1961
Schaye, J. *et al.*, 2015, MNRAS **446**(1), pp. 521-554
Smith, R. K. *et al.* 2001, ApJ **556**(2), pp. L91-L95
White, S. D. M. & Frenk, C. S., 1991, ApJ **379**, pp. 52-79

Silvia Martocchia

What controls the onset of chemical multiple stellar populations in globular clusters?

S. Martocchia et al.
Astrophysics Research Institute, LJMU
s.martocchia@2016.ljmu.ac.uk

Once thought to be formed by simple stellar populations, where each star shares the same abundance and age within some small tolerance, globular clusters (GCs) have been observed to host multiple populations (MPs) of stars. This evidence has manifested through star-to-star light elements abundance variations (C, N, O, Na), which are not observed in field stars of the same metallicity. These chemical anomalies also show anti-correlations in some elements, such as the Na-O anti-correlation (Carretta et al. 2009) and the C-N anti-correlation (Cannon et al. 1998). Furthermore, evidence for MPs may be assessed through photometry, by looking at splittings and/or spreads in the clusters colour-magnitude diagrams, from the Main Sequence (MS), up to the Red Giant Branch (RGB) and Horizontal Branch (HB), by using suitable colour combinations (e.g., Piotto et al. 2015), sensitive to the elements that vary between the subpopulations.

The origin of MPs is still under debate (e.g., D'Antona et al. 2014, Bastian et al. 2015), and multiple models have been put forward. In the most popular MP formation models, a secondary population (SP) of stars is formed from the ejecta of massive evolved stars from a first population (FP), diluted with some amount of unprocessed material (e.g. Decressin et al. 2007; D'Ercole et al. 2008; de Mink et al. 2009). While the nature of stellar polluters changes in different models, none of these scenarios can reproduce the main observational properties of MPs without making ad hoc assumptions (e.g. Bastian et al. 2015, Bastian & Lardo 2015). Indeed, we still lack a self-consistent explanation of the physical processes at the basis of the MP formation and which property controls whether a GC will host MPs or not.

The presence of multiple populations in GCs appears to be ubiquitous in the most nearby galaxies. Milky Way GCs have been largely studied (Gratton et al. 2012) and almost all old (i.e., >10 Gyr) clusters surveyed so far have been found to host MPs, as well as in the Fornax dwarf galaxy (Larsen et al. 2014), in the Sagittarius dwarf galaxy (Carretta et al. 2014), in the Large Magellanic Cloud (LMC, Mucciarelli et al. 2009) and in the Small Magellanic Cloud (SMC, Niederhofer et al. 2016, Hollyhead et al. 2017). While MPs are commonly detected in massive and old clusters, light elements variations are not found in clusters of comparable age but lower mass (e.g., 10^4 M$\odot$, E3, Salinas & Strader 2015). Such evidence led many to support cluster mass as the controlling property on whether a GC will host MPs (Gratton et al. 2012). Nonetheless, the lack of chemical spreads in relatively young (~1-2 Gyr), but still massive (few times 10^5 M$\odot$) clusters found by Mucciarelli et al. 2008 suggested that cluster age may play a key role.

We present here the main result from our Hubble Space Telescope (HST) photometric survey. This consists in HST observations of 9 star clusters in the LMC/SMC. All sources have similar masses (~10^5 M$\odot$), but span a wide range of ages (from 1.5 Gyr up to 11 Gyr). The main goal of our survey is to test whether MPs are exclusively found in ancient GCs, and hence, to shed light on the physical property that controls the onset of MPs. Previous results of the survey had shown that MPs were present at ages of 6 Gyr (NGC 339 and NGC 416, Niederhofer et al. 2017a, b), but also that they were not detected in a ~1.5 Gyr old cluster (NGC 419, Martocchia et al. 2017). We report here the final results from our survey by complementing our analysis with the remaining four clusters, namely NGC 1783, NGC 1806, NGC 1846 and NGC 1978.

We used a filter combination of the form (F343N-F438W)-(F438W-F814W)≡CUnBI, which proved to be very powerful at separating subpopulations of stars with different C and N abundances. For each cluster in our survey, we fit a two-components Gaussian to CUnBI colour distribution in order to search for colour bimodality, hence subpopulations. Then, we defined δ^{RGB}(CUnBI) as the difference between the means of the two Gaussian components in the colour distribution (Fig. 1). This gives a robust indication on the level of N enrichment present in clusters which host MPs. We report evidence of multiple stellar population in the 2 Gyr cluster NGC 1978, while we do not detect MPs in the ~1.5-1.7 Gyr clusters NGC 1783, 1806 and 1846. We already found evidence for MPs in NGC 121 (age ~11 Gyr), NGC 339, NGC 416 (~6 Gyr) and Lindsay 1 (~8 Gyr). This surprisingly points toward an age effect, marking cluster age as one of the major parameter controlling the presence of MPs in clusters (Fig. 1). This finding also leads towards a fresh new perspective on to the onset of MPs, since this is completely unexpected for all suggested scenarios for the origin of MPs.

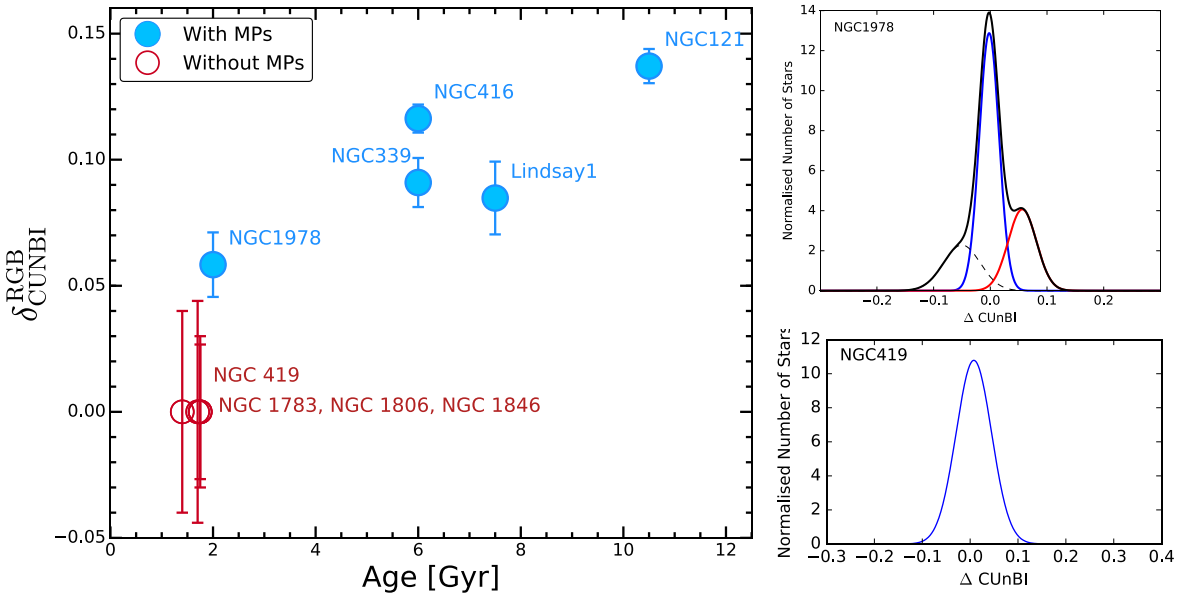

Figure 1. Left Panel: δ^{RGB}(CUnBI) as a function of Age for all 9 clusters in our HST photometric survey. Clusters which are found to host multiple populations are indicated with blue filled circles while clusters which do not show MPs are marked with red open circles. Right Panel: histograms of the distribution in ΔCUnBI verticalised colours for NGC 1978 (top) and NGC 419 (bottom). Superimposed curves represent the Gaussian multiple components fit. The fit found that NGC 1978 is best described by 3 components while only one component is found for NGC 419.

Maisie Rashman

Astronomy meets Conservation Biology: Adapting astronomical source detection techniques to detect animal sources in thermal images obtained by unmanned aerial systems

M. RASHMAN

May 2, 2017

The spectral energy distribution of warm-blooded vertebrates peaks at wave- lengths within the infrared range making this the ideal wavelength to monitor vulnerable species in the field of conservation biology. Using UAVs (unmanned aerial vehicles) and thermal-infrared cameras, high volumes of biodiversity sur- vey data can be obtained for a fraction of the time and cost of more tradi- tional methods; however data analysis techniques are poorly developed and thus greatly increase the time taken to extract meaningful scientific output. Astronomical source detection techniques are well developed for the detection and identification of astronomical bodies at infrared wavelengths and have been successfully automated for many years. We are adapting our knowledge of and experience using infrared data in astronomy to detect and identify warm blooded vertebrates in terrestrial infrared data collected by UAVs. Figure 1 shows a schematic flow chart of the four major components of the pipeline we are developing to fully automate this process.

Working with survey footage obtained in component 1 of the pipeline, we aim to evaluate the physics behind the intensity emitted by living beings at these wavelengths and to investigate how unique this is to each species. To evaluate the physical aspect of fauna detection thoroughly in component 2, we first need to understand the relationship between the intensity we observe and the true emitted intensity of the subject. Much like stars, the observed flux is

Figure 1: Flow chart of pipeline

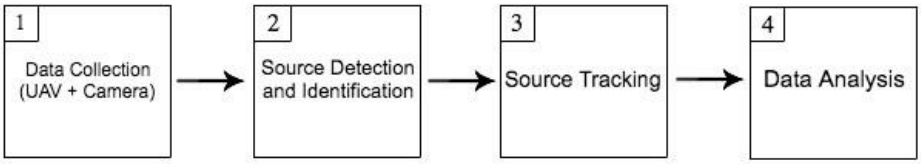

highly dependent on both the camera resolution and the atmosphere between the subject and the camera. If objects are poorly resolved a higher surface area is recorded per pixel and the flux averaged, the resulting measured temperature values will be dependent on the surrounding environment. In addition to this the emitted flux is subject to radiative transfer effects such as the absorption and emission processes of the air column between the camera and subject. To fully understand these effects on the intensity and temperature values we are working closely with Knowsley Safari Park to study a range of species and model these effects to determine how critical a role they play in transforming observed intensity values, and how this knowledge can be adapted to correct for these effects in real bio-diversity survey data.

Kirsty Taggart

CONSTRAINING GRB AND SLSN PROGENITORS USING A LARGE, UNBIASED SAMPLE OF NEARBY CORE-COLLAPSE SUPERNOVAE

Kirsty Taggart
Astrophysics Research Institute
Liverpool Science Park, IC2
E-mail address: K.L.Taggart@2016.ljmu.ac.uk

In the past 10 years we have come to realise that the range of end-points of massive stars is strikingly diverse. What produces this diversity? It appears that the environment plays a critical role. Both superluminous super- novae (SLSNe) and long duration gamma ray bursts (LGRBs) are found preferentially in faint, low mass galaxies. However we do not know the reason for this. The host galaxy properties of extragalactic transients can be used to study these progenitor populations. However, the high redshift nature of SLSNe and long duration LGRBs makes environmental studies of their galaxies difficult and a comparison sample of core collapse supernova (ccSNe) is lacking. Fortunately, with the advance of wide-field surveys we have increasingly large samples of these transient hosts at low redshift, allowing statistical comparison of the populations.

We have compiled the largest photometric catalogue of nearby SLSN, LGRB and ccSN hosts from a variety of sky surveys. We present this multi-wavelength photometry spanning from UV to near IR in a comprehensive study of the host galaxy populations. We model the observed spectral energy distribution (SED) of these host galaxies with the program Le Phare in order to derive physical properties, such as stellar mass and star formation rate. In this model, we assume the galaxy SED can be approximated by a single-age stellar population. An example of a best-fit SED to one of the CCSNe can be seen in Figure 1 and from this model we derive a stellar mass of 1.3×10^8 $M_\odot$ and a star-formation rate of 0.2 $M_\odot$/yr. We compare the stellar mass distributions, luminosity distributions and starburst fractions of transient host populations against each other and to the predicted distribution for the star forming population. This work is a step forward in understanding the progenitor population at low-redshift to aid the characterisation of high-redshift transients and help constrain the connection between ccSNe, SLSNe and LGRBs.

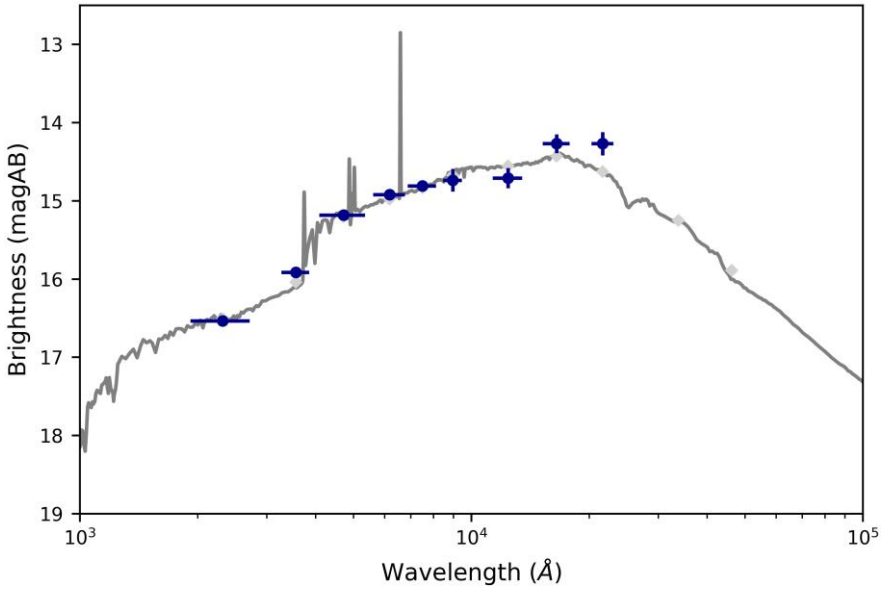

Figure 1. An example of the spectral energy distribution of CGCG012-116, a dwarf galaxy hosting the ccSNe ASASSN-16ab. The black points are the observed

magnitudes,The solid grey line displays the best-fit model of the SED. The squares in a lighter shade are the model predicted magnitudes.

Rebecca Randles

The voice of STEM: using student interviews to discuss expected learning gains.

R J Randles
School of Built Environment, Liverpool John Moores University, Henry Cotton Building, Webster Street, Liverpool, L3 2ET.
E-mail Address**:** R.Randles@2013.ljmu.ac.uk

Abstract. Following the creation of the teaching excellence framework there has been much discussion surrounding measuring student learning gains. Existing measures assume that all subjects emphasise the same skill areas. This research focuses on Science, Technology, Engineering and Mathematics (STEM) subjects specifically and interviews these students to ask them about their current and expected learning gains during their course. Critical thinking was found to be a key area of skill development with writing found to be of less importance. The interviews also revealed that measuring skills and development alone is not enough and the areas which may influence this should also be considered. The next steps in this research is to create a measure that is specifically tailored towards the skills developed on STEM subjects.

Keywords. Higher Education, Learning Gain, Students, STEM, University.

1. Introduction

The Teaching Excellence Framework (TEF) has been announced as a new framework to be implemented in higher education institutions. The idea behind this framework is to be able to grade academic institutions on their teaching quality so they are able to make improvements where needed and to allow students to be able to compare institutions when choosing where to attend (Raban and Cairns, 2015). TEF is expected to be in place with disciplinary action by the academic year of 2019/20. Recently, student learning gains has been identified as a key criterion of TEF as it will show evidence of the universities strengths and weaknesses in their teaching practices (Johnson, 2015, Johnson, 2016).

Currently, within the UK, the only widely used student outcomes assessments are the national student survey (NSS) and the UK engagement survey (UKES) which measure student engagement and satisfaction with their course. Whilst these assessments may be somewhat useful to higher education institutions, they fail to measure the gains that students have achieved (Maskell and Collins, 2017). Learning gain has been defined by the higher education funding council for England (HEFCE) as the distance travelled in students skills, competencies, content knowledge or personal development (McGrath et al., 2015).

The emergence of TEF has not only pressured institutions to drive up academic quality but has also shed light into the lack of Learning Gain measures within the UK (Jensen et al., 2008). Several pilot studies have begun to be conducted by HEFCE with 13 collaborative institutional projects with the involvement of over 70 institutions. The projects have combined the cross-sectional and longitudinal approaches to learning gain measures, as well as a range of methodologies such as standardised tests, grades and surveys. (HEFCE, 2016)

The work being conducted by HEFCE has been heavily influenced by the United States (US) who are already strides ahead of the UK with their learning gain climate. The US have several accountability initiatives in place which include the Voluntary System of Accountability (VSA) which asks institutions to use one of four measures to report college learning for example the collegiate learning assessment (CLA) (Liu et al., 2012). With the development of learning gain at its early stages in the UK, looking at

the US has allowed the UK to learn from their mistakes and to try to utilise their existing measures. However, there has been much scrutiny around these measures as they all assume that every degree emphasises the same skills, which is not the case. Therefore, it should be considered that these measures should be tailored towards specific subjects or subject groups.

Science, Technology, Engineering and Mathematics (STEM) are, arguably, the most vital subjects in order for the UK economy to strive (D'Aguiar and Harrison, 2016). Recently, the number of individuals choosing STEM-related careers has declined while the number of STEM-based careers available has increased and become much more diverse (Franz-Odendaal et al., 2016). Concerns have begun to emerge about the employment readiness of graduates of STEM subjects (Smith, 2007) however, the UK commission for employment and skills investigated this and found that only 14% of employers of STEM graduates felt that they were not employment ready (UKCES, 2012). The development of a measure that is specifically tailored to STEM subjects will allow institutions to see whether there is an increase or decline in their STEM student's ability and put necessary actions in place to improve if necessary or to confirm the effectiveness of their teaching.

In order to tailor a measure to a specific group of subjects, it is important to get the voice of the students themselves as they are the most able to inform us of the skills that they are and aren't developing. By discussing this across Science, technology, engineering and mathematics it will give the ability to see where the overlap in these skills are to allow to create this measure that applies across STEM rather than relying solely on literature.

2. Methodology

2.1 Design

Qualitative design was chosen due to the depth it can achieve and its flexibility in light of emerging findings. The use of in-depth individual interview methods was chosen as not to limit the research.

2.2 Participants and Recruitment

Participants were 7 undergraduate students who studied STEM subjects at Liverpool John Moores University. Participants were between the ages of 19 – 37, 57% of these participants were female and 43% were male. The mean age of participants was 23.71 with a standard deviation of 6.10. Participants were selected through both opportunity and purposive sampling. Although the selection of the participants was convenient, the group was specifically targeted to be students of STEM subjects.

2.3 Procedure

Participants were invited to interview in private rooms on Liverpool John Moores University Premises. Prior to the interview starting, participants were given an information sheet which they were encouraged to read as well as a written consent form that they were required to sign. Interviews were recorded using a Dictaphone and each lasted around 20 minutes in length. A Semi-Structured Interview Schedule was used by the researcher which consisted of both questions and prompts, the researcher could adapt this when needed and added some prompts to use in later interviews. Participants were debriefed by being given a debriefing sheet at the end of the interview.

2.4 Ethical Considerations

The participants were assured that their anonymity would remain intact throughout the whole interview and that the researcher would be the only one to hear the actual recording. Furthermore, the participants were informed that they could stop at any time and had the right to withdraw any information given. The participants were also made aware that there are no right or wrong answers, to reassure them and to not make the participants feel pressured to answer in a specific way. Finally, the participant was given a debriefing sheet that included the researchers contact information should the participants have any questions, comments or concerns.

3. Analysis

The findings of the interviews found four main themes; Skills Developed, Skills Not Developed, Personal Development and Learning Gain Influences. Figure one shows the higher and low level themes which derived from the interviews. Students discussed the skills which they have developed during their degree with a all of students having an emphasis on critical thinking for example "Critical analysis is key. I'd say the ability to problem solve in STEM fields is arguably the most important asset you have." However, students felt that they had not developed their writing skills much, one student suggested "I

don't think my writing has really improved but I think that's just because of the nature of my course." This was not found to be the case in the Sciences as one student noted "Now I can read back my own work and fix the writing because I know what should be there."

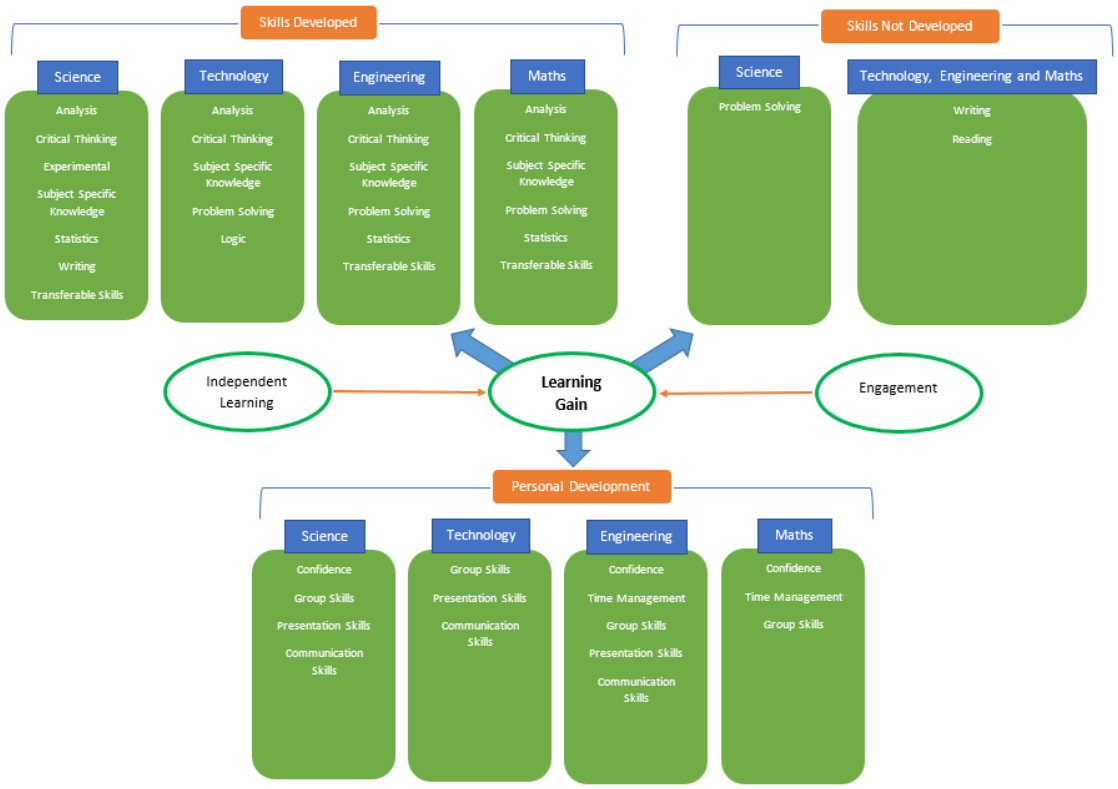

Figure one: Shows the themes found in the interviews as well as the two influences on the gains.

Student's personal development was also found to be an important Learning Gain in STEM subjects. Presentation, communication and group work were all mentioned in every interview. One student stated that "We do presentations as a key thing through-out the degree" and another student mentioned the difficulties of group work "We did a group project this year and it's the first time I've ever done a group project in my life. It was hard." Finally, there was a strong mention of the importance of independent learning and engagement as it was suggested "I think a lot of it is not necessarily what you do in class" as well as "engagement is massively important". Therefore, engagement and independent learning were chose as two constructs that influence learning gain, as shown in figure 1.

4. Conclusion and Future Steps

This research has started a unique method of looking at student learning gains by focusing specifically on STEM subjects. Having the voice of the students specifically, rather than solely using the literature, makes this research specific to these subjects within this university and is tailored to the areas in which they learn. It was surprising to find that the majority of students believed their reading and writing to had not been developed, which was an exception in the case of Science, something which has been a focus of many learning gain measures; this highlights the importance of considering learning gain as being subject-specific. In addition to this, the interviews shed light on the idea that it is not enough just to measure skills and development alone, but that there are two areas of influence on learning gain which also need to be looked into; independent learning and engagement. The next stages of this research will involve the creation of a questionnaire that will then be given to STEM undergraduate students across a period of two years.

Acknowledgements

I would like to thank my director of studies, Dr. Alison Cotgrave and my supervisors Dr. David McIlroy and Dr. Mark Pogson for helping me tremendously with participant recruitment for this stage of my research. Without their help, I would have struggled to get a good representation of STEM students in this stage of the project.

References

D'Aguiar, S. & Harrison, N. 2016. Returning from earning: UK graduates returning to postgraduate study, with particular respect to STEM subjects, gender and ethnicity. *Journal of Education and Work,* 29**,** 584-613.

Franz-Odendaal, T. A., Blotnicky, K., French, F. & Joy, P. 2016. Experiences and Perceptions of STEM Subjects, Careers, and Engagement in STEM Activities Among Middle School Students in the Maritime Provinces. *Canadian Journal of Science, Mathematics and Technology Education,* 16**,** 153-168.

HEFCE. 2016. *Learning Gain* [Online]. Available: http://www.hefce.ac.uk/lt/lg/work/.

Jensen, B., Fraine, B. D., gaer, E. V. d., Ryska, R., Frederiksen, S., Schjørring, P., Pascal, C., Grift, W. v. d., Hægeland, T., Jakubowski, M., Ferrão, M. E. & Cankar, G. 2008. Measuring Improvements in Learning Outcomes: Best Practices to Assess the Value-added of Schools. *OECD*.

Johnson, J. 2015. Green Paper - Fulfilling our Potential: Teaching Excellence, Social Mobility and Student Choice. *In:* SKILLS, D. F. B. I. A. (ed.).

Johnson, J. 2016. Success as a Knowledge Economy: Teaching Excellence, Social Mobility and Student Choice. *In:* SKILLS, D. F. B. I. A. (ed.).

Liu, O. L., Bridgeman, B. & Adler, R. M. 2012. Measuring Learning Outcomes in Higher Education: Motivation Matters. *Educational Researcher,* 41**,** 352-362.

Maskell, E. C. & Collins, L. 2017. Measuring student engagement in UK higher education: do surveys deliver? *Journal of Applied Research in Higher Education,* 9.

McGrath, C. H., Guerin, B., Harte, E., Frearson, M. & Manville, C. 2015. Learning Gain in Higher Education. *In:* CORPORATION, R. (ed.). Cambridge, UK: HEFCE.

Raban, C. & Cairns, D. 2015. Where do we go from here? *Perspectives: Policy and Practice in Higher Education,* 19**,** 107–115.

Smith, H. 2007. Stem Review: The Science, Technology, Engineering, Maths Supply Chain. London: The Council for Industry and Higher Education.

UKCES 2012. UK Commission's Employer Skills Survey 2011: UK Results. *In:* SKILLS, U. C. F. E. A. (ed.).

Jacob Greene

Non-invasive in-situ measurement of blood lactate using microwave sensors during progressive incremental exercise

Jacob Greene [1], Julien Louis [2], Olga Korostynska [3], and Alex Mason [4,5,*]
[1]Department of Built Environment, Faculty of Engineering and Technology, BEST Research Institute, Liverpool John Moores University, Liverpool, L3 3AF, UK; J.Greene@2013.ljmu.ac.uk
[2]Faculty of Science, School of Sports and Exercise Science, Liverpool John Moores University, Liverpool, L3 3AF UK; J.B.Louis@ljmu.ac.uk
[3]Department of Civil Engineering, Faculty of Engineering and Technology, Liverpool John Moores University, Liverpool, L3 3AF, UK; O.Korostynska@ljmu.ac.uk
[4]Animalia, Norwegian Meat and Poultry Research Centre, Okern 0513, Oslo, Norway
[5]Department of Built Environment, Faculty of Engineering and Technology, Liverpool John Moores University, Liverpool, L3 3AF, UK; A.Mason1@ljmu.ac.uk

Abstract. Blood lactate concentration (La) is one of the most frequently measured parameters during performance testing and clinical trials. The purpose of this trail was to test a novel real-time non-invasive sensor, which measures blood lactate values using electromagnetic radiation during progressive incremental cycling. Microwave sensors provide a real-time method of analysis, which is cost-effective, robust and has many practical applications from a sport and athletic stand point. During the study, data was collected for blood lactate (mmol/l), heart rate (bpm), and S11/S21 recordings. The data in this paper showed a typical curvilinear La response to incremental exercise in healthy untrained subjects, furthermore, there was a positive collation (R = 0.78) between lactate pro 2 measurements and sensor recording when configured in the S_{11} measurement mode and located on the test subjects arm. This research has shown evidence of a microwave sensor successfully predicting blood lactate in healthy untrained human subjects using a non-invasive technique. Future research is aimed at measuring endurance trained athletes due to their physiological adaptations involving lactate threshold.
Key words. Lactate, Non-invasive, Microwave, Sensor, Exercise

1. Introduction

Over recent decades, technology has evolved in the professional sporting environment, with ever more acceptance that meticulous attention to detail can make the difference between winning and losing. However, the process of collecting accurate data requires adapted equipment and methods which are often expensive and invasive. Advances in technology have permitted endurance athletes, sports teams, and physicians to monitor player movements [1], workloads [2], and biometric indicators [3] enabling optimisation of athletic performance and also reducing the risk of injury. To date, there are a few technologies that allow the analysis of real-time physiological factors. The sensors in this research allow further data to be collected for individual physiological player monitoring. Sensors that determine physiological response to changes in competition and training allow many benefits for sports practitioners such as nutritionists, injury rehab professionals, and strength and conditioning coaches, etc. This ability undoubtedly will lead to a more individualized approach for the athletes, which is vital at the elite end of the performance spectrum. The aim of the study was to analyse the coloration between the gold standard method against a novel non-invasive sensor which measures blood lactate values using electromagnetic radiation during progressive incremental cycling.

2. Lactate

Blood lactate levels are key to performance, monitoring of lactate is a fundamental necessity for athletes in terms of training and competition, knowing levels of lactate accumulation allow for improvements of the lactate threshold. The lactate threshold indicates the physical training level of an athlete, showing a finely tuned interplay of parameters that influence the balance between lactate production and lactate clearance.

The normal lactate response to progressive, incremental exercise is that lactate increases gradually at first

and then more rapidly as the exercise becomes more intense, it is reported that normal resting values of blood lactate range from 0.5-1.5mM [4]. During the initial onset of exercise lactate changes little, during easy to moderate intensity exercise (i.e. between 50% and 65% $V_{O2\ max}$), lactate isn't released into the muscle, and most likely due to production of lactate is balanced out due to clearance by oxidation. However, at approximately 65% of $V_{O2\ max,}$ coinciding with a rise in adrenaline, muscle lactate release starts to increase steeply, during exercise above 65% $Vo2_{max}$ values can be as high as 12mM [5]. This sudden increase occurs when the glycolytic flux and lactate production exceeds that which can be cleared by mitochondria, then the excess glycoltic flux is released as lactate. In the course of extensive physical exercise and extreme conditions this level may further increase upwards of 25mM which may also be observed 3-8 minutes' post exercise[6].

Currently the most effective technique of measuring blood lactate (La) is using the Lactate Pro 2 LT-1730 (ARKRAY). The Lactate Pro 2 only requires 0.3 µL of blood which is the smallest volume needed in the world of all current blood sampling lactate equipment. It takes 15 seconds to measure the sample with automatic calibration. However, a non-invasive method to measure blood lactate values has many practical applications within the world of sports science and medical settings. The traditional method of pricking the fingertip several times per day for many years is not only impractical and frustrating for athletes and patients but also has negative consequences such as development of scarring/callous formation, decreases in sensibility as well as perception hindrance[7].

3. Methods

The subjects were required to perform a bout of progressive incremental exercise commencing at 80 WATTS staying between 60-80 RPM (revolutions per minute) for a duration of five minutes on an ergometer bike, at the end of this period measurements were noted and exercise intensity increased by 20 WATTS every minute whist measurements were taken every two minutes. Once the participant reached maximal voluntary exhaustion, a recovery period of ten minutes with measurements recorded every two minutes. During the study results for blood lactate (mmol/l) concentration was collected and analysed (lactate Pro 2, Arkray Global Business Inc.; Shiga, Japan) via finger prick capillary blood samples of only 0.3 µL, adhering to universal procedures, as well as heart rate (bmp) using a Polar T31-CoDed in the final 10 seconds of each stage.

3.1 Electromagnetic Sensor

The sensor is designed such that the electromagnetic field is most intense close to the surface of the sensor so that the field may penetrate through the skin of a target and interact with the fluids beneath, this technique uses extremely low levels of radiation (lower than that of mobile-phones) avoiding any exposure to harmful radiation. Maintaining a field close to the sensor surface has some advantages, namely that of reducing interference from objects other than the surface it is directly attached to. The sensor was attached to the forearm directly over the flexor difitorum profundous (Figure 1) and connected to a separate Rohde and Schwarz ZVL13 Vector Network Analyser (VNA), where S_{11} and S_{21} measurements were recorded every 30 seconds via a bespoke LabView interface. The equipment was configured to capture data between 10 MHz and 4 GHz, with 4000 discrete data points recorded. The equipment was set to output 0 dBm (1 mW) power. The system configuration was selected based upon discussion with commercial partners, particularly in relation to issues such as cost and size of a future "all-in-one" wearable solution.

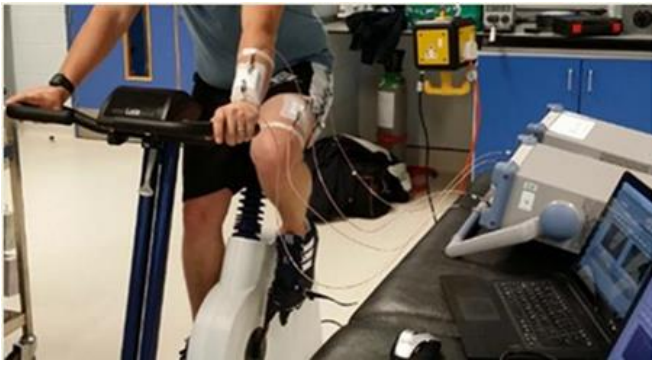

Figure 1: Experimental setup, showing participant on ergometer with sensors attached and appropriate data acquisition hardware.

4. Results

4.1 Lactate (mmol/L)

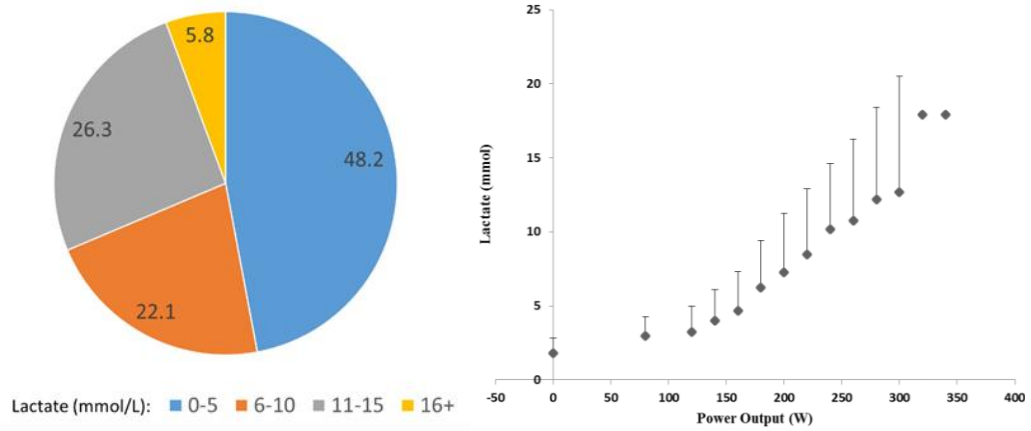

(a) (b)

Figure 2: (a) Pie chart showing the spread of lactate data collected from participants across all lactate intervals in absolute and percentage terms respectively. (b) Blood lactates (mean ± SD) response to progressive, incremental exercise test.

It was reported that there was a significant positive correlation between Lactate (mmol/L) and power output (W) (figure 2b) (r_{15} = 0.98, P < 0.001). Blood lactate was analysed against power output and reported using Pearson's correlation. Blood lactate increases linearly as power output increases in proportion to time. Due to maximal exhaustion being relative to the individual subject and their training status, the number of lactate levels ranging above 16 mmol was low (figure 2b).

4.2 Electromagnetic sensors

Using a PMI method to reduce the necessary dataset acquired from the sensor, and a NN machine learning algorithm to create a predictive model, it was demonstrated that a good correlation (R = 0.78) could be obtained when the sensor was configured in the S_{11} measurement mode, and located on the arm of the test subjects.

4.3 Heart rate (bmp)

It was reported there was a significant correlation between heart rate (bmp) and power output (W) (r_{23}=0.96, P= 0.001), heart rate was analysed against power output and reported using Pearson's correlation, this data only included heart rates up until voluntary exhaustion. It was reported that there was no significant positive correlation between blood lactate (mmol/L) and heart rate (bmp) (r_{12}=0.48, P=0.882). Lactate was analysed against heart rate and reported using Pearson's correlation.

5. Conclusion

This current paper has shown evidence of a microwave sensor successfully predicted blood lactate in human subjects using a non-invasive technique positioned on the forearm during progressive incremental cycling. Current blood sampling does not give enough resolution to understand whether a subjects lactate level is rising or falling, and therefore deciding on an intervention strategy can be challenging. Thus, being able to track the direction of lactate change is perhaps as important as knowing its absolute value. Previous research by regarding this technology has demonstrated the ability to detect a variety of different substances such as, lactate in water and types of oils and to successfully detect lactate in cerebrospinal fluid [8-10]. This shows application of this technology could provide masses of benefits to a variety of different practitioners within the world of sports and performance who want to be able to quantify previously difficult performance markers both in the laboratory and out on the field. The use of a non-invasive sensor will allow for durability, portability, and real time analysis of blood lactate levels. Further research will aim to measure the sensors capability in detecting parameters such as muscle glycogen and hydration levels non-invasively, which will have applications both in the lab and out in the field by improving the accuracy of research protocols and tracking the physiological adaptations to exercise. Although this technique is a promising concept, further research and development is needed before the sensors will influence the world of sports and exercise science. This research aims to work towards developing sensors which are more flexible in structure to manipulate to the surface of the skin and the anatomy it is places upon, and measuring lactate values about the 16mmol range using endurance trained due to their physiological adaptations and increased lactate threshold.

References

1. Loader, J., et al., *Classifying training drills based on movement demands in Australian football.* International Journal of Sports Science and Coaching, 2012. **7**(1): p. 57-68.
2. Mooney, M.G., et al., *Reliability and validity of a novel intermittent peak running speed test for Australian football.* The Journal of Strength & Conditioning Research, 2011. **25**(4): p. 973-979.
3. Foster, C.D., et al., *Heart rate responses to small-sided games among elite junior rugby league players.* The Journal of Strength & Conditioning Research, 2010. **24**(4): p. 906-911.
4. Phypers, B. and J.T. Pierce, *Lactate physiology in health and disease.* Continuing Education in Anaesthesia, Critical Care & Pain, 2006. **6**(3): p. 128-132.
5. Stanley, W.C., et al., *Systemic lactate kinetics during graded exercise in man.* American Journal of Physiology-Endocrinology And Metabolism, 1985. **249**(6): p. E595-E602.
6. Glaister, M., et al., *Familiarization and reliability of multiple sprint running performance indices.* The Journal of Strength & Conditioning Research, 2007. **21**(3): p. 857-859.
7. Heinemann, L., *Finger pricking and pain: a never ending story.* Journal of diabetes science and technology, 2008. **2**(5): p. 919-921.
8. Korostynska, O., et al., *Novel method for vegetable oil type verification based on real-time microwave sensing.* Sensors and Actuators A: Physical, 2013. **202**: p. 211-216.
9. Blakey, R., et al., *Real-time microwave based sensing method for vegetable oil type verification.* Procedia Engineering, 2012. **47**: p. 623-626.
10. Mason, A., et al., *A resonant co-planar sensor at microwave frequencies for biomedical applications.* Sensors and Actuators A: Physical, 2013. **202**: p. 170-175.

Daniel Yazdani

Robust optimization over time using a new particle swarm optimization

D Yazdani, T T Nguyen and J Wang
Liverpool Logistics, Offshore and Marine Research Institute, Faculty of Technology and Engineering, Liverpool John Moores University
E-mail address: D.Yazdani@2016.ljmu.ac.uk, T.T.Nguyen@ljmu.ac.uk, J.Wang@ljmu.ac.uk .

Abstract. Dynamic optimization problems (DOPs) are optimization problems that change over time, and most investigations in this area are focused on tracking the moving optimum efficiently. However, continuously tracking a moving optimum is not practical in many real-world problems because changing solutions frequently is not possible or very costly. Recently, another practical way to tackle DOPs has been suggested: robust optimization over time (ROOT). In ROOT, the main goal is to find solutions that can remain acceptable over an extended period of time. In this paper, a new multi_swarm PSO algorithm is proposed in which dif-ferent swarms track peaks and gather information about their behaviour. This in-formation is then used to make decisions about the next robust solution. The main goal of the proposed algorithm is to maximize the average number of environ-ments during which the selected solutions' quality remains acceptable. The exper-imental results show that our proposed algorithm can perform significantly better than existing work in this aspect.

Keywords. Robust optimization over time; Dynamic optimization problems; Tracking moving optima; Particle Swarm Optimization; Multi-swarm algorithm

1. Introduction

Many real-world optimization problems are dynamic and changing over time. Most of previous studies in this domain focus on tracking the moving optimum [1]. However, this is not practical in many cases since changing solutions may be very costly, and changing the solution frequently is not possible. As a result, there is a gap between academic research and real-world scenarios in this domain. Recently, a new approach for solving DOPs was proposed to address the above concern that aims at finding solutions that are robust over the course of time [2]. A robust solution is one that is not necessarily the best solution in the environment, but at least is acceptable. A found robust solution can be utilized until its quality degrades to an unacceptable level in the current environment. In case the current robust solution becomes unsatisfactory, a new robust solution must be chosen. Therefore, the task for addressing the DOPs in this approach is not to find the best solutions in each environment but to find robust solutions that can remain acceptable for a large number of environments. The process of finding such a sequence of robust solutions is referred to as robust optimization over time (ROOT) [2,3].

In [2] ROOT was proposed as a new perspective on DOPs. In [4], a new framework for ROOT algorithms was proposed in which the algorithm searches for robust solutions by means of local fitness approximation and prediction. In this framework, an adapted radial-basis-function was used as the local approximator and an autoregressive model as the predictor. The metric in this framework uses the average of current fitness value of a solution, its p previous fitness values (by approximator) and its q future fitness values (by predictor) to search for robust solutions. In [5], authors proposed two different robustness definitions and metrics, namely survival time and average fitness. The survival time is the maximum time interval in which the fitness of the robust solution remains acceptable, and the average fitness is the fitness value of the robust solution in a pre-defined time window. Then, two metrics and also performance indicators were defined based on these two definitions. In this framework, an autoregressive model is used as the predictor. In [12], a new multi-objective method was proposed to find robust solutions that can maximize both of survival time and average fitness. In this paper, we propose a new algorithm for ROOT based on multi-swarm PSO. The main goal of this algorithm is to maximize the average number of environments that the robust solutions remain acceptable i.e., we focus on the survival time definition of ROOT [5,6].

The remainder of this paper is structured as follows. Section 2 presents the pro-posed algorithm. In Section 3, a new generic performance indicator is presented for ROOT and the experimental result, analysis and comparison with previous works are shown in this section. In the final section, we summarize the main findings and suggest directions for future work.

2. A new PSO algorithm for robust optimization over time

In this section, a new algorithm based on Multi-swarm PSO [8] is proposed for ROOT. In the proposed algorithm, Multi-swarm PSO behaves in a similar way to previous multi-swarm algorithms proposed to track a moving optimum, *i.e.*, our algorithm tries to find all peaks and track them after each environmental change. However, while tracking peaks, our algorithm gathers information about the behaviour of all peaks. Then, our algorithm uses this information to choose a robust solution on peaks that have the most suitable characteristics based on the aim to maximize the number of environments that a robust solution remains acceptable.

From another point of view, our algorithm predicts the robustness of solutions based on this information. In order to highlight the difference of our algorithm with previous works [4,5], it is worth mentioning that in the previous frameworks, specific estimators were adopted and used in order to search for robust solutions. In addition, the fitness function for algorithms was based on average of these estimated values. But, our algorithm is different in that we use the normal fitness function for dynamic optimization and use information the algorithm has gathered to make decisions about which peak is the best for choosing a robust solution. So, in the proposed algorithm we do not use any specific estimator and the algorithm relies on previous behaviour of peaks in order to predict future of candidate robust solutions on them.

In the proposed algorithm, there is a *Finder_swarm* that is responsible for searching for uncovered peaks. Additionally, there are *Tracker_swarms* that have two main tasks, namely tracking peaks and gathering information about the behaviour of their covered peak. Each Tracker_swarm stores in its memory the difference between fitness value of the best found position in each environment with its fitness value after environmental change. The average of these values (named *Fit_drop*) shows how much the fitness value of points close to the top of the peak is expected to change after an environmental change. In addition, each *Tracker_swarm* stores the Euclidean distance between its *Gbest* at the end of successive environments, and the average of these distances reflect the *shift_severity* of each peak.

At the beginning, there is only one *Finder_swarm* in the problem space. After it converges to a peak [8], a new Tracker_swarm is created in place of the *Finder_swarm*, and the *Finder_swarm* is re-initialized to continue its global search for finding another possibly uncovered peak. On the other hand, the Tracker_swarm performs a local search for exploiting its peak and aims to reach the top of it.

In the proposed algorithm, exclusion mechanism [7] is used to avoid covering each peak by more than one *Tracker_swarm*. If the *Finder_swarm* converges to a covered peak (if the Euclidean distance between *Gbest* of *Finder_swarm* with *Gbest* of each *Tracker_swarm* is less than r_{excl} [[8]8]), it will be re-initialized. Moreover, if the Euclidean distance between *Gbest* of two *Tracker_swarms* is less than a value r_{excl}, then the older swarm is kept because of its valuable memory and the other one is removed.

For change detection, the algorithm re-evaluates all *Gbest* positions of all *Tracker_swarms* in each iteration and if any obtained fitness value is different from the saved ones, then a change in the environment is detected. After change detection, first of all, all *Tracker_swarms* store the difference of the new fitness values of their *Gbest* with their saved value to obtain *Fit_drop*. After this, all *Pbest* positions [13] in *Finder_swarm* re-evaluate and a re-diversification mechanism [[8]8] is done by all *Tracker_swarms* based on obtained *Shift_Severity* value for each peak.

In the proposed algorithm, robust solutions are chosen from the best found positions by all *Tracker_swarms* according to a decision making process based on current fitness value as well as *Fit_drop*. For making a decision about the current robust solution, its quality is checked at the end of each environment based on a user-defined lower bound threshold δ [5,6]. Having this type of threshold is realistic in many real-world problems where there is a specification indicating the acceptability of a solution. If the fitness value of the robust solution is better than δ, then it is deemed acceptable and the robust solution is kept for at least another environment, otherwise the algorithm must choose a new robust solution.

The next robust solution will be a *Gbest* position of one of the *Tracker_swarms*. The best location for the next robust solution is a peak with the highest fitness value and lowest *Fit_drop*. In the proposed algorithm, the next robust solution position is placed on the *Gbest* of a *Tracker_swarm* which is chosen by (1):

$$C = argmax_{i=1}^{i=S}(f(Gbest_i) - Fit\_Drop_i) \quad (1)$$

where S is the number of *Tracker_swarms*, $f(Gbest_i)$ is the *Gbest* fitness value of the i^{th} *Tracker_swarm*, C is the index of a *Tracker_swarm* in which the next robust solution is located. This equation suggests how much the fitness value of a peak solution is dropped in the next environment, based on the difference between it's the current fitness value and the past behaviour (*Fit_drop*). The equation allows choosing a robust solution that may likely keep its quality for a greater number of changing environments.

3. Experimental results and their analysis

In this section, the proposed algorithm is tested on a modified version of the Moving Peak Benchmark [[9]9] (mMPB) [[5]5] in which each peak has its own *height_severity* and *width_severity*.

In the proposed algorithm, the problem is solved by multi_swarm PSO as a maximization problem. Our algorithm tries to track moving peaks and gathers information about them. Additionally, it uses this information as well as *Gbest* fitness values of *Tracker_swarms* for choosing the next robust solution in its decision making process. The main goal of this process is that the chosen robust solutions keeps their quality above the threshold δ over a larger number of environments. As a result, the average number of environments that each robust solution remains acceptable is used as a performance measure as follows:

$$\text{Average } Robustness = \frac{Number\ of\ Environments}{Number\ of\ Robust\ Solutions} \qquad (2)$$

where *number of environments* shows how many times the environment changes, and *number of robust solutions* indicates the number of times that the algorithm changed the robust solution because the existing robust solutions no longer remains acceptable. The parameter setting of the proposed algorithm is the same as [8]. Table 1 shows the experimental results of the proposed algorithm. In table 1, *Offline_error* [[11]11] shows the performance of Multi_swarm PSO. Additionally, RS_error shows the average error of robust solutions in all environments and *RS_Fit* shows the average fitness value of robust solutions in all environments. Also the numbers in parentheses are *standard_error*.

The average error of robust solutions decreases when δ increases because the proposed algorithm tried to keep fitness value of robust solutions above δ and change them if their fitness value came under δ. As a result, with higher values of δ, fitness values of acceptable robust solution increases, and the error decreases. Therefore, when δ increases, the average fitness value of robust solutions increases, at the expense of requiring more changes.

Table 1. Results of the proposed algorithm on mMPB with δ=40, 45, and 50.

δ	Offline_error(std_error)	RS_error(std_error)	RS_Fit(std_error)	Average Robustness(std_error)
40	0.02(0.01)	9.31(0.25)	53.15(0.28)	8.34(0.63)
45	0.02(0.01)	6.96(0.22)	55.82(0.20)	6.83(0.65)
50	0.02(0.01)	5.20(0.14)	58.13(0.14)	4.24(0.18)

To compare the result of proposed algorithm with that of previous works in the field of ROOT, in [[12]12], the number of robust solutions for the proposed Multi-objective ROOT algorithm and the ROOT algorithm from [5] are reported. Since the experiments in [12] were done on the same benchmark and for the same number of environments as this paper, the *Average Robustness* of existing works *i.e.* works in [5] and [12] can be calculated by (2) and compared with our algorithm.

Table 2. The Average Robustness obtained by the three algorithms on mMPB.

	Average Robustness		
δ	Fu's Algorithm [[5]5]	Guo's Algorithm [[12]12]	Proposed Algorithm
40	2.30	2.67	**8.35**
45	1.91	2.08	**6.83**
50	1.53	1.61	**4.25**

4. Conclusion

In this paper, a new multi-swarm PSO algorithm has been proposed for robust optimization over time (ROOT). The main goal of the proposed algorithm is finding robust solutions that remain acceptable for a longer time, *i.e.*, solutions with fitness quality above an acceptance threshold over a number of environments. The proposed algorithm differs from previous work to find ROOT solutions. We use PSO

Tracker_swarms that track peaks and gather information about how they react to changes. Then, the selection of the next robust solution is based on this information. The experimental results show that our proposed algorithm performs significantly better than existing work in terms of Average Robustness.

5. Acknowledgements

This work is supported by a Dean Scholarship by the Faculty of Engineering and Technology, Liverpool John Moores University, and is partially supported by a T-TRIG project by the UK Department for Transport, a Newton Institutional Links project by the British Council and a Newton Research Collaboration Programme (3) by the Royal Academy of Engineering.

6. References

[1] Nguyen T T, Yang S and Branke J 2012 Evolutionary dynamic optimization: A survey of the state of the art *Swarm and Evolutionary Computation* pp 1–24

[2] Yu X, Jin Y, Tang K and Yao X 2010 Robust optimization over time – a new perspective on dynamic *IEEE Congress on Evolutionary Computation* pp 1–6

[3] Fu H, Sendhoff B, Tang, K and Yao X 2012 Characterizing environmental changes in robust optimization over time *IEEE Congress on Evolutionary Computation* pp 1–8

[4] Jin, Y, Tang, K, Yu X Sendhoff, B and Yao X 2013 A framework for finding robust optimal solutions over time *Memetic Computing* 5(1) pp 3–18

[5] Fu H, Sendhoff B, Tang K and Yao X 2013 Finding robust solutions to dynamic optimization problems *Applications of Evolutionary Computation, Lecture Notes in Computer Science* pp 616–625

[6] Fu H, Sendhoff B, Tang K and Yao X 2015 Robust optimization over time: problem difficulties and benchmark problems *IEEE Transaction on Evolutionary Computation* 19(5) pp 731–745

[7] Blackwell T and Branke J 2006 Multiswarms, exclusion, and anti-convergence in dynamic environments *IEEE Transactions on Evolutionary Computation* 10(4) pp 459–472

[8] Yazdani D, Nasiri B, Sepas-Moghaddam A and Meybodi M R 2013 A novel multi-swarm algorithm for optimization in dynamic environments based on particle swarm optimization *Applied Soft Computing* 13(4) pp 2144–2158

[9] Branke J 1999 Memory enhanced evolutionary algorithms for changing optimization problems *IEEE Congress on Evolutionary Computation* pp 1875–1882

[10] Eberhart R C and Shi Y 2001 Comparing inertia weights and constriction factors in particle swarm optimization *IEEE Congress on Evolutionary Computation* pp 84–88

[11] Yang S and Li C 2010 A clustering particle swarm optimizer for locating and tracking multiple optima in dynamic environments *IEEE Transactions on Evolutionary Computation* 14 (6) pp 959–974

[12] Guo Y, Chen M, Fu H and Liu Y 2014 Find robust solutions over time by two-layer multi-objective optimization method *IEEE Congress on Evolutionary Computation* pp 1528–1535

[13] Kennedy J and Eberhart R 1995 Particle swarm optimization *IEEE International Conference on Neural Networks* 4 1942-1948

Ross Kelly

Investigating the role of lactate and proton efflux in extracellular acidification using a pH dependent *in silico* model of hepatic glycolytic flux

Ross A. Kelly[a], Joseph Leedale[b], Andy Harrell[c], Daniel A. Beard[d], Amy E. Chadwick[e] and Steve Webb[a1]

[a] Department of applied mathematics, Liverpool John Moores University, Byrom Street, Liverpool, L3 3AF.

[b] Department of Mathematical Sciences, University of Liverpool, Liverpool L69 7ZL, UK

[c] GlaxoSmithKline, David Jack Centre for Research, Park Road, Ware SG12 0DP, UK

[d] Department of Molecular & Integrative Physiology, University of Michigan, Ann Arbor, MI 48109, USA

[e] MRC Centre for Drug Safety Science, the Department of Clinical and Molecular Pharmacology, The University of Liverpool, Ashton Street, Liverpool L69 3GE, UK

Abstract

The role of lactate/H^+ efflux as the predominant driving force of extracellular acidification rate (ECAR) during *in vitro* extracellular flux analysis (EFA) was investigated using a novel mathematical model of hepatic bioenergetics, which is pH-dependent with respect to reaction equilibria and enzyme kinetics. *In silico* ECAR was modelled using the liver-specific monocarboxylate transporter 1 (MCT1) flux; recognising that lactic acid exists as its lactate anion and a proton at physiological pH. Glycolytic proton production rate (PPR_{gly}) was separated from *in vitro* ECAR measurements by accounting for the EFA media buffering power, followed by deducting calculated respiratory contributions to acidification. The model was validated with *in vitro* HepG2 cell EFA data and used to analyse PPR_{gly} as a function of MCT1 flux. Sensitivity analysis revealed MCT1 transporter constants K_{eq} and V_{max} ranked as the two most sensitive parameters within the model. The validated model accurately simulated *in vitro* hepatic PPR_{gly}, eliciting lactate/H^+ efflux via the MCT1 as a suitable driver of glycolytic rate. The model emphasises the importance of separating PPR_{gly} from ECAR when scrutinizing *in vitro* EFA data quantitatively, especially when used to explore potential drug induced bioenergetic toxicity, due to ECAR also being a function of respiratory acidification.

Keywords

Extracellular acidification rate, proton production rate, lactic acid, MCT1, extracellular flux analysis, *in silico*, hepatic glycolytic flux

1. Introduction

Extracellular flux analysis (EFA) is gaining momentum as a versatile, high throughput method of assessing cellular bioenergetics for a plethora of biological points of interest, boasting inclusion in over 1500 peer reviewed publications (1) and is commonly used as a method of investigating drug-induced mitochondrial dysfunction in a wide variety of different cellular systems (2-4). EFA, using any of the XF analysers (Seahorse instruments), is accomplished by the use of biosensors within a specialised sensor cartridge that measure rates of oxygen consumption and proton efflux. The majority of investigations centre on changes in cellular respiration, quantified by deviations of oxygen consumption rate (OCR), with up until recently, the concomitant ECAR measurements assumed indicative of glycolytic flux. Respiratory contributions to ECAR may be easily quantified by measuring the buffering power (BP) of the EFA media, allowing quantification of the media's ability to manage changes in pH, while also considering the maximum amount

of H^+ generated per oxygen molecule consumed (5, 6). Depending upon the experimental conditions and cell type ECAR may be either almost entirely respiratory, or almost entirely glycolytic (5). Despite this, separation of glycolytic specific acidification remains largely underutilised. Such neglect to differentiate between the two outputs may stem from the ambiguities surrounding the source of ECAR. Glycolytic acidification is widely accepted to be a function of lactic acid efflux into the extracellular space, with subsequent weak acid dissociation occurring at physiologically relevant media pH (7.0 – 7.4) as a result of lactic acid having a pKa value of 3.86 (7).

This paper describes a unique pH-dependent, thermodynamically-driven kinetic model of hepatic glycolysis, capable of computing a comprehensive dynamic pH time course that is representative of EFA ECAR measurements. The model captures the rapid binding and unbinding of protons and metal ions with all modelled biochemical species in order to compute a total proton stoichiometry. Accounting for complete proton stoichiometry is crucial, as model ECAR/PPR_{gly} output is calculated by using lactate/H^+ efflux through the liver specific monocarboxylate transporter 1 (MCT1) (11). The model is aligned with *in vitro* liver specific experimental data, such that simulated ECAR changes are a function of lactate/H^+ efflux. ECAR sensitivity was determined during sensitivity analysis, yielding the most sensitive model parameters coupled to the respective biochemical reactant. The model was subsequently used to predict changes in extracellular acidification during *in vitro* media removal, consequently eliciting the potential metabolic and physical consequences with respect to ECAR that would not be possible experimentally. This model is the first of its kind with respect to simulating ECAR/PPR_{gly} via the MCT1 as a function of hepatic glycolytic rate only, by deducting respiratory contributions to extracellular acidification.

2. Methods

2.1 *Model Development*

The mathematical model of hepatic glycolysis consists of 26 state variables, 14 enzyme-mediated reactions and two transport fluxes, housed in two compartments: Cytoplasm and Extracellular space (Figure 1). Variable and reaction abbreviations are given in **Error! Reference source not found.** and 2 respectively. Reaction and transporter kinetics are modelled using kinetic terms and parameters sourced from the literature, or by fitting to experimental flux data. A comprehensive list of all kinetic terms can be found in the appendix. Flux units for the model are given as mM min^{-1}.

2.1.3 *Kinetic equations and parameters*

Transporter and glycolysis enzyme reaction equations, as well as initial parameter estimates, are all sourced from the literature (Table 2 Appendix), predominantly from a comprehensive model of human hepatic glucose metabolism from Koenig et al. (9). Additional reaction equations and parameters are based on experimental data from both the literature and experimental data. V_{max} values have been selected from the literature when possible, or derived from experimental data when unavailable. All literature sourced parameter values can be found in supplementary information appendix B. For model alignment with experimental data, certain model parameters were adjusted using unconstrained nonlinear optimization (Nelder-Mead), starting with an initial literature-based parameter estimate. All rate equations and parameters are liver specific, and can be found in the appendix along with their corresponding references.

3. Results and Discussion

3.1 *Sensitivity analysis*

Testing the sensitivity of a metabolic model with respect to its parameters is a crucial way of assessing its robustness. Variables that are most receptive to parameter perturbations can be identified by measuring changes in time-course simulations following parameter variation and, consequently, parameters that must be treated with care when measured and used can also be defined. Sensitivity analysis may be presented in many forms depending upon the state of the system. For this model, we elected to measure the percentage mean change of the j^{th} variable with respect to a -99% to +400% change in the i^{th} parameter (Equation 8). We define V_j as the j^{th} variable over time; V_j^{ibase} is the j^{th} variable over time with the base value for the i^{th} parameter;. V_j^{ival} is the j^{th} variable over time with a perturbed value for the i^{th} parameter; with ival ϵ [-99,400%] of its base value. We denote Mean (V_j(t)) as the mean value of the jth variable over the time course t ϵ [0,300]mins, where || denotes absolute value.

A parameter is classed as mildly sensitive (*MS*) if a change in any variable as a result of parameter manipulation is between 1 - 10% absolute mean change relative to the parameter change, and sensitive (*S*) if >10% is observed over a 300-minute simulation (Figure 1). A comprehensive list of all parameters may be found in the supplementary information. Sensitivity analysis presented 8 sensitive parameters: phosphofructokinase (PFK) V_{max} (*MS*), triosephosphate isomerase (TPI) K_{eq} (*MS*), dihydroxy-acetone phosphate (DHAP) K_m (*MS*), glyceraldehyde dehydrogenase (GAPDH) K_{eq} (*MS*), K_m NAD (*MS*), lactate

dehydrogenase (LDH) V_{max} (*MS*), MCT1 K_{eq} (*S*) and V_{max} (*S*). The two most sensitive parameters with respect to lactate, K_{eq} and V_{max} for the MCT1 transporter are expressed as % mean change of its initial value, (given in the supplementary information appendix B) (Figure 5). Additional parameter sensitivity plots can be located in the supplementary information. With two out of three MCT1 transporter parameters registering as sensitive, parameter selection for this enzyme mediated reaction must be carefully considered, especially when MCT1 transporter flux is to be used for simulating ECAR.

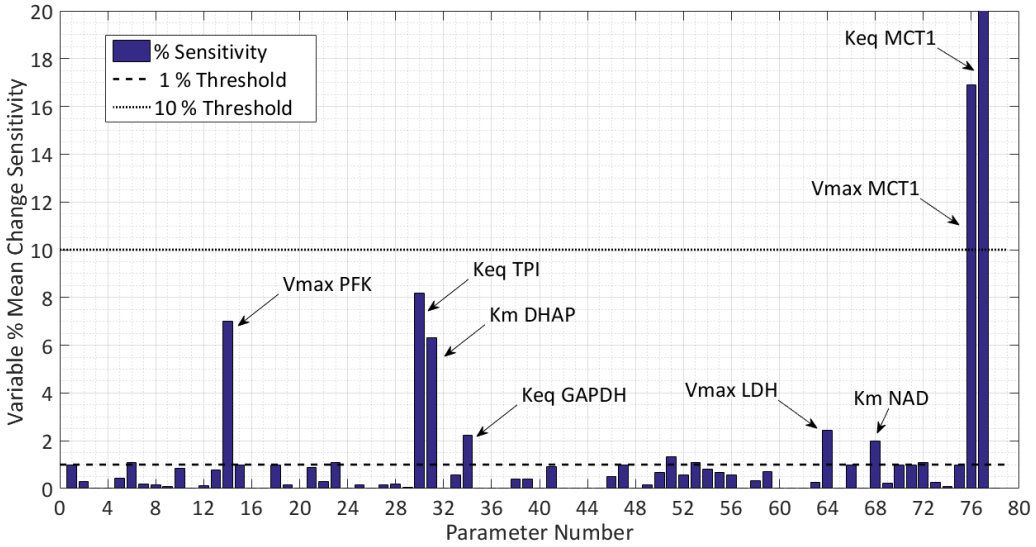

Figure 1. Sensitivity analysis. 78 model parameters were varied between -99% to +400% of their default values to identify the maximum % mean change in any variable and provide a measure of sensitivity relative to parameter change variation. The 8 most sensitive parameters are annotated.

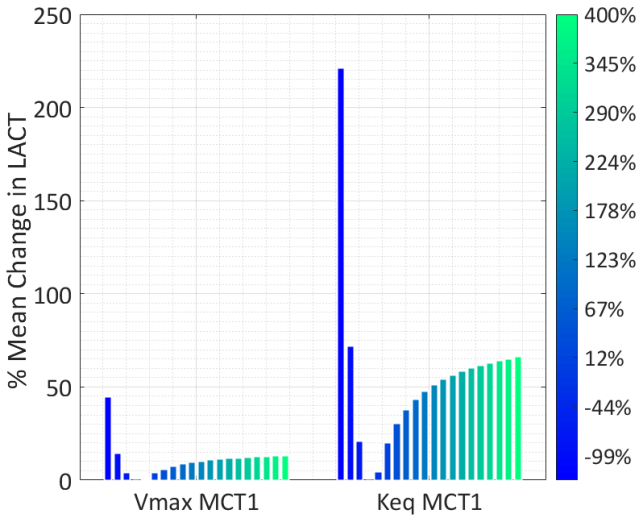

Figure 2. Sensitive model parameters illustrating changes in intracellular lactate concentration. % mean changes in intracellular lactate concentration as a function of sensitive parameter manipulation are shown compared to their initial steady state condition. Lactate is more susceptible to changes in the equilibrium constant, Keq, than to the Vmax of MCT1 co-transporter kinetics.

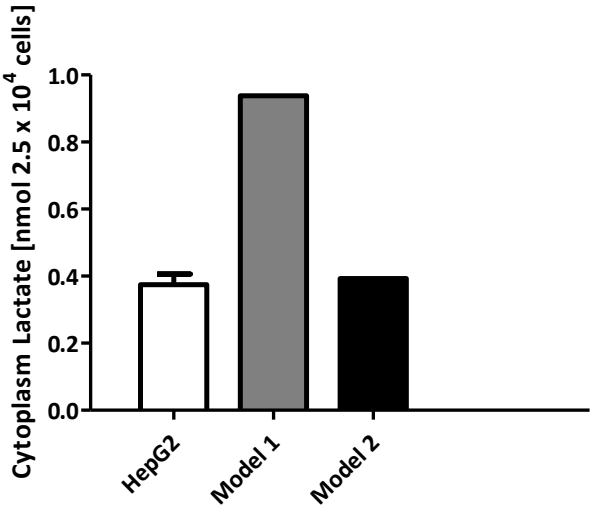

Figure 3. Intracellular lactate concentration after 48 hr: Model intracellular lactate concentration was aligned with experimental data from HepG2 cells after 48 hr. Model 1 simulation represents the lactate concentration pre-parameter adjustment with all model parameters obtained from the literature, with Model 2 simulation indicative of post-parameter adjustment.

Figure 2 shows the effects of changes in Vmax MCT1 and Keq MCT1 on intracellular lactate concentrations. The initial parameter was altered from -99 % to +400 % in 21 iterations, as shown with the

21 bars for each plot. Evidently, intracellular lactate concentration is more sensitive to the MCT1 equilibrium constant than the Vmax. However, both parameters satisfy the sensitive criteria threshold (Figure 1).

3.3 *Model parameterization: Cytoplasm lactate content*

In order to accurately choose the values for the identified sensitive parameters, the model was fitted to *in vitro* intracellular lactate concentration. Luk et al. measured the intracellular lactate concentration of HepG2 cells during their study of the effects of miR-122 on pyruvate kinase (18). Their data was used for comparison of the model simulations of the cytoplasm concentration of lactate over an extended time course of 48 h. Initial simulations were improved upon by fitting the two sensitive parameters of the MCT1 (Figure 3). Parameter adjustment was performed using unconstrained nonlinear optimization as described in the methods section, such that V_{max} MCT1 and K_{eq} MCT1 values adjusted from 33 mM min^{-1} and 1, to 2.0 x 10^{-3} mM min^{-1} and 1.15 x 10^{2} respectively, where equilibrium constants are unitless. Steady state cytoplasm levels of lactate in the model prior to parameter adjustment were approximately three times higher than *in vitro* amounts. Minor adjustment to the MCT1 V_{max} parameter provided a more comparable *in vitro – in silico* intracellular steady state concentration of lactate, while simultaneously leaving other variable and flux steady state concentrations largely unaltered (% changes in steady states given in the supplementary information).

3.4.1 *Model Validation: Simulating EFA PPR_{gly} & ECAR*

The model was validated by comparison EFA PPR_{gly} and ECAR experimental data that was not used for the original parameterization. The model was used to recreate EFA analysis data obtained experimentally (Appendix) generating both profiles for ECAR and PPR_{gly} using the MCT1 flux term. Furthermore, the model was used to simulate EFA, capturing the cell incubation and media change prior to EFA, assessing the model's ability to respond to extracellular changes that are cannot be measured experimentally. The *in vitro* experiment therefore consists of a 1440 min (24 h) incubation in high glucose environment (25 mM), followed by extracellular lactate and glucose removal during a 60 min incubation in unbuffered media prior to EFA. Glucose is reintroduced at t = 1500 min after the end of the glucose-free incubation, followed by 120 min of measurements. The model simulation was normalized to the average protein content of the respective wells (Figure 4).

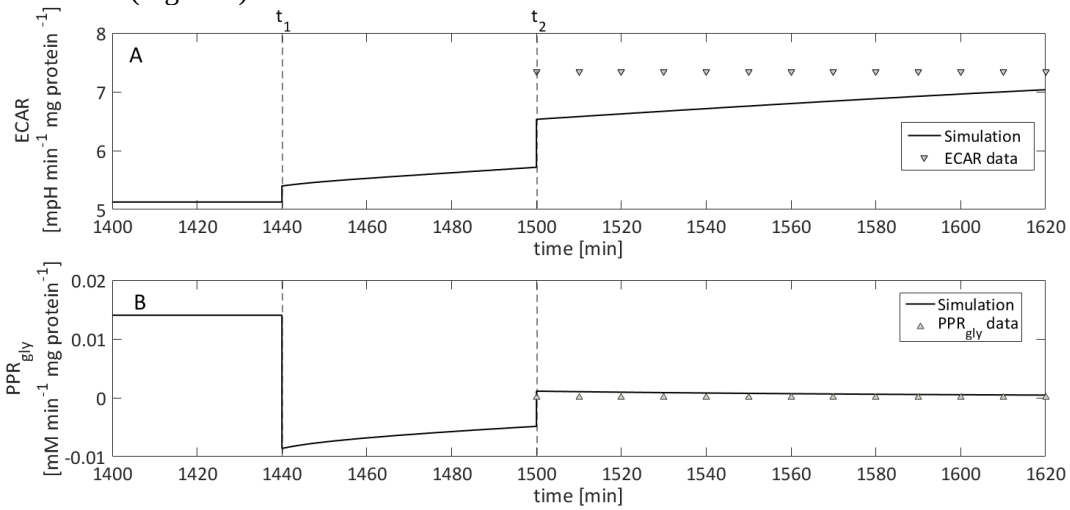

Figure 7. ECAR and PPR_{gly} simulation. A, model simulation of ECAR (*solid line*) compared to *in vitro* ECAR (*triangles*) normalized to protein content, taken from 5 mM glucose EFA results (Figure 2.). B, model simulation of PPR_{gly} (*solid line*) compared to *in vitro* PPR_{gly} (*triangles*) normalised to protein content for 5 mM glucose experiments. PPR_{gly} data was taken from EFA results (Figure 2) followed by adjusting each ECAR measurement for respiratory contributions, as well as extracellular media buffering power. At t_1 all extracellular model variables are reset to zero to mimic *in vitro* media change, at t_2 glucose is reintroduced at 5 mM, using this concentration as the initial parameter and rate expressions from the literature are based on this concentration. Full simulation time course can be found in the supplementary information.

Simulated ECAR and PPR_{gly} is in good accordance with experimental observations. Simulated ECAR was expectedly short of experimental values, owing to the omission of respiratory contributions within the model. The model was able to accurately simulate PPR_{gly} using the MCT1 flux only, suggesting that

lactate/H^+ is likely responsible for glycolytic extracellular acidification, which is in good agreement with the literature (19-21). As is apparent in Figure 4, the model is better suited to recapitulate PPR_{gly} rather than ECAR, likely due to the model comprising of glycolytic acidification mechanisms only. It is then unsurprising that simulated ECAR falls short of experimental data. The model simulates the changes in extracellular acidification as a function of changes in extracellular environment at t_1 where extracellular glucose and lactate are removed, as well as t_2 when 5 mM of glucose is introduced (Figure 4). The resulting PPR_{gly} is therefore a function of extracellular homeostasis, suggesting that extracellular glucose and lactate concentration play a greater role in ECAR and PPR_{gly} levels than expected.

4. Conclusion

A novel pH-dependent model of hepatic glycolytic flux was constructed and used to simulate *in vitro* HepG2 ECAR and PPR_{gly}. Mathematically expressing glycolytic rate as a function of the MCT1 is unique to this work and as such, gives credence to lactate and proton efflux as the predominant driving force of PPR_{gly}. Extracellular flux analysis using HepG2 cells elucidated the relationship between ECAR and OCR dependent upon extracellular glucose concentrations. Specifically, a distinct metabolic switch was observed from respiratory to glycolytic activity when cells were exposed to glucose after brief fasting (60 min). Measuring the buffering power of EFA media allowed the determination of respiratory contributions to ECAR thus enabling the separation of ECAR due strictly to glycolytic acidification (Appendix). These calculations highlighted that glycolysis is the predominant driver for extracellular acidification. This work illustrates the important discrepancies between ECAR and calculated PPR_{gly}, with ECAR simulations falling short of experimental data. We therefore strongly recommend the use of PPR_{gly} rather than ECAR as an indicator of cellular glycolytic rate. Overall, the model demonstrates that MCT1 flux, and subsequently H^+/lactate flux, in the context of glycolytic flux is more than capable of recapitulating *in vitro* PPR_{gly}. These findings supports lactic acid as the predominant source of glycolytic acidification, while simultaneously illuminating the shortcomings of using ECAR as an indicator of glycolytic rate. The construction and simulations of this model are testament to the quality of parameterized models currently available in the literature, as well as the development of toolsets such as BISEN that aid the generation of multi-compartment systems of ODE's that account for dynamic ionic buffering and thermodynamics. Overall, the model highlights the inadequacy of using ECAR as an indicator of glycolytic rate when glycolytic specific acidification is so readily accessible. Furthermore, modelling the glycolytic rate as a function of the MCT1 transporter flux in terms of PPR_{gly} facilitates negative flux expression depending upon transporter directionality, avoiding asymptotic results when using logarithms to recapitulate ECAR. Finally, this work will impact the way extracellular flux analysis results are expressed in the field of bioenergetics, recommending the use of PPR_{gly} rather than ECAR when measuring glycolytic energy metabolism.

References

1. Technologies A. Publications with Seahorse XF Data. 2017.
2. Kamalian L, Chadwick AE, Bayliss M, French NS, Monshouwer M, Snoeys J, et al. The utility of HepG2 cells to identify direct mitochondrial dysfunction in the absence of cell death. Toxicology in Vitro. 2015;29(4):732-40.
3. Sauerbeck A, Pandya J, Singh I, Bittman K, Readnower R, Bing G, et al. Analysis of regional brain mitochondrial bioenergetics and susceptibility to mitochondrial inhibition utilizing a microplate based system. Journal of Neuroscience Methods. 2011;198(1):36-43.
4. Wills LP, Beeson GC, Trager RE, Lindsey CC, Beeson CC, Peterson YK, et al. High-throughput respirometric assay identifies predictive toxicophore of mitochondrial injury. Toxicology and applied pharmacology. 2013;272(2):490-502.
5. Mookerjee SA, Brand MD. Measurement and Analysis of Extracellular Acid Production to Determine Glycolytic Rate. Journal of visualized experiments : JoVE. 2015(106):53464.
6. Mookerjee SA, Goncalves RL, Gerencser AA, Nicholls DG, Brand MD. The contributions of respiration and glycolysis to extracellular acid production. Biochimica et biophysica acta. 2015;1847(2):171-81.
7. Database POC. Lactic Acid. National Center for Biotechnology Information. 2014.
8. Gille C, Bölling C, Hoppe A, Bulik S, Hoffmann S, Hübner K, et al. HepatoNet1: a comprehensive metabolic reconstruction of the human hepatocyte for the analysis of liver physiology. Molecular Systems Biology. 2010;6(1).

9. König M, Bulik S, Holzhütter H-G. Quantifying the Contribution of the Liver to Glucose Homeostasis: A Detailed Kinetic Model of Human Hepatic Glucose Metabolism. PLoS computational biology. 2012;8(6):e1002577.
10. Yang Y, Nadanaciva S, Will Y, Woodhead JL, Howell BA, Watkins PB, et al. MITOsym®: A Mechanistic, Mathematical Model of Hepatocellular Respiration and Bioenergetics. Pharmaceutical Research. 2015;32(6):1975-92.
11. Halestrap AP, Wilson MC. The monocarboxylate transporter family--role and regulation. IUBMB life. 2012;64(2):109-19.
12. Vanlier J, Wu F, Qi F, Vinnakota KC, Han Y, Dash RK, et al. BISEN: Biochemical Simulation Environment. Bioinformatics. 2009;25(6):836-7.
13. Daniel. A. Beard HQ. Chemical Biophysics. W. Mark Saltzman SC, editor. Cambridge Texts in Biomedical Engineering: Chambridge Texts; 2008. 311 p.
14. Pollock AS. Intracellular pH of hepatocytes in primary monolayer culture. The American journal of physiology. 1984;246(5 Pt 2):F738-44.
15. Diaz-Ruiz R, Rigoulet M, Devin A. The Warburg and Crabtree effects: On the origin of cancer cell energy metabolism and of yeast glucose repression. Biochimica et Biophysica Acta (BBA) - Bioenergetics. 2011;1807(6):568-76.
16. Vander Heiden MG, Cantley LC, Thompson CB. Understanding the Warburg Effect: The Metabolic Requirements of Cell Proliferation. Science (New York, NY). 2009;324(5930):1029-33.
17. Warburg O. On the origin of cancer cells. Science. 1956;123(3191):309-14.
18. Liu AM, Xu Z, Shek FH, Wong KF, Lee NP, Poon RT, et al. miR-122 targets pyruvate kinase M2 and affects metabolism of hepatocellular carcinoma. PLoS One. 2014;9(1):e86872.
19. Kato Y, Ozawa S, Miyamoto C, Maehata Y, Suzuki A, Maeda T, et al. Acidic extracellular microenvironment and cancer. Cancer Cell International. 2013;13:89-.
20. Abrahams M, Eriksson H, Bjornstrom K, Eintrei C. Effects of propofol on extracellular acidification rates in primary cortical cell cultures: application of silicon microphysiometry to anaesthesia. British journal of anaesthesia. 1999;83(3):467-9.
21. Dietl K, Renner K, Dettmer K, Timischl B, Eberhart K, Dorn C, et al. Lactic acid and acidification inhibit TNF secretion and glycolysis of human monocytes. Journal of immunology (Baltimore, Md : 1950). 2010;184(3):1200-9.
22. Nuttall FQ, Ngo A, Gannon MC. Regulation of hepatic glucose production and the role of gluconeogenesis in humans: is the rate of gluconeogenesis constant? Diabetes/metabolism research and reviews. 2008;24(6):438-58.
23. Radziuk J, Pye S. Hepatic glucose uptake, gluconeogenesis and the regulation of glycogen synthesis. Diabetes/metabolism research and reviews. 2001;17(4):250-72.
24. Cryer PE. Glucose counterregulation: prevention and correction of hypoglycemia in humans. The American journal of physiology. 1993;264(2 Pt 1):E149-55.
25. Feher J. 2.9 - ATP Production I: Glycolysis. Quantitative Human Physiology. Boston: Academic Press; 2012. p. 171-9.
26. Feher J. 2.10 - ATP Production II: The TCA Cycle and Oxidative Phosphorylation. Quantitative Human Physiology. Boston: Academic Press; 2012. p. 180-90.
27. Halestrap AP. Monocarboxylate transporter 1. UCSD nature molecule pages. 2009.
28. Jackson VN, Halestrap AP. The kinetics, substrate, and inhibitor specificity of the monocarboxylate (lactate) transporter of rat liver cells determined using the fluorescent intracellular pH indicator, 2',7'-bis(carboxyethyl)-5(6)-carboxyfluorescein. The Journal of biological chemistry. 1996;271(2):861-8.
29. Okamoto T, Kanemoto N, Ban T, Sudo T, Nagano K, Niki I. Establishment and characterization of a novel method for evaluating gluconeogenesis using hepatic cell lines, H4IIE and HepG2. Arch Biochem Biophys. 2009;491(1-2):46-52.

Supplementary information for "Investigating the role of lactate and proton efflux in extracellular acidification using a pH dependent *in silico* model of hepatic glycolytic flux"

Ross A. Kelly[a], Joseph Leedale[b], Andy Harrell[c], Vinnakota KC[d], Daniel A. Beard[d], Amy E.

Chadwick[e] and Steve Webb[a1]
[a] Department of applied mathematics, Liverpool John Moores University, Byrom Street, Liverpool, L3 3AF.
[b] Department of Mathematical Sciences, University of Liverpool, Liverpool L69 7ZL, UK
[c] GlaxoSmithKline, David Jack Centre for Research, Park Road, Ware SG12 0DP, UK
[d] Department of Molecular & Integrative Physiology, University of Michigan, Ann Arbor, MI 48109, USA
[e] MRC Centre for Drug Safety Science, the Department of Clinical and Molecular Pharmacology, The University of Liverpool, Ashton Street, Liverpool L69 3GE, UK
Address correspondence to: Dr Steven Webb, Department of Applied Mathematics, Liverpool John Moores University, James Parsons Building Byrom Street, Liverpool, L3 3AF, Tel: 0151 231 2217, Email: S.D.Webb@ljmu.ac.uk

1. Supplementary information contents

Supplementary Figure S1	Variable time course
Supplementary Figure S2	Flux time course
Supplementary Figure S3	Variable sensitivity analysis
Abbreviations	List of abbreviations used in the publication
Table S1	Model variables
Table S2	Reaction & transport fluxes
Table S3	Model ODE's
Appendix B	Enzyme & transporter kinetic terms and parameters values
Appendix C	Model thermodynamics & pH calculations
Appendix D	Statistical analysis
Appendix E	*In vitro* EFA

2. Description of Matlab Codes and Data files for simulating steady state hepatic glycolytic flux

steady_states.m	Driver program to simulate model steady states
PPR_dXdT.m	Model ODE file
plot_steady_states.m	File generating variable and flux steady state plots
setup.mat	Data file containing model parameters
x0.mat	Data file containing variable initial conditions

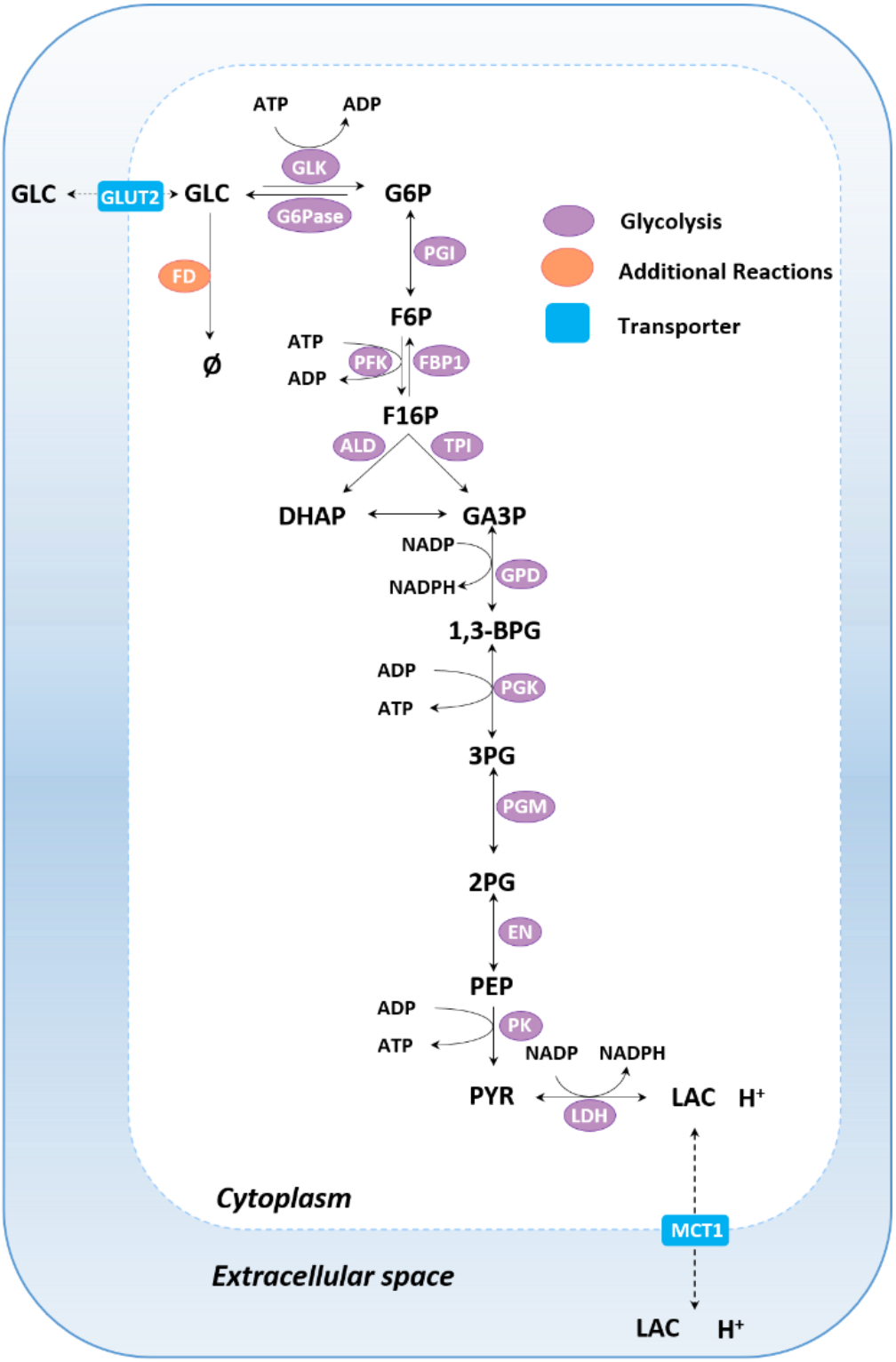

Figure 1. Schematic of human hepatic bioenergetic model. Biochemical model comprising of two compartments: cytoplasm and extracellular space. Glycolytic enzymes are shown in purple, transporter reactions are depicted as blue rectangles and oxidative phosphorylation is portrayed in orange. Reaction descriptions can be found in Table 2. See appendixfor additional information.

Model simulations were generated using Matlab 2015b, with absolute integration tolerance *absTol* = 10^{-10} and relative integration tolerance *relTol* = 10^{-4} with steady state solutions represented by changes in all concentrations less than the *absTol* for a timespan of ≥ 300 min. Complimentary variable time course solutions to main ECAR/PPR_{gly} simulations (Figure 7 main article) are shown in Figures S1 (variables vs time) and S2 (fluxes vs time). Extracellular variables are removed at t=20, with glucose reintroduced at 5

mM at t=20 in order to replicate *in vitro* minor starvation prior to EFA.

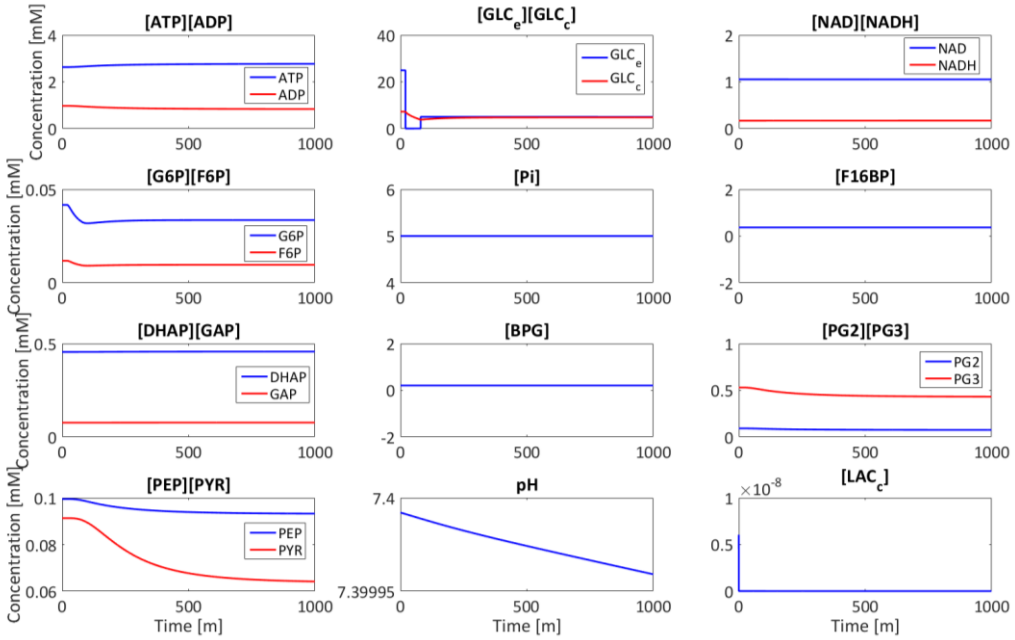

Supplementary Figure S1: Model variable time course simulation comparable to *in vitro* experiment (Figure 7 main article). All extracellular variables are removed at t=20, followed by reintroduction of glucose (5 mM) at t=80. All variables are held in the cytoplasm compartment denoted _c, with the exception of any denoted _e, which are held in the extracellular compartment.

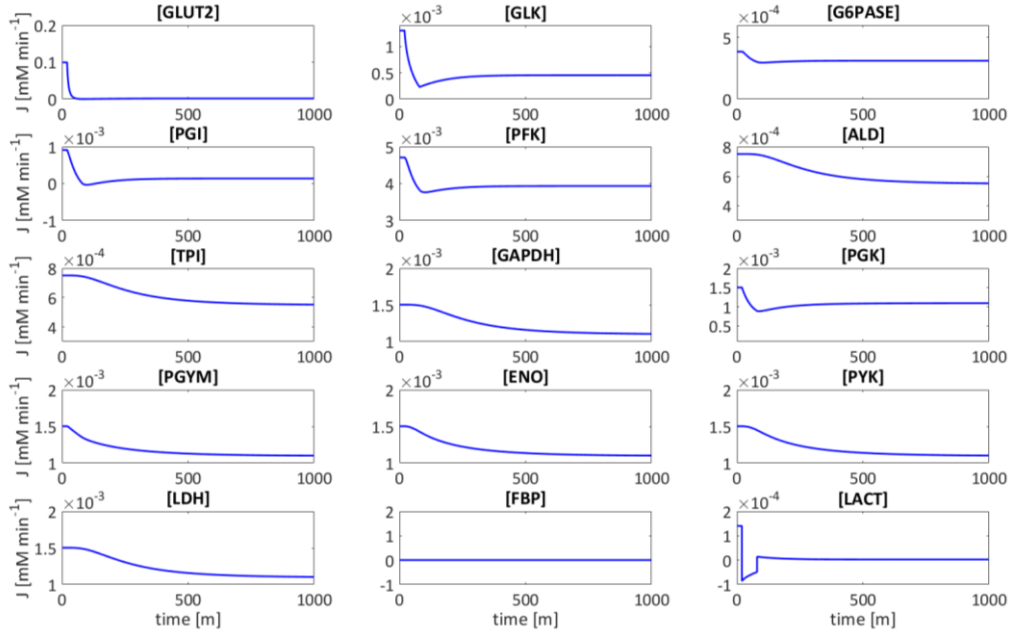

Supplementary Figure S2: Model enzyme and transporter flux time course simulation comparable to *in vitro* experiment (Figure 7). All extracellular variables are removed at t=20, followed by reintroduction of glucose (5 mM) at t=80. Model fluxes are expressed as mM $min^{-1.}$

Sensitivity analysis

Figure 5 in the main paper describes the % mean changes as a result of perturbations of two of the most sensitive parameters. Figure S3 illustrates the sensitive variables for the remaining sensitive parameters: Vmax PFK, Keq TPI, and Km DHAP.

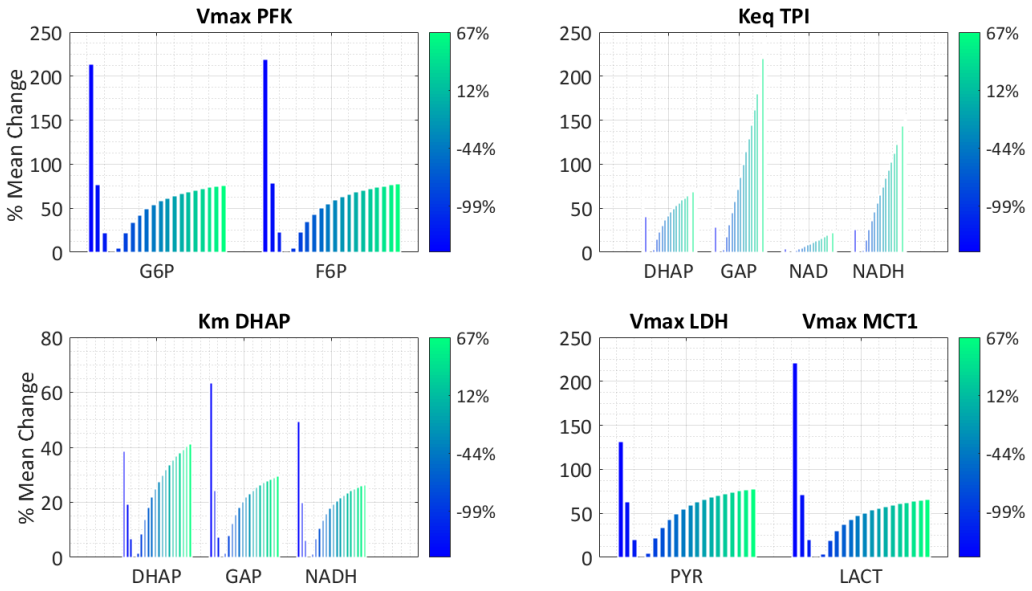

Supplementary Figure S3: Sensitive model parameters illustrating changes in intracellular variable concentration. % mean changes in model variable concentration as a function of sensitive parameter manipulation are shown compared to their initial steady state condition.

Figure S3 illustrates which model variables are most affected by the changes in the most sensitive parameters during sensitivity analysis. Cytoplasm redox status variables NAD and NADH are affected as a result of changes of Keq TPI and Km DHAP. For future iterations of the model where oxidative phosphorylation / TCA cycle is included, maintaining physiologically relevant concentrations of these two variables is crucial in order to recapitulate respiratory energy metabolism.

2.2 *Modelling pH-dependent enzyme kinetics and reaction equilibria: BISEN*

The hepatic glycolysis model was constructed using Matlab, utilising the Biochemical Simulation Environment (BISEN) suite (1). BISEN is an open-source tool that assists in generating a set of differential equations for simulating biochemical systems, accounting for dynamic proton and metal ion buffering, thermodynamics and reaction equilibria. Detailed instructions on how to use BISEN and how it works have been published (1). Briefly, the state variables refer to the biochemical reactants within the model which are the sum of its interconvertible biochemical species. For example, ATP is a *reactant* that represents the sum of its related *species*: ATP^{4-}, $HATP^{3-}$, $MgATP^{2-}$ etc. By accounting for the rapid interconversion of all species with metal ions and protons, the differences in state depending upon the pH can be modelled, whilst accounting for a complete proton stoichiometry. Each biochemical equation has its own associated equilibrium constant and the standard-state free energy of reaction, Δ_rG^0, that is independent of pH yet dependent upon changes in temperature and ionic strength. Overall, this allows favorability of a reaction to change as a result of a pH change (2).

Appendix A: Model Components

The glycolytic flux model is based on the kinetic model of human hepatic glucose metabolism presented by Konig et al (3), gaining its pH-dependency and interwoven thermodynamics using the BISEN toolset (1). The model comprises of 14 enzyme mediated kinetic reactions and 2 transport fluxes between a two compartment systems representing the cellular cytoplasm, where glycolysis is located, and the extracellular space. Compartment volumes are expressed as a ratio of total well volume. Compartment volumes and corresponding water fractions were set in the overall BSL construction file. In this model, the cytoplasm compartment represents the total intracellular volume occupied by 25E+03 cells, calculating using the density of liver tissue and radius of a HepG2 cell. Using a value of 9.0E-06 m for the cell radius r, the volume of 25E+03 cells V_1, was calculated assuming a spherical cell.This yields a single cell intracellular volume of 3.0536E-15 m^3.

The density of liver tissue is 1.077 g ml^{-1} and 1 m^{-3} = 1 L at this density (4). Using these values and scaling up from a single cell to 25E+03 cells therefore gives a total intracellular volume of 7.364E-08 L. The extracellular volume in this model is not the entire well volume but a microchamber volume. This is because EFA lowers a fluorescent measuring probe approximately 200 µm above the cell monolayer at the

bottom of the well to measure OCR and ECAR creating a transient micro chamber. The extracellular compartment volume of the microchamber volume is 2.0E-06 L.
The compartments are then set as a fraction of the total volume. The total volume occupied by the cells and microchamber as a fraction of the total model volume is 0.0368/100 and 99.9632/100 respectively, with the total water fraction for both compartments being initially set to 1. Cytoplasm pH is set to a constant pH 6.8, as the source of intracellular proton production is omitted. Intracellular inorganic phosphate was held constant at 5 mM, in line with the Konig model (3). Intracellular free phosphate (Pi) is carefully maintained in cellular physiology by mechanisms not included within this model and was therefore held constant also. In the extracellular compartment, free magnesium and potassium ions were also held constant as the media used in EFA is an unbuffered solution (Table S1, S2, S3).

Table S1: Model Variables

Variable	Abbreviation	Compartment	Initial Concentration (mM)
Glucose	GLC	Cytoplasm	5.000
ATP	ATP	Cytoplasm	2.800
ADP	ADP	Cytoplasm	0.800
Glucose-6-phosphate	G6P	Cytoplasm	0.120
Fructose-6-phosphate	F6P	Cytoplasm	0.005
Inorganic phosphate	Pi	Cytoplasm	5.000
Fructose-1,6-phosphate	F16P	Cytoplasm	0.020
1,3-bisphospho-glycerate	BPG	Cytoplasm	0.300
Fructose-2,6-phosphate	F26P	Cytoplasm	0.004
Dihydroxyacetone-phosphate	DHAP	Cytoplasm	0.300
Glyceraldehyde-phosphate	GHAP	Cytoplasm	0.100
NAD	NAD	Cytoplasm	1.220
NADH	NADH	Cytoplasm	0.00056
2-phospho-D-glycerate	PG2	Cytoplasm	0.030
3-phospho-D-glycerate	PG3	Cytoplasm	0.270
Phosphoenolpyruvate	PEP	Cytoplasm	0.150
Pyruvate	PYR	Cytoplasm	0.100
Lactate	LAC	Cytoplasm	0.500
Protons	H	Cytoplasm	6.8 (pH)
Magnesium ions	Mg	Cytoplasm	5.000
Potassium ions	K	Cytoplasm	8.000
Glucose	GLC_e	Extracellular	5.000
Lactate	LAC_e	Extracellular	0.000
Protons	H_e	Extracellular	7.4 (pH)
Magnesium ions	Mg_e	Extracellular	0.000
Potassium ions	K_e	Extracellular	0.000

Table S1: Model biochemical reactants including their corresponding abbreviation (Figure 1), allocated compartment and initial concentration. Extracellular variables are distinguished from cytoplasm variables using subscript "e".

Tables S2: Reaction Transport Fluxes

Reaction	Abbreviation	Description
Glucokinase	GLK	GLC + ATP → ADP + G6P + H
Glucose-6-phosphatase	G6Pase	G6P + H2O →G6P+ Pi
Phosphoglucose isomerase	PGI	G6P ⇋ F6P
Phosphofructokinase	PFK	F6P + ATP → F16P + ADP + H
Fructose-1,6-bisphosphatase	FBP1	F16P + H2O → F6P + Pi

Aldolase	ALD	F6P ⇋ DHAP + GAPH
Triosephosphate isomerase	TPI	DHAP ⇋ GAPH
Glycerald-3-P dehydrogenase	GAPDH	GAPH + Pi + NAD ⇋ BPG + NADH + H
Phosphoglycerate kinase	PGK	BPG + 2 ADP ⇋ PG3 + 2 ATP
Phosphoglycerate mutase 1	PGYM	PG3 ⇋ PG2
Enolase / phosphopyruvate hydratase	ENO	PG2 ⇋ PEP
Pyruvate Kinase	PYK	PEP + 2 ADP + H ⇋ PYR + 2 ATP
Lactate dehydrogenase	LDH	PYR + NADH + H ⇋ LAC + NAD
Glucose Storage (Glycogenolysis)	FD	GLC → Ø
Glut-2-transporter	GLUT2	GLC_e ⇋ GLC
Monocarboxylate transporter 1	MCT1	LAC+ H⇋ LAC_e + H_e

Table S2 Model biochemical reactants including their corresponding abbreviation (Figure 1), allocated compartment and initial concentration. Extracellular variables are distinguished from cytoplasm variables using subscript "e".

Table S3: Model ODE's

Reaction fluxes are represented by J, with subscripts to denote the appropriate reaction (description in Appendix B). Model fluxes are expressed in mM min^{-1}.

Variable	Expression
d[GLC] $/dt$ =	$- J_{GLK} + J_{G6PASE} - J_{FD} + J_{GLUT2}$
d[ATP] $/dt$ =	$- J_{GLK} - J_{PFK} + 2\ J_{PGK} + 2\ J_{PYK}$
d[ADP] $/dt$ =	$J_{GLK} + J_{PFK} - 2\ J_{PGK} - 2\ J_{PYK}$
d[G6P] $/dt$ =	$J_{GLK} - J_{G6PASE} - J_{PGI}$
d[F6P] $/dt$ =	$J_{PGI} - J_{PFK} + J_{FBP1}$
d[F16P] $/dt$ =	$J_{PFK} - J_{FBP1} - J_{ALD}$
d[BPG] $/dt$ =	$J_{GAPDH} - J_{PGK}$
d[DHAP] $/dt$ =	$J_{ALD} - J_{TPI}$
d[GHAP] $/dt$ =	$J_{ALD} + J_{TPI} - J_{GAPDH}$
d[NAD] $/dt$ =	$- J_{GAPDH} + J_{LDH}$
d[NADH] $/dt$ =	$J_{GAPDH} - J_{LDH}$
d[PG2] $/dt$ =	$J_{PGK} - J_{PGYM}$
d[PG3] $/dt$ =	$J_{PGYM} - J_{ENO}$
d[PEP] $/dt$ =	$J_{ENO} - J_{PYK}$
d[PYR] $/dt$ =	$J_{PYK} - J_{LDH}$
d[LAC] $/dt$ =	$J_{LDH} - J_{LACT}$
d[GLC_e] $/dt$ =	$- J_{GLUT2}$
d[LAC_e] $/dt$ =	J_{LACT}

Model simulations

Time course, reaction flux and steady state simulations were produced via integration of the resulting ordinary differential equations (ODE's) (Supplementary Table S3) using the variable order stiff solver ode15s (Matlab®). The model does not include the tricarboxylic acid cycle (TCA) and is therefore devoid of cytoplasmic proton production. Therefore, cytoplasm proton concentration was held constant at physiological pH of 6.85 (5). The extracellular compartment was aligned with experimental conditions used in EFA by setting a low extracellular buffering capacity, comparable to that of unbuffered EFA media. Compartment volumes were also set to mimic EFA by assigning the cytoplasm / intracellular volume as the volume occupied by the 2.5×10^4 cells seeded per well, and the extracellular volume as 200 µl for the total extracellular volume of each well used in the EFA. For the BISEN inputs these volumes were expressed as a percentage giving the cytoplasm volume as 0.0368 % and the extracellular volume as 99.9632 %.

In silico – in vitro ECAR coupling

In silico ECAR and PPR_{gly} was simulated as a function of the MCT1 transport flux, J_{MCT1}, expressed in mM min^{-1}. Conversion from *in silico* transport flux of mM min^{-1} to the *in vitro* PPR pmol min^{-1} measurement was accomplished using Equation 1, and total model ECAR (mpH min^{-1}) was converted

using Equation 2. Note, this conversion equation also includes normalization for experimental protein content, where *PNF* is the protein normalization factor which is equal to the total protein content per well.

$$PPR = \frac{1 \times 10^9 \, (J_{MCT1})}{PNF} \tag{1}$$

$$ECAR = \frac{\left(-\log 10 \left(\frac{J_{MCT1}}{1 \times 10^3}\right)\right) 1 \times 10^{-3}}{PNF} \tag{2}$$

Appendix B: Flux Expressions & Corresponding Parameters

All enzyme mediated/transporter reactions used in the model are addressed in this section, with its parameter values with it. Each reaction is illustrated, followed by the kinetic term, with parameters tabulated below. All parameter values are taken from the Konig model (3), with any adjusted parameters specified when appropriate.

Glucokinase (GLK):

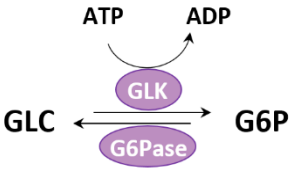

$$gk_{free} = \frac{[GLC]^{n_{gkrp}}}{[GLC]^{n_{gkrp}} + \left(k_{gkrp}^{GLC}\right)^{n_{gkrp}}} \left(1 - \frac{b_{gkrp}[F6P]}{[F6P] + k_{gkrp}^{F6P}}\right) \tag{B.1}$$

$$J_{GLK} = v_{max} \, gk_{free} \frac{[ATP]}{k_m^{ATP} + [ATP]} \frac{[GLC]^n}{[GLC]^n + \left(k_m^{glc}\right)^n} \tag{B.2}$$

Parameter	Value	Units
n	1.60E+00	
k_m^{glc}	7.50E+00	mM
k_m^{ATP}	2.60E-01	mM
n_{gkrp}	2.00E+00	
k_{gkrp}^{GLC}	1.50E+01	mM
k_{gkrp}^{F6P}	1.00E-02	mM
b_{gkrp}	7.00E-01	
v_{max}	2.52E-02	mM min^{-1}

Glucokinase is regulated by the Glucokinase regulator protein which is a competitive inhibitor for glucose. This regulatory binding mechanism of this protein is dependent upon glucose and fructose-6-phosphate and in turn alters the k_m for glucose.

Glucose-6-phosphatase (G6Pase):

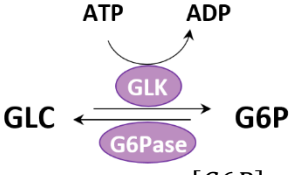

$$J_{G6PASE} = v_{max} \frac{[G6P]}{k_m^{G6P} + [G6P]} \tag{B.3}$$

Parameter	Value	Units

k_m^{G6P}	2.00E+00	mM
v_{max}	1.89E-02	mM min^{-1}

Glucose-6-phosphate isomerase (PGI):

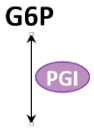

$$J_{PGI} = \frac{\frac{v_{max}}{k_m^{G6P}}\left([G6P] - \frac{[F6P]}{K_{eq}}\right)}{1 + \frac{[G6P]}{k_m^{G6P}} + \frac{[F6P]}{k_m^{F6P}}} \quad \text{(B.4)}$$

Parameter	Value	Units
K_{eq}	5.17E-01	
k_m^{G6P}	1.82E-01	mM
k_m^{F6P}	7.10E-02	mM
v_{max}	4.20E-01	mM min^{-1}

Phosphofructokinase (PFK):

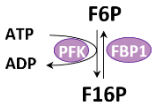

$$J_{PFK} = v_{max}\left(1 + \frac{[F16P]}{k_a^{F16P}}\right)\left(\frac{[G6P][ATP]}{k_i^{F16P}k_m^{ATP} + k_m^{F6P}[ATP] + k_m^{ATP}[F6P] + [ATP][F6P]}\right) \quad \text{(B.5)}$$

Parameter	Value	Units
k_m^{ATP}	1.11E-01	mM
k_m^{F6P}	7.70E-02	mM
k_i^{F16P}	1.20E-02	mM
v_{max}	7.18E-03	mM min^{-1}
k_a^{F16P}	1.00E-03	mM

Fructose-1,6-bisphosphatase (FBP):

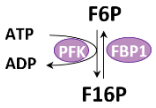

$$J_{FBP} = \frac{v_{max}}{1 + \frac{[F26P]}{k_i^{F26P}}}\left(\frac{[F16P]}{[F16P] + k_m^{F16P}}\right) \quad \text{(B.6)}$$

Parameter	Value	Units
k_i^{F26P}	1.00E-03	mM
k_m^{F16P}	1.30E-03	mM
v_{max}	4.33E-03	mM min^{-1}

Aldolase (ALD):

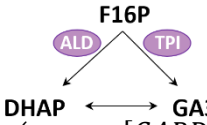

$$J_{ALD} = \frac{\frac{v_{max}}{k_m^{F16P}}\left([F16P]\frac{[GAPDH][DHAP]}{K_{eq}}\right)}{1+\frac{[F16P]}{k_m^{F16P}}+\frac{[GAPDH]}{k_i^{GAPDH}}+\frac{[DHAP]([DHAP]+k_m^{GAPDH})}{k_m^{DHAP}\,k_i^{GAPDH}}+\frac{[F16P][GAPDH]}{k_m^{F16P}k_{i2}^{GRAP}}} \quad \text{(B.7)}$$

Parameter	Value	Units
K_{eq}	9.76E-05	mM
k_m^{F16P}	7.10E-03	mM
v_{max}	4.20E-03	mM min^{-1}
k_m^{DHAP}	3.64E-02	mM
k_m^{GAPDH}	7.10E-03	mM
k_i^{GAPDH}	5.72E-02	mM
k_{i2}^{GRAP}	4.2E-01	mM

Triosephosphate isomerase (TPI):

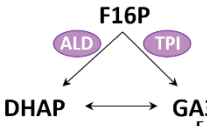

$$J_{TPI} = \frac{v_{max}}{k_m^{DHAP}}\left(\frac{[DHAP]-\frac{[GAPDH]}{K_{eq}}}{1+\frac{[DHAP]}{k_m^{DHAP}}+\frac{[GAPDH]}{k_m^{GAPDH}}}\right) \quad \text{(B.8)}$$

Parameter	Value	Units
K_{eq}	5.45E-02	mM
k_m^{DHAP}	5.90E-01	mM
v_{max}	4.20E-03	mM min^{-1}
k_m^{GAPDH}	4.20E-01	mM

Glyceraldehydephosphate dehydrogenase (GAPDH):

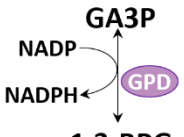

$$J_{GAPDH} = \frac{\frac{v_{max}}{k_{NAD}\,k_{GAPDH}k_{Pi}}\left([NAD][GAPDH][Pi]-\frac{[BPG][NADH]}{K_{eq}}\right)}{\left(1+\frac{[NAD]}{k_{NAD}}\right)+\left(1+\frac{[GAPDH]}{k_{GAPDH}}\right)+\left(1+\frac{[Pi]}{k_{Pi}}\right)+\left(1+\frac{[NADH]}{k_{NADH}}\right)\left(1+\frac{[BPG]}{k_{BPG}}\right)-1} \quad \text{(B.9)}$$

Parameter	Value	Units

K_{eq}	8.68E-02	
k_{NAD}	5.00E-02	mM
v_{max}	4.20E-03	mM min^{-1}
k_m^{GAPDH}	5.00E-04	mM
k_{Pi}	3.90E+00	mM
k_{NADH}	8.30E-03	mM
k_{BPG}	3.50E-02	mM

Phosphoglycerate Kinase (PGK):

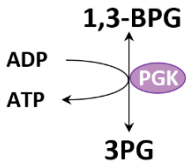

$$J_{PGK} = \frac{\frac{v_{max}}{k_{ADP}\,k_{BPG}}\left([ADP][BPG] - \frac{[ATP][PG3]}{K_{eq}}\right)}{\left(1+\frac{[ADP]}{k_{ADP}}\right)+\left(1+\frac{[BPG]}{k_{BPG}}\right)+\left(1+\frac{[ATP]}{k_{ATP}}\right)+\left(1+\frac{[PG3]}{k_{PG3}}\right)-1} \quad \text{(B.10)}$$

Parameter	Value	Units
K_{eq}	7.00E+00	
k_{ADP}	3.50E-01	mM
v_{max}	4.20E-03	mM min^{-1}
k_{BPG}	2.00E-03	mM
k_{ATP}	4.80E-01	mM
k_{PG3}	1.20E+00	mM

Phosphoglycerate mutase (PGM):

$$J_{PGM} = \frac{v_{max}\left([PG3] - \frac{[PG2]}{K_{eq}}\right)}{[PG3] + k_{PG3}\left(1 + \frac{[PG2]}{k_{PG2}}\right)} \quad \text{(B.11)}$$

Parameter	Value	Units
K_{eq}	1.84E-01	
k_{PG3}	5.00E+00	mM
v_{max}	4.20E-03	mM min^{-1}
k_{PG2}	1.00E+00	mM

Enolase (ENO):

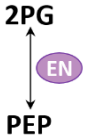

$$J_{ENO} = \frac{v_{max}\left([PG2] - \frac{[PEP]}{K_{eq}}\right)}{[PG2] + k_{PG2}\left(1 + \frac{[PEP]}{k_{PEP}}\right)} \quad \text{(B.12)}$$

Parameter	Value	Units
K_{eq}	5.45E-01	
k_{PG2}	1.00E+00	mM
v_{max}	3.60E-03	mM min^{-1}
k_{PEP}	1.00E+00	mM

Pyruvate Kinase (PK):

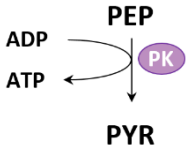

$$f = \frac{[F16P]^{n_{fbp}}}{[F16P]^{n_{fbp}} + \left(k_{fbp}^{dp}\right)^{n_{fbp}}} \quad \text{(B.12)}$$

$$\alpha_{inp}^{dp} = (1-f)\left(\alpha^{dp} - \alpha_{end}\right) + \alpha_{end} \quad \text{(B.13)}$$

$$\alpha_{inp}^{p} = (1-f)(\alpha^{p} - \alpha_{end}) + \alpha_{end} \quad \text{(B.14)}$$

$$k_{pep,inp}^{dp} = (1-f)\left(k_{pep}^{dp} - k_{pep}^{min}\right) + k_{pep}^{min} \quad \text{(B.15)}$$

$$k_{pep,inp}^{p} = (1-f)\left(k_{pep}^{p} - k_{pep}^{min}\right) + k_{pep}^{min} \quad \text{(B.16)}$$

$$v^{dp} = v_{max}\,\alpha_{inp}^{dp}\left(\frac{[PEP]^{n^{PEP}}}{[PEP]^{n^{PEP}} + \left(k_{pep,inp}^{dp}\right)^{n^{PEP}}}\right)\left(\frac{[ADP]}{[ADP] + k_{ADP}}\right)\left(\alpha_{base}^{dp} + \left(1-\alpha_{base}^{dp}\right)f\right) \quad \text{(B.17)}$$

$$v^{p} = v_{max}\,\alpha_{inp}^{p}\left(\frac{[PEP]^{n^{PEP}}}{[PEP]^{n^{PEP}} + \left(k_{pep,inp}^{p}\right)^{n^{PEP}}}\right)\left(\frac{[ADP]}{[ADP] + k_{ADP}}\right)\left(\alpha_{base}^{p} + \left(1-\alpha_{base}^{p}\right)f\right) \quad \text{(B.18)}$$

$$v^{dp} = v_{max}\,\alpha_{inp}^{dp}\left(\frac{[PEP]^{n^{PEP}}}{[PEP]^{n^{PEP}} + \left(k_{pep,inp}^{dp}\right)^{n^{PEP}}}\right)\left(\frac{[ADP]}{[ADP] + k_{ADP}}\right) \quad \text{(B.19)}$$

$$J_{PK} = (1-\gamma)v^{dp} + \gamma v^{p}$$

Parameter	Value	Units
n^{PEP}	3.50E+00	
n^{FBP}	1.80E+00	
v_{max}	4.62E-02	mM min^{-1}
k_{pep}^{dp}	1.10E+00	mM
k_{min}^{dp}	8.00E-02	mM
α^{dp}	1.00E+00	
α^{p}	1.10E+00	
α_{end}	1.00E+00	
k_{fbp}^{dp}	1.60E-04	mM
k_{fbp}^{p}	3.50E-04	mM
α_{base}^{dp}	8.00E-02	
α_{base}^{p}	4.00E-02	
k_{ADP}	2.30E+00	mM

Phosphofructokinase is one of several integral enzymes with hepatic glycolysis as it has an interconvertible phosphorylation state denoted γ. If γ = 1, the enzyme is modelled in its phosphorylated state and therefore simulates the presence of the hormone insulin leading to increased glycolytic flux. If γ = 0, the enzyme is modelled in its dephosphorylated state and therefore simulates the presence of the hormones epinephrine and glucagon which reduce glycolytic flux. When modelling carcinoma cells such as HepG2 cells, glycolytic flux is increased compared to that of normal cells due to the Warburg effect explained earlier. Therefore, when modelling hepatocarcinoma glycolytic flux, any interconvertible phosphorylation states kinetic equations use γ = 1.

Lactate dehydrogenase (LDH):

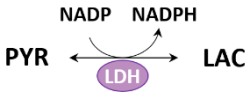

$$J_{LDH} = \frac{\frac{v_{max}}{k_m^{PYR}\, k_m^{NADH}}\left([PYR][NADH] - \frac{[LAC][NAD]}{K_{eq}}\right)}{\left(1 + \frac{[NADH]}{k_m^{NADH}}\right)\left(1 + \frac{[PYR]}{k_m^{PYR}}\right)\left(1 + \frac{[LAC]}{k_m^{LAC}}\right)\left(1 + \frac{[NAD]}{k_m^{NAD}}\right) - 1} \quad \text{(B.20)}$$

Parameter	Value	Units
K_{eq}	2.78E-04	
k_m^{PYR}	4.95E-01	mM
v_{max}	1.26E-02	mM min^{-1}
k_m^{NADH}	2.70E-02	mM
k_m^{LAC}	3.20E-01	mM
k_m^{NAD}	9.84E-01	mM

Glucose transporter 2 (GLUT2):

$$J_{GLUT2} = \frac{\frac{v_{max}}{k_m^{GLC}}\left([GLC\_e] - \frac{[GLC\_c]}{K_{eq}}\right)}{1 + \frac{[GLC\_e]}{k_m^{GLC}} + \frac{[GLC\_c]}{k_m^{GLC}}} \quad \text{(B.21)}$$

Parameter	Value	Units
K_{eq}	1.00E+00	
k_m^{GLC}	4.20E+01	mM
v_{max}	4.20E-03	mM min^{-1}

Monocarboxylate transporter 1 (LACT):

$$J_{LACT} = \frac{\frac{v_{max}}{k_m^{LAC}}\left([LAC\_e] - \frac{[LAC\_c]}{K_{eq}}\right)}{1 + \frac{[LAC\_e]}{k_m^{LAC}} + \frac{[LAC\_c]}{k_m^{LAC}}} \quad \text{(B.22)}$$

Parameter	Value	Units
K_{eq} (Pre-adjustment)	1.00E+00	
k_m^{LAC} (Pre-adjustment)	8.00E-01	mM
v_{max} (Pre-adjustment)	5.42E-03	mM min^{-1}
K_{eq} (Post-adjustment)	1.15E+02	
k_m^{LAC} (Post-adjustment)	6.93E-09	mM
v_{max} (Post-adjustment)	2.00E-03	mM min^{-1}

Monocarboxylate transporter 1 is the liver specific enzyme responsible for transport of lactic acid. In this instance, lactate is transported in its anionic form as LAC^- with co-transportation of a proton. This is due to the lactic acid having a pKa value of 3.82 which as a result means at pH 7.4 this weak carboxylic acid will exist in its dissociated form. This is very important when modelling extracellular acidification.

Glycogenolysis (FD):

$$J_{FD} = \frac{v_{max}\,[GLC]^n}{k_m^{GLC^n} + [GLC]^n} \quad \text{(B.23)}$$

Parameter	Value	Units
n	1.00E+01	
k_m^{GLC}	9.00E+00	mM
v_{max}	1.00E+00	mM min^{-1}

Appendix C: Model thermodynamics & pH calculations

The model was constructed using the Biochemical Simulation Environment (BISEN), an open source computational toolset used to generate large ODE models in Matlab, capable of accounting for biochemical thermodynamics, rapid equilibria of multiple species while generating a dynamic proton and metal ion profile (1). The software, user manual (tutorial examples) are available at www.bbc.mcw.edu/BISEN. The interwoven thermodynamics and subsequent dynamic pH time course generation is in full within the publication "Dynamics of muscle glycogenolysis modelled with pH time course computation and pH-dependent reaction equilibria and enzyme kinetics" (6).

Briefly, the state variables refer to the biochemical reactants within the model which are the sum of its interconvertible biochemical species. For example, ATP is a *reactant* that represents the sum of its related *species*: ATP^{4-}, $HATP^{3-}$, $MgATP^{2-}$ etc. By accounting for the rapid interconversion of all species with metal ions and protons, we are able to model the differences in state depending upon the pH, as well as accounting for a complete proton stoichiometry. Each biochemical equation has its own associated equilibrium constant and Gibbs standard-state free energy of reaction $\Delta_r G^0$ that is independent of pH yet dependent upon changes to temperature and ionic strength. Overall, this allows favorability of a reaction to change as a result of a pH change (2).

Appendix D: *in vitro* data statistical analysis

Significant changes between extracellular glucose concentrations were determined using Prism software as described in the methods section. One-way analysis of variance was determined using a one-way ANOVA with a Newman-Keuls Multiple comparison test to determine significance between all concentrations of glucose.

ECAR analysis

Table Analyzed	ECAR Normalized			
One-way analysis of variance				
P value	P<0.0001			
P value summary	***			
Are means signif. different? (P < 0.05)	Yes			
Number of groups	10			
F	384.2			
R squared	0.9665			
Bartlett's test for equal variances				
Bartlett's statistic (corrected)	5.51			
P value	0.7877			
P value summary	ns			
Do the variances differ signif. (P < 0.05)	No			
ANOVA Table	SS	df	MS	
Treatment (between columns)	2.287	9	0.2541	
Residual (within columns)	0.07937	120	0.000661	
Total	2.366	129		
Newman-Keuls Multiple Comparison Test	Mean Diff.	q	Significant? P < 0.001?	Summary
0 vs 5.0	-0.5022	70.4	Yes	***
0 vs 12.5	-0.3569	50.04	Yes	***
0 vs 15.0	-0.3478	48.76	Yes	***

0 vs 25.0	-0.3404	47.72	Yes	***
0 vs 10.0	-0.3137	43.98	Yes	***
0 vs 2.5	-0.2827	39.63	Yes	***
0 vs 7.5	-0.2442	34.23	Yes	***
0 vs 1	-0.2095	29.38	Yes	***
0 vs 0.1	-0.1145	16.05	Yes	***
0.1 vs 5.0	-0.3877	54.35	Yes	***
0.1 vs 12.5	-0.2425	33.99	Yes	***
0.1 vs 15.0	-0.2333	32.71	Yes	***
0.1 vs 25.0	-0.2259	31.67	Yes	***
0.1 vs 10.0	-0.1992	27.93	Yes	***
0.1 vs 2.5	-0.1682	23.59	Yes	***
0.1 vs 7.5	-0.1297	18.18	Yes	***
0.1 vs 1	-0.09508	13.33	Yes	***
1 vs 5.0	-0.2926	41.02	Yes	***
1 vs 12.5	-0.1474	20.66	Yes	***
1 vs 15.0	-0.1382	19.38	Yes	***
1 vs 25.0	-0.1308	18.34	Yes	***
1 vs 10.0	-0.1042	14.6	Yes	***
1 vs 2.5	-0.07315	10.26	Yes	***
1 vs 7.5	-0.03462	4.853	Yes	***
7.5 vs 5.0	-0.258	36.17	Yes	***
7.5 vs 12.5	-0.1128	15.81	Yes	***
7.5 vs 15.0	-0.1036	14.53	Yes	***
7.5 vs 25.0	-0.09623	13.49	Yes	***
7.5 vs 10.0	-0.06954	9.749	Yes	***
7.5 vs 2.5	-0.03854	5.403	Yes	***
2.5 vs 5.0	-0.2195	30.77	Yes	***
2.5 vs 12.5	-0.07423	10.41	Yes	***
2.5 vs 15.0	-0.06508	9.124	Yes	***
2.5 vs 25.0	-0.05769	8.088	Yes	***
2.5 vs 10.0	-0.031	4.346	No	**
10.0 vs 5.0	-0.1885	26.42	Yes	***
10.0 vs 12.5	-0.04323	6.061	Yes	***
10.0 vs 15.0	-0.03408	4.777	No	**
10.0 vs 25.0	-0.02669	3.742	No	**
25.0 vs 5.0	-0.1618	22.68	Yes	***
25.0 vs 12.5	-0.01654	2.319	No	ns
25.0 vs 15.0	-0.00739	---	No	ns
15.0 vs 5.0	-0.1544	21.64	Yes	***
15.0 vs 12.5	-0.00915	---	No	ns
12.5 vs 5.0	-0.1452	20.36	Yes	***

Table S5: Statistical analysis of *in vitro* EFA using different concentrations of glucose. Significance between average ECAR normalised to basal ECAR and protein content are shown, with *P*-values < 0.05 = *, *P*-values < 0.01 = ** and *P*-values < 0.001 = ***.

All concentrations of extracellular glucose were significant when compared to the control where the

extracellular concentration of glucose is equal to zero (Figure S4).

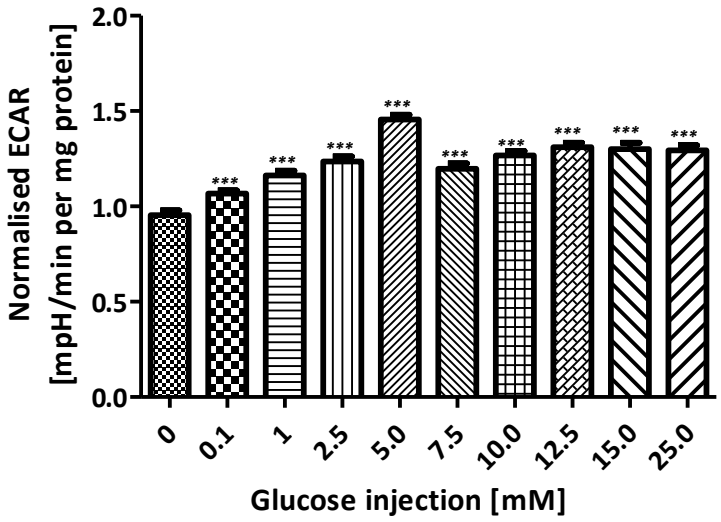

Figure S4: Statistical analysis of *in vitro* EFA ECAR using different concentrations of glucose showing all concentrations used above zero were significant. *P*-values < 0.001 = ***.

OCR analysis

Table Analyzed	OCR Normalized			
One-way analysis of variance				
P value	P<0.0001			
P value summary	***			
Are means signif. different? (P < 0.05)	Yes			
Number of groups	10			
F	15.88			
R squared	0.5436			
Bartlett's test for equal variances				
Bartlett's statistic (corrected)	6.709			
P value	0.6674			
P value summary	ns			
Do the variances differ signif. (P < 0.05)	No			
ANOVA Table	SS	df	MS	
Treatment (between columns)	0.1026	9	0.0114	
Residual (within columns)	0.08615	120	0.000718	
Total	0.1887	129		
Newman-Keuls Multiple Comparison Test	Mean Diff.	q	Significant? P < 0.001?	Summary
25.0 vs 0	-0.08932	12.02	Yes	***
25.0 vs 0.1	-0.06621	8.90	Yes	***

		9		
25.0 vs 1	-0.06442	8.669	Yes	***
25.0 vs 2.5	-0.04373	5.885	No	**
25.0 vs 5.0	-0.02905	3.909	No	ns
25.0 vs 12.5	-0.02263	---	No	ns
25.0 vs 15.0	-0.01409	---	No	ns
25.0 vs 10.0	-0.01156	---	No	ns
25.0 vs 7.5	-0.01	---	No	ns
7.5 vs 0	-0.07932	10.67	Yes	***
7.5 vs 0.1	-0.05621	7.563	Yes	***
7.5 vs 1	-0.05442	7.323	Yes	***
7.5 vs 2.5	-0.03373	4.539	No	*
7.5 vs 5.0	-0.01905	---	No	ns
7.5 vs 12.5	-0.01263	---	No	ns
7.5 vs 15.0	-0.00409	---	No	ns
7.5 vs 10.0	-0.00156	---	No	ns
10.0 vs 0	-0.07776	10.46	Yes	***
10.0 vs 0.1	-0.05464	7.353	Yes	***
10.0 vs 1	-0.05286	7.113	Yes	***
10.0 vs 2.5	-0.03217	4.329	No	*
10.0 vs 5.0	-0.01749	---	No	ns
10.0 vs 12.5	-0.01106	---	No	ns
10.0 vs 15.0	-0.00253	---	No	ns
15.0 vs 0	-0.07523	10.12	Yes	***
15.0 vs 0.1	-0.05212	7.014	Yes	***
15.0 vs 1	-0.05033	6.773	Yes	***
15.0 vs 2.5	-0.02964	3.989	No	*
15.0 vs 5.0	-0.01496	---	No	ns
15.0 vs 12.5	-0.00854	---	No	ns
12.5 vs 0	-0.06669	8.975	Yes	***
12.5 vs 0.1	-0.04358	5.864	Yes	***
12.5 vs 1	-0.04179	5.624	Yes	***
12.5 vs 2.5	-0.0211	2.84	No	ns
12.5 vs 5.0	-0.00642	---	No	ns
5.0 vs 0	-0.06027	8.111	Yes	***
5.0 vs 0.1	-0.03716	5	No	**
5.0 vs 1	-0.03537	4.76	No	**

5.0 vs 2.5	-0.01468	---	No	ns
2.5 vs 0	-0.04559	6.135	Yes	***
2.5 vs 0.1	-0.02248	3.025	No	ns
2.5 vs 1	-0.02069	---	No	ns
1 vs 0	-0.0249	3.351	No	ns
1 vs 0.1	-0.00179	---	No	ns
0.1 vs 0	-0.02311	---	No	ns

Table S6: Statistical analysis of *in vitro* EFA using different concentrations of glucose. Significance between average OCR normalised to basal OCR and protein content are shown, with *P*-values < 0.05 = *, *P*-values < 0.01 = ** and *P*-values < 0.001 = ***.

Significance between 0 mM and all other concentrations of extracellular glucose is shown in Figure S5.

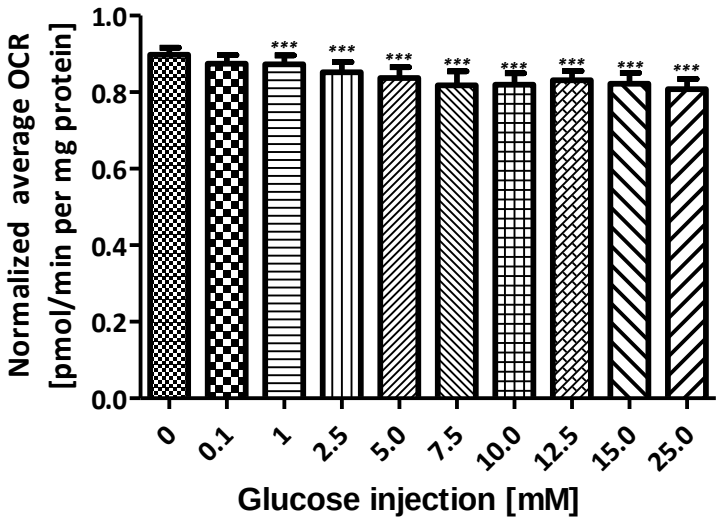

Figure S5 Statistical analysis of *in vitro* EFA OCR using different concentrations of glucose showing all concentrations used above zero were significant. *P*-values < 0.001 = ***.

Appendix E

2.2.1 *Materials*

All extracellular flux analysis consumables were purchased from Seahorse Biosciences (North Billerica, MA, USA). HepG2 cells were purchased from European Collection of Cell Cultures (ECACC, Salisbury, UK). Dulbecco's modified media, Phosphate Buffered Saline (PBS) and Rat tail Collagen I were purchased from Life Technologies (Paisley, UK). All other reagents were purchased from Sigma Aldrich (Dorset, UK).

2.2.2 *Cell Culture*

HepG2 cells were maintained in DMEM high-glucose media (glucose 25 mM) supplemented with foetal bovine serum (10% v/v), L-glutamine (2 mM), sodium pyruvate (1 mM) and HEPES (1 mM). Cells were incubated at 37ºC under humidified air containing 5% CO_2. Cells were used up to passage 17.

2.2.3 *Extracellular Flux Analysis Assay*

HepG2 cells were collected on the day of the experiment by trypsinisation and then washed thrice with serum- and glucose-free media. The cells were then plated onto a collagen coated (50 µg/ml in acetic acid

0.02 M), XF 96-well cell culture microplates (2.5×10^4 cells /100 µl medium/well) overnight in high glucose (25 mM). Culture medium was removed from all wells and replaced with 175 µl of unbuffered glucose free Seahorse Assay media, supplemented with sodium pyruvate (1 %v/v) and L-glutamate (1% v/v) pre-warmed to 37ºC. Cells were incubated in a CO_2 free incubator at 37ºC for 1 h. Before rate measurement, the XFe96 Instrument (Seahorse biosciences, North Billerica, MA) mixed the assay media in each well for 10 min, allowing the oxygen partial pressure to equilibrate. The oxygen consumption rate (OCR) and extracellular acidification rate (ECAR) were measured simultaneously thrice, establishing a baseline rate. For each measurement there was a 3 min mix followed by 3 min wait time to restore normal oxygen tension and pH in the transient microenvironment surrounding the cells. Glucose injections (0.1 – 25 mM) occurred at the end of the basal measurement cycles at 16 min, followed by 10 further measurements. The overall assay duration was 95 min.

2.2.4 *BCA Protein Quantification Assay*

Post extracellular flux analysis, assay medium was removed from all wells. Addition of 50 µl of ATP releasing agent to each well and the plate was shaken (1 min, 300 RPM). A standard curve was prepared using the BSA stock (2 mg BSA/ml in ATP releasing agent). Working reagent (WR) was prepared by adding 50 parts bicinchonic acid to 1 part copper sulphate. 5 µl of cell lysate was plated into a clear 96 well plate followed by addition of 200 µl of WR before incubation (37ºC, 30 min). The absorbance was then measured at 580 nm on a Labsystems Multiskan plate reader. Protein content was then calculated by comparing known protein concentration absorbance from the standard curve. Protein concentrations were then used to normalise the extracellular flux data giving overall rates of ECAR and OCR as mpH min^{-1} well $protein^{-1}$ and pmol min^{-1} well $protein^{-1}$, respectively.

2.2.5 *Buffering Capacity*

EFA assay media buffering capacity was measured at 37 ºC using a pH probe. HCL (0.1 M) was charged in 6 x 20 µl aliquots to 10 ml of assay media, while changes in pH were recorded. Media buffering power was calculated from the gradient of the line of best fit after plotting the change in pH vs nmol H^+ added per 7 µl (4).

2.2.6 Statistical analysis

Statistical significance was ascertained using Prism 5 software via a one way ANOVA, with values expressed as a mean ± standard deviation (S.D) taken from four independent experiments (n=4).

3.2 *EFA media buffering power & PPR_{gly} calculation*

EFA glucose-free media buffering power (BP) was calculated after measuring changes in pH after the addition of hydrochloric acid (HCL), using the gradient of the line of best fit for the data (Figure 3). The calculated value for EFA unbuffered media of 0.0005 mpH/nmol H^+ in 7 µl, calculated as the gradient of the line of best fit, ranks considerably lower than for various other types of media, as shown in Table.3. However, this is somewhat unsurprising as EFA media is inherently unbuffered by default to facilitate the detection of small changes in acidity rather than mask them.

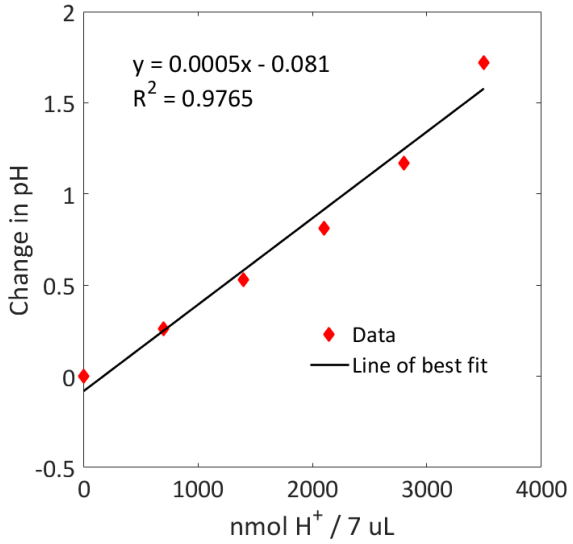

Figure 3. Glucose free EFA media buffering power. The buffering power of unbuffered glucose-free EFA media was measured by adding 0.1 M HCl aliquots to 10 ml of media, followed by calculating the gradient of the slope from the resulting pH change.

Assay medium	BP	Composition	Reference
EFA unbuffered medium	5×10^{-4}	sodium pyruvate (1 %v/v) and L-glutamate (1% v/v), pH 7.4 37oC	This paper
KRPH 0.1% BSA	4.5×10^{-2}	2 mM HEPES, 136 mM $NaCl_2$, 2 mM NaH_2PO_4, 3.7 mM KCl, 1 mM $MgCl_2$, 0.1% w/v fatty-acid-free BSA, pH 7.4, 37ºC	(7)
KRPH 1.0% BSA	3.5×10^{-2}	2 mM HEPES, 136 mM NaCl, 2 mM NaH_2PO_4, 3.7 mM KCL, 1 mM $MgCl_2$, 0.1% w/v fatty-acid-free BSA, pH 7.4, 37ºC	(7)
minimal TES Buffer	1×10^{-2}	1.3 mM $CaCl_2$, 120 mM NaCl, 0.4 mM KH_2PO_4, 3.5 mM KCL, 2 mM $MgCl_2$, 20 mM TES, 15 mM glucose 0.1% w/v fatty-acid-free BSA, pH 7.4, 37ºC	(7)
XF DMEM	1×10^{-1}	5 mM glucose, 2 mM glutamine, 0.4 mM sodium pyruvate, pH 7.4, 35ºC	(7)
XF RPMI	4.10E-02	(Bicarbonate-free) 11 mM glucose, 2 mM glutamine, 1 mM NaH_2PO_4, pH 7.4, 35ºC	(7)

Table 3: Buffering power and composition of different types of media.

Determination of the media BP allows for the calculation of the buffering capacity (BC) and respiratory contributions to ECAR. The BC can be entered directly into the EFA analyzer to account for the media BP for its readings and is therefore extremely useful for future experiments. Buffering capacity is calculated from the experimentally determined BP using Equation 3.

$$BC = \frac{1.0 \times 10^{-9}}{BP} = 2.0 \times 10^{-6} \left(\frac{\frac{\text{pH}}{\text{nmol}} \text{H}^{+} \text{in } 7\mu\text{L}}{7\mu\text{L}} \right)$$

where

$$BP = 5.0 \times 10^{-4} \left(\frac{\text{pH}}{\text{nmol}} \text{H}^{+} \text{in } 7\mu\text{L} \right) \quad (3)$$

Total proton production rate (PPR_{tot}) was calculated using Equation 4, using the average experimentally derived ECAR post glucose injection for 5 mM glucose (10.2 mpH min^{-1} mg $protein^{-1}$) (Figure 2), divided by the BP.

$$PPR_{tot} = \frac{ECAR}{BP} = 2.04 \times 10^{4} \left(\frac{\text{pmol H}^{+}}{\text{min mg protein}} \right) \quad (4)$$

Subsequently, the respiratory contributions PPR_{resp} were calculated using Equation 6, where pK1 is the overall pKa for $CO_{2(aq)} + H_2O \rightarrow HCO_3^-$ = 6.093, H^+/O_2 is the derived acidification for the metabolic transformation of glucose oxidation = 1, OCR_{tot} = 17.78 pmol O_2 min^{-1} mg $protein^{-1}$ for 5 mM over 10 measurements, OCR_{rot} = 5.17 pmol O_2 min^{-1} mg $protein^{-1}$ (7, 8). Thus,

$$PPR_{resp} = \left(\frac{10^{\mathrm{pH}-\mathrm{pK_1}}}{1+10^{\mathrm{pH}-\mathrm{pK_1}}}\right)\left(\frac{\max H^+}{\mathrm{O_2}}\right)(OCR_{tot} - OCR_{rot}),$$
$$= 1.09087E+01\left(\frac{\text{pmol H}^+}{\text{min mg protein}}\right) \quad (5)$$

Finally, using Equations 5-6, PPR_{gly} was calculated by subtracting respiratory acidification contributions from the total proton production rate giving a PPR_{gly} value of 3.0389E+04 pmol H^+ min^{-1} mg $protein^{-1}$.

$$PPR_{tot} = PPR_{gly} + PPR_{resp}\ , \quad (6)$$

Giving

$$PPR_{gly} = PPR_{tot} - PPR_{resp} = 2.0389E+04\left(\frac{\text{pmol H}^+}{\text{min mg protein}}\right) \quad (7)$$

The difference between PPR_{gly} and PPR_{resp} of 11 pmol H^+/ min per mg protein and is relatively small. This is unsurprising as the unaltered EFA data in Figure 2 implies an inverse relationship between ECAR and OCR and therefore minimal respiratory contributions to ECAR. Nevertheless, regardless of this particular cell lines proclivity to fund ECAR with predominantly glycolytic acidification, it is a worthy and facile endeavor for the sake of understanding the cellular bioenergetic output.

3.1 *Extracellular Flux Analysis*

The effects of changes in extracellular glucose concentration (0-25 mM) on ECAR and OCR for HepG2 cells was examined. ECAR was expressed in mpH/min per mg protein, including respiratory contributions to acidification, and OCR as pmol/min per mg protein. In this experiment, bioenergetic measurements are normalized to total well protein content and for basal readings prior to glucose injection (Figure 2). Prior to EFA, the cells were starved for 60 mins in media devoid of glucose. While the relationship between glucose concentration and ECAR/OCR is minimal, there is a definitive switch in energetic metabolism from respiratory to glycolytic, prior to accounting for respiratory acidification, post exposure to glucose. The introduction of glucose following a minor starvation period induces an increase in ECAR and decrease in OCR. This is hypothesized to be the result of an increase in glycolytic energy metabolism, which generates ATP from glucose at a faster rate than oxidative phosphorylation. Note that regardless of respiratory contributions to acidification in this instance, the concomitant reduction in OCR immediately after glucose exposure lends credibility to this as ECAR increases regardless of OCR decrease. The ability of carcinoma cell lines, including HepG2, to exhibit this phenomena is well characterized and has been reported previously (9). Average ECAR increased significantly after introduction of all concentrations of glucose compared to no introduction of glucose (*P*-values < 0.001). Average OCR after the introduction of all concentrations of glucose apart from 0.1 and 1 mM, was a significant decreased compared to no introduction of glucose (*P*-values < 0.001). Complete description of significant changes can be found in the supplementary information Appendix D.

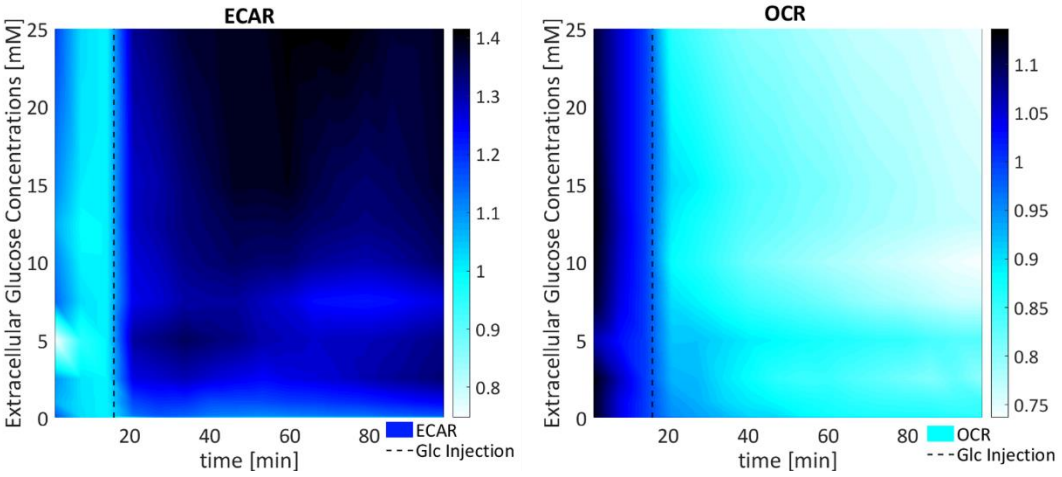

Figure 2. The effect of extracellular glucose on ECAR and OCR. HepG2 cells were exposed to serial concentrations of glucose (0.1-25mM) at t = 16 min (dashed line). ECAR and OCR is expressed in colour according to the colour bar in mpH/min per mg protein (basal) and pmol/min per mg protein (basal), respectively. Measurements indicated are an average of n=4.

References

1. Vanlier J, Wu F, Qi F, Vinnakota KC, Han Y, Dash RK, et al. BISEN: Biochemical Simulation Environment. Bioinformatics. 2009;25(6):836-7.
2. Daniel. A. Beard HQ. Chemical Biophysics. W. Mark Saltzman SC, editor. Cambridge Texts in Biomedical Engineering: Chambridge Texts; 2008. 311 p.
3. König M, Bulik S, Holzhütter H-G. Quantifying the Contribution of the Liver to Glucose Homeostasis: A Detailed Kinetic Model of Human Hepatic Glucose Metabolism. PLoS computational biology. 2012;8(6):e1002577.
4. Overmoyer B. Uniformity of liver density and nonheme (storate) iron distribution. Archives of pathology & laboratory medicine. 1987;111(6):5.
5. Pollock AS. Intracellular pH of hepatocytes in primary monolayer culture. The American journal of physiology. 1984;246(5 Pt 2):F738-44.
6. Vinnakota K, Kemp ML, Kushmerick MJ. Dynamics of muscle glycogenolysis modeled with pH time course computation and pH-dependent reaction equilibria and enzyme kinetics. Biophysical journal. 2006;91(4):1264-87.
7. Mookerjee SA, Brand MD. Measurement and Analysis of Extracellular Acid Production to Determine Glycolytic Rate. Journal of visualized experiments : JoVE. 2015(106):53464.
8. Mookerjee SA, Goncalves RL, Gerencser AA, Nicholls DG, Brand MD. The contributions of respiration and glycolysis to extracellular acid production. Biochimica et biophysica acta. 2015;1847(2):171-81.
9. Warburg O. On the origin of cancer cells. Science. 1956;123(3191):309-14.

Harry Pointon

Dynamic alterations: Proposal for an alternate autonomous flight regime.

Harry A G Pointon
General Engineering Research Institute, Faculty of Engineering and Technology, Liverpool John Moores University, James Parson Building, 3 Byrom St, Liverpool, L3 3AF
Email address: H.A.Pointon@2016.ljmu.ac.uk

Abstract: When mapping large spaces using autonomous aerial vehicles, a boustrophedon or raster path is generally employed to generate a total coverage path. This raster path is fixed throughout the flight with no alterations, excepting object avoidance or meteorological factors. Mapping systems involving 3D reconstruction often utilise structure from motion techniques, whereby images are captured at regular intervals during the flight and used to generate a point-cloud offline. An inherent problem with the feature-invariant raster scan method is the "shadowing" effect caused by single direction capture during flight over objects protruding in the Z-axis. A method for countering this shadowing effect is to reverse the flight path and re-capture the space. However this is costly in terms of flight time, and is only required over the sections of the space featuring the objects. This paper proposes an alternate flight path regime dealing with an active optimisation approach. Monitoring of the environments topology via the capture sensors allows detection of problematic geometry; from this data, actions may be taken to avoid the scanning defects which would otherwise be caused. It is suggested the overall efficacy of this approach is to be determined via comparison of models generated from identical sample spaces using a dynamically optimised path and a feature-invariant path, in terms of statistical mesh metrics, and operator assessment.

Keywords: UAV, autonomous, 3D reconstruction, dynamic path alteration, path planning, object avoidance, path optimisation.

Introduction

There is currently the technology to capture and generate 3 dimensional maps of large areas; however these systems usually rely upon the input of a human operator for efficient coverage [1]. With the increasing processing power of compact systems and the expanding working envelopes of multirotor platforms, effective autonomous mapping is becoming a reality [2] [3] [4]. UAVs can be applied to many areas for use in data capture, and sensor deployment. While the units themselves are relatively lost cost the operating requirements can be prohibitive if the human teams are limited. For example, the cost of training a single operator to the Civilian Aviation Authority requirements is in the region of £1200. While the pilot is operating the UAV their work load must be taken up by another team member, while observers and flight assistants could also be necessary. If however the role of pilot could be reduced to that of flight monitoring while an autonomous system controls and fulfils the UAV mission these costs could be managed. While control systems may be able to better stabilise a multirotor the object identification and path optimisation capabilities of a trained pilot exceed that of current systems. Development in the area of path optimisation would lead to a reduction is operating costs for such systems.

In the applications of search and rescue or the mapping of an unknown area a system of path planning

termed “Complete Coverage Path Planning” or “CCPP” is used [5] [6] [7] [8]. In the most basic form, unpopulated regions may be assigned a path with little geometric complexity. Primary methods for route generation centre around so called “raster” paths, these may take the form of boustrophedon square fringe patterns or square spiral paths [7] [8]. There is significant research in generating these “CCPP” routes for 2 dimensions or in applications involving a space bound to a plane which varies in the third dimension [1]. Using local-altitude sensing equipment such as LiDAR the path of the agent may be altered to compensate for undulations in the search or mapping space. These modifications aid in the acquisition of consistent images or data throughout the flight. However, this flight regime requires the generated path be free from obstacles either natural in the form of trees, or artificial such as pylons, towers or walls. Object or collision avoidance systems may be integrated into the command structure for UAVs deployed in spaces liable to such complications. When considering mapping a cluttered space, in 3 dimensions using a pseudo-holonomic platform with no prior knowledge of the environment, existing single route planning algorithms are not sufficient. Where pseudo-holonomic refers to the assumption that although a multirotor requires pose-modification to translate in the x and y axis this may be considered negligible for the purposes of path generation. Efficacy of generated paths is judged by some standard factors; the time required for the flight, the flight path length and the total coverage of the space expressed as a ratio of the space covered to that uncovered by the path [6] [8].

Existing Work

Two main schools of thought and application are prevalent when viewing path planning and path generation. The first involves the generation of paths based upon data already known about the space, its topology, geometry and boundary conditions [8]. From this data a path is generated which fulfils requirements, such as point to point navigation, total coverage of a space or object avoidance. The second scheme revolves around assumed ignorance of the environment with little to no initial data provided. This regime may include Simultaneous Localisation And Mapping (SLAM), whereby an agent continuously collecting environmental data constructs a map of the environment from its movements and alters the path actively [3]. The first method may be carried out offline and separately from the active control segments of the system. The second is an online process which runs in concert with the other systems, actively collecting and distributing data to increase knowledge of the environmental and optimise the path.

Jin and Tang proposed and demonstrated a method for covering large outdoor spaces using an offline “seed curve” searching algorithm. In this application the agent is a ground vehicle, and therefore is terrain locked, however the work is applicable to single local-altitude mapping using UAVs. Due to the system implementation being agriculture any successful path is reusable therefore initial generation cost is more flexible. Thus the data required for path generation using this method is more expansive. The system requires terrain models along with the space boundary geometry to function. In search and rescue applications or spaces of unknown topology this renders the “seed curve” algorithm in this arrangement inviable. Cui et al published a paper on their progress and the development of a small scale multirotor for autonomous navigation. The main focus of their work is the navigation of agents in unknown cluttered environments using SLAM driven systems. The path planning structure employed relies upon a two stage process; Firstly the initial configurational stage, where the boundary conditions of the space are analysed and a path generated using the A* path planning method. This is then followed by the active stage where a vector field collision avoidance system is employed. The nature of the application of this system is not a coverage focused system, but rather a point to point navigation solution. In this application however the system is shown to be highly effective. Due to the application of the proposed system being a multirotor UAV random coverage path planning such as that proposed by Liu et al are inviable due to the extended path lengths. Grid based systems such as those investigated by Shivashankar et al show good coverage in online situations; however these systems are wholly investigated in 2D scenarios. The simulations conducted by Shivashankar et al demonstrated a “Delayed Greedy-Scan” (DGS) to be the most efficient scheme when compared to the “Greedy Scan” (GS), the Closest-First Scan (CFS) and Iterated WaveFront (IWF) methodologies. The DGS, GS and CFS approaches generated solutions in 5 to 10 seconds while the IWF strategy took on average an “order of magnitude longer” [9], while processing technology and implementation will vary the general demonstration of processing time would hold for an online processing system onboard a UAV. Considering the findings of the work the DGS strategy would be the most relevant. In the work conducted by Shivashankar et al the grid was generated via an overlay method whereby all cells are identical quadrilaterals. Yazici et al performed a series of experiments and simulations based around multi-agent Sensor-driven coverage using a cell based system, however unlike

Shivashankar et al the cells were generated via a Generalised Voronoi diagram to compensate for the "narrow nature" [10] of the testing environment.

Proposed Method

To investigate the efficacy of dynamic path alteration in response to environmental data when applied to a cluttered unknown space the methodology laid out in this section is proposed. Testing would be carried out using a purpose built multirotor optimised for flight duration to aid testing iteration. Current UAVs available do not present with sufficient flight characteristics. Using low discharge capacity, high storage Lithium Polymer batteries and accepting a reduction in manoeuvrability or payload capacity, flight times of 30 minutes are entirely plausible [11]. Experimental analysis would be conducted outdoors using GPS as the primary mode of localisation in concert with LiDAR for local-altitude monitoring. Following the demonstrated success of a two phase path planning system by Cui et al it is suggested that this method be employed in the investigation of dynamic path alteration mapping. The initial stage remaining the offline configurational process, whereby boundary conditions are identified and the most effective CCPP generated. The second, online stage however would be modified to both include collision avoidance and data capture optimisation simultaneously. The work conducted by Shivashankar et al may be employed in the online stage to generate path modifications which may show the most efficient avoidance action. With some modification this may also allow the inclusion of Generalised Voronoi cell generation to compensate for the irregular topology anticipated in the testing phase. An investigation is required to determine the effect of variable topology on a pre-defined CCPP, and a judgement must be made as to the efficacy of including the topological variations into the dynamic alterations. If terrain variations cause a significant loss in efficiency to the path then the implementation of an online variation of Jin and Tang's "seed curve" algorithm may be required.

In order to assess the effectiveness of the dynamic alteration path approach in comparison to the standard object avoidance only CCPP scheme, a sample space is to be flown and a 3D reconstruction generated using photogrammetry techniques. The generated models may then be compared in terms of mesh elements and coverage regarding artefacts such as shadowing and uncaptured spaces. The comparison of these data sets along with flight time and path efficiency metrics would inform the confirmation or refutation of the hypothesis that a dynamically altered path approach would be more efficient than simple CCPP methods.

Conclusions

Through the combination of path planning approaches described in this work a more robust form of UAV control may be derived. Implementation of such a system is not restricted to one form of problem, for thermal oriented scanning, 2D infrared or spectral image data may be used to trigger the path alterations, for gas sampling or nuclear radiation monitoring 1D point data may be integrated. From the proposed work described an alternate form of autonomous flight may be derived. With the application of more sophisticated autonomous flight regimes UAV systems may bear more responsibility in mission optimisation freeing the operators to concentrate on other tasks.

Works Cited

[1] J. Jin and L. Tang, "Coverage path planning on three-dimensional terrain for arable farming," *Journal of Field Robotics*, vol. 28, no. 3, pp. 424-440, 2011.

[2] K. Alisher, K. Alexander and B. Alexandr, "Control of the Mobile Robots with ROS in Robotics Courses," in 25th DAAAM International Symposium on Intelligent Manufacturing and Automation, Vienna, 2014.

[3] J. Aulinas, Y. Petillot, J. Salvi and X. Lladó, "The SLAM problem: a survey," in 2008 conference on Artificial Intelligence Research and Development, Amsterdam, 2008.

[4] S. Dogru and L. Marques, "Towards Fully Autonomous Energy Efficient Coverage Path Planning for Autonomous Mobile Robots on 3D Terrain," in 2015 European Conference on Mobile Robots (ECMR), Lincoln, 2015.

[5] A. Chaves, P. Cugnasca and J. Neto, "Adaptive Search Control Applied to Search and Rescue Operations Using Unmanned Aerial Vehicles (UAVs)," IEEE LATIN AMERICA TRANSACTIONS, vol. 12, no. 7, pp. 1278-1283, 2014.

[6] L. Yang, J. Qi, D. Song, J. Xiao, J. Han and Y. Xia, "Survey of Robot 3D Path Planning Algorithms," Journal of Control Science and Engineering, vol. 1, p. 22, 2016.

[7] A. Khan, I. Noreen and Z. Habib, "On complete coverage path planning algorithms for non-holonomic mobile robots: Survey and challenges," Journal of Intelligent and Robotic Systems, vol. 74, no. 3, 2013.

[8] M. Julia, A. Gil and O. Reinoso, "A comparison of path planning strategies for autonomous exploration and mapping of unknown environments," Autonomous Robots, vol. 33, no. 4, pp. 427-444, 2012.
[9] V. Shivashankar, R. Jain, U. Kuter and D. Nau, "Real-Time Planning for Covering an Initially-Unknown Spatial Environment.," in Artificial Intelligence Research Society Conference, Palm Beach, 2011.
[10] A. Yazici, G. Kirklik, O. Parlaktuna and A. Sipahioglu, "A Dynamic Path Planning Approach for Multi-Robot Sensor-Based Coverage Considering Energy Constraints," in IEEE International Conference on Intellogent Robots and Systems, St. Louis, 2009.
[11] Ø. Magnussen, G. Hovland and M. Ottestad, "Multicopter UAV design optimization," in Mechatronic and Embedded Systems and Applications (MESA),, Senigallia, 2014 .
[12] J. Cui, S. Lai, X. Dong and B. Chen, "Autonomous Navigation of UAV in Foliage Environment," Journal of Intelligent & Robotic Systems, vol. 80, no. 1, pp. 100-118, 2016.
[13] M. Davoodi, F. Panahi, A. Mohades and S. Naser-Hashemi, "Clear and smooth path planning," Applied soft computing, no. 32, pp. 568-579, 2015.
[14] O. Cetin, I. Zagil and G. Yimaz, "Establishing obstacle and collision free communication relay for UAVs with artificial potential fields.," Journal of Intelligent and Robotic SYstems, vol. 69, no. 1, pp. 361-372, 2013.
[15] Y. Kim, D.-W. Gu and I. Postlethwaite, "Real-time path planning with limited information for autonomous unmanned air vehicles," Automatica, vol. 44, no. 3, pp. 696-712, 2008.

Ben Mcloughlin

Sensor roll & pitch stabilisation for an UAV-based LiDAR system

McLoughlin B, J: Bezombes F:
Liverpool John Moores University, Engineering and Technology Research Institute, James Parsons Building, 3 Byrom Street, Liverpool L31 3AF
B.McLoughlin@2011.ljmu.ac.uk

Applications for light detection and ranging (LiDAR) technology have become more flexible due developments focusing on compact devices that are compatible with external components. Such advancements in LiDAR technology have provided consumers with opportunities to mount lightweight and robust LiDAR devices onto unmanned aerial platforms. The adaptability of unmanned technology is appealing due to their deployment capabilities within smaller areas at lower flying altitudes. LiDAR devices such as the Velodyne HDL32, the device used in this study, have the ability to gather 700,000 distance measurements per second and therefore generate a point cloud on a frame-by-frame basis. However, in order to merge multiple frames to produce a complete 3D point cloud map, it is therefore a vital factor to monitor the change in attitude and orientation of the sensor as it moves during flight. This work focuses on the investigation of an inertial sensor filtering algorithm in an attempt to stabilise roll and pitch angles generated from dead reckoning sensors pre-built within the LiDAR system. The method presented proposes the use of a complementary filtering algorithm framework implemented after identifying a threshold based on readings calibrated from the sensor at 0° . Results show that initial pre-filtered roll and pitch angles experience high levels of drift over time. With this expected, trigonometric calculations from accelerometers are combined with noisy gyroscopic data to stabilise roll and pitch with an accuracy of +- 1° before the integration with GPS and magnetometers, this C++ based algorithm also has the flexibility to be deployed on-board a small embedded device as a real time data filtering system.

Keywords: UAV, LiDAR, Complementary Filtering, Point Cloud, Velodyne,

1.0 Introduction

1.1 Background

Airborne LiDAR (Light Detection and Ranging) is progressively becoming a more suitable implementation of laser sensing technology to systematically survey surface topography and generate precise fine-scaled 3D georeferenced maps of a subjected environment. Advancements in LiDAR system technology have seen previous sizable and weighty systems becoming less frequently implemented in favor of the design of miniature and compact LiDAR devices. These compact products can therefore integrate with more robust and easily deployable aerial based platforms such as an UAV. The use of an UAV based LiDAR system has revolutionised aerial mapping technology as the ability of a small unmanned aerial vehicle to access small and confined areas along with improved maneuvering capabilities and flexibility to operate at lower altitudes is very appealing to researchers and industrialists worldwide (1) (2).

Light Detection and Ranging, also abbreviated as LiDAR, is an optical measurement technology which incorporates the use of light in the form of a pulsed laser to measure varying distances (3) (4). As a laser is pulsed, it is reflected of an object in the surrounding environment and the time taken to return to the LiDAR is related to the finite speed of light to calculate the distance that the object is away from the position of the sensor. This theory is known as the Time of Flight principle (5). A mathematical representation of this can be seen in Eq.1.

$$distance = c * t/2 \quad \text{Eq. 1}$$

Where;
c = finite speed of light = 299,792,458 m/s
t = time of laser flight (s)

The Velodyne HDL-32E LiDAR system is one of a few well known LiDAR devices on the current market. Weighing at just 1kg it can be easily integrated with an unmanned aerial vehicle resulting in a functioning airborne mapping system. The HDL32 system consists of 32 lasers rapidly firing capturing a rate of 700,000 distance measurements per second. Each distance measurement is then integrated with the corresponding horizontal and vertical angles recorded at the time that each distance measurement was acquired. These variables are then substituted into trigonometric equations to calculate the 3D spatial co-ordinates of that subjected distance measurement (6). Therefore, this process results in the generation a spatial 3D map or *point cloud* representation of an environment, a typical example from the HDL-32 is shown in Fig. 1.

However, point clouds generated from the HDL-32 are produce on a *frame-by-frame* basis, where 1 frame is the equivalent of 1 full revolution of the upper rotating section of the LiDAR device. As shown in Fig.1, spatial resolution of the single frame map is very low. Therefore, in order to produce a dense and high resolution point cloud map it is necessary to combine multiple frames as the sensor moves due to the flight path of the UAV. The combination of point clouds is known as point cloud registration. However, when utilizing the registration process it is vital to monitor the position and orientation of the sensor at all times as this will allow for the accurate frame merging process.

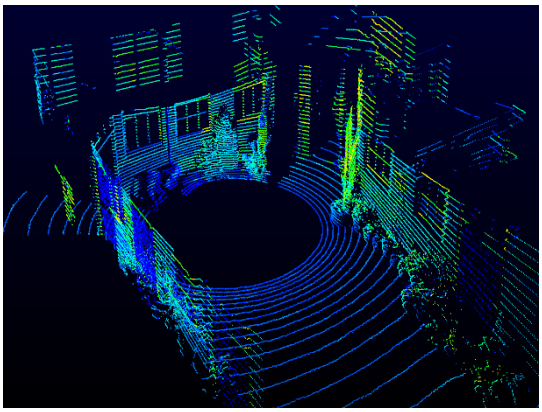

The HDL32 has a built in 9 degree of freedom (9DOF) inertial measurement unit (IMU) located within the stationary lower section of the device. An IMU is a system which uses inertial sensors such accelerometers and gyroscopes to monitor accelerations of a body along X, Y & Z and angular displacement around X, Y & Z respectively (6). However, these inertial sensors are prone to noise and drift over time and therefore can produce significant errors within readings. Therefore, it is vital that data filtering algorithms are applied to the outputted readings from the accelerometers and gyroscopes to reduce the magnitude of error.

1.2 Aim

The main aim of this study is to implement a fluent and efficient sensor filtering algorithm to operate on noisy inertial dead reckoning sensors in an attempt to stabilise the Euler angles (roll & pitch) of a ridged body, in this case the Velodyne HDL-32. The accurate monitoring of position and orientation is the key to generating highly precise 3D point cloud maps during an aerial scanning process.

2.0 Methods

2.1 Calibration

Theoretically, when the HDL32 is stationary and retaining an upright position, readings produced from the internal gyroscopes and accelerometers should produce 0g and 0deg/s for X & Y from accelerometers and roll, pitch and yaw for gyroscopes respectively, whereas the Z axis for accelerometers at a stationary position should read 1g as this is the magnitude of the downwards force acting on the HDL32 due to gravity. However, readings from the internal position monitoring sensors are producing readings which assume the HDL32 is moving and adjusting roll and pitch.

The raw sensor values can be seen in Fig. 2. The fluctuations and offsets are due to noise and drift that these sensors experience. Therefore, to enable accurate primary readings the sensors within the IMU were calibrated to calculate how much the readings were ranging from the correct value of 0 (1g for Z axis of accelerometer) whilst at a stationary position.

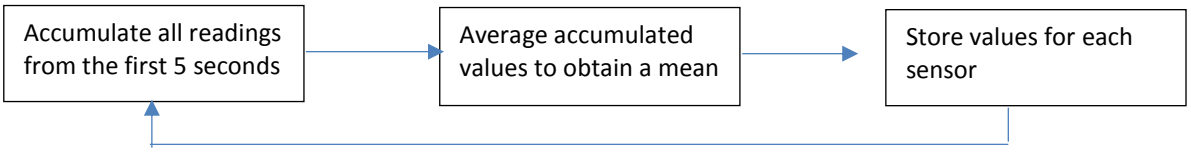

Fig 2 – Calibration process

This process was repeated 25 times to obtain a mean for each sensor. This allowed for temperature stabilization of the HDL32 to neglect the effect temperate change has on sensor readings. All 25 values where then averaged to acquire a final offset value for both accelerometers and gyroscopes. This value was then subtracted from every reading acquired from the sensors to offset the readings and account for noise.

2.2 Roll & Pitch Calculations

2.2.1 Accelerometers

The magnitude of forces acting on accelerometer axis' can be implemented into mathematical algorithm to calculate Euler angles of a rigid body. Equation 2 shows how forces which are quantified in units of G acquired from accelerometers can be used to calculate roll (φ) and pitch (θ).

$$tan\emptyset = \frac{Gpy}{Gpz} \quad \text{Eq. 2}$$

$$tan\varphi = \frac{-Gpx}{\sqrt{Gpy^2 + Gpz^2}} \quad \text{Eq. 3}$$

Roll and pitch angles can be isolated from Equation 2 by applying the inverse tangent (arctan) trigonometric method.

2.2.2 Gyroscopes

Readings from the gyroscopes were acquired in the degrees per second format (deg/s). Therefore, in an attempt to monitor roll and pitch, an algorithm was used to calculate the amount of degrees rotated within a specified time frame *t*. The HDL32 provided time stamps with every reading, therefore Equation 3 was implemented to obtain roll and pitch measurements.

$$freq = t - t_{-1} \quad \text{Eq. 4}$$

$$displacement(\text{deg}) = gyro\left(\frac{deg}{s}\right) * freq\ (s) \quad \text{Eq. 5}$$

$$Roll\ (\text{deg}) \mathrel{+}= displacement(\text{deg}) \quad \text{Eq. 6}$$

This algorithm was also used for the calculation of the pitch angle, however, using the respective gyroscope reading.

2.2.3 Complementary Filter

When considering the subject of robotics, using inertial sensors as a means of robot pose estimation and orientation tracking is and will continue to be a useful system to implement. However, with limitations of accelerometers and gyroscopes previously explained, raw data from such sensors cannot be integrated without filtering. In steps the Complementary Filter (CF). Occasionally preferred to the sophisticated Kalman Filter (KF) (which is not covered in this study), the CF integrates readings from the accelerometers and gyroscopes to provide the best possible outcome by *complementing* the error from each inertial sensor to calculate angle of orientation. On the short term, the filter uses the data from the gyroscope as it is very precise and not susceptible to external forces and on the long term the CF uses accelerometer data as it does not drift with time.

The CF algorithm is shown below.

$$angle = \tau * \big(angle + (newRate * dt)\big) + ((1 - \tau) * newAngle) \qquad \text{Eq. } 7$$

Where;
τ = coefficient used to tune the filter
newRate = angle measured from gyro(deg/s)
dt = sample frequency (s)
newAngle = angle measured from accelerometer using atan2 (deg)

3.0 Results & Discussion

Roll and pitch angles acquired from raw unfiltered and pre-calibrated readings from the gyroscopes and accelerometers at a stationary position can be found in Figures 2 and 3 respectively. Figure 2 shows that the roll and pitch angles acquired from the gyroscopes initially are accurate but severely increase over time. This is a clear example of gyroscopic drift as the LiDAR is stationary and readings should be near 0 degrees. Similarly, roll angles calculated from the accelerometers has a clear offset of approximately 2 degrees. This shows that readings prior to f[illegible] vibrations. Pitch readings, however, Figure 3 shows that pit[illegible] approximately 1 degree. However, they are seen to converge towards the neutral line of 0 degrees, which are considered fairly accurate results.

Fig 3 – Roll & Pitch gyroscope (unfiltered)

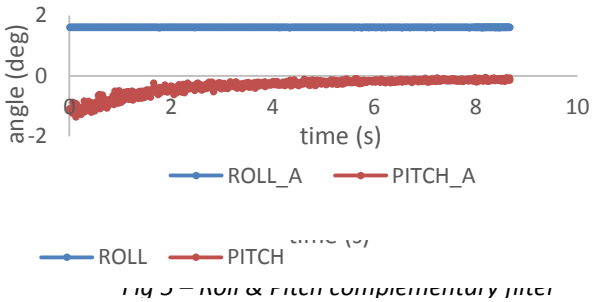

On the other hand, when integrating the complementary filter into both roll and pitch readings results in a clear effect of angle stabilization and reduction of noise and drift. As shown in Fig 5, roll angles are seen to experience small fluctuations at first but as the filter settles, the roll angles are seen to near perfectly align with the 0 degree neutral line. This is a significant improvement compared to roll angles produced from the gyroscopes and accelerometers alone. However, pitch angles experience initial fluctuations but with a larger magnitude but as the filter settles, readings become smoothers but not as accurate as the roll readings with an offset of approximately 0.25 degrees.

4.0 Conclusions

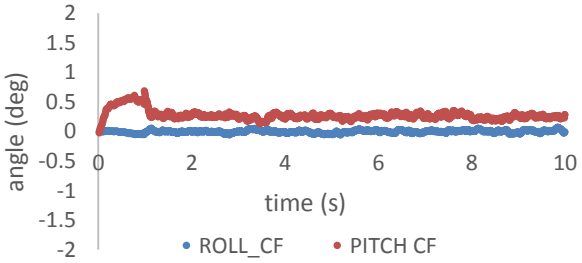

In conclusion, the CF framework successfully stabilised roll and pitch angles acquired from very noisy initial sensors. The CF operated on inaccurate sensor data acquired at 0 degrees to reduce offsets and improve orientation and position monitoring data. However, values acquired for pitch angles acquired from the CF where not as accurate as roll angles but an error of approximately 0.25 degrees is an acceptable error value without the use of further position enhancing technology such as GPS and magnetometers.
For future work, the implementation of a sophisticated Kalman Filter (KF) shall be used to compare datasets from the CF and to decide which algorithm stabilises roll and pitch angles with increased accuracy.

Refereneces

1. *Unmanned Aerial Vehcile Unique Cost Estimating Requirements.* Malone, P, Apgar, H and Stukes, S. s.l. : IEEE, 2013. 2-9 March 2013, Aerospace Conference. INSPEC Accession Number: 13502727.

2. *Assessing the Feasibility of UAV-Based LiDAR for High Resolution Forest Change Detection.* Wallace, L O, Lucieer, A and Watson, C S. Melbourne : International Archives of the Photogrammetry, Remote Sensing and Spatial Information Sciences, 2012. Vols. XXXIX-B7. XXII ISPRS Congress held 25/08/12 - 01/09/12.

3. *Accuracy Assessment of LiDAR-Derived Digital Elevation Models Based on Approximation Theory.* XiaoHang, L, Hai, H and Peng, H. 6, s.l. : Remote Sensing, 2015, Journal of Remote Sensing, Vol. 7, pp. 7062-7079.

4. *Airborne laser scanning - An introduction and overview.* Wehr, A and Lohr, U. 1992, ISPRS Journal of Phototgramm. Remote Sensing, Vol. 54, pp. 68-82.

5. *Joint Temperature-Lasing Mode Compensation for Time-of-Flight LiDAR Sensors.* Alhashimi, A, Varangolo, D and Gustafsson, T. 12, s.l. : MDPI, 2015, Journal of Sensors, Vol. 15, pp. 31205-31223.

6. Velodyne. Velodyne HDL-32E Manual. *Velodyne LiDAR.* [Online] 2012.

Temitope Sam Osdusina

The potential application of a leader-follower formation flight in developing an airborne adjustable stereo vision system

Sam-Odusina T.J[1], Bezombes F[1], Shaw A[1]
[1] General Engineering Research Institute, Liverpool John Moores University

Abstract

This paper suggests an adjustable airborne stereo vision system based on a swarm of UAVs could potentially provide a flexible, cost-effective and relatively accurate solution to 3D reconstruction and measurement in comparison to existing ground and airborne measurement technology of a similar class. This paper addresses a customized path planner strategy to autonomously navigate a single UAV to preassigned GPS waypoints as a first step towards achieving this goal. The natural extension of this work would be autonomous formation flight of multiple UAVs to allow deployment of our proposed airborne 3D measurement system

Keywords

UAV, Stereovision, GPS

1. Introduction

In the last decade, Unmanned Aerial Vehicles (UAVs) have become the subject of much research in military and civilian applications due to their unique capabilities to explore areas that are inaccessible or dangerous to humans. This makes UAVs particularly effective in surveillance, monitoring, and remote sensing applications. This study focuses on advancing the use of UAVs for 3d reconstruction and measurement in remote sensing applications. In particular, for measurement of buildings, objects and other region of interest.

A lot of previous approaches in the past focused on LIDAR for automatically building high dense 3D dense point cloud data simply because this technique leads to dense and accurate point cloud [1]. For example, Luke *et al* [2] demonstrated the use of LIDAR systems in forest inventory to produce highly dense 3d point clouds by optimally combine observations from a Micro-Electromechanical System (MEMS)-based Inertial Measurement Unit (IMU), a GPS receiver and High Definition (HD) video. Although quite a reliable system, the spatial accuracy of the resultant point clouds is affected by the inaccuracy in position prone to GPS receiver systems. In addition, whilst the airborne data derived from LIDAR system can provide the outline and shapes of buildings, roofs etc. from unconventional viewing positions. It is becoming increasing difficult to mount these sensors on modern UAVs due to their weight constraints and high power consumption. Even if these systems are managed to be mounted on UAVs and used for reconstruction of 3d models, optical images will still be needed for coloring and texturing of the derived 3d models. These limitations draw attention to cameras, which are lightweight, fast with lower energy consumption in comparison to LIDAR systems.

A classical approach that has been presented in [3] involves using a low-resolution onboard camera, which incorporates a real time optical-flow based vision system to perform autonomous localization as well as three-dimensional scene mapping. The major drawback of an optical-based approach is its reliance on translation motion of the camera to generate flow fields, hence it cannot be used on a rotorcraft UAV that is hovering or moving slowly. Subsequent research has achieved three-dimensional scene mapping using Structure from Motion (SfM). This approach involves recovering of a set of 3-D structure and time-varying motion parameters from a set of observed image features. Clapuyt *et al.* [4] implemented such approach in order to assess the reproducibility of 3D topographic reconstructions based on aerial images acquired by a UAV platform. There are however many critical issues and limitations related to the SfM problem. Firstly, extracting visual information for feature detecting and matching is a challenging task and often lead to correspondence miss-matches.

Secondly, it is well known that the mathematical system describing the SFM problem suffers

from the scale ambiguity.

Hence, it impossible based on images alone to estimate the absolute scale of the scene captured [3]. This means real distances to perceived objects cannot be recovered unless additional knowledge of the absolute distance between camera positions is known.

Computational stereo vision has been studied and applied to UAVs for many years for altitude and motion estimates [5], obstacle detection and avoidance [6] and 3D terrain mapping [7]. This method involves using a calibrated, rigid set of two cameras to capture 3d information taken from different viewpoints at a single instant in time. Stereo correspondence algorithms [8, 9] are used to find similar matches between image planes in both cameras. Once these matches are found, triangulation techniques can be used to calculate the true 3D position generated from the projected image points. The two cameras shutters in a stereo setup are synchronized together so that camera motion does not affect the calibration procedure. Changes in the scene are also synchronized between the two images. Thus, dynamic changes in the environment do not affect the accuracy of the result [10]. In 3d terrain mapping, the key advantage of stereo over monocular structure from motion is that terrain can be reconstructed from a single synchronized pair of calibrated images hence stereovision can capture 3d information from a hovering vehicle. Stereo-based methods also offer the advantage of eliminating the scale ambiguities that are inherent in monocular systems [11]. K *et al* [10] implemented a stereo setup where two cameras were rigidly mounted on an autonomous helicopter with a 1.5m separation between the cameras for real-time generation of 3-D terrain models. The spatial accuracy and precision of a terrain map generated from a stereo vision setup depend on baseline (distance between the two cameras), the available luminance and texture of the scene, camera resolution and distance to the object in the scene. In stereo processing, a short baseline results in estimated distance, which will be less precise due to narrow triangulation. For more precise distance measurements, longer baselines are required. With a longer baseline, however, stereo matching becomes difficult, and thus there is a greater possibility of a false match. Therefore, there is a trade-off between precision and accuracy (correctness) in matching [12].

The motivation for our approach derives from the point of view of employing stereo as an airborne measuring device, where the technique is flexible, cost-effective and relatively accurate in comparison to existing measurement technology of a similar class. Our novel approach involves deploying a swarm of UAVs, each equipped with a camera and a pre-determined separation between each UAV pair as a cooperative sensor platform. The configurable distance between any two UAVs in the fleet will allow for an adaptable stereo pair base-length length, which frees up the restrictions of a pair of cameras mounted on a single UAV. This setup would allow robust data redundancy and adjustable accuracy for measurement. In order to deploy a swarm of UAVs, we first investigate how we can autonomously navigate a single UAV .The use of open source hardware is heavily relied on in achieving this goal.

This paper is organized as follows. In Section2, the open source hardware and the path planner algorithm utilised to autonomously navigate a single UAV are discussed. Section 3 discusses the software stack responsible for communicating with the autopilot and Section 4 discusses the flight-testing phase and results obtained and finally Section 5 highlights the conclusions and future work of the project.

2. System Description

A. *Hardware*

For the purpose of this research, the UAV platform used is a DJI F450 as shown in Figure 1 below. It is a standard X-frame quadcopter that has been assembled using parts from various manufacturers. The UAV is equipped to have essential features necessary for flight. The UAV has two pairs of counter-rotating blades that are propelled by four brushless DC motors which permit the vehicle to move in 6-degree of freedom (DOF) by varying the speeds of the four rotors. It is also equipped with a battery of 2200mah and 11.1v, RC receiver, GPS module and a power module, which provides a stable power supply to the system and in addition, accurately measures the battery voltage/current consumption. In order to communicate with the ground control station and other UAVs, the UAV is also equipped with 433MHz RF wireless module that is capable of receiving MAVLink packets as discussed in Section 2B below.

The autopilot system used in Figure 1 is the Pixhawk. This system offers a complete flight stack running

on powerful hardware. It includes a 32bit ARM Cortex M4 processor with a 32-bit STM32F103 failsafe co-processor, a 3 axis 16-bit gyroscope, a 3 axis 14-bit accelerometer/magnetometer and a barometer [13].

Figure 1: X-frame quadcopter

B. Communication System

The MAVLink protocol facilitates communication between the UAVs and the ground station. This communication protocol was developed at ETH Zurich for the Pixhawk MAV project [14]. It is a lightweight header protocol that has only 8 bytes overhead per packet and has built-in packet-drop detection, amongst other useful features and is designed to be used with a wide range of wired and wireless links. All MAVLink messages are generated from an XML protocol specification file. Currently, code generators for C89-compatible C, Python, and Java are available. The code generated contains all messages defined in XML specifications as well as functions for message packing and unpacking [14]. While it has a standard library of messages, custom messages can also be implemented using a generator and XML. The protocol has been utilized in a number of UAV projects and supports communication with multiple vehicles, making it particularly useful in this project.

C. Path Planner Strategy

We implement a path planner that is capable of constructing an array of waypoints from a starting to an ending point specified by the user. The user is required to specify the initial, final waypoints and the waypoint separation (resolution) for the UAV. We make a reasonable assumption that there would be no obstacles within this region of the flying area hence, it is sufficient to have a straight path connecting the starting and ending waypoints.

Figure 2: path between initial and final waypoints

Each waypoint can be thought of to consist of a Longitude (degrees) -X AND Latitude (degrees) - Y position.

$$WP_s = [X_s Y_s] \quad (1)$$

$$WP_f = [X_f Y_f] \quad (2)$$

$$WP_{(i)} = \left[X_{(i)} Y_{(i)}\right] \quad (3)$$

$$WP_{(i+1)} = \left[X_{(i+1)} Y_{(i+1)}\right] \quad (4)$$

Where WP_s is the starting waypoint and WP_f is the final waypoint. Intermediate waypoints $WP_{(i)}$ and

$WP_{(i+1)}$ are generated using the *linspace()* method from pythons numpy library to generate a row of vectors of equally spaced points between the starting and final waypoints

The waypoint separation or the distance between successive waypoints or shown below as

$$D = \sqrt{(X_{(i+1)} - X_i)^2 + (Y_{(i+1)} - Y_i)^2} \quad (5)$$

Figure 3 below shows a logical flow chart explaining the UAV flight plan.

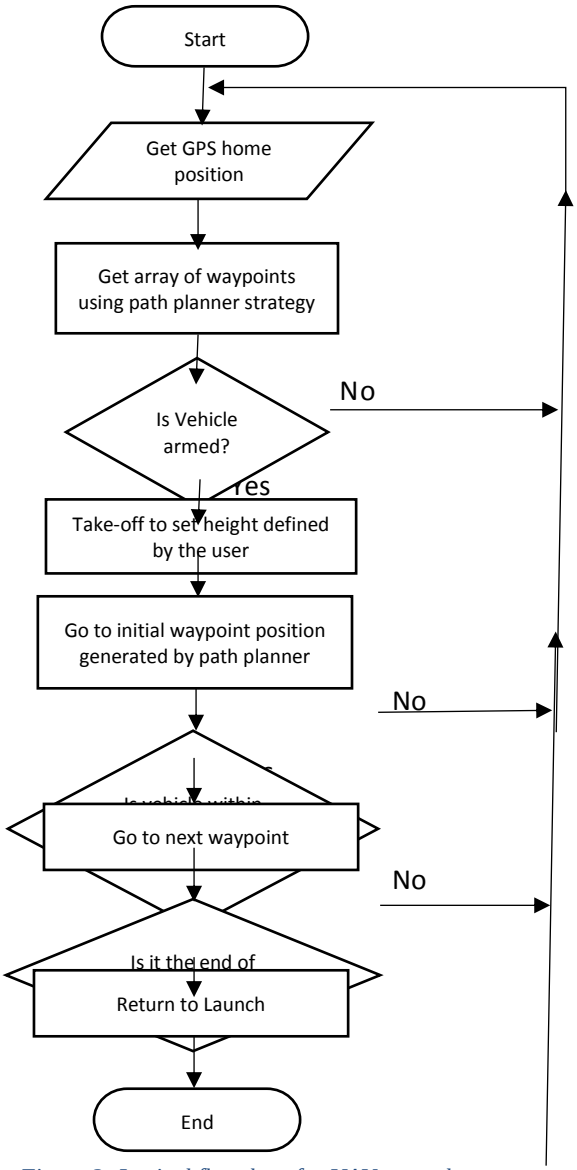

Figure 3: Logical flowchart for UAV control

3. Software Implementation

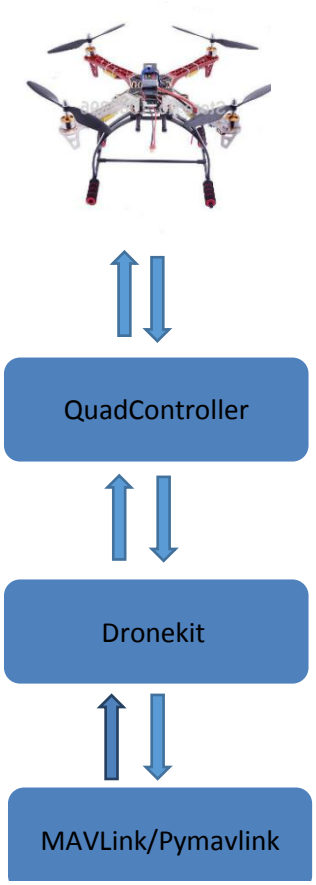

Figure 4: Software stack for communicating with MAVLink enabled vehicles

By default, MAVLink provides binding to the C programming language, which would enable the transmission of C-type encoding commands. However, a python a library named Pymavlink built upon the C library provides Python bindings and allows for the transmission of Python like-objects with MAVLink. We utilize the use of a scripting language like Python to provide extremely simple and friendly syntax that can easily display structures without having to write a lot of formatting code for each of the messaging types. The Pymavlink library is not directly implemented in this application but provides the first layer of abstraction in the software stack as shown in Figure 4. Built upon the Pymavlink module is the Dronekit API developed by 3D Robotics [15]. This was utilized as the development platform for our system. Though this library is extensive, well -documented and provides high-level classes for general vehicle control it still does not provide all of the functionality that we require for vehicle control and for this reason, we implemented our own wrapper module built upon Dronekit called QuadController. The QuadController module contains a *QuadControlle*r class that wraps up several crucial Dronekit methods, as well as provide new methods for pre-planned trajectories for the vehicle to follow based on our Path planner strategy as discussed in Section 2C.

6. Flight Testing and Results

Flight-testing was done in two phases. The first phase was ground testing using Software in the Loop (SITL) simulation/modelling to identify and fix any bugs in the code that could lead to unexpected behaviour of the aircraft in flight. The second phase involved testing on the actual hardware. The vehicle was commanded to automatically take off to a height of 5m and thereafter the autopilot's flight mode was changed to *Guided,* which allowed guiding of the vehicle to a target GPS location where the user specified the waypoint separation distance between successive waypoints. Once the vehicle reached its target GPS location it was then commanded to *ReturntoLaunch* (RTL) where the vehicle returns back to its initial home position. A security pilot acted as failsafe throughout the experiment.

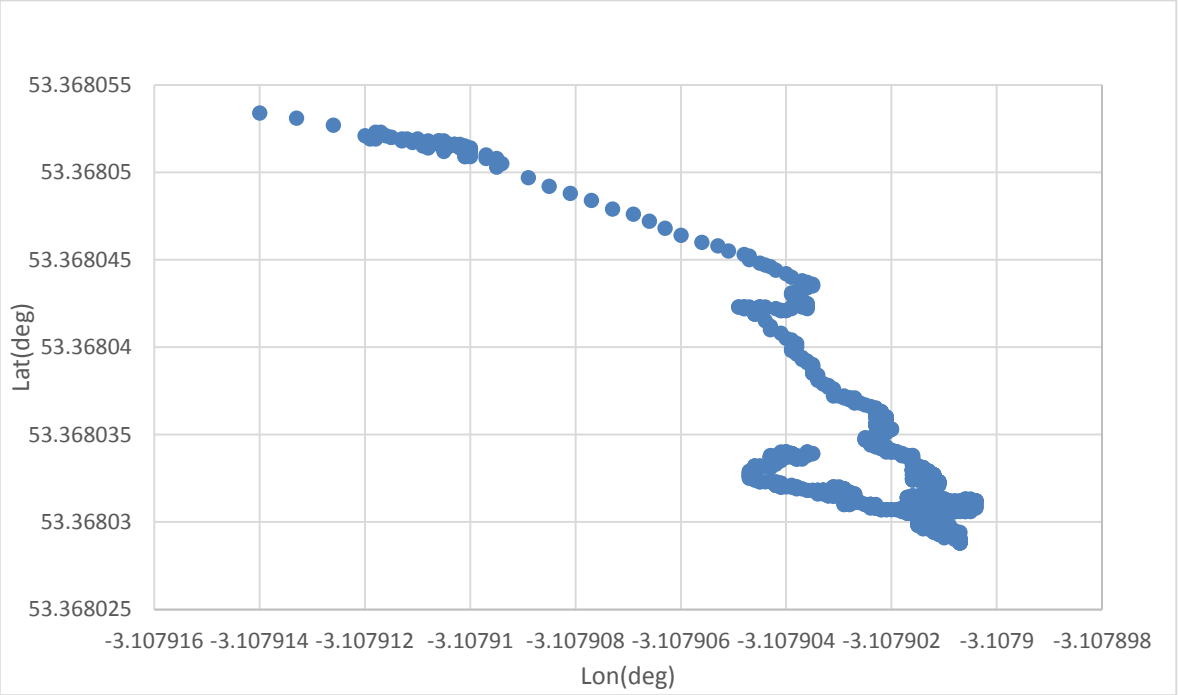

Figure 5: The real-time GPS path of UAV

Figure 5 above shows the path travelled by the UAV with the path planner solution implemented. Although it works well, it is observed that the UAV does not travel an exactly straight path, as we would expect. This because of external disturbances such as the wind, which introduces challenges. In addition, GPS inaccuracy plays a vital role. GPS accuracy is generally within a 4 to 5-meter radius.

7. Conclusions and Future Work

In this work, we investigate how we can autonomously navigate a single UAV to pre-assigned GPS coordinates. Open source hardware and software have been heavily utilized in achieving this goal. Since autonomous navigation of a single UAV has proven successful, our future work includes autonomous formation flight of multiple UAVs, to allow an adaptable stereo pair base length, which can potentially provide an adjustable accuracy in 3D measurements.

References

1. Kedzierski, M. and A. Fryskowska, *Terrestrial and Aerial Laser Scanning Data Integration Using Wavelet Analysis for the Purpose of 3D Building Modeling.* SENSORS, 2014. **14**(7): p. 12070-12092.
2. Luke, W., L. Arko, W. Christopher, and T. Darren, *Development of a UAV-LiDAR System with Application to Forest Inventory.* Remote Sensing, 2012(6): p. 1519.
3. Kendoul, F., I. Fantoni, and K. Nonami, *Optic flow-based vision system for autonomous 3D localization and control of small aerial vehicles.* Robotics and Autonomous Systems, 2009. **57**(6–7): p. 591-602.
4. Clapuyt, F., V. Vanacker, and K. Van Oost, *Reproducibility of UAV-based earth topography reconstructions based on Structure-from-Motion algorithms.* Geomorphology, 2016. **260**: p. 4-15.
5. Eynard, D., P. Vasseur, C. Demonceaux, and V. Frémont, *Real time UAV altitude, attitude and motion estimation from hybrid stereovision.* Autonomous Robots, 2012. **33**(1-2): p. 157-172.
6. Beyeler, A., J.C. Zufferey, and D. Floreano, *Vision-based control of near-obstacle flight.* AUTONOMOUS ROBOTS, 2009. **27**(3): p. 201-219.
7. Tahar, K.N., A. Ahmad, and W.A.A.W.M. Akib. *UAV-based stereo vision for photogrammetric survey in aerial terrain mapping*. 2011.

8. Fusiello, A., V. Roberto, and E. Trucco. *Efficient stereo with multiple windowing*. 1997. IEEE.
9. Kolmogorov, V. and R. Zabih, *What energy functions can be minimized via graph cuts?* IEEE transactions on pattern analysis and machine intelligence, 2004. **26**(2): p. 147-159.
10. Stefanik, K., J. Gassaway, K. Kochersberger, and A. Abbott, *UAV-based stereo vision for rapid aerial terrain mapping.* GIScience and Remote Sensing, 2011. **48**(1): p. 24-49.
11. Kitt, B., A. Geiger, and H. Lategahn. *Visual odometry based on stereo image sequences with RANSAC-based outlier rejection scheme*. 2010.
12. Okutomi, M. and T. Kanade, *A Multiple-Baseline Stereo.* IEEE Transactions on Pattern Analysis and Machine Intelligence, 1993. **15**(4): p. 353-363.
13. 3DR. *Pixhawk AutoPilot System*. 2016; Available from: https://store.3dr.com/products/3dr-pixhawk.
14. Meier, L., P. Tanskanen, F. Fraundorfer, and M. Pollefeys, *THE PIXHAWK OPEN-SOURCE COMPUTER VISION FRAMEWORK FOR MAVS.* The International Archives of the Photogrammetry, Remote Sensing and Spatial Information Sciences, Vol XXXVIII-1/C22, Pp 13-18 (2012), 2012: p. 13.
15. Dronekit. *Dronekit-Developer tools for drones*. 2015; Available from: http://dronekit.io/.

Alex Moore

Modelling Cultural Heritage Using UAVs

Moore A. J.; Bezombes F. A.; De Groote I. E.; Lilley F.
General Engineering Research Institute, Liverpool John Moores University,
James Parsons Building, Byrom Street, Liverpool, L3 3AF
E-mail address: A.J.Moore1@2010.ljmu.ac.uk

Abstract. This paper aims to provide a discussion of the techniques used in acquiring and processing wide-scale aerial data. In conjunction with a European Horizon 2020 research project, DigiArt, Unmanned Aerial Vehicles (UAVs) were used to acquire data over a wide area and at varying altitudes. The site chosen was that of the former palace of Philip II of Macedon in the ancient city of Aigai, currently known as Vergina, Greece. A camera was used to capture the data as video, recording at a resolution of 3840x2160. The camera was mounted using a stabilising gimbal to a DJI F550 hexacoptor UAV. It also provided a 'first person view' video signal for the pilot to use to ensure every aspect of the site was covered. As the data was being acquired over a week, the changing weather conditions had to be accounted for with the resulting videos needing to be colour balanced before modelling to give the illusion of a homogeneous model. After image processing, the modelling software, Pix4D mapper, was used to create the models. Each flight provided a discrete model and they needed to be merged together to form a continuous model, this was also performed in Pix4D. The resulting model spanned an area approximately 2km^2 with the high and low altitude flights providing varying amounts of detail. This type of data acquisition technique has proved to be invaluable for archaeological work due to its speed and relative ease compared with traditional methods.

Keywords. 3-D modelling, Photogrammetry, Pix4D, UAVs, Structure from motion, Archaeological site, Palace of Aigai

1. Introduction

The Palace of Aigai is a site of historical interest in Greece and was surveyed using a hexacopter Unmanned Aerial Vehicle (UAV), the work was undertaken as part of the DigiArt project, a Horizon 2020 research project (No. 665066). This collaborative pan-European project contains partners from Belgium *Grotte Préhistorique Scladina*; France *CNRS* [1]; Switzerland *Pix4D*; Greece *CERTH* [2] & *The Royal Palace and Tombs of Aigai* and the United Kingdom *Vulcan UAV* & *LJMU* [3]. The Royal Palace and Tombs of Aigai are the subject of this examination. It was originally the purpose of the project to only model the Palace, however the opportunity to survey other parts of the ancient city presented itself and so context for the Palace, with regard to its position in the landscape, can more easily be given. It is the intention for the end-result of this work to be the application of these models in virtual-reality (VR) environments, meaning people can visit these sites of historical and cultural interest even if they would otherwise be unable to. This paper investigates the methods used to create a model of the site and describes any issues which needed to be overcome.

2. Archaeological Site

The ancient city of Aigai (Αἰγαί), the location of which may be seen in Figure 1, was the first capital of

[1] Centre National De La Recherche Scientifique.

[2] Centre for Research & Technology, Hellas.

[3] Liverpool John Moores University.

Macedon [4] from 808 to 399 B.C.E. Aigai lost its place as the capital of the Macedonian empire during the reign of Archelaus I (reigned 413-399 B.C.E.) although it was kept as a ceremonial palace and the religious centre of the empire. Philip II of Macedon ascended to the throne in 359 B.C.E and was assassinated in the Palace's Theatre in 336 B.C.E., which allowed his son, Alexander the Great (Alexander III of Macedon), to reign over the Macedonian empire.[1]

a b

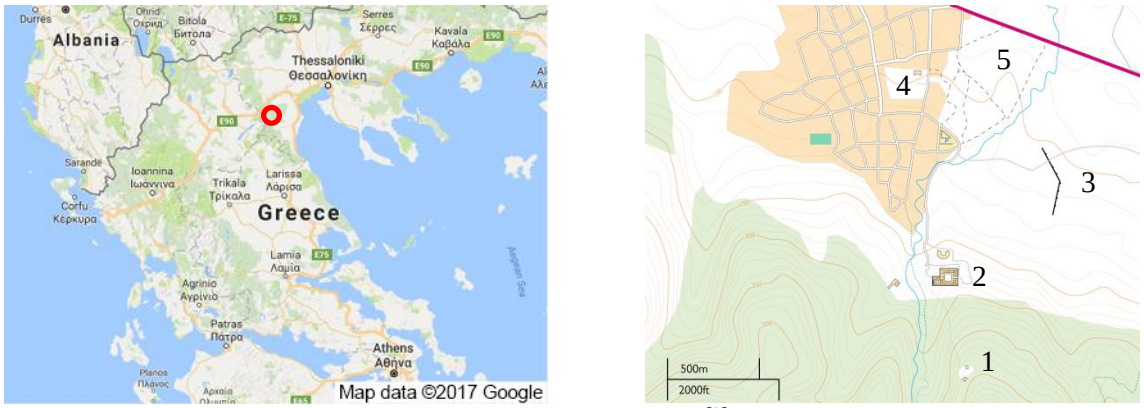

Figure 1. The location of Vergina (Aigai) in Modern Greece[2] shown by the red circle (a) and a map of the ancient city (b) showing 1 Acropolis; 2 Palace Complex; 3 City Wall; 4 Tomb; 5 Necropolis.[3]

3. Data Acquisition

3.1. Equipment

The equipment used for the project:

- DJI F-550 Hexacopter
- 5 Amp-hour 4S LiPo Battery
- Taranis X9D Controller
- Fat shark FPV system
- GoPro Hero 4 Black
- Tarot T-D2 GoPro gimbal

3.2. Method

The GoPro camera was set to record video at a resolution of 3840x2160p[5] and at 30 frames per second (fps), with the camera's post-production specific 'protune' setting engaged to ensure the highest quality output. An analogue video feed (CVBS [6]) was taken from the GoPro's 10-pin USB connection, which also provided power, and passed through to the on-board Fat shark transmitter. This video feed allowed the UAV to be flown with first-person-view (FPV), ensuring manual coverage of the site as the pilot was able to see what was being recorded while flying.

The GoPro was mounted on a Tarot T-2D gimbal to give stability to the camera and to allow manual control of the recording angle, the gimbal mount was also equipped with anti-vibration pads to minimise the artefacts caused by the GoPro's electronic rolling shutter interacting with the vibration of the system. While the pilot was engaged with flying the UAV, it was kept in full view by observers who were close-by to the pilot at all times. Under the current UAV configuration a flight time of 8 minutes was able to be utilised without depleting the battery below 20% from a charge of 90-99%.

4. Data processing

4.1. Image colour matching

Whenever exterior data is acquired over a long period of time, multiple days, it cannot be assumed that the weather and lighting will remain constant. This was indeed the case with this model's dataset with the days changing from direct, bright sunshine to overcast. The captured videos were processed to match the brightness, colour temperature and saturation of the separate models before the 3-D reconstruction processing began. This colour-correction work was undertaken using the non-destructive workflow in Adobe's suite of Premier Pro CC and Speedgrade CC to reduce the number of times the image data

[4] Macedon, also known as Macedonia, was an ancient empire which spread from the Adriatic to the Aegean Seas in the north of what is now Greece. It lasted from 808 to 168 B.C.E.[1]

[5] With digital video there are two designations for the type of data recorded, full-frame recording where the sensor is scanned in its entirety and the resulting image recorded as a discrete frame, known as progressive (p), or half-frame recording where the even horizontal lines of the sensor are scanned and recorded to a frame followed by the odd horizontal lines in a sequential frame, known as interlaced (i).

[6] CVBS (colour, video, blanking and sync) is more commonly known as 'composite video' and was, in this instance, encoded using the NTSC television standard.

undergoes ‘lossy’ compression. Lossy compression irrevocably removes some of the image data, meaning it may appear the same to humans, but can cause issues with computer processing if the data has been compressed multiple times. Ensuring the data remained as ‘pure’ as possible in the pre-reconstruction processing results in a more accurate 3-D model. The image data underwent two lossy compression stages, the original recording from the GoPro is h.264 compressed and the output from Adobe Premiere Pro is a JPEG-compressed still image.

4.2. Creation of a homogeneous model

The technique used to reconstruct the 3-D data is structure-from-motion [SfM]. SfM uses a series of overlapping images to reconstruct depth-information, in a similar manner to how bi-optic vision systems, like human eyes, reconstruct the 3-D world but with many more images.[4][5] Two or more images are required to create a model, with an overlap of 90% between images being preferable. For these UAV-based models, the recorded video is used so more than 100 images are used on each model.

The model consists of nine individual flights, resulting in nine discrete models. The videos were sampled at one frame per second and exported as a series of JPEG images. These individual datasets had a sufficient amount of overlap with one another to allow them to be merged, this was done by creating points with a known location, manual tie-points, in the models which were to be merged. After the model had incrementally been amalgamated using this method, the alignment could be checked to ensure all models had remained in their correct positions. The alignment was checked by creating more manual tie-points and examining the computed pixel-error and computed position of the manual tie-point on all relevant images. The model densification steps can be run after the alignment; these steps include creating the dense point-cloud and textured triangle-mesh.

5. Resulting Model

The resulting model spans an area of approximately 2km^2, with the longest linear-distance of 2km being between that of the acropolis (1) and a structure on the necropolis (5) seen in Figure 2b as the left-hand most building in the cluster of two at the bottom-left of the model.

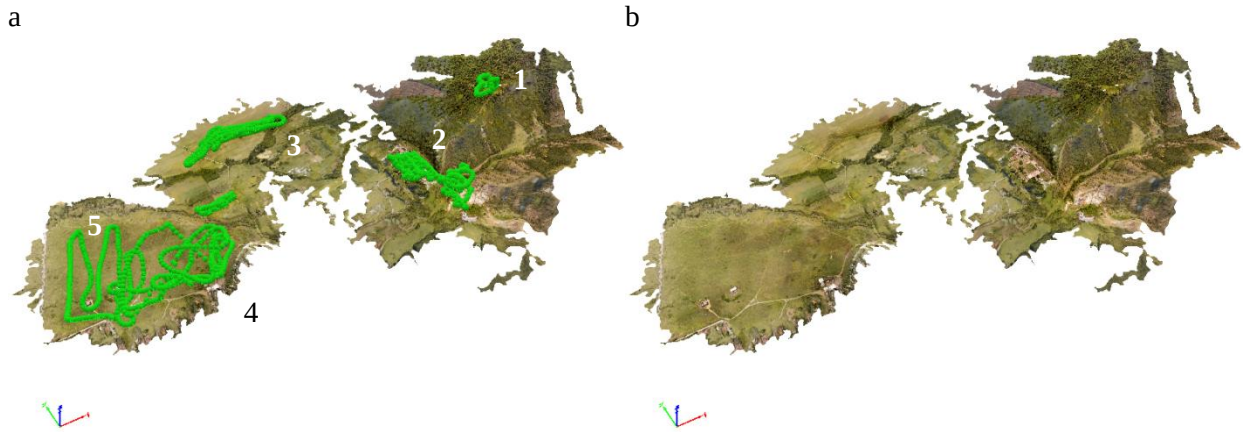

Figure 2. The resulting textured triangle-mesh model, with computed camera positions in green (a) and without (b). The numbers in [a] correspond to those in figure 1, although it should be noted the ‘Tomb’ is absent from this model and an approximate location is shown.

As can be seen in Figure 2, the model extends only around the areas which were flown. The camera angle also had a major impact on what was able to be reconstructed. The valley model consists of a considerable amount more area than was actually covered by the UAV due to the camera being angled more horizontal, at approximately 30°, compared with that of the necropolis, angled at approximately 45°. Having the camera at a more shallow angle can cause issues with the texture quality, when the camera’s seen-distance increases, the amount of haze caused by atmospheric particulates also increases. When the model is being reconstructed as a whole, the contrast between textures created from long-range and short-range images can be quite noticeable, with the former causing the texture to become milky.

Figure 3. Detail of the Palace site within the model.

The Palace model shown in Figure 3 contained the lowest-altitude flights, approximately 3m, to ensure the most accurate and detailed reconstruction of the whole model. As the camera utilises a fisheye lens with an approximate field-of-view of 160°, it was necessary to fly at this altitude over the Palace to maintain a ground-sampling-distance [7] (GSD) of 2.72cm/pixel, this is in comparison to the rest of the model which, using its high-altitude flights, maintained a GSD of 5.74cm/pixel. Not only would a higher GSD (lower value, more precise) aid with reconstruction of the model, the resulting texture overlay for the polygon mesh would contain more details resulting in a more realistic model.

6. Conclusions and Future work

While the high-altitude flights ensured more overall coverage, it was imperative to retain the low-altitude flights which gave greater detail around the palace. In an ideal world, the whole area would have been modelled in a manner which would allow a GSD similar to that of the Palace model, however there is a compromise between speed-of-acquisition of the data and the required detail for the model, with only those areas undergoing close scrutiny having the low-altitude flights. Using a UAV has drastically increased the areas able to be surveyed, although at a lower GSD than a purely ground-based method. This trade-off between GSD and speed-of-acquisition depends on the end requirements of the model. Methods of increasing the GSD precision while maintaining the speed-of-acquisition are being investigated, as well as a comparison of the use of GoPro videos, stills and high-quality DSLR/mirrorless images in UAV data acquisition.

Acknowledgements

The author would like to thank the supervisory team of Dr Frederic Bezombes, Dr Isabelle De Groote and Dr Francis Lilley for their assistance and guidance throughout this European-funded, Horizon 2020 (Digiart, No. 665066), project.

References

1. Adams W. L., Anson E. M., Archibald Z., Asirvatham S. R., Carney E., Christesen P., … Worthington I.; *A Companion to Ancient Macedonia (Blackwell Companions to the Ancient World)*; Roisman J. & Worthing I. (eds.); Wiley-Blackwell; Published 2010; ISBN 978-1-405-17936-2
2. GOOGLE MAPS; *Map of Greece*; [online]; Google; 2017; Available from: https://www.google.co.uk/maps/@39.2120021,22.6164399,7.5z ; Accessed April 2017
3. OpenStreetMap; *Map of Vergina*; [online]; OpenStreetMap; 2016; Available from: https://www.openstreetmap.org/#map=14/40.4831/22.3158; Accessed April 2017; Re-drawn 2016, Moore A. J.
4. Dhond U. R., Aggarwal J. K.; *Structure from stereo-a review* in *IEEE Transactions on Systems, Man and Cybernetics*; Vol. 19, No. 6; Pages 1489-1510; Nov/Dec 1989; Published 1989
5. Marr D., Poggio T.; *A Computational Theory of Human Stereo Vision* in *Proc. of the Royal Society of London*; Series B; Biological Sciences; Vol. 204; No. 1156; Pages 301-328; Published January 1979

[7] The ground-sampling-distance is the distance, in centimetres, covered on the ground in comparison to the distance covered from the centre of one pixel to the centre of an adjoining pixel. The result is a value in 'centimetres per pixel (cm/pixel)'.

Mohammed Sufian

Investigating the capability of precision in robotic grinding

Mohammed Sufian, Xun Chen, Dingli Yu

General Engineering Research Institute, Liverpool John Moors University (LJMU), Liverpool, United Kingdom M.Sufian@2016.ljmu.ac.uk, X.Chen@ljmu.ac.uk, D.Yu@ljmu.ac.uk

Abstract- Most robotic grinding focus on the surface finish rather than accuracy and precision. However ever increased demand on complex component manufacture requires to advance robot grinding capability so that more practical and competitive accurate systems can be developed. The current study focuses on improving the level of accuracy of robotic grinding, which is a significant challenge in robot application because the kinematic accuracy of robot movement is much more complex than normal CNC machine tools. Aiming to improve accuracy and efficiency the work considers all quality of measures including surface roughness and the accuracy of size and form. For that to be done, a repeatability test is firstly preformed to observe the distributions of the joint positions and how well the robot responds to its programmed position using a dial gauge method and a circuit trigger method. After that, a datum setting method is performed to assess the datum alignment with the robot. Hence, a mathematical model based on regression analyses applies towards the collected data to observe closely any error correlation when setting up a datum to perform the grinding procedure

Keywords - Robot, Repeatability, Datum identification

I. INTRODUCTION

The use of robots in industrial applications has been widespread in the manufacturing industry from handling to production tasks such as welding, sealing, finishing, de-burring, flattering, polishing and grinding. Robots have the ability to create cutting cycles in X, Y and Z linear directions as well as two additional rotary axes, often defined as A and B. This rotary axis can tilt the position of the tool or the workpiece in many different ways, which adds flexibility and uncertainty in machining complex parts with complex geometry surfaces. Robotic machining have been found very attractive in many industrial applications as many believe that it decreases machining time and produces a quality surface finish. According to the white paper published by the robotic industries association in 2009 [1], the robotic machining products and services constitute less than 5 % of existing robotic sales, but was seen as a growth application segment in the future. Applications involve the pre-machining of parts made from harder materials, with robots performing various processes at loose tolerances. Due to the limited robot rigidity and payload, the applicable depth of cut and feed rate must be kept small, which limit the material removal rate and the machining efficiency [2]. Therefore, most robotic grinding focuses on the surface finish improvement, but not on the accuracy of component size and form in the process. This paper presents a current research work in LJMU that focuses on improving the level of accuracy in robotic grinding precision, which is a significant challenge in robot applications because the kinematic accuracy of robot movement is much more complex than normal computer numerical control (CNC) machine tools. The initial work includes performing repeatability tests as well as datum finding to support the process monitoring and control strategy, to provide a reliable and accurate movement, and to ensure smooth grinding and surface finishing.

II. ROBOT REPEATBILITY

Industrial robots are used in many applications but still cannot compete with computer numerical control (CNC) machine tools for multiple axis applications in terms of accuracy and repeatability. Repeatability is the ability of a robot to return to the same spot with minor slightest variation whereas accuracy is a measure of the distance error associated with the desired and achieved point. These two factors are interrelated and most commonly used amongst all machining performance characteristics. Brethe et.al [3] investigated the repeatability of a KUKA industrial robot and the distributions of the angular positions of the joints to show that these distributions can be considered as Gaussian. They computed a repeatability test at different locations within the workspace of the robot using the experimental angular covariance matrix and the stochastic ellipsoid modelling. A high variability was observed in the measured data and a method of drawing the distribution of the 15 sample repeatability index is used to compare the computed and measured repeatability. Riemer and Edan [4] evaluated the impact of target location on robot repeatability. Experimental results showed a significant statistical difference between repeatability at different work-volume locations. Especially the heightof the target point was found to be a major factor determining the repeatability of a point within the workspace. In order to understand the performance of an articulated industrial KUKA robot in use, a set of experiments is designed to evaluate its repeatability. The objective is to observe how well the robot will return to its programmed location at 4 different positions in 3 Cartesian coordinate directions. The tests were performed at an offset distances of 100 mm and at a speed of 30% & 10% of the operational speed robot (2 m/s).

III. EXPERIMENTAL PROCEDURE

As the focus is on finding a datum location, the performing repeatability is vital to visualize how well the robot responds to its programmed position in order to define a datum. The experiments are done with two different methods, using (1) a dial gauge that being install at the end of the manipulator and (2) a contact probe as the switch of a simple electrical circuit to determine contact and store the contact points into robot computer. A light bulb is connected in to the electrical circuit to indicate contact. By measuring various locations on workpiece surface, the datum plane will be found based on a mathematical regression method. Firstly, a gauge indicator with 0.005 ~ 5 mm was used to measure the position repeatability of the robot. The indicator is securely mounted on the robot arm at the end joint to ease the measurement procedure and to ensure accuracy. For each run, the robot controller adjusts the motion and meets the conditions adapted in the robot. A single algorithm was created to run the robot with two different speeds to assess the consistency. A constant robot overall speed is set to 2 m/s the measurement is done at 10% and 30% of this speed to take at 4 different positions on work table shown in Figure 1 along 3 Cartesian coordinate directions (x, y, z).

Figure 1: Robot WorkSpace

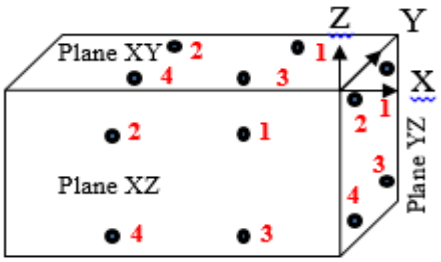

Figure 2: 3D Model of Surface Block with Positions

After that, a circuit contact method is performed based on the best location chosen using the circuit contact method. This method is a procedure where a probe is used to determine the contact points at different surfaces on the workpiece block. When the probe contacts the workpiece surface, the bulb in the circuit lights up and the robot controller registers the contact point position in the robot workspace. Figure 2 illustrates a 3D model of the three surfaces of the block used for detection.

IV. DATUM PLANE MODELLING

The multiple regression analysis is most useful to determine the relationship between one dependent variables to multiple independent variable with the best accuracy. The regression analysis was done towards the data collected from robot movement and measurement. Mathematical formula was derived to be calculated by Matlab software first. A matrix calculation formula was then made ready for robot implement. The proposed calculations are made to observe the difference in error correlation between experimental and model calculated results. A common formula of a plane in space can be presented as:

$$aX + bY + cZ + d = 0 \quad (1)$$

where variables X, Y and Z are the coordinates of the points on the plane; a, b, c and d are constants that defines the plane position. All points coordinates on the plane should satisfy the equation 1, therefore:

$$aX_i + bY_i + cZ_i + d = 0 \quad \text{for } i, \ldots, n \quad (2)$$

Considering the measurement errors ε, the measured points on plane XY should satisfy:

$$Z_i = b_0 + b_1X_i + b_2Y_i + \varepsilon_i \text{ for } i, \ldots, n \quad (3)$$

where $b_0 = -d/c$, $b_1 = -a/c$ and $b_2 = -b/c$. By defining $\mathbf{Z} = (Z_1, Z_2, \ldots, Z_n)'$, $\mathbf{B} = (b_1, b_2, \ldots, b_n)'$, $\boldsymbol{\varepsilon} = (\varepsilon_1, \varepsilon_2, \ldots, \varepsilon_n)'$ and

$$X = \begin{pmatrix} 1 & X_1 & Y_1 \\ 1 & X_2 & Y_2 \\ \vdots & \vdots & \vdots \\ 1 & X_n & Y_n \end{pmatrix}$$

then, the regression function becomes

$$Z = X B + \varepsilon \quad (4)$$

By solving the equation 4, the coefficients of plane XY can be calculated by

$$B = (X' X)^{-1} X' Z \quad (5)$$

With multiple regression the datum planes and errors could be identified.

V. RESULTS & DISCUSSIONS

Based on the full set of results, the best position is only illustrated in this paper to briefly discuss the effect of the repeatability to perform the grinding process. However, for all positions at three different coordinate directions (X, Y, Z). The test is taken at 2 different speeds and a 100 mm offset distance are set for each measuring point to allow the dial gauge to perform the detection process.

Plane YZ: 100mm offset and 10% 2 m/s

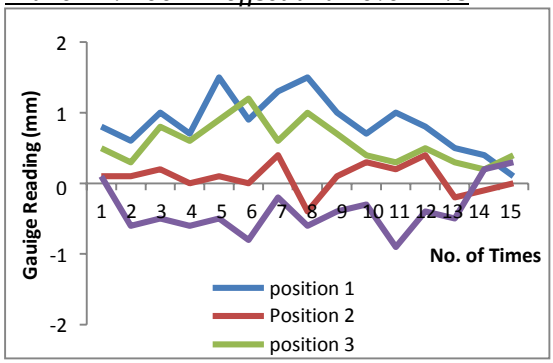

Plane XZ: 100mm offset and 10% of 2 m/s

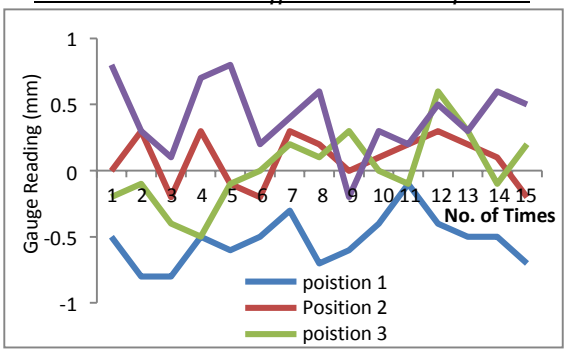

Plane XY: 100mm offset and 10% of 2m/s

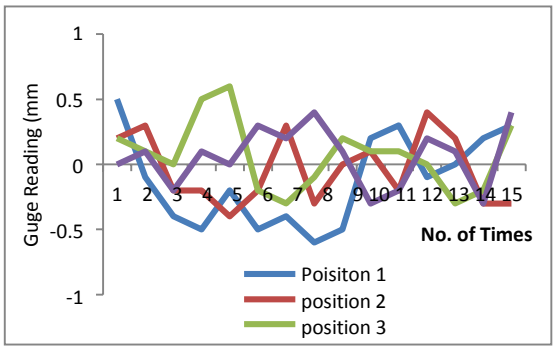

Figure 3: Dail gauge method

Figure 3 shows the results from the experiment test for three plane surfaces and four positions to insure consistency within the experiment. Each point is detected by taking (x, y, z) coordinates and each plane surface is considered according to the global movement of the robot. The results from position 2, 3 and 4 show a similar variation in terms of expected readings at 100 mm offset and 10% of the speed. Depending on the block position on the workspace and the coordinate the robot is detecting, results show there is significant differences in all positions. For example, on plane YZ positon 3 and 1 are high over the limit of zero were we expected to be whereas positon 2 and 4 are closer to the zero limit by few millimeters. This indicates that the repeatability at this point is very good due to the fact that the variation in reading is close to the zero point which was expected. In another hand, looking at plane XY and XZ in all positions the variation in results is expected due to the changes of locations of the block in the work table. The main challenge of robots is that their low positioning accuracy and stiffness in the gears and bearings of the joints and the structure. Therefore, the variations in these results could be the main reason for trajectory errors during repeatability process. However, from the results the higher the speed percentage the less likely the repeatability result will perform well and gauge reading will not become zero. Position 2 seems to be the best as it shows that it is more consistent and readings become close to the initial point (zero).

In order to eliminate the influence of measuring errors on the geometrical accuracy a datum identification experiment is conducted by using an electrical circuit method to detect four different points at XY, YZ and XZ datum planes, which are minimum number for using the regression method. Four points on each datum plane are illustrated in Fig. 2. Each point detected is based on equal distance from each sides of the plane of the workpiece to allow an approximate full detection of the whole plane. For example, looking at plane XY the robot travels at only x or y coordinate directions to next test point while remains constant at z direction. In this way, the accuracy and repeatability of the z measurement can be assured. The coordinates were collected based on the average value of three trials to ensure consistency in results, total average of data of plane XY is given in Table I, which a similar level of data variations presents for all planes. All data points are collected based on global coordinate system movement of the robot. In this test, the robot moving speed is 0.2 m/s. For regression analyses only

TABLE I

Plane XY			
Coordinates (mm)			
	X	**Y**	**Z**
Point 1	856.3293	-823.6441	762.4155
Point 2	826.7246	-823.6226	761.6107
Point 3	824.9632	-869.3411	761.6254
Point 4	852.2498	-872.1230	761.5779

TABLE II

Plane XY			
Regression values 0.0142X + 0.0081Y + Z + 756.7175 = 0			
	Z – Values	**Z -est.**	**Error**
Point 1	762.4155	762.2058	0.2096
Point 2	761.6107	761.7856	-0.1749
Point 3	761.6254	761.3903	0.2351
Point 4	761.5779	761.7552	-0.1774

(x, y, z) coordinates are required. The theoretical method is based on equation 3, 4 and 5 shown in the mathematical model section, a set of matrices is used integrate data to for each plane to visualize the error correlation. The matrix solution shown in equation 5 can implement in robot to determine the workpiece datum plane in the robot coordinate system. Table II shows results from theoretical calculations in comparison of measurement results.

The multiple regression method estimates the parameters of workpiece datum planes and provides a response model to assess robot performance. From the regression results the predicted dependent variable known as x, y and z from aforementioned equations were identified. It can be seen that the error ranges between 0.02% to 0.05% on all planes which proves that the repeatability of the results is constant and the surface plane is approximately straight in terms of its location.

VI. CONCLUSION

A repeatability test is presented in this paper to observe the distributions of the joint positions and how well the robot responds to its programmed position using a dial gauge method and a circuit trigger method. After that, a datum setting method is performed to assess the datum alignment with the robot. Hence, a mathematical model based on regression analyses is developed towards the collected data to observe closely any error correlation when setting up a datum to perform the grinding procedure. Based on the collected data the following conclusions are as follows:

- Better repeatability is achieved based on the low robot moving speed.
- Minimum error is achieved based on the 10% of robot speed, whereas at the higher speed the value is 20% higher.
- Based on regression results, the error ranges between 0.02% to 0.05% on all planes which proves that the repeatability is constant and the surface plane is approximately straight in terms of its location.

VII. REFERENCES

[1] Allen, M. P., 1997. Understanding Regression Analysis. New York & London: Plenum Press, New York. Anon., 2009. Robotics Industries. [Online] Available at: www.robotics.org [Accessed 23 03 2015].

[2] Chen, Y. & Dong, F., 2013. Robot machining: recent development and future research issues. The International Journal of Advanced Manufacturing Technology, 66(9), pp. 1489-1497.

[3] Brethe, J., Vasselin, E., Lefebvre, D. & Dakyo, B., 2005. Determination of the Repeatability of a Kuka Robot Using the Stochastic Ellipsoid Approach. Proceedings of the 2005 IEEE International Conference on Robotics and Automation, pp. 4339-4344.

[4] Riemer, R. & Edan, Y., 2000. Evaluation of influence of target location on robot repeatability. Robotica, 18(4), pp. 443- 449.

Imitation of Superhydrophobic Surface Effects on Large-Scale Surface Textures

Phillip Taylor
P.Taylor@2011.ljmu.ac.uk
James Wharton
J.Wharton@2009.ljmu.ac.uk
Professor Xun Chen
X.Chen@ljmu.ac.uk
General Engineering Research Institute, Byrom Street Liverpool, L3 3LN

Abstract. Past research has successfully reduced the aerodynamic drag by manufacturing micro-geometries onto a solid surface which resist the penetration of fluid into textured grooves forming a pocket of trapped air. In these 'superhydrophobic' surfaces, the liquid-gas interface provides negligible resistance to the fluid motion, hence a reduction in drag forces. The practical application of superhydrophobic surfaces is limited due to manufacturability, required fluid properties and the instability of the trapped gas region. Recent research has suggested the potential to replicate the drag reducing mechanisms of superhydrophobic surfaces in the absence of a trapped gas region. If successful, such surfaces will be easy to manufacture and will function for a wide variety of liquid and gas flows. In this paper, a clear and concise outline of the superhydrophobic mechanism will be presented, and relevance to large-scale flows will be discussed. Numerical results will be presented for a simple surface geometry designed to promote flow separation, and hence, a 'drag-free' region of flow. Results of drag reducing/increase will be compared with an identical geometry containing an ideal trapped gas region to critically analyse the necessity of the trapped gas region for drag reduction.

Keywords. Superhydrophobic surfaces, Laminar, Sinusoidal grooves, OpenFOAM.

1. Introduction

In the case of fluid flowing over a solid surface, friction based drag forces (viscous forces) act on the fluid. Fluid flowing through a pipe or channel is driven by a pressure gradient. The drag forces resist fluid motion and create a loss of pressure along the channel, increasing the required energy input to maintain fluid flow. A crucial breakthrough in reducing viscous drag occurred with the discovery that the microtextures on the leaf of the lotus plant served to resist the penetration of water into the textured grooves [1]. As a result, pockets of trapped air would form within the texture. At the liquid-gas interface (shear-free region), there would be negligible drag forces acting on either the liquid or on the surface [2]. The same effect can occur for a secondary liquid state in place of trapped gas [3]. Further investigation found that for a surface with a periodically occurring shear-free region, the viscous drag forces could be decreased beyond that of a smooth surface [4-8], with pressure loss reduction on the order of 50% . A limiting factor of these investigations was the assumption of a completely flat interface between the liquid and the trapped gas. Curvature of the interface can reduce the drag reduction, and even create an overall drag increase if the interface protrudes into the flow [9]. The practical application of superhydrophobic surfaces with large slip lengths is limited by the instability of large gas pockets [10]. As an alternative to superhydrophobic surfaces, surfaces of large-scale textures of longitudinal riblets have been found to produce drag reduction in turbulent fluid flow, with streamwise-aligned riblets producing drag reductions of up to 10% [11]. For laminar flows, riblets with a wide variety of cross-sectional geometries have been investigated [12-14], however, only a negligible drag reduction has been achieved. Recent research has shown that sufficiently deep, spanwise-aligned grooves promote the separation of fluid shear-layers from the crest [15], forming a free-shear region and significantly reducing the viscous drag. However, for simple groove shapes, the distribution of pressure in the groove gives rise to a large pressure drag force which counteracts the reduction of viscous drag [16-17].

The current paper investigates the influence of a region of trapped gas on the viscous drag and pressure drag of a simple sinusoidal surface in laminar channel flow.

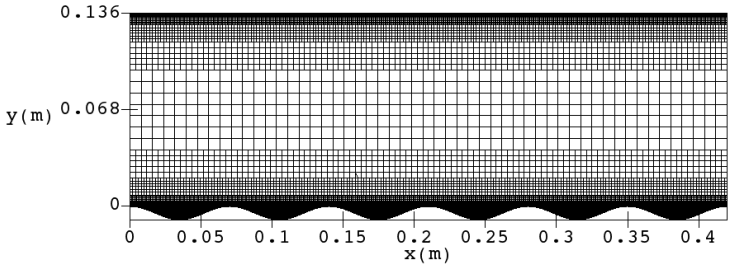

Figure 1: An image of the computational domain and discretized mesh.

2. Methodology

Consider a three-dimensional channel with a smooth, flat upper wall and a textured lower wall. The channel is assumed to have infinite length and width. The flow is assumed to be fully developed. With these assumptions, a small section of a full channel is modelled. The domain has dimensions of $L_x \times L_y = 6.18h \times 2h$ where subscripts x and denote the streamwise and wall-normal directions respectively and h denotes the channel half-height. The lower wall texture consists of a spanwise aligned sinusoidal groove given by the definition in (1). The groove is periodic with wavelength $\lambda = 1.029h$ and depth $k = 0.136h$, and the crest is located at the point $y = 0$.

$$y = \frac{k}{2}\left(cos\left(\frac{2\pi}{\lambda}\right) - 1\right), \qquad (1)$$

Four surface configurations were investigated. One configuration considered a sinusoidal groove of a continuous no-slip boundary condition. Three configurations modelled a region of trapped gas within the groove, with an ideally flat gas-liquid interface, modelled by a free-slip boundary conditions, placed at three different heights above the groove trough k_g/k, where k_g is the vertical distance between the free-slip boundary and the trough. The numerical simulations were carried out using the opensource code OpenFOAM v4.1. The domain was discretized using a cartesian mesh, with split-hexahedra cells in the near wall region of the lower wall. The flow is driven by a body force to produce a specified bulk velocity, u_{av}. The flow properties are specified by the Reynolds number $Re_h = hu_{av}/\nu$, where ν viscosity of the fluid. In all cases, two values of Reynolds number, $Re_h \approx 66.6$ and $Re_h \approx 666$, are tested by varying the fluid viscosity and keeping the bulk velocity constant.

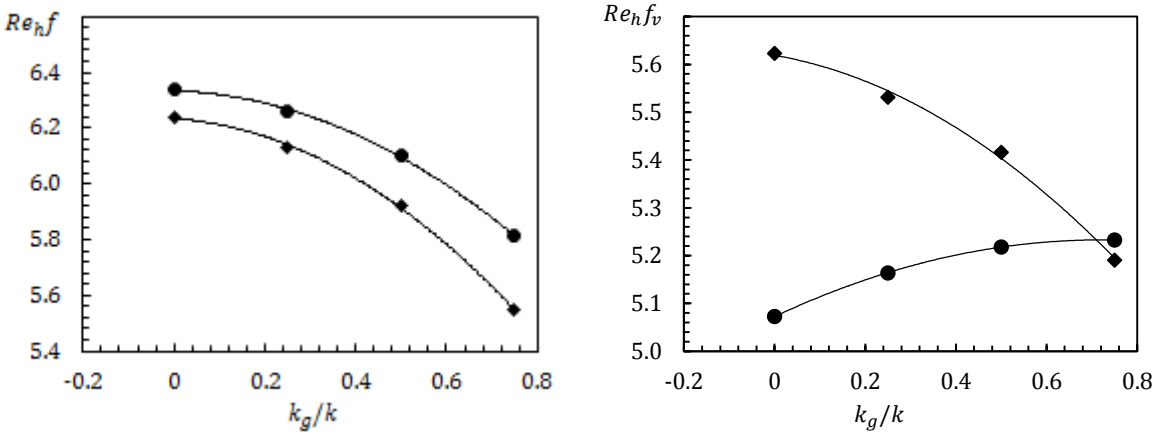

Figure 2: Plots of a) total drag component $Re_h.f$ and b) viscous drag component $Re_h.f_v$ [defined in (2)] against the relative depth of the trapped gas region k_g/k. Results are shown for high Reynolds number (circles) and low Reynolds number flows (diamonds).

3. Results and Discussion

Results are compared for three variables; viscous drag component, pressure drag component and total drag. Drag is defined by the dimensionless friction factor is defined in (2), and contains a pressure drag component f_p, and a viscous drag component f_v. For comparision between flows, the friction factor is normalised with the Reynolds number; $Re_h.f$.

$$f_p = D_x/\rho A_0 u_{av}^2, \qquad f_v = F_x/\rho A_0 u_{av}^2, \qquad f = f_p + f_v, \qquad (2)$$

Where D_x is, the total pressure drag, force acting on the lower wall, and F_x is the total viscous drag force acting on the lower and upper walls. For a channel with smooth upper and lower walls; $Re_h.f = 6$. For each simulated case, figure 2 displays results for the total drag component $Re_h.f$, and viscous drag component $Re_h.f_v$. For all cases, the viscous component of $Re_h.f$ decreases below that of a smooth, no-slip channel. The minimum viscous drag component occurred for a flow of $Re_h = 681.0$ with free-shear region present. As shown in figure 3a, the shear layers separate from the downwards slope, reattaching downstream on the upwards slope. During separation, the shear-layer acts as a shear-free interface between the fluid and a trapped vortex with the groove. The vortex exerts a negative shear-stress on the area under the separated shear layer, which acts with the direction of the flow. The positive influence of the negative shear-stress is overcompensated by added pressure forces due to the distribution of pressure across the vortex.

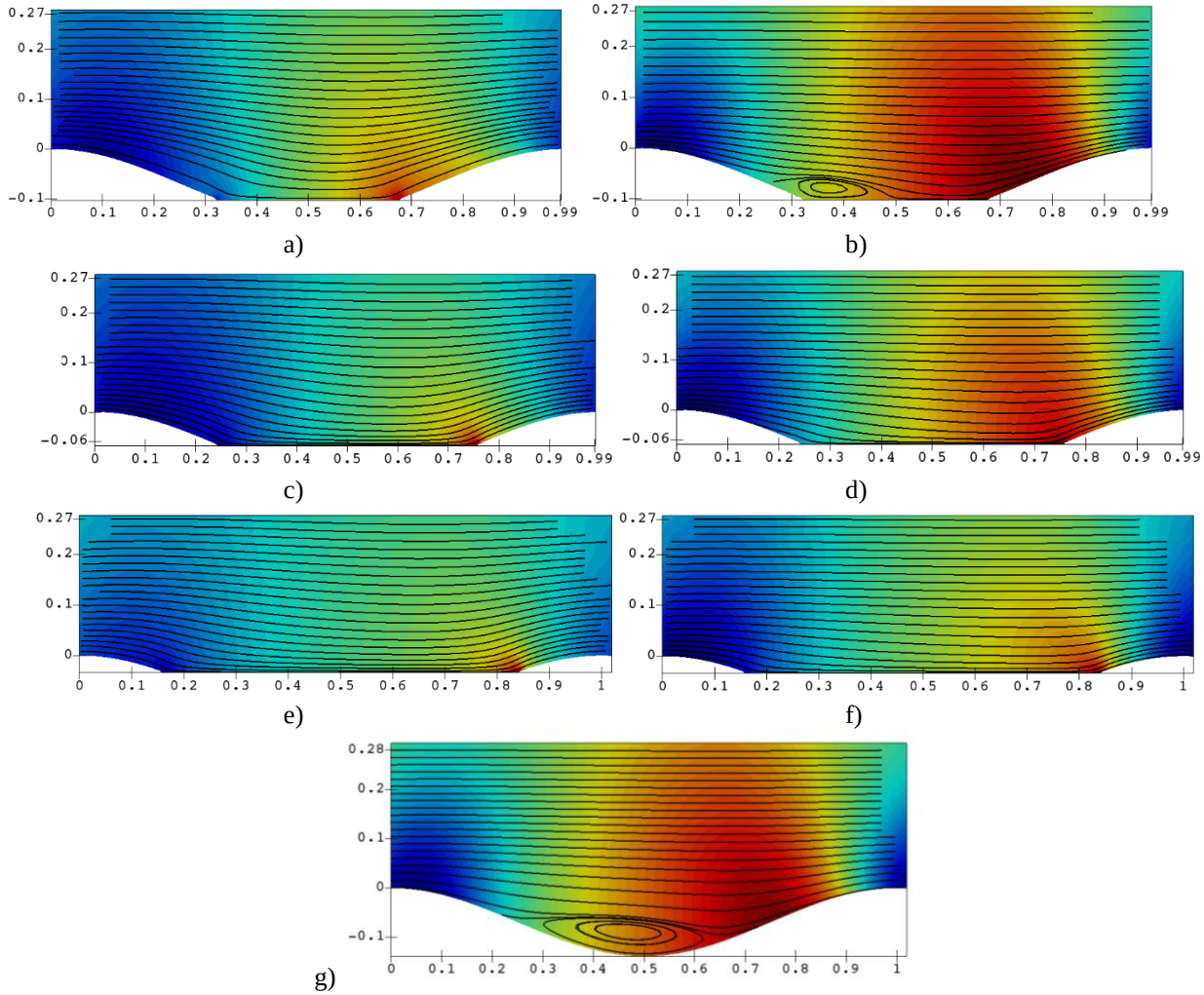

Figure 2: Streamline and pressure contour plots in the near-wall region of the flower textured wall. The x-axis and y-axis indicate streamwise coordinates in units of λ, wall-normal coordinates in units of h. For lower Reynolds numbers, plots are shown for a) $k_g/k = 0.25$, c) $k_g/k = 0.5$ and $k_g/k = 0.75$. For higher Reynolds number flows, plots are shown for b) $k_g/k = 0.25$, d) $k_g/k = 0.5$, f) $k_g/k = 0.75$ and e) $k_g/k = 0$.

In agreement with past literature, increasing the Reynolds number in each surface scenario raised the value of $Re_h f$. From figure 2, the non-linear relationship between $Re_h f$ and k_g/k does not depend on the Reynolds number. However, Reynolds number is seen to have a significant effect on the variation of the viscous drag component $Re_h f_v$. For low Reynolds numbers, the viscous drag decreases monotonically as the shear-free region grows. Shear-layer separation does not occur, and hence, for a continuous surface with no free-slip boundary condition, the full wetted area of the groove is exposed to fluid shear-layers, producing the largest observed value of $Re_h f_v$. Referring to figure 1 (a, c, e), the largest pressure gradients occur at the points connecting the free-slip boundary and the solid surface, due to the rapid acceleration and deceleration of the fluid shear layer moving from no-slip to free-slip boundaries. The pressure drag component decreases gradually as k_g/k increases, resulting in an overall reduction of $Re_h . f$ (provided that the depth of the shear-free region comprises at least 50% of the total groove area).

4. Conclusions

At large Reynolds numbers, the shear layer separates from the downwards slopes of the groove, producing a recirculating vortex within the trough. The separated shear layer simulates a free-slip boundary, protecting a significant portion of the surface from high velocity fluid. The back-flowing fluid in the vortex exerts a negative shear stress, acting with the flow. The separated shear layer proved to be a superior mechanism of viscous drag reduction, in comparison to an ideal trapped gas pocket, represented by a free-slip region. However, it is shown that the crucial effect of a trapped gas region is the protection of the textured surface from significant pressure variation. As such, whilst the viscous drag component increased with the depth of the shear-free region, the pressure drag component decreased at a high rate resulting in an overall drag increase.

References

[1] Barthlott W and Neinhuis C 1997 Purity of the sacred lotus, or escape from contamination in biological surfaces *Planta*, **202**, 1-8.

[2] Rothstein J P 2010 Slip on superhydrophobic surfaces *Annu. Rev. Fluid Mech.* **42**, 89-109.

[3] Chen H, Gao Y, Stone H A and Li J 2016 "Fluid bearing" effect of enclosed liquids in grooves on drag reduction in microchannels *Physics Review Fluids*, **1**, 083904.

[4] Maynes D, Jeffs K, Woolford B, Webb B W 2007 Laminar flow in a microchannel with hydrophobic surface patterned microribs oriented parallel to the flow direction.*Physics of Fluids* **19**, 093603.

[5] Davies J, Maynes D, Webb B W aand Woolford B 2006 Laminar flow in a microchannel with superhydrophobic walls exhibiting transverse ribs *Physics of Fluids* **18**, 087110.

[6] Ou J, Perot B, and Rothstein J P 2004 Laminar drag reduction in microchannels using ultrahydrophobic surfaces *Physics of Fluids* **16**, 4635-4643.

[7] Maynes D, Jeffs K, Woolford B and B W Webb 2007 Laminar flow in a microchannel with hydrophobic surface patterned microribs oriented parallel to the flow direction *Physics of Fluids* **19**, 093603.

[8] Ou J and Rothstein J P 2005 Direct velocity measurements of flow past drag-reducing ultrahydrophobic surface *Physics of Fluids* **17**, 103606.

[9] Teo C J and Khoo B C 2010 Flow past superhydrophobic surfaces containing longitudional groove: effects of interface curvature *Microfluid Nanofluid* **9**, 499-511.

[10] Lee C, Choi C-H and K C-J 2016 Superhydrophobic drag reduction in laminar flows: a critical review *Exp. Fluids* **57**, 176.

[11] Bechert D W, Bruse M, Hage W, Van Der Hoeven J G T and Hoppe G 1997 Experiments on drag-reducing surfaces and their optimization with an adjustable geometry *J. Fluid Mechanics* **338**, 59-87.

[12] Mohammadi A and Floryan J M 2013 Groove optimization for drag reduction *Physics of Fluids* **25**, 113601.

[13] Mohammadi A and Floryan J M 2015 Numerical analysis of lamainr drag-reducing grooves *J. of Fluids Engineering* **137**, 041201.

[14] Chu D C and Karniadakis G E 1993 A direct numerical simulation of laminar and turbulent channel flow *J. Fluid Mech.* **250**, 1-42.

[15] Niavarani A and Priezjev N V 2009 The effective slip length and vortex formation in laminar flow over a rough surface *Physics of Fluids* **21**, 052105.

[16] Mohammadi A and Floryan J M 2013 Pressure losses in grooved channels *J. Fluid Mech.* **725**, 23-54.

[17] Saha S, Klewickl J C, Ooi A and Blackburn H M 2015 On scaling pipe flows with sinusoidal transversely corrugated walls: analysis of data from the laminar regime *J. Fluid Mech.* **779**, 245-274.

Rosie Horner

Biomimicry- Can copying the micro-topography pattern of the Cockle *Cerastoderma edule* give antifouling properties to marine steel?

R Horner [1,3]**, P French** [1,4] **and S Durr** [2,5]
[1] General Engineering Research Institute, Byrom St, Liverpool L3 3AF
[2] School of Natural Sciences and Psychology, Byrom St, Liverpool L3 3AF
[3] R.Horner@2015.ljmu.ac.uk
[4] P.French@ljmu.ac.uk
[5] S.T.Durr@ljmu.ac.uk

Abstract. Biofouling is the unwanted attachment of marine organisms to a surface. It is a costly problem for maritime industries, but it also reduces the survival of fouled marine organisms. However, some marine organisms have evolved defence mechanisms to the problem in the form of micro-scale patterns on their surface. This study uses bio-inspiration of these micro-scale patterns from the common cockle shell to produce patterns on steel using laser processing to reduce biofouling. Steel patterns are submerged in the waterbody at the Albert Dock, Liverpool, and data is collected on settlement of marine organisms on each pattern. The results show that bio-inspired micro-scale patterns are reducing the amount of settlement. Therefore there is potential for bio-inspired micro scale laser patterns to be used as a non-toxic, eco-friendly and universal anti-fouling technology in Martine industries.
Keywords. Fouling, bio-fouling, bio-mimicry, bio-inspiration, micro-textures, antifouling,

1 Introduction

Biofouling is described as the colonisation process of a solid surface submerged in the marine environment (Wahl, 1989). This colonisation of surfaces by marine organisms is a costly problem maritime industries as biofouling can weaken surfaces, increase rust and corrosion and increase drag of ships. It has been estimated that the US navy alone has spent an average of 1 billion US dollars on problems related to biofouling on their ships in the last 15 years (Schultz *et al*, 2011). As money is being lost through biofouling, therefore there is a large market for antifouling (AF) coatings and technologies.

Biofouling has negative effects on maritime industries, however, biofouling also has negative effects on marine organisms. Fouled organisms have a reduction in mobility and reproduction (Buschbaum and Reise, 1999). Reduced mobility will inhibit the fouled organism's ability to forage for food, and escape predators and therefore it will be more likely to die. Reduced reproduction will mean that the fouled organism is less likely to pass on their genes to the next generation. However, there is an instinctive evolutionary pressure to survive and pass on genes to the next generation. This evolutionary pressure to survive has resulted in natural defence mechanisms to develop within species to reduce the effects of biofouling. One of these natural defence mechanisms is micro-topographies on the outermost surface of the skin. Due to convergent evolution, this type of defence mechanism is seen across a wide range of species including mussels, crabs, sharks and whales (Scardino et al, 2003; Bers & Wahl, 2004; Kirschner and Brennan, 2012; Baum et al, 2002).

This research aims to target the gap in the AF market for a universal, non-toxic, eco-friendly antifouling technology by using laser processing to produce micro-topographies on marine grade steel that mimic the patterns produced on the surface of marine organisms as a natural biofouling defence. We hope that by mimicking the natural defences of marine organisms we can reduce biofouling on steel that is used

in maritime industry and provide a safe alternative in the AF market. This project is focused on reducing settlement within the biofilm layer, as this layer is the first to form, and it encourages further settlement of larger macro-foulers. By targeting the biofilm layer, there is less chance of macro-foulers settling as the diatoms and bacteria that is often used as food for larger species will not be present in abundance.

2 Methods

This study focuses on the micro-topography pattern of the common cockle *Cerastoderma edule*. Cockle shell samples were collected from Thurstaston beach, UK, and cleaned in ethanol to remove any debris. The shell was placed under a 3D topography scanner (GFM) and the surface topography was observed (figure 1).

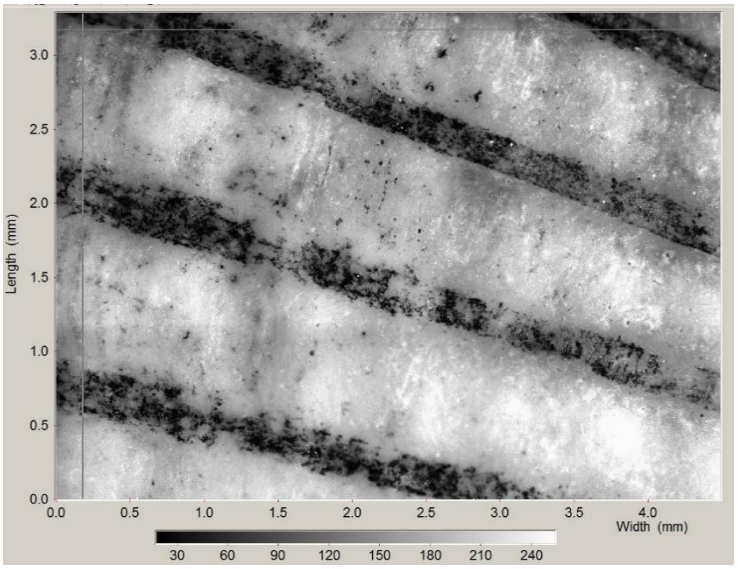

Figure 1 3D scan of Cockle shell *C. edule* with depth (um) shown by grayscale chart.

The scans revealed that the topography of the shell is straight ridges with valleys between the ridges. With this as inspiration, the laser parameters are programmed and 4 surfaces were produced to mimic the straight lined ridge type pattern of the Cockle shell.

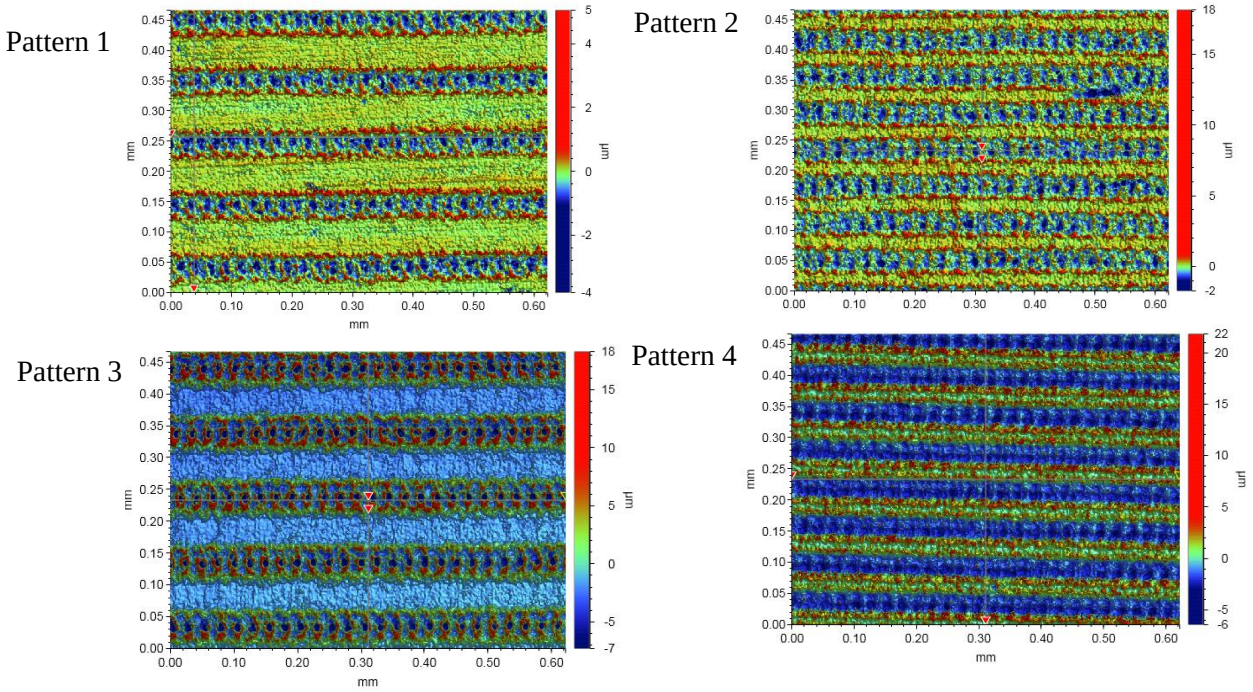

Figure 2 3D scan of Cockle inspired patterns produced using laser processing with height (um) shown by colour chart.

The laser processed steel with patterns 1, 2 ,3 and 4 were submerged in the Albert Dock, Liverpool, for a week along with a control panel which was a smooth surface and had no laser processing. There were 5 replicates per pattern.

2.1 Data Collection

Once removed from the dock, panels were preserved in ethanol and photographed under x50 magnification. The number of individuals (a single marine organism) were counted. Statistical analysis of the data collected was carried out in SPSS. A three factor nested ANOVA was used as well as Post hoc Dunnet's test.

3 Results

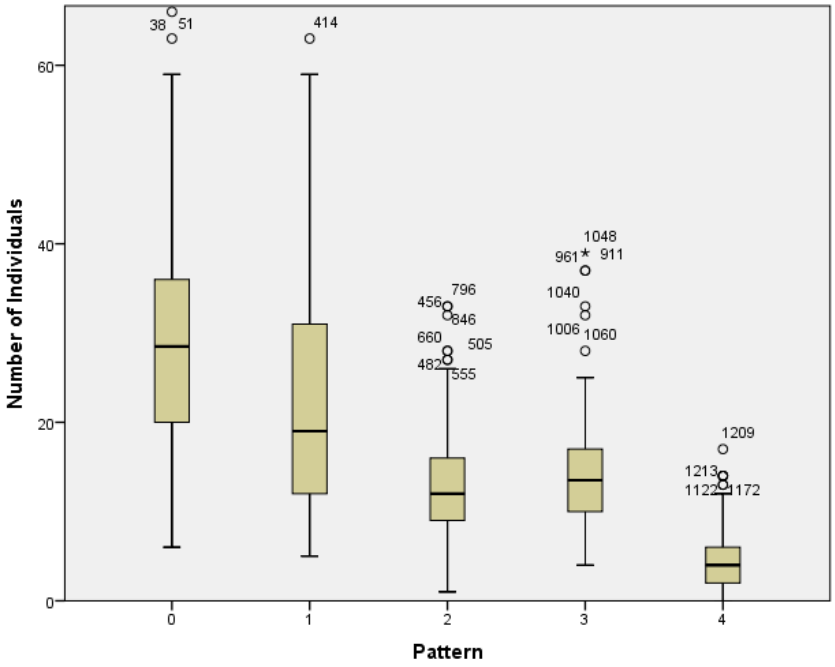

Figure 3 Number of Individuals per Pattern where Pattern 0 is the unprocessed control. All patterns were significantly different ($p<0.01$) expect Pattern 2 and Pattern 3.

All of the patterns showed a significant decrease in the number of marine organisms settled on the surface compared to the control pattern ($p<0.01$). Pattern 4 (figure 3) had the least amount of settlement, therefore was the best AF pattern.

4 Discussion

We have found that laser processing a micro topography pattern onto a steel surface has reduced the settlement of marine organisms. These results are consistent with previous studies on micro-topography patterns such as Sharklet ™ and others on silicones (Schumacher *et al*, 2007), however, these previous studies have been lab based, and tested using only one alga species *Ulva*. Whereas, our results are from a field work study, which is a greater reflection of the real world as our surfaces are submerged in a fully functioning ecosystem, where species interactions and environmental conditions can also effect settlement. This highlights the importance of this study as there are very few field work tests of micro-topographies as an antifouling technology.

It is easier for micro-fouling species such as diatoms and bacteria to settle on smooth surfaces such as the unprocessed control than the micro-topography patterns. The number of attachment point is reduced when the surface is not flat, therefore the individual cannot have full contact with the surface (figure 4), leading to reduced attachment of individuals on micro-topography patterns.

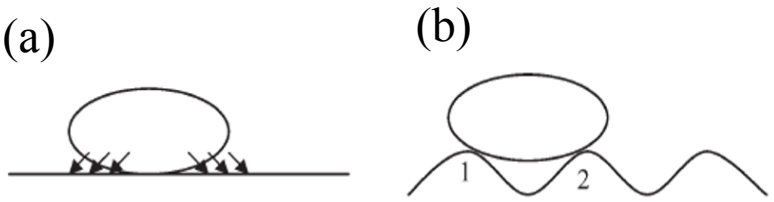

Figure 4 A schematic illustration of theoretical attachment points of a diatom; (a) attachment on a flat surface and (b) attachment where micro-topography is smaller than the diatom adapted from (Adapted from Scardino *et al*, 2006).

Pattern 4 was the best AF pattern, as it had the least number of individual organisms settled on the surface. Pattern 4 had narrow flats and and deep valleys and it is these characteristics that are similar to the small narrow valleys of the Cockle shell topography that have made it a good antifouling surface. The patterns with larger flats (P1 and P3) had a higher medium settlement than patterns with narrower flats (P2 and P4) because the larger flats allowing a larger flatter space between laser spots for settlement like in Figure 4a to occur.

Table 1 Characteristics of the laser processed patterns.

	Larger flat	Narrow flat
Shallow ridge	Pattern 1	Pattern 2
Deep ridge	Pattern 3	Pattern 4

5 Conclusion

Overall, the concept of using laser processed micro-topographies inspired by natural surfaces to produce an anti-fouling technology looks promising as this study clearly demonstrates laser processing micro-topographies reduces settlement of marine organisms. This study focuses on the patterns produced by *C. edule*, however, for the whole of the PhD project lots of different species will be studied including shore crabs *Carcinus maenas* and mussels *Mytilus edulis*. The hope is that characteristics from these species can be combined in the laser processing stage, to produce an optimum pattern that will be able to be commercialised as an AF technology.

6 References

Baum, C., Meyer, W., Stelzer, R., Fleischer, L.-G., & Siebers, D. (2002). Average nanorough skin surface of the pilot whale (Globicephala melas, Delphinidae): considerations on the self-cleaning abilities based on nanoroughness. Marine Biology, 140(3), 653-657.

Bers, A. V., & Wahl, M. (2004). The influence of natural surface microtopographies on fouling. Biofouling, 20(1), 43-51.

Buschbaum, C. and K. Reise (1999). Effects of barnacle epibionts on the periwinkle Littorina littorea (L.). Helgoland Marine Research 53: 56-61.

Corbett, J. J., and H. W. Koehler (2003), Updated emissions from ocean shipping, J. Geophys. Res., 108, 4650-4661.

Kirschner, C. M., & Brennan, A. B. (2012). Bio-inspired antifouling strategies. Annual review of materials research, 42, 211-229.

Scardino, A., & de Nys, R. (2004). Fouling deterrence on the bivalve shell Mytilus galloprovincialis: a physical phenomenon? Biofouling, 20(4-5), 249-257.

Scardino, A. J., Harvey, E., & De Nys, R. (2006). Testing attachment point theory: diatom attachment on microtextured polyimide biomimics. Biofouling, 22(1), 55-60.

Schultz, M. P., Bendick, J. A., Holm, E. R. & Hertel, W. M. (2011). Economic impact of biofouling on a naval surface ship. Biofouling, 27, 87-98.

Wahl, M. (1989). Marine epibiosis. I. Fouling and antifouling: some basic aspects. Marine Ecology Progress Series, 58, 175-189.

Khaled Al-Badani, James Ren, Lisa Li, David Allanson
Department of Maritime and Mechanical Engineering
James Parson Building, Byrom Street, Liverpool, L3 3AF
K.A.Mohamed@2015.ljmu.ac.uk ; X.J.Ren@ljmu.ac.uk

Abstract:

This paper will discuss key material parameters that affect the dynamic behaviour of droplet formation. The achieved work will examine theoretical methodologies, experimental techniques and numerical modelling, using ANSYS FLUENT, to critically analyse and highlight optimization methods regarding the formation of pendant droplet. The investigation will compare results from published data, experimental work and numerical results, concerning the effect of key material parameters (e.g. density, dynamic viscosity, surface tension) as well as boundary conditions (e.g. nozzle exist diameter, flowrate) on the dynamic behaviour of the droplet.

Keywords - Computer Modelling, Droplet Formation, Material Distortion, Materials Forming, Welding.

1. Introduction

The fluid dynamic fundamentals of droplet formation, has been an extended research topic of interest for many years, due to its various applications in many engineering systems and manufacturing procedures. This includes welding, biotechnologies, 3D printing, biochemical, biomedical fields and many more. The volume and the characteristics of droplet formation are generally depended on various factors such as material properties, microfluidics and fluid mechanics. An extensive range of theoretical studies, experimental work and computational analyses, have been performed over the past decade to improve the understanding of the droplets dynamics during dripping mode. X Zhang et al [1] stated that the formability of droplets, occurring from a capillary tube end, have two main modes. These are: Jetting – (which occur at high flow velocity) which is the results a coherent laminar jet, originates from the tube, before breaking into a small separate drops, due to Rayleigh instability [2]. Dripping – (occur only within slow flow velocity) is the results of the liquid flowing out of the tube as a small periodic drops.

The dripping mode can be divided into two main stages. The first stage corresponds with the quasi-static growth of the drop. This stage ends when the surface tension becomes incapable of holding the weight of the drop. The second stage is the nicking, which is caused by the destabilizing effect of the surface tension, and it generally starts during the breaking up stage of the droplet.

The nicking stage results in creating a conceal shape in the upper section of the droplet, and a spherical shape in the lower section. The length of the liquid thread that is linking the upper and lower section simultaneously, will increase as the droplet reaches the critical breaking point, where the spherical section is detached from the upper section of the droplet [3]. As for the rest of the fluid, it rapidly withdrawals because of the surface tension effect, which may leads to another break up of small droplets called satellite drops [4].

The main challenge in analysing the dynamic behaviour of a pendent droplet lies in introducing a theoretical model of the problem. Many academic papers have attempted to work out the droplet volume theoretically, as a function of the fluid flowrate, material properties and exist nozzle geometry. The assumption was based on a simple macroscopic force balances, in which the breaking up and the nicking processes are followed by static growth. Nevertheless, all these findings could not fully describe the complete shape of the droplet.

The well-known limitations and complications of theoretical two dimensional models, were overcome by the arrival of numerical methods. These approaches utilize computational powers, to simulate the free surface flow, via Computational Fluid Dynamics solvers (CFD). Zhang and Stones [5], as well as Schulkes [6] were one of the first people produced a CFD numerical study of a two-dimensional axisymmetric model of droplet, *via* the application of boundary conditions/elements and boundary integral method. Although these methods were not completely accurate on some factors, they were able to compute the Navier-Stokes equations for a laminar multiphase flow.

Nowadays, there are numerous numerical techniques that can be utilized to solve the flowing fluid problem for droplet simulations. Methods such as Finite Element solvers, Spectral Element solvers, Boundary Element solvers and many other more. However, the multiphase Volume of Fluid (VOF) solver can be considered as the most reliable code for solving free surface smearing of the droplet formation. This is because it has the transient formulation schemes to solve multiphase laminar flow, with high details such as the separation process, viscos elongation effect and satellite drops [7]. In this work, ANSYS FLUENT will be utilised to form a droplet using a 2-D quarter axysimetical model *via* Volume of Fluid solver. The work will investigate factors influencing the overall shape and size of the droplet (e.g. density, surface tension and dynamic viscosity). The results from the numerical investigation will be assessed against experimental data and other published results conducted with Water-Glycerine solutions.

2. Experimental Setup and Procedure

To fully comprehend the dynamic behaviour of a pendant droplet, different concentration levels of Glycerine-Water solutions were utilized for the experiment and computational simulation process. Changing the magnitude of Glycerine levels, within the solution (from 0% to 100%), will give complete freedom of controlling the Density (ρ), Dynamic Viscosity (μ) and Surface Tension (τ).

The Glycerine-Water solutions were prepared by mixing the desired percentage of glycerine with a distilled water, via a measuring cylinder. The density and the dynamic viscosity were calculated experimentally using Stock's Law ball bearing method [8].

This work utilized Theta Optical Tensiometer apparatus, which operate a high speed camera with image analysis, to visualise pendant droplets and to measure contact angle. The apparatus generate quantitative information regarding the overall length of the hanging drop, length of the nicking, estimation of the overall droplet volume, as well as the breaking up time. The experimental apparatus also uses a syringe, which is located on an anti-vibration table, to generate droplets. Two types of syringes, with external diameter (R_0) of 0.8 and 1.6mm, were utilised in the experiment, to investigate the droplet's dynamic effects produced by different exist dimensions. Fig 1 a typical developed Glycerine-Water Droplet visualized by the Theta Optical Tensiometer apparatus.

Figure 12: A typical fluidic pendant droplet generated using experimental apparatus

3. Mathematical Model

The analysed Glycerine-Water solution is assumed to be an incompressible Newtonian fluid. For a 2D quarter axsymmetric model, the viscosity and the density will have a polar coordinate system of r,θ,z located within the centre of the nozzle exist. It needs to be noted that the value of coordinate z is at an increase rate due to gravitational force. The maximum velocity of the fluid acting on the z coordinate, is defined as:

$$U = 2Q/\pi R_0^2 \text{ ---------- Equation 1}$$

Where R_0: The radius of the Nozzle outer diameter; Q: The flowrate of the flowing solution.

Equation 1 enables the Navior Stocks equation to be governed within the following non-dimensional form:

$$Re\left(\frac{\partial \underline{u}}{\partial t} + \underline{u} + \nabla \underline{u}\right) = \nabla . \underline{\tau} + St\underline{k} \text{ ---------- Equation 2}$$

$$\nabla . \underline{u} = 0 \text{ ---------- Equation 3}$$

Where $\underline{u}$: Non-dimensional velocity Vector; t: Time period; $\underline{k}$: Unit Vector in the direction of the gravitational force; $\underline{\tau}$: Newtonian stress tensor of the flowing fluid, which can be defined as the following equation:

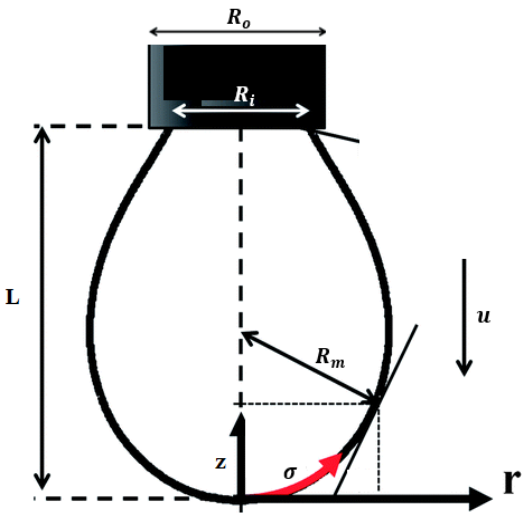

Figure 13: Forces schematics and boundary conditions for a Pendant droplet.

$$\underline{\tau} = -pI + [\nabla u + (\nabla u)^T] \text{ ---------- Equation 4}$$

The non-dimensional form of the Navior Stokes equation clearly links the flow behavior with the Reynolds number, which is used to determine the relationship between the inertial and viscous forces together, to help predict the flow pattern behavior during movement.

$$Re = \rho v L/\mu$$ ---------- Equation 5

Where ρ: The density of the flowing fluid; U: Mean velocity of the flow; D: Characteristic length scale; μ: Dynamic viscosity.

Stokes number is also used to determine the ratio of viscous flow against the gravitational forces. It can be calculated as follow:

$$St = \rho g R_0^2/\mu U$$ ---------- Equation 6

It needs to be noted that the surface tension also plays a big factor when analysing the flow behavior. It is introduced via Equation 7 which determine the free surface boundary condition of the flow.

$$\underline{u}.\underline{n} = 0\ ,\ \underline{\tau}.\underline{n} = \underline{n}\frac{1}{Ca}2H$$ ---------- Equation 7

Where Ca: Measures the relative importance of viscous and surface tension stresses; H: The curvature of the free surface. The first condition is known as the Kinematic condition, which state that there is no mass transfer across the free surface.

4. Results and Discussion

Two analysing methods, Quantitative and Qualitative, have been performed to understand the dynamic behaviour of droplet formation and to establish the validity of the achieved work. The quantitative method will focus on analysing the effect of changing the syringe exist dimension, increasing the volumetric flow rate and the influence of increasing the Dynamic Viscosity, within the investigated five solutions. As for the qualitative study, it will focus analysing the development of the droplet length, changes within the interface shape, elongation effect and the appearance of the secondary satellite droplets.

4.1 Quantitative Study

Many recent studies associated the dynamic behaviour of droplets with the capillary/nozzle exist size [9-10]. Hence, the first study investigate the effect of decreasing the size of the nozzle (R_0=1.6mm to 0.8mm), on the breakup time and flowrate, for the 20% and 50% Glycerine-Water solutions. Figure 3 compares between produced experimental results and numerical data in regards to studying the dripping process. It is to be noted that the time between subsequent break-off decreases rapidly when the nozzle diameter,R_0, is reduced. This 10% decrease in time between subsequent break-off, is due to the viscous effect which is higher in the 50% glycerine-water solution than the 20% solution. It can also be noted that increasing the value of the flowrate resulted in reducing the time between breakoff.

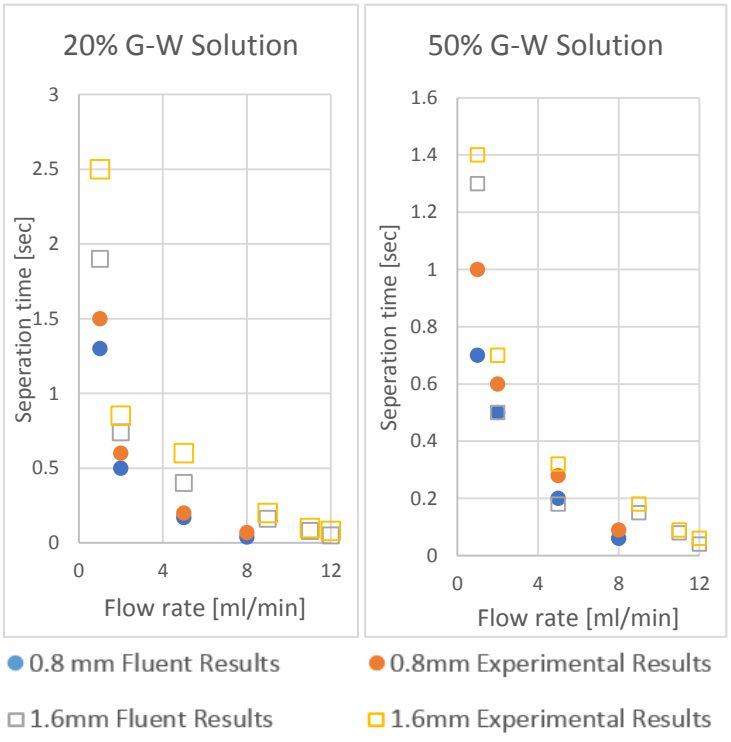

Figure 14: The effect of changing the nozzle exist size R_0 and the volumetric flow rate Q on the dynamics behavior of the droplet

To futher analyse the effect of increasing the dynamic viscosity and the density values within the Glycerine-Water solutions, the results from the experimental and FLUENT numerical data, were compared against other published results [10]. Figure 5 compares the increasing effect of dymainc viscosity values, through the five investigated solutions, on the limiting droplet length L_d. Figure 7 investigate the difference between break-up times, as the volumetric flowrate is increased from 1ml/min to 18ml/min, for the same five different solutions. The produced FLUENT numerical results showes high resmblance with experimental results and published data from Fawehinmi et al[9] FLOW 3D droplet simulation, as well as Wilkes et al [11] numerical findings.

4.2 Qualitative Study

Figure 6 (a&b) shows droplet development stages and elongation effect during droplet formation, for a 50% glycerine water solution with flowrate of 1ml/min. The interface shape obtained from FLUENT is compared against CFX and FLOW-3D simulations from Fawehinmi et al[9]. The simulated results showed a good agreement with the experimnetal data in the values of the droplet length L_d and overall volume. More demonstration of the free surface shape/interface during the droplet breaking up process, can be seen in Figure 6 (c&d), which compares the shape before the break up process between the three numerical codes. The data shows that the FLUENT model was able to simulate the long thin liquid lines, for solutions with high surface tension values.

5. Conclusion

In this work, five different types of Glycerine-Water soultion concentrations have been anaylsed experimentally, with an aim of producing a numerical model with similar fluid dynamic bahaviour. The simulation focused on highlighting the free surface smearing of the multiphase flow, droplet length, speration time and subsequent of satellite drops. The overall results from the qualititave and quantitittave studies showed a high resmebalnce with experimental results and other referenced work.

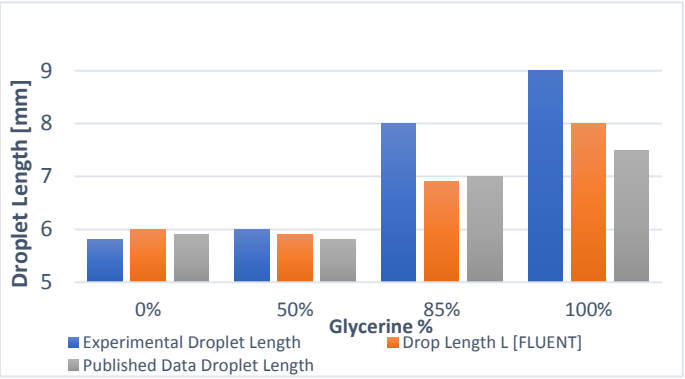

Figure 15: The effect of increasing the viscosity on the droplet length.

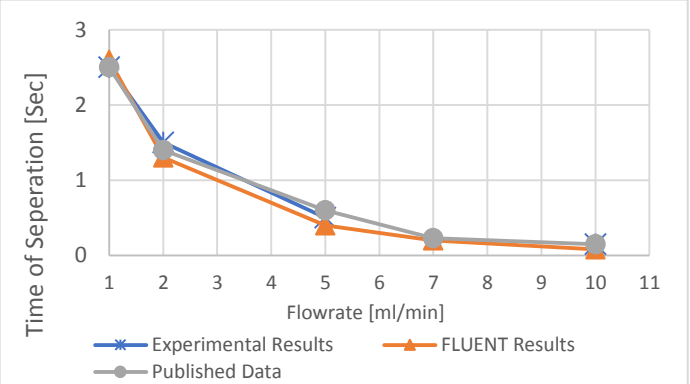

Figure 16: The effect of increasing the viscosity on the droplet length.

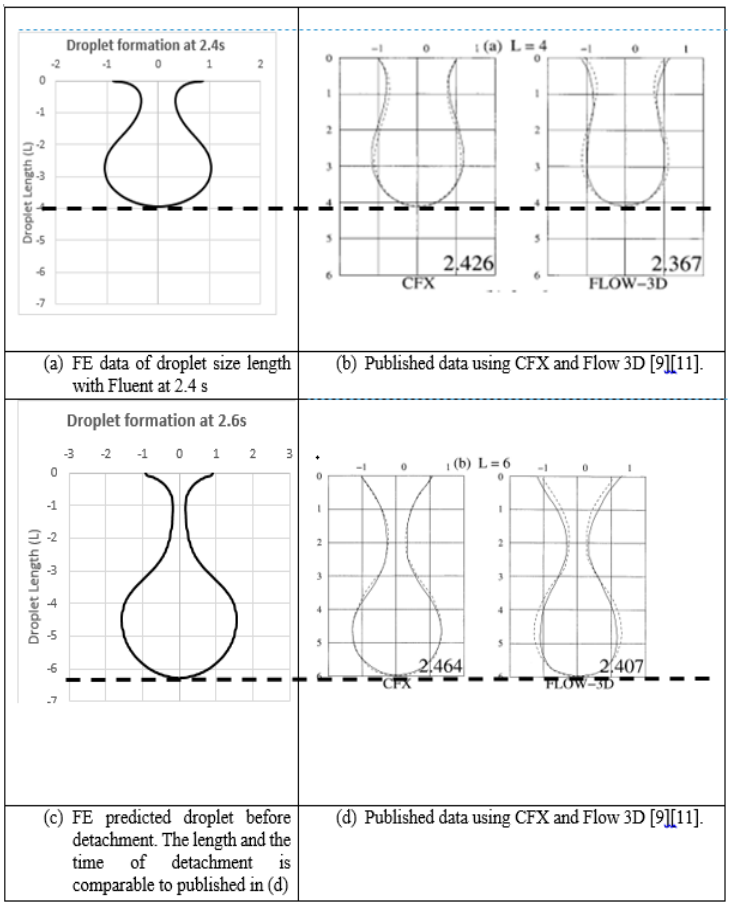

(a) FE data of droplet size length with Fluent at 2.4 s

(b) Published data using CFX and Flow 3D [9][11].

(c) FE predicted droplet before detachment. The length and the time of detachment is comparable to published in (d)

(d) Published data using CFX and Flow 3D [9][11].

6. References

[1] Zhang, Xiaoguang. "Dynamics of growth and breakup of viscous pendant drops into air." Journal of colloid and interface science 212.1 (1999): 107-122.
[2]Eggers, Jens. "Theory of drop formation." Physics of Fluids (1994-present) 7.5 (1995): 941-953.
[3] Lord Rayleigh, and Strutt, John William. "On the instability of jets." Proc. London Math. Soc 10.4 (1878).
[4] Zhang, Xiaoguang, and Osman A. Basaran. "An experimental study of dynamics of drop formation." Physics of Fluids (1994-present) 7.6 (1995): 1184-1203.
[5] Zhang, D. F., and H. A. Stone. "Drop formation in viscous flows at a vertical capillary tube." Physics of Fluids (1994-present) 9.8 (1997): 2234-2242.
[6] Schulkes, R. M. S. M. "The evolution and bifurcation of a pendant drop." Journal of Fluid Mechanics 278.83 (1994): 100.
[7] Zhang, Xiaoguang. "Dynamics of drop formation in viscous flows." Chemical Engineering Science 54.12 (1999): 1759-1774.
[8] Batchelor, George Keith. An introduction to fluid dynamics. Cambridge university press, 2000.
[9] Fawehinmi, O. B., et al. "A combined experimental and computational fluid dynamics analysis of the dynamics of drop formation." Proceedings of the Institution of Mechanical Engineers, Part C: Journal of Mechanical Engineering Science 219.9 (2005): 933-947
[10] Batchelor, George Keith. An introduction to fluid dynamics. Cambridge university press, 2000.
[11] Wilkes, Edward D., Scott D. Phillips, and Osman A. Basaran. "Computational and experimental analysis of dynamics of drop formation." Physics of Fluids (1994-present) 11.12 (1999): 3577-3598.

Ali Al-Attabi

The impact of organic loading rate on the removal efficiency of nitrate-nitrogen using sequencing batch reactor

Ali W Alattabi[1,2]**, Clare Harris**[1] **Rafid Alkhaddar**[1]**, and Ali Alzeyadi**[1]
[1] Liverpool John Moores University, Department of Civil Engineering, Liverpool, UK; emails: aliwaheid@gmail.com; C.B.Harris@ljmu.ac.uk; R.M.Alkhaddar@ljmu.ac.uk
[2] University of Wasit, Faculty of Engineering, Department of Civil Engineering, Kut, Wasit, Iraq

Abstract. Several industries discharge huge quantities of wastewater, which has a negative impact on nearby water bodies. Moreover, the treatment of this wastewater requires a large area, which could be a challenge as construction sites are normally limited in size. Compared to the conventional wastewater treatments methods, sequencing batch reactors (SBRs) are lower cost and have smaller area requirements and sludge bulking rarely occurs. This study was performed to optimise potassium nitrate loading rate and study its effects on nitrate-nitrogen (NO_3-N) removal efficiency in a sequencing batch reactor (SBR) treating synthetic wastewater. Four SBR reactors were used in this study; the working volume of each one is 5l. The reactors were operated under different potassium nitrate concentrations (50, 100, 150 and 200 mg/l). The results showed that increasing potassium nitrate concentration from 50 to 100 and to 150 mg/l did not affect the NO_3-N removal efficiency. However, increasing potassium nitrate concentration from 150 to 200 mg/l degreased the NO_3-N removal efficiency. The results obtained from this study, which operated for 60 days, showed that the SBR could biodegrade up to 92.2% for NO_3-N with potassium nitrate concentration between 50 and 150 mg/l, and a stately settling performance occurred during that range.

Keywords. Nitrate; organic loading rate; industrial wastewater; sequencing batch reactor; sludge settling performance.

9. Introduction

Industrial wastewater contains large concentrations of organic matter, nitrogen, phosphorus and other trace elements such as carbon, calcium, potassium and iron. These pollutants must be treated before they are discharged into rivers and other waterbodies; otherwise, the wastewater will damage the ecosystem, kill fishes and microorganisms in the waterbodies, and negatively affecting other animals that use these waterbodies, and having a detrimental effect on human health if people use the water. There are several types of treatment technologies that deal with this type of wastewater, such as chemical treatment, biological treatment and electrocoagulation. Biological wastewater treatment is considered to be one of the most convenient technologies to treat industrial wastewater due to its economic advantages regarding operation costs. However, conventional biological treatment takes up a large amount of land and utilises several tanks in its operation; therefore, alternatives such as the sequencing batch reactor are being investigated and used [1, 2].

The SBR is a wastewater treatment system that works on the same principle as the activated sludge process (ASP). It has been implemented successfully for treating domestic, industrial and other types of wastewater [3]. Additionally, the SBR is a fill and draw system which works in a cyclical time sequence, which means that it can operate in a smaller area than the conventional wastewater treatment methods. The SBR works as

an equalisation, neutralisation and biological treatment and secondary clarifier in a single tank through a timed control sequence, which makes it environmentally friendly technology. During one cycle, SBR technology has five operating steps – Fill, React, Settle, Draw and Idle. Due to its one tank design and setup simplicity, SBR has recently become an attractive technology. As shown in Fig. 1, the SBR system outdoes the conventional activated sludge system by including all treatment steps in one tank, while in the conventional activated sludge system, the treatment units are in separate basins [4]. A considerable number of researchers have been optimising the SBR operating conditions to gain a better removal efficiency for undesired wastewater pollutants [5, 6]. One of the SBR's operating conditions is organic loading rate (OLR), which is considered to be a significant operating parameter in the SBR's design and operation. The growth rate of microorganisms in biological systems is dependent on the OLR. At a high OLR, microbial growth might rise dramatically, while at a low OLR, microorganism starvation takes place [7].

Due to the limited knowledge on the impact of the organic loading rate on the SBR performance, this study was performed to find the effects of OLR on the effluent quality and sludge settling performance in a sequencing batch reactor.

10.Material and Methods

2.1 Experimental set-up of the SBR

Fig. 1 shows one of the four reactors used in this study. The capacity of each is 6.5L and the working volume is 5L; 1.5L of bacteria (biomass) plus 3.5L of synthetic wastewater were added to each reactor. The parameters of pH, DO, temperature and ORP were monitored online via sensors installed in each reactor. The four SBR reactors were operated with different potassium nitrate concentrations: 50 mg/l, 100 mg/l, 150 mg/l and 200 mg/l respectively. Influent and effluent samples were taken from each reactor to measure the removal efficiency and settling performance and relate it to the OLR.

2.2 Synthetic wastewater

The activated sludge (bacteria) used to biodegrade the organic matter was gained from Liverpool Wastewater Treatment Works, Sandon Docks, Liverpool, UK. The synthetic domestic wastewater was prepared by mixing the following chemicals with deionised water [8]: 500 mg glucose/L; 200 mg $NaHCO_3$/L; 25 mg NH_4Cl/L; 25 mg KNO_3/L; 5 mg KH_2PO_4/L; 5 mg $MgSO_4.7H_2O$/L; 1.5 mg $FeCl_3.6H_2O$/L; 0.15 mg $CaCl_2.2H_2O$/L. All reagents used in this study were purchased from Sigma-Aldrich, UK.

2.3 Nutrient analysis

In this research, the influent and effluent samples were taken from the SBR reactors before and after the treatment cycle using a peristatic pump, and then the samples were filtered using a vacuum pump containing 0.45 μm filter paper. The parameters of NO_3-N and SVI were analysed according to the standard methods [9].

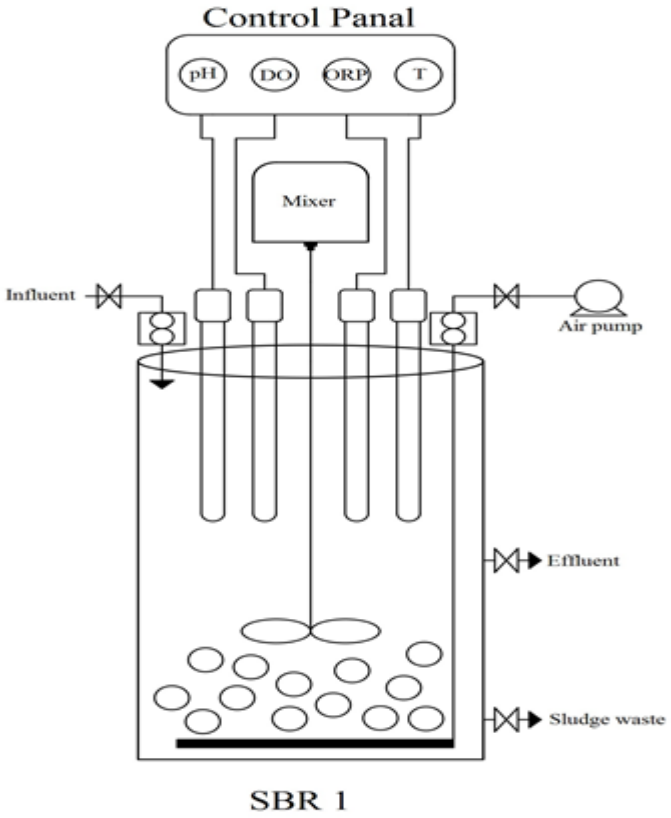

Fig. 1 Schematic diagram of one SBR

11.Results and discussion

3.1 The effect of OLR on NO_3-N removal

The influent and effluent concentrations and removal efficiency for NO_3-N under different OLRs are shown in Fig. 2. There was no big difference in the removal efficiency for NO_3-N after increasing the potassium nitrate from 50 mg/l to 100 mg/l and 150 mg/l; the average removal efficiency for NO_3-N under 50 mg/l was 92.2%, and, after raising the potassium nitrate concentration to 200 mg/l, the average removal efficiency for NO_3-N became 91.6%. Finally, when the glucose concentration was raised to 150 mg/l, the average removal efficiency for NO_3-N became 91.8%. However, when increasing the potassium nitrate concentration to 200 mg/l, the removal efficiency dropped dramatically; the average removal efficiency for NO_3-N during the 200 mg/l OLR was 87.6%. This result agreed with [10], who stated that at high ORL the removal of COD and nitrogen would be decreased. However, [11] reached high COD and nitrogen removal rates even under high ORL.

3.2 The effect of OLR on sludge characteristics

The effect of OLR on sludge settling performance is shown in Fig. 3. The average SVI concentration for the 50 mg/l OLR was 32 ml/g, and it can be clearly seen that increasing the OLR to 100 mg/l did not affect the solid settling performance and the SVI was 33 ml/g. However, raising the OLR to 150 mg/l negatively affected the solid settling performance and the SVI was raised to 37 ml/g. Further increasing the OLR to 200 mg/l made the settling even slower and the SVI was increased to 40 ml/g. In the same vein, [12] stated that increasing the OLR will lead to a proportional increase in biomass concentration, which will result in high SVI and the settleability of the solids will decrease. This agreed with [13], who reported an increase in the concentration of suspended solids when the initial concentration of COD was increased, which would also lead to an increase in the SVI and a subsequent drop in the solids' settleability.

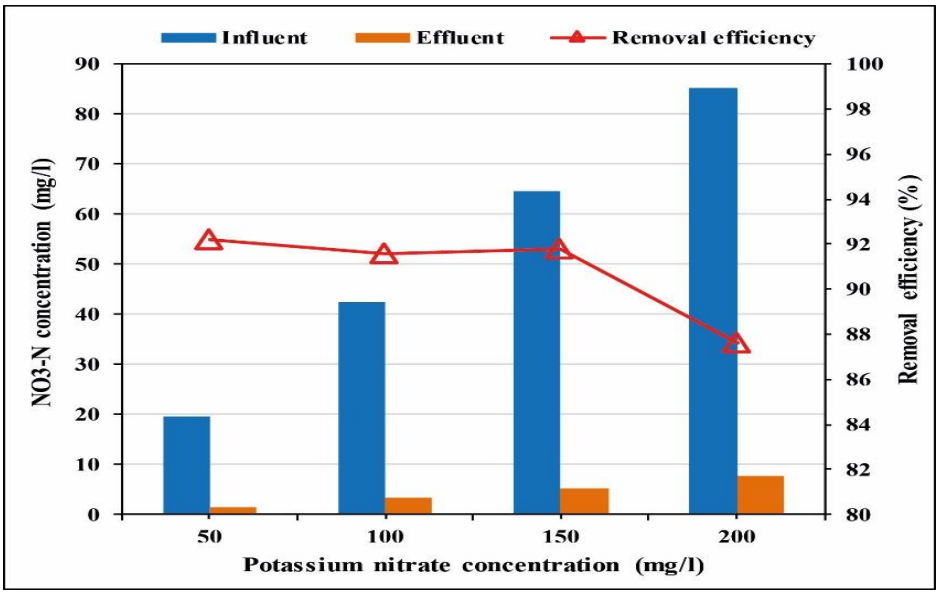

Fig. 2 The effects of OLR on the removal efficiency of ammonia

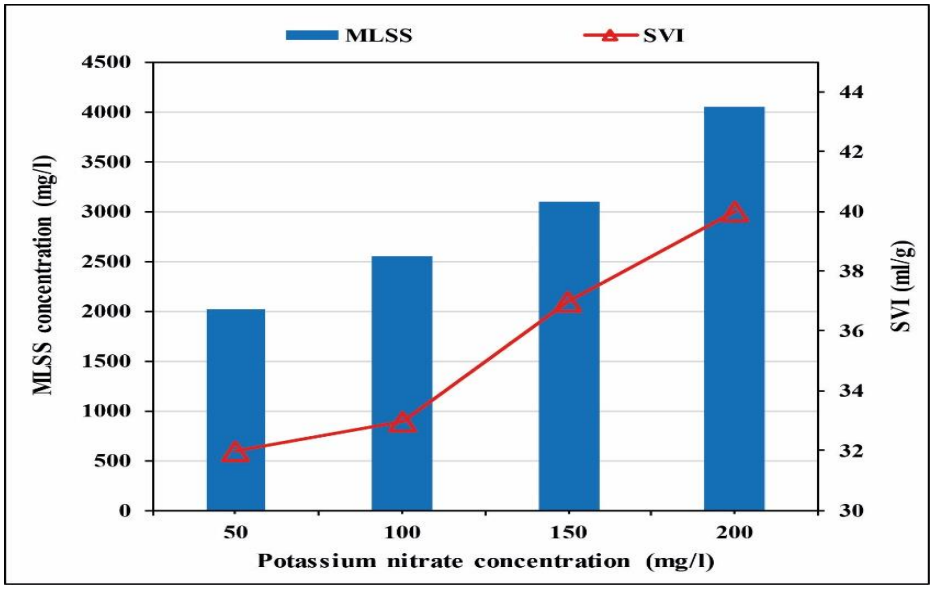

Fig. 3. The effects of OLR on the sludge characteristics

3.3 pH, DO, ORP and temperature profiles

The results from monitoring the pH, DO, ORP and temperature for one cycle of treatment are shown in Fig. 4. The pH, DO, ORP and temperature values at the end of the 6 h treatment cycle were between 6.3-8.4, 0.1-5.9 mg/l, -110-205 mV and 7.5-10.5 C respectively. At the beginning of the treatment, the ORP profile started to decrease from 50 mv to -110 mv. From that point, the degradation of COD started, which is indicated by the increase in the ORP profile [14]; the COD degradation was completed when the ORP reached 205 mv and the oxidation of ammonia started [15]. The pH profile was narrow in this study and it flocculated between 6.3 and 8.4. Thus, the ORP profile is more significant in this study than the pH profile. The ORP profile was increased in the same pattern as the DO profile because ORP and DO are related to each other in a linear formula [16].

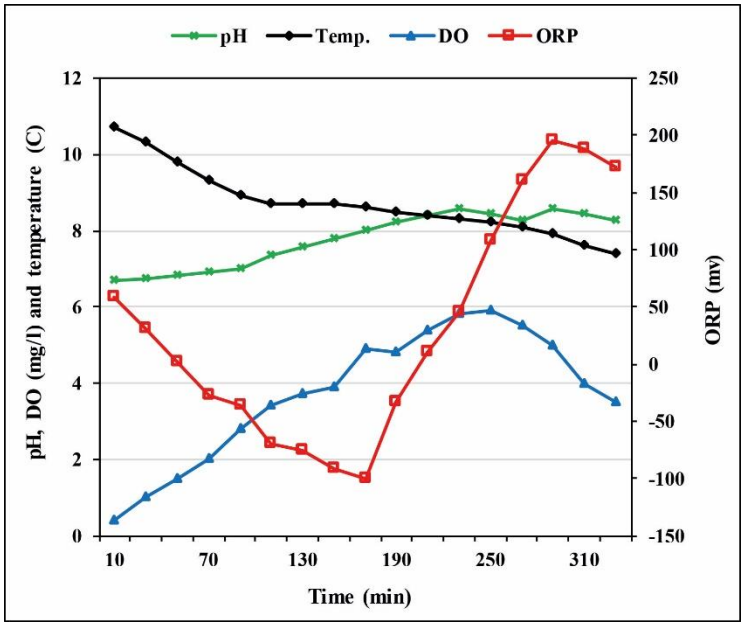

Figure 4. DO, pH, temperature and ORP for a sample SBR cycle (6 hours).

4. Conclusion

SBR was investigated to treat synthetic industrial wastewater. The effects of four different organic loading rates on the performance of four SBRs were examined. NO_3-N was tested to determine the SBR treatment efficiency, and the SVI was used to determine the sludge settling performance. The results showed that SBR technology could work efficiently with potassium nitrate concentrations between 50 mg/l and 150 mg/l and could biodegrade up to 92.2% for NO_3-N, and a steady sludge settling performance occurred during that range. However, increasing the glucose concentration to 200 mg/l decreased the removal efficiency and increased the settling time. Hence, the OLR was found to be a significant parameter that influences the operation of an SBR.

Acknowledgement

The financial support from the Ministry of Higher Education and Scientific Research, Iraq, and University of Wasit for the first author is highly appreciated.

References

[1] Hasan, H. A., Abdullah, S. R. S., Al-Attabi, A. W. N., Nash, D. A. H., Anuar, N., Rahman, N. A. & Titah, H. S., Removal of ibuprofen, ketoprofen, COD and nitrogen compounds from pharmaceutical wastewater using aerobic suspension-sequencing batch reactor (ASSBR). Separation and Purification Technology., 157, 215–221, 2016.

[2] Alattabi, A. W. N., Harris, C. B., Alkhaddar, R. M. & Alzeyadi, A., The effects of hydraulic retention time on the sludge characteristics and effluent quality in an ASSBR, *International Conference for Students on Applied Engineering (ICSAE)*, 458-462, 2016. doi: 10.1109/ICSAE.2016.7810235.

[3] Diya'uddeen, B. H., Rahim Pouran, S., Abdul Aziz, A. R., Nashwan, S. M., Wan Daud, W. M. A. & Shaaban, M. G., Hybrid of Fenton and sequencing batch reactor for petroleum refinery wastewater treatment. *Journal of Industrial and Engineering Chemistry*, 25, 186-191, 2015.

[4] Ishak, S., Ahmed, A. M. & Isa, M. H., Refinery wastewater biological treatment: A short review. *Journal of Scientific & Industrial Research*, 71, 251–256, 2012.

[5] Ma, F. & Guo, J. B., Application of bio-augmentation to improve the activated sludge system into the contact oxidation system treating. *Petrochemical Wastewater Bioresource Technology*, 100, 597–602, 2009.

[6] Alattabi, A. W., Harris, C. B., Alkhaddar, R. M. & Alzeyadi, A, The relationship between operating condition and sludge wasting of an aerobic suspension sequencing batch reactor (ASSBR) treating phenolic wastewater. *The Second BUiD Doctoral Research Conference*, 417-423, 2016.
[7] Razi, A. F., Pendashteh, A., Chuah, A. L., Radiah, D. A. B., Sayed, S. M. & Zainal, Z. A., Review of technologies for oil and gas produced water treatment. *Journal of Hazardous Materials*, 170, 530-551, 2009.
[8] Khaing, T-H., Li, J., Li, Y., Wai, N. & Wong, F. S., Feasibility study on petrochemical wastewater treatment and reuse using a novel submerged membrane distillation bioreactor. *Separation and Purification Technology*, 74, 138–143, 2010.
[9] El-Naas, M. H., Alhaija, M. A. and Al-Zuhair, S., Evaluation of a three-step process for the treatment of petroleum refinery wastewater. *Journal of Environmental Chemical Engineering*, 2(1), 56-62, 2014.
[10] Bagheri, M., S. A., M., Ehteshami, M. & Bagheri, Z., Modeling of a sequencing batch reactor treatingmunicipal wastewater using multi-layer perceptronand radial basis function artificial neural networks. *Process Safety and Environmental Protection*, 93, 111–123, 2015.
[11] Alattabi, A. W. N., Abdullah, S. R. R. and Hasan, H. A., Effects of initial organic loading and pharmaceutical compounds on the removal of COD, Ibuprofen and Ketoprofen in SBR. *Integrated Journal of Engineering Research and Technology*, 2(1), 88-100, 2015.
[12] USEPA, *Wastewater technology fact sheet: Sequencing batch reactors*. Washington, DC: US *Environmental Protection Agency*, 1999.
[13] Leong, M. L., Lee, K. M., Lai, S. O. & Ooi, S. O., Sludge characteristics and performances of the sequencing batch reactor at differences influent phenol concentrations. *Desalination*, 270, 181-187, 2011.
[14] Du, R., Peng, Y., Cao, S., Wu, C., Weng, D., Wang, S. and He, J., Advanced nitrogen removal with simultaneous Anammox and denitrification in sequencing batch reactor. Bioresource Technology, 2014, 162, 316-22.
[15] Miao, L., Wang, K., Wang, S., Zhu, R., Li, B., Peng, Y. and Weng, D., Advanced nitrogen removal from landfill leachate using real-time controlled three-stage sequence batch reactor (SBR) system. Bioresource Technology, 2014, 159, 258-65.
[16] Kishida, N., Kim, J., Chen, M., Sasaki, H. and Sudo, R., Effectiveness of oxidation-reduction potential and pH as monitoring and control parameters for nitrogen removal in swine wastewater treatment by sequencing batch reactors. Journal of Bioscience and. Bioengineering, 2003, 96, 285–290.

Khaled Takrouri

Performance of MPI and Hybrid Parallelisation Approaches for using the DNS code CHAPSim to Simulate Turbulent Flows

Khaled Takrouri and Mehdi Seddighi
Department of Maritime and Mechanical Engineering James Parson Building, Byrom Street, Liverpool, L3 3AF
K.W.Takrouri@2016.ljmu.ac.uk M.Seddighi@ljmu.ac.uk

Abstract:
This article discusses the assessment and improvement of parallelisation performance of an in-house DNS (Direct Numerical Simulation) computer code (CHAPSim). Three parallelisation techniques, namely, MPI, OMP and hybrid MPI+OMP which are used in parallelisation of CFD (Computational Fluid Dynamics) codes are discussed. A hybrid MPI OMP parallel programming is implemented in the in-house DNS code. The parallelisation performance was examined for both MPI and OMP+MPI models. The improvement in the performance of the code in terms of speedup ratios was analysed and the constrains of the hybrid model are specified in terms of the problem size against the number of MPI ranks and OMP threads.

Keywords
MPI, OMP, Hybrid Parallelization, DNS, Turbulence modelling

1. Introduction

The three main approaches used in CFD are Direct Numerical Simulations (DNS), Steady/Unsteady Reynolds Averaged Simulations (RANS/URANS) and Large Eddy Simulations (LES). Direct Numerical Simulation (DNS) is considered potentially the most accurate method for solving turbulent flows, but needs extremely high computational resources. The governing equations are discretised and solved numerically for instantaneous quantities, with no turbulence models. Direct Numerical Simulations requires a grid size proportional to the Reynolds number of interest. The number of required grid points and mathematical operational is proportional to $Re^{9/4}$ and $Re^{11/4}$, respectively [1]. This implies a very high computational cost for the case of higher Reynolds numbers. Reynolds Averaged N-S equations (RANS) methods are mainly based on Reynolds Decomposition; where each variable is calculated in two parts; average and fluctuations together. The equations are derived by averaging N-S equations and six other additional unknowns called Reynolds stresses. Large Eddy Simulations (LES) is an intermediate technique between both the DNS and RANS methods. It is based on the elimination of smaller scales as they are universal, homogenous and unaffected by the boundary layers using low pass filtering. Using RANS and LES method decreases the computational cost however they are not as accurate as DNS as they do not cover all scales of motion [2].

MPI is a standardised portable message passing specification for memory distributed systems. MPI libraries are scalable for large size problems demanding high number of cores. MPI is a popular parallelization methods as it offers a wide range free libraries compatible with many HPC facilitates in addition to being free and optimized for a wide range high-speed networks. On the other hand, the main drawback of the use of MPI is its complexity to program [3].

OpenMP is used for shared memory parallelisation. OpenMP is considered easy to program compared the complexity of the use of MPI libraries. The implementation of OpenMP is a gradual iterative progression, where the code does not have to be written from scratch to apply the parallelization directives to the serial version of the code. The use of OpenMP is limited to problems requiring less than 16 cores which made it unpractical for CFD applications but also opened the way to parallel MPI OMP technique as a useful method to improve and optimise the performance of CFD codes [4].

The hybrid MPI OMP method combines the use of MPI functions together with the OMP directives to improve the performance of pure MPI codes. Henty [5] listed the cases where the use of hybrid technique could be beneficial for the performance of the code as follows: The occurrence of inefficient MPI implementations or situations where shared memory algorithms are more efficient than the distributed memory algorithms.

Improvements of parallelization in CFD code.

The 1-D decomposition also known as the slab decomposition is a simple way to perform parallel computations on distributed and shared memory systems. For 1-D Decomposition the computational domain is decomposed in one direction. For the case of 1-D decomposition the number of slices within the domain is specified with respect to the number of processors assigned for the simulation [6]. The 1-D decomposition method is limited to smaller size problems as the decomposition in only performed in one direction which limits it use to simulations that require less than 1000 cores. Li and Laizet [6] developed a 2- D decomposition tool and showed its effect on the performance of the codes solving differential equations for three dimensional Cartesian meshes. However, to demonstrate the impact of using the 2-D decomposition on the performance of the code, the code must be re-structured which is complex and time consuming. The use of hybrid MPI OMP technique is an effective optimisation technique to improve the performance of MPI CFD codes. Rabenseifner [7] reviewed various MPI+OMP programming models and compared them against pure MPI simulations. The study included the effect of using different compilers and hardware on the efficiency of the hybrid parallelization techniques and proposed the overlapping communication and computation scheme which solved the data mismatch problems when executed with the cray compiler. Bassi et al. [8] tested the efficiency of the hybrid MPI/OMP on their DNS code and found that the improvement in the performance is mainly dependant on the number of MPI ranks, number of OpenMP threads for a problem of a certain size.

2. Methodology:

2.1 Governing Equations

The in-house code CHAPSim is used to study the physics of the turbulent flow over both smooth and textured surfaces. Navier-Stokes equations are solved using Direct Numerical Simulations. The Dimensionless form of the continuity and momentum equations are expressed as shown:

$$\frac{\partial u_i}{\partial x_i}=0 \qquad \text{Eq. (1)}$$

$$\frac{\partial u_i}{\partial t} + u_j \frac{\partial u_i}{\partial x_j} = -\frac{\partial p}{\partial x_i} + \frac{1}{Re}\nabla^2 u_i \qquad \text{Eq. (2)}$$

Where i,j,k =1,2,3 represents the stream-wise, wall-normal and span-wise direction, respectively. The length, velocity, time and pressure are normalized with the channel half-height, δ, characteristic velocity U, time scale $\frac{\delta}{U}$ and pressure ρU^2 where ρ is the density and $Re = \frac{U\delta}{\nu}$ where ν denotes kinematic viscosity. A second-order finite difference method is used for spatial discretization on rectangular grids, Rung-Kutta scheme to solve non-solenoidal velocity and Crank-Nicholson for the viscous terms. The time advancement of equations is based on a fractional step method introduced by Kim and Moin [9]. The resulting Poisson equation is solved using a 2-D Fast Fourier Transformation taking advantage of the flow periodicity in the stream-wise and span-wise directions. For further information about the numerical methods and techniques used through the code refer to [10], [11] and [12].

2.2 Parallelization approach

CHAPSim was originally parallelized using 1-D decomposition Message Passing Interface (MPI). Performance of the code is examined in collaboration with the Performance, Optimisation and Productivity (POP) centre through running a series of scalability tests. The performance of the code was tested on single and multiple nodes. Also, the size of MPI communications associated with each function were measured and the OMP directives were applied for the functions with the highest amount of generated MPI communications. The followings are identified as the main issues which cause degradation in parallelisation performance of the MPI version of the code: 1-The large number of smaller MPI messages accompanied the short period code regions causing a large amount of MPI communication messages. 2- The use of large nested FOR loops specially the ones accompanied with the MPI_SEND_RECIVE () Functions. The OMP directives were applied to the nested for loops that included MPI functions. OMP directives were applied to both serial and parallelized for loops using the syntax suggested in [2].

3. Results:

Simulations are performed for a steady channel flow using a computational domain with dimension of $12.8\delta \times 2\delta \times 6.4\delta$. The domain is meshed using $256 \times 256 \times 256$ points in the stream-wise, wall-normal and span wise directions, respectively. The in-house code is validated against the benchmark data generated

by Moser et al. [13] in terms of the mean and fluctuations turbulence velocities as shown in Fig. (1). The simulation is performed at $Re = 2800$, where Reynolds number is based on the bulk velocity and channel half-height. The equivalent friction Reynolds number is $Re_{tau} \approx 180$. All simulations have been conducted on the UK national supercomputer facility (Archer) using the INTEL compiler.

The efficiency of using the hybrid parallelization techniques is demonstrated in figure 2. It is clear from Fig. (2-a) that the speed-up is improved using the hybrid approach compared to the MPI only. The improvement in the speedup ratios between the two models is due to the lower performance of the hybrid model for single node compared with the MPI only model. The actual improvement in performance is shown in Fig. (2-b) that represents the actual number of time steps calculated for 20 minutes' period, against the number of cores used. It is shown that the hybrid model improvement can be achieved for the case of 256^3 mesh size only using 40 to 80 cores. In other words, the benefit of using the hybrid model is valid for the case of choosing a suitable number of MPI ranks and OMP threads for the targeted problem size.

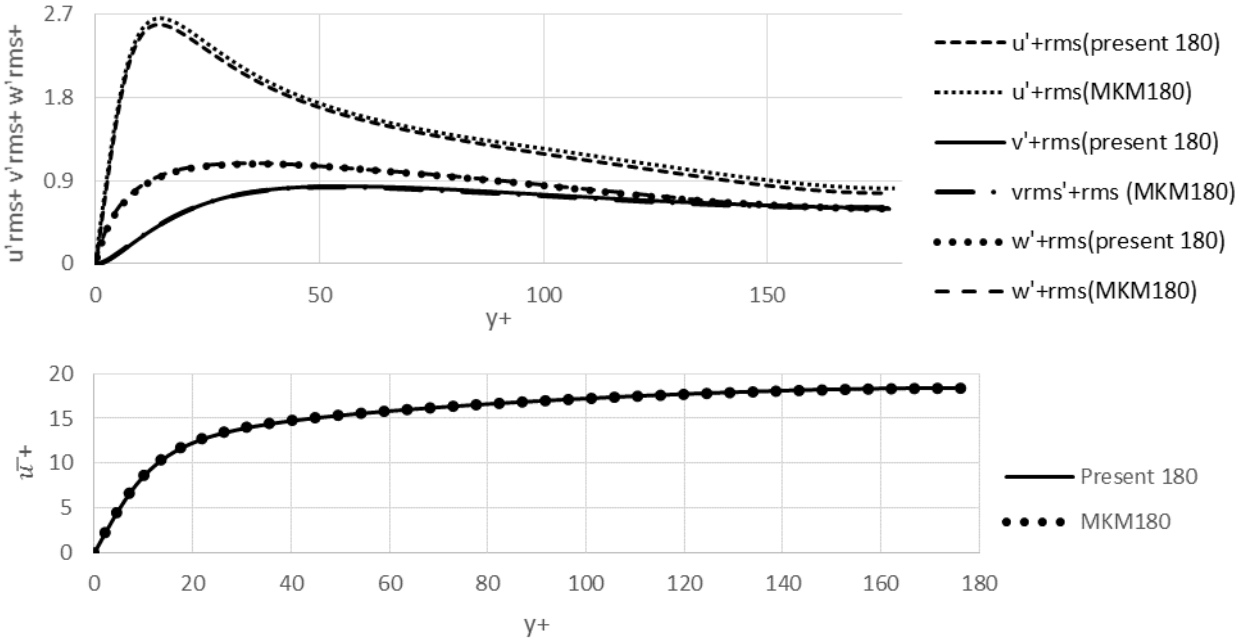

Figure 1 Validation of the simulations using CHAPSim for steady channel flow, against Code Validation Moser et al [13].

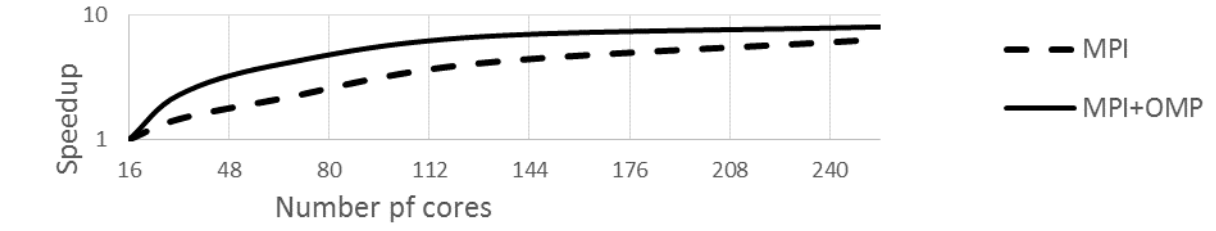

(a)

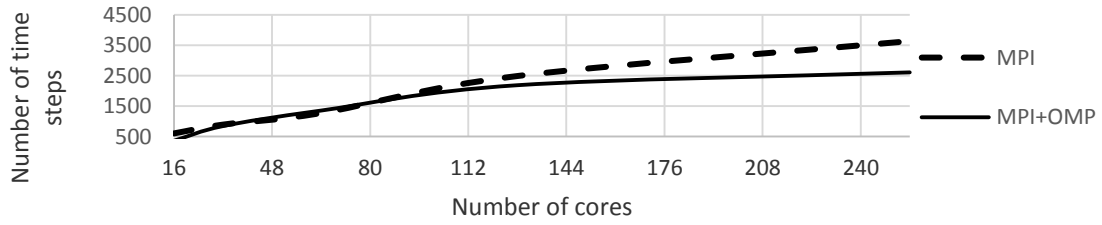

(b)

Figure 2 Code scalability using MPI and MPI+OMP: Tests using MPI and MPI+OMP (a) speed-up; (b) number of time steps

4. Conclusions

Performance of Message passing interface (MPI) and a hybrid (MPI/OMP) parallelization techniques on the code scalability was examined for an in-house code DNS code CHAPSim. The simulation was performed for a turbulent channel flow. Turbulence statistics from the simulated channel flow are validated against some benchmark data. The OpenMP directives applied on the most time consuming nested "FOR" loops showed a significant impact on the performance of the code in terms of the speedup ratios. The performance of the MPI only model with one single node was better than the performance of the code using the hybrid technique; which justify the bump in performance scalability wise. The actual increase of performance obtained by the progress of the code at constant period of time showed the improvement is only achievable for certain combinations of MPI ranks, OMP threads and mesh size in the x, y and z directions. The use of hybrid MPI/OMP technique is beneficial in improvement of the performance of CFD codes as it is simple and gradual to implement on any DNS code. The performance of Hybrid CFD codes are highly depending on the hardware and software of the supercomputing facility, however, the fact that the OMP directives can be ignored and prevented from working without any changes on the code makes it a very convenient improvement additive to any CFD code.

Acknowledgement

The authors gratefully acknowledge the financial supports by Faculty of Engineering, Liverpool John Moores University. This work made use of ARCHER supercomputing facility sponsored by EPSRC through the UK Turbulence Consortium (UKTC) (grant no. EP/L000261/1).

References

[1]Moin. P and Mahesh.K, 1998, *Annual Reviews Fluid Mechanics, **30,** 539-578*

[2] Spalart. V, 2000, *Inter-national Journal of heat and fluid flow*, **21**,252-263.

[3] Mallon.D.A et al. , 2009, Performance Evaluation of MPI, UPC and OpenMP on Multicore Architectures, *European Parallel Virtual Machine/Message Passing Interface Users' Group Meeting. Springer* Berlin Heidelberg.

[4] Hoeflinger.J, Alavilli.P, Jackson.T and Kuhn.B, 2000, Producing Scalabe Performance with OpenMP Experiments with two CFD Applications, Parallel Computing, 27, 391-413

[5] Henty.D.S, 2000, Performance of Hybrid Message-Passing and Shared-Memory Parallelism for Discrete Element Modeling, Dallas, USA, *Proceedings of the 2000 ACM/IEEE Conference on Supercomputing,1-9*

[6] Nling. L and Laizet. S, 2010, 2DECOM&FFT – A Highly Scalable 2D Decomposition Library and FFT Interface, *Cray User Group Proceedings*, Scotland, UK, 1-13.

[7] Rabenseifner. R, 2003, Hybrid Parallel Programming on HPC platforms, Germany, Fifth European Workshop on OMP, EWOMP, 22-26.

[8] Bassi.F, Colombo.A, Crivellini.A, Franciolini.M, 2016, Hybrid OpenMP/MPI Parallelization of High-Order Discontinuous GALERKIN CFD/CAA Solver, Crete Island, Greece, VII European Congress on Computational Methods in Applied Sciences and Engineering. 1-21

[9] Kim. J and Moin. P, 1985, Journal of Computational Physics, 59(2), 308-325.

[10] He.S and Seddighi.M, 2013, Journal of Fluid Mechanics, 715, 60-102

[11] Seddighi. M, 2011, Study of turbulence and wall shear stress in unsteady flow over smooth and rough wall surfaces. PhD Thesis.

[12] Orlandi.P, 2012, Fluid flow phenomena: A numerical toolkit. Kluer Academic Publishers.

[13] Moser. D, Kim. J and Mansour. N,1999, Physics of Fluids, 11(4), 943-945.